

THE GROWTH AND STRUCTURE OF NICKEL OXIDE FORMED ON THE  
(100), (110) AND (111) CRYSTAL FACES OF NICKEL

THE GROWTH AND STRUCTURE OF NICKEL OXIDE FORMED ON THE  
(100), (110) AND (111) CRYSTAL FACES OF NICKEL

by

NGUYEN NGOC KHOI, B.Sc., M.Sc.

A Thesis

Submitted to the School of Graduate Studies  
in Partial Fulfilment of the Requirements  
for the Degree  
Doctor of Philosophy

McMaster University

June, 1972

© Nguyen Ngoc Khoi 1973

DOCTOR OF PHILOSOPHY (1972)  
(Metallurgy and Materials Science)

McMASTER UNIVERSITY  
Hamilton, Ontario

TITLE: The Growth and Structure of Nickel Oxide  
Formed on The (100), (110) and (111) Crystal  
Faces of Nickel

AUTHOR: Nguyen-ngoc-Khoi, B.Sc. (Georgia Institute of  
Technology, Atlanta, Georgia  
U.S.A.)  
M.Sc. (Georgia Institute of  
Technology, Atlanta, Georgia  
U.S.A.)

SUPERVISOR: Professor W. W. Smeltzer

NUMBER OF PAGES: xiv, 248

#### SCOPE AND CONTENTS

In this thesis, the growth and structure of nickel oxide on three single crystal faces of nickel, viz the (100) (110), and (111), in the temperature range from 500 to 800°C have been investigated.

A study has been made on the morphological development of the oxide and its structures by electron microscopy, X-ray diffraction and scanning electron microscopy in order to correlate these structures with the kinetics. Measurements of the kinetics for oxide growth on the different nickel crystal faces have shown non-parabolic behaviour and marked anisotropy in reaction rates due to the differences in crystallographic orientations. The deviation from parabolic behaviour and anisotropy in reaction rates are shown

to be associated with the structural defects arising in the oxide layer during the growth process, epitaxial relationships between the metal and oxide, and orientation relationships between the oxide grains in the scale. The development of epitaxy can be justified in terms of the coincidence of a close packed direction between the metal and the oxide. Preferred growth leads to the formation of a duplex scale.

A model for growth of the nickel oxide films and scales based on the simultaneous diffusion of nickel across the films via lattice defects and short-circuit paths is advanced to correlate the oxidation kinetics with the oxide structure. It is assumed in this model that the decrease in the density of the short-circuit diffusion sites at nickel oxide grain boundaries is determined by oxide grain growth processes. This model is shown to account satisfactorily for the observed oxidation kinetics of the (100) and (111) nickel faces. Also, the values for nickel grain boundary diffusion coefficients have been calculated for the first time for oxide on these two faces.

## ACKNOWLEDGMENTS

This thesis was carried out under the guidance of Dr. W. W. Smeltzer to whom I wish to express my thanks for suggesting the problem, for his continuous guidance and encouragement throughout the stages of this project.

The author is indebted to Dr. J. D. Embury for the help with the interpretation of the microscopy results and many fruitful discussions.

Thanks are due to the staff and graduate students of the McMaster Metallurgy department for their help and friendship, in particular I wish to thank Mr. R. Foster for assistance in the construction of the apparatus, Messrs. Dave Hodgson and Tom Bryner for the photographic work, Messrs. R. Jarochowicz and T. Tandi for the assistance with the electron microscope.

The project was supported by grant of the National Research Council of Canada to Dr. Smeltzer and the McMaster Graduate Fellowship and the Ontario Graduate Fellowship to the author.

## TABLE OF CONTENTS

	<u>Page</u>
CHAPTER 1 INTRODUCTION	1
CHAPTER 2 LITERATURE REVIEW	5
2.1 Introduction	5
2.2 Epitaxy	6
2.3 Oxidation of nickel	7
2.3.1 Structural investigation	8
(a) Polycrystalline substrate	8
(b) Single crystal substrate	12
2.3.2 Oxidation kinetics	31
(a) Reaction mechanisms at intermediate temperature	31
(b) Reaction mechanism at high temperature	34
(c) Calculation of the parabolic rate constant	35
CHAPTER 3 EXPERIMENTAL PROCEDURE AND OXIDATION APPARATUS	42
3.1 Sample preparation	42
3.2 Oxidation apparatus	44
3.3 Oxidation procedure	46
3.4 Stripping the oxide	46
3.5 Examination of the oxide films by transmission electron microscopy	48

	<u>Page</u>
3.6 Examination of the oxide cross section by scanning electron microscopy	48
3.7 X-ray studies of the oxide scales	49
CHAPTER 4 EXPERIMENTAL RESULTS	50
4.1 Surface preparation investigations	50
4.2 Transmission electron microscopy for the (100) nickel face	53
4.2.1 Specimen exposure: 5 min.	55
4.2.2 Specimen exposure: 10 min.	62
4.2.3 Specimen exposure: 20 min.	65
4.2.4 Specimen exposures: 30 and 40 min.	65
4.2.5 Specimen exposures: 70 and 120 min.	68
4.2.6 Specimen exposures: 3 and 5 hr.	68
4.2.7 Crystallite size and distribution	73
4.2.8 Summary of the results of the (100) face	76
4.3 Transmission electron microscopy results for (110) nickel face	80
4.3.1 Specimen exposure: 15 min.	80
4.3.2 Specimen exposure: 30 min.	85
4.3.3 Specimen exposure: 60 min.	85
4.3.4 Specimen exposure: 2 hr.	89
4.3.5 Specimen exposure: 3 hr.	92
4.3.6 Specimen exposure: 4 hr.	92
4.3.7 Specimen exposure: 6 hr.	97
4.3.8 Crystallite size and distribution	97
4.3.9 Summary of the results of the (110) face	97
4.4 Transmission electron microscopy results for the (111) nickel face	102
4.4.1 Specimen exposure: 10 min.	102
4.4.2 Specimen exposure: 85 min.	104
4.4.3 Specimen exposure: 60 min.	109
4.4.4 Specimen exposure: 120 min.	110
4.4.5 Specimen exposure: 4 hr.	114
4.4.6 Specimen exposure: 6 hr.	114
4.4.7 Crystallite size and distribution	117
4.4.8 Summary of the results of the (111) face	117

	<u>Page</u>
4.5 X-ray diffraction results of the thick oxide films	120
4.6 Scanning electron microscope results of the thick oxide film	134
4.6.1 Results for the (100) nickel face	134
4.6.2 Results for the (110) nickel face	139
4.6.3 Results for the (111) nickel face	146
4.7 Oxidation kinetics. Results from a gravimetric investigation	150
CHAPTER 5 DISCUSSION OF RESULTS	156
5.1 General considerations	156
5.2 Structural considerations	157
5.2.1 Development of the oxide structure	157
5.2.2 Morphological development of the oxide layers	166
5.2.3 Oxide growth model	169
5.2.4 Concluding remarks concerning the oxide structure	179
5.3 Oxidation kinetics	181
5.3.1 Consideration of diffusion model	181
5.3.2 Mathematical analysis	184
5.3.3 Testing different models of f	185
5.3.4 Curves fitting	189
5.3.5 Evaluation of the grain boundary oxidation diffusion constants	195
5.3.6 Conclusions from studies of the oxidation kinetics	203
5.4 Correlations between the structure and kinetics	204
CHAPTER 6 SUGGESTIONS FOR FURTHER WORK	206
CHAPTER 7 CONCLUSIONS	208
APPENDIX A THE CONSTRUCTION OF THE RECIPROCAL LATTICE PLANES	211



	<u>Page</u>
APPENDIX B	
INDEXING OF THE ELECTRON	
DIFFRACTION PATTERNS	228
APPENDIX C	
SOURCES OF ERRORS	237
REFERENCES	241

## LIST OF ILLUSTRATIONS

<u>Figure</u>	<u>Subject</u>	<u>Page</u>
2.3.1(i)	The "O-Ni" intermediate structures found on the (100) nickel face	14
2.3.1(ii)	The "O-Ni" intermediate structures found on the (110) nickel face	16
2.3.1(iii)	The "O-Ni" intermediate structures found on the (111) nickel face	17
2.3.1(iv)	Schematic diagram of oxide orientations found on the (100) nickel face	25
2.3.2	Parabolic rate constant for nickel oxidation versus reciprocal temperatures	41
3.2	Schematic diagram of the oxidation apparatus	45
4.1.1	Lane pattern of (100) face of nickel after mechanical polishing	52
4.1.2	Reflection diffraction pattern of (100) for nickel after mechanical polishing	52
4.1.3	Oxide formed on mechanically polished surface	54
4.1.4	Reflection diffraction of (100) face of nickel after electro-polishing	54
4.1.5	Reflection diffraction of surface after reduction in H <sub>2</sub> or vacuum anneal	54
4.2.1(d)-(g)	Electron micrographs of (100) nickel specimens exposed for 5 min	57

<u>Figure</u>	<u>Subject</u>	<u>Page</u>
4.2.2(a)-(f)	Electron micrographs of specimen exposed for 10 min	63
4.2.3(a)-(e)	Electron micrographs of specimen exposed for 20 min	65
4.2.4(a)-(f)	Electron micrographs of specimen exposed for 30 and 40 min	69
4.2.5(a)-(f)	Electron micrographs of specimen exposed for 70 and 120 min	71
4.2.6(a)-(f)	Electron micrographs of specimen exposed for 180 and 300 min	74
4.2.7 (a)	Crystallite size distribution for oxide films formed on the (100) nickel face at 500°C	77
4.2.7 (b)	Average crystallite size versus oxidation time	78
4.3.1(a)-(n)	Electron micrographs of (110) nickel specimen exposed for 15 min	82
4.3.2(a)-(k)	Electron micrographs of specimen exposed for 30 min	86
4.3.3(a)-(f)	Electron micrographs of specimen exposed for 60 min	90
4.3.4(a)-(g)	Electron micrographs of specimen exposed for 120 min	93
4.3.5(a)-(f)	Electron micrographs of specimen exposed for 180 min	96
4.3.6(a)-(d)	Electron micrographs of specimen exposed for 240 min	98

<u>Figure</u>	<u>Subject</u>	<u>Page</u>
4.3.8(a)	Crystallite size distribution for oxide film formed on the (110) face at 500°C	99
4.3.8(b)	Average crystallite size vs oxidation time	100
4.4.1(a)-(g)	Electron micrographs of (111) nickel specimen exposed for 10 min	105
4.4.2(a)-(d)	Electron micrograph of specimen exposed for 35 min	108
4.4.3(a)-(g)	Electron micrographs of specimen exposed for 60 min	111
4.4.4(a)-(d)	Electron micrographs of specimen exposed for 120 min	113
4.4.5(a)-(d)	Electron micrographs of specimen exposed for 240 min	115
4.4.6(a)-(d)	Electron micrographs of specimen exposed for 360 min	116
4.4.7 (a)	Crystallite size distribution for oxide films formed on the (111) nickel face at 500°C	118
4.4.7 (b)	Average crystallite size vs oxidation time	119
4.5.1	Texture coefficients of the oxide formed on the (100) nickel face	127
4.5.2	Texture coefficients of the oxide formed on the (110) nickel face	129
4.5.3	Texture coefficients of the oxide formed on the (111) nickel face	132

<u>Figure</u>	<u>Subject</u>	<u>Page</u>
4.6.1(a) - (h)	Scanning electron micrographs of surface and cross section views of (100) nickel specimens	136
4.6.2(a) - (1)	Scanning electron micrographs of surface and cross section views of (110) nickel specimens	141
4.6.3(a) - (h)	Scanning electron micrographs of surface and cross section views of (111) nickel specimens	147
4.7.1(a)	Oxidation kinetics for the (100) nickel face	152
4.7.1(b)	Oxidation kinetics for the (110) nickel face	153
4.7.1(c)	Oxidation kinetics for the (111) nickel face	154
5.2.1	Schematic diagram showing the morphological development of the oxide structure	158
5.3.2(a)	Plot of $\ln \left( \frac{dx^2}{dt} - K_L \right)$ versus time for the three metal faces	188
5.3.2(b)	Plot of $\frac{1}{\left( \frac{dx^2}{dt} - K_L \right)^2}$ versus time for the (100) nickel face	190
5.3.2(c)	Plot of $\frac{1}{\left( \frac{dx^2}{dt} - K_L \right)^2}$ versus time for the (111) nickel face	191
5.3.4(a)	Curve fitting of the experimental data to equation (5-29) for the (100) nickel face	193

<u>Figure</u>	<u>Subject</u>	<u>Page</u>
5.3.4(b)	Curve fitting of the experimental data to equation (5-29) for the (111) nickel face	194
5.3.5(a)	Boundary diffusion oxidation constant, $K_B$ , versus reciprocal of temperature	200
5.3.5(b)	Plot of $K_B f(t)$ versus reciprocal of temperature	202

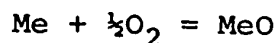
## LIST OF TABLES

<u>Table</u>	<u>Title</u>	<u>Page</u>
2.3.2	Parabolic rate constant	40
4.5.1	Texture coefficient of the (100) face	126
4.5.2	Texture coefficient of the (110) face	128
4.5.3	Texture coefficient of the (111) face	131
4.6.1	SEM results for the (100) nickel face	138
4.6.2	SEM results for the (110) nickel face	145
4.6.3	SEM results for the (111) nickel face	149
5.3.5(a)	Boundary diffusion oxidation constants for the oxide on the (100) nickel face (evaluated from $K_p(t)$ )	196
5.3.5(b)	Boundary diffusion oxidation constants for the oxide on the (100) nickel face (evaluated from the slope S)	197
5.3.5(c)	Boundary diffusion oxidation constants for the oxide on the (111) nickel face (evaluated from $K_p(t)$ )	198
5.3.5(d)	Boundary diffusion oxidation constants for the oxide on the (111) nickel face (evaluated from the slope S)	198

## CHAPTER 1

### INTRODUCTION

Oxidation of a metal is an heterogeneous reaction involving a gas and a solid. The chemical reaction can be simply written as:



when Me is a divalent metal, O the oxygen, and MeO the oxide. The product MeO, unless it is volatile usually adheres to the metal and shares many of the physical properties with the parent solid.

In spite of its simple overall chemical equation, oxidation is a complex chemical process involving many variables and reaction mechanisms. The oxidation process can be regarded as made up of the following steps: adsorption of oxygen, formation of the nuclei and the lateral spreading of these nuclei to form a continuous film. Adsorption and nucleation are functions of the surface properties such as crystallographic orientation, crystal defects and impurities, hence of surface preparation.

The formation of a continuous film when it is compact and adherent separates the oxygen and the metal and further reaction is only possible if the reactants can be transported through this superficial layer. Thermally activated solid



state diffusion via lattice defects has been shown by many investigators (1,2) to be the main mechanism for transport at high temperature; parabolic oxidation behaviour, a consequence of this type of transport, has accordingly been consistently observed.

Often deviations from the parabolic law have been observed and different models and mechanisms proposed to explain these deviations. For formation of thin films at relatively low temperature, Cabrera and Mott (3) have proposed a film growth model which takes into account the presence of an electric field set up by the chemisorbed oxygen to derive equations for most of the observed growth rates. In the scaling range at high temperature, most deviations from the parabolic law have been found to be associated with the physical breakdown of the scales such as blistering, loss of adhesion, formation of pores and oxide volatility. However, for the growth of thin oxides prior to the onset of parabolic behaviour, most metals oxidize too rapidly to be explained by lattice diffusion.

Marked deviation from parabolic behaviour have been consistently observed in the intermediate temperature range from approximately 300 - 800°C. Temperature coefficients of the reaction rate constant often show an activation energy of less than half the value for true lattice diffusion. Furthermore, oxidation studies of many single crystal faces of metal have reported considerable anisotropy in reaction

rates due to crystallographic orientation alone<sup>(4)</sup>. These observations have been made at thicknesses ( $>1\mu$ ) beyond the region of electric field transport and on cubic oxides such as NiO and  $\text{Cu}_2\text{O}$  where lattice diffusion should be completely isotropic. All these observations are at variance with explanations based on lattice diffusion alone and another type of transport mechanism must be invoked.

Structural studies of the oxide films<sup>(5,6)</sup> have shown that these films are highly defective: they contain dislocations, pores and usually are made up of very small crystallites. Consequently many investigators have advanced the hypothesis that rapid growth can occur by diffusion in the lattice and along paths of low resistance offered by these defects. Perrow et al<sup>(7)</sup> have demonstrated that these structural defects can act as short circuit diffusion path in the oxidation of polycrystalline nickel in the intermediate temperature range and more recently Cathcart<sup>(8)</sup> has shown that the anisotropy in reaction rates observed in the oxidation of the single crystal faces of nickel can be justified by the density and type of defects set up by the growth mechanism.

In the present investigation the nature and distribution of the structural defects in thin nickel oxides thermally grown on the three single crystal faces of nickel exposed to oxygen are studied by the techniques of transmission electron microscopy, X-ray diffraction and scanning electron microscopy. Nickel was chosen for a number of reasons.

Besides being the most important metal in the development of high temperature alloys, oxidation of nickel gives a compact, adherent, face centered cubic (NaCl) nickel oxide. The oxygen solubility is low and the thermal expansion coefficients of nickel and nickel oxide are almost identical. In addition, ample diffusion data of nickel in nickel oxide is available from the literature.

The experimental results are presented to support the hypothesis underlining the importance of these types of defects in the oxidation mechanism of thin films. These defects are set up by the growth process itself; the crystallographic relationships between the metal substrate and the growing oxide result in epitaxial nucleation and preferential growth which in turn affect the distribution and nature of these defects. A literature review is presented according to these ideas and experimental results are used to correlate with the kinetics data. Finally, an oxide growth model is proposed to rationalise observations.

## CHAPTER 2

### LITERATURE REVIEW

#### 2.1 Introduction

The formation and growth of an oxide film on a metal substrate proceeds by many reaction mechanisms such as adsorption, nucleation and diffusion. The detailed description of these processes has been extensively examined in monographs by Benard<sup>(9)</sup>, Hauffe<sup>(10)</sup>, Kofstad<sup>(11)</sup>, Kubaschewski and Hopkins<sup>(4)</sup>.

Since the oxide usually adheres to the metal, many of its physical properties have been found to be related to the substrate. One of the most commonly observed features in many deposit-substrate systems is that a particular orientation relationship exists between the deposit and substrate. This property was first systematically studied by Royer<sup>(12)</sup> in 1928 who introduced the term "epitaxy" to define the crystallographic relationship between the two crystalline surfaces.

The existence of an epitaxial relationship does not mean however that the substrate structure is necessarily continued across its interface and into the deposit altered only by the expansion or contraction in lattice parameter. This is illustrated by the frequently reported epitaxial

relationship in FCC structures: (111) oxide //(100) metal with  $[0\bar{1}1]$  oxide //  $[011]$  metal. The coincidence of the  $\langle 110 \rangle$  directions which are the close-packed direction in the FCC structure has been found to be the most frequently observed. Gerdes and Young<sup>(13)</sup> have reviewed 3000 papers yielding 600 orientation relationships between the deposit and substrate. 86% of these relationships for the FCC, HCP and NaCl type structures can be accounted for by the parallel alignment of the close-packed directions.

Very often the nuclei have different orientations and the formation of a continuous film depends on the growth, migration and coalescence of these nuclei. Pashley<sup>(14)</sup> has shown that the films thus formed are highly defective and contain crystallite boundaries, twins and dislocations which are all intrinsic parts of the growth mechanism. These types of defects can play an important role in the growth of oxide films since they have been shown<sup>(8)</sup> to alter profoundly the transport mechanism of the reactants.

## 2.2 Epitaxy

The formation of an oriented overgrowth on a crystal-line surface involves the creation of an interface between the deposit and substrate. While it is generally agreed that the preferred orientation of the deposit will be in such a way as to minimize this interfacial energy, the mechanism and criteria for this minimization remain elusive and often difficult to define. Many theoretical considerations have

been advanced to justify epitaxial conditions, all of which are by no means equally accepted today, but often are useful to explain a portion of the experimental results. (See, for example, review articles by Neuhaus<sup>(15,16)</sup>, Siefert<sup>(17)</sup> and Pashley<sup>(18,19)</sup>).

The theories which have received broadest application in the literature include: (1) the least misfit between the two lattice planes in contact at the interface (Royer<sup>(12)</sup>), (2) the fulfilment of the coordination number (Drabble<sup>(20)</sup>), (3) the specification of the interfacial reactions (Engel<sup>(21,22)</sup>), (4) the minimization of the interfacial energies (Bauer<sup>(23,24)</sup>, Bauer et al<sup>(25)</sup>), (5) the pseudomorphic accommodation by dislocations (Van der Merve<sup>(26)</sup>, Frank and Van der Merve<sup>(27)</sup>), (6) the Brownian migration of crystallites (Masson, Metois and Kern<sup>(28)</sup>), (7) and the thermodynamic consideration of nucleation phenomena (Walton<sup>(29)</sup>, Hirth and Pound<sup>(30)</sup>, Robins and Rhodin<sup>(31)</sup>, Feder et al<sup>(34)</sup>, Kenty and Hirth<sup>(33)</sup>). Among these theories the simple concept of misfit was the most generally accepted and has been used as one of the criteria in other theories. The thermodynamic considerations of nucleation phenomena<sup>(33)</sup> have been most successful but by no means complete since many parameters important to the epitaxial condition such as deposition rate, impingement flux, interfacial energies and epitaxial temperatures have been justified.

### 2.3 Oxidation of nickel

### 2.3.1 Structural investigations

Oxidation of nickel leads to the formation of only one type of oxide, nickel oxide, having a NaCl structure with a lattice parameter of 4.1769 Å (34). The solubility of oxygen in nickel has been determined to be only .044 at % at 1000 °C<sup>(35)</sup>. The coefficients of thermal expansion of nickel and nickel oxide differ only by .05% in the temperature range from 25 - 1000 °C. The investigations on growth of the oxide and its morphology, accordingly, can be broadly divided into two groups, those dealing with the oxidation of polycrystalline nickel and those dealing with the oxidation of nickel single crystal faces.

(a) Polycrystalline nickel substrate. The early oxidation stage of polycrystalline nickel in an H<sub>2</sub>/H<sub>2</sub>O atmosphere at 1100 °C was studied by Martius<sup>(36)</sup>. The most noticeable feature was the occurrence of the largest density of nuclei at metal grain boundaries. The number and the shape of the oxide nuclei on the metal surface varied with each individual grain, depending on crystallographic orientation. The initial oxide always appeared as discrete nuclei which grew laterally to form a continuous layer.

Perrow et al<sup>(7)</sup> investigated the structures of thin oxide films formed at 500 and 600 °C on mechanically polished surfaces. The films were found to consist of small crystallites ranging from 200 to 800 Å in size and the oxide thickness and orientation varied from one metal grain to another.

With continued exposure to oxygen, structural changes and grain growth occurred and dislocations were often observed.

Texture studies of thick oxide scales formed on mechanically polished samples were reported by Gulbransen and Hickman<sup>(37)</sup>. At 1 torr oxygen pressure and above 600°C, the oxide developed a fiber texture. This texture was believed to arise by growth processes as the oxide thickened and not to be influenced by the substrate. This preferred growth has been confirmed by other workers<sup>(38,39)</sup> to be the (001) plane of nickel oxide lying parallel to the metal surface. The influence of the metal substrate was later investigated by Goswami who oxidized a fiber textured vapor deposited nickel<sup>(40)</sup>. The studies showed that during the initial stage of oxidation the oxide has its fiber texture parallel to the metal, becomes randomly oriented with further exposure and finally exhibits a preferred orientation. The type of orientation was found to depend on the oxidation conditions.

The microstructure of the scales has been subjected to many controversial interpretations. Sartell and Li<sup>(41)</sup> reported the oxide scales formed between 900 and 1200 °C to consist of two distinct layers. Since platinum markers were located between these two layers, it was concluded that the inner layer grew by anion movement. Ilscher and Pfeiffer<sup>(42)</sup> have oxidized nickel containing 0.1% Mn and also found the wire marker buried within the scale, the inner oxide layer



exhibiting a noticeable porosity. In an extensive study, Berry and Paidassi<sup>(43)</sup> have shown that at or below 900°C a single oxide layer is formed its thickness varying from grain to grain. Above 900°C, a duplex scale consisting of a compact columnar outer layer is observed along with a fine grained porous inner layer. Both of these layers grew parabolically. The ratio of their thicknesses (outer/inner) varied from 0.4 at 1000°C to 0.2 at 1200°C. The presence of the two layers would appear to be associated with traces of impurities since studies made on 99.98% nickel have reported only one layer while two layers are observed on 99.95 and 99.97% nickel.

In a rather elaborate investigation, Rhines and Wolf<sup>(44)</sup> have attributed the origin of the inner layer to the presence of growth stresses. The following experimental evidence has been presented by the authors. In the initial stage of oxidation, columnar void free grains extending from the metal oxide interface to the oxide gas interface were observed. The formation of these columnar grains is due to the outward diffusion of nickel ions. Oxygen may also diffuse inwards via the boundaries between these columnar grains resulting in the formation of new oxide within the boundaries. The appearance of this oxide, causes the development of grain boundary pressure and as a result new fine grain oxide is formed at the metal/oxide interface.

In view of these conflicting observations many mecha-

nisms have been proposed to explain the morphological development of the oxide structure. To the present, however, an unique mechanism has not been advanced to account for the diverse experimental results. It has been suggested that the boundary between the oxide layers within a scale is simply the original metal surface. Indeed observations have shown that the interface is often flat, but it is difficult to justify this argument. If it is the original interface, it should be observed on every sample and should be relatively insensitive to metal impurities. The ratio of the thickness of the two layers also, should correspond to the volume of the nickel consumed if metal diffusion only occurs when it is converted from metal to oxide. This expansion, which is only 18%, is much smaller than the inner layer thickness.

The position of the markers at the interface between the two layers has led to the postulation of mobile anions, but there is little or no evidence of oxygen diffusion via lattice defects. The diffusion coefficient of oxygen in nickel oxide was found to be  $10^3$  slower than of nickel at  $1000^\circ\text{C}$ <sup>(45)</sup>. Oxygen diffusion via grain boundaries is possible, but it is difficult to justify the presence of the two layers by this mechanism unless one accepts the argument of Rhines and Wolf.

Birks and Rickert<sup>(46)</sup> have proposed a different mechanism based on the oxide plasticity. It is argued that insufficient plastic flow leads to the loss of adhesion between the

oxide and the metal. This will happen readily in a metal deficit oxide where there is a "metal consumption zone". The loss of adhesion will restrict the flow of nickel, causing a drop in the chemical potential of nickel and a rise in the potential of oxygen. Nickel oxide will dissociate and supply oxygen to the metal surface. New oxide is formed and the inner layer continues to grow by the same mechanism while the outer layer grows by the outward migration of nickel. This phenomenon will not be observed at high temperature where the oxide is sufficiently plastic to prevent loss of adhesion.

(b) Single crystal nickel substrate. The structural studies of oxides formed on single crystal faces usually deal with the epitaxial relationships between the oxide and metal. The development of epitaxy can be partially understood by the study of the adsorption of oxygen on the metal surface. Due to its low penetrating power, low energy electron diffraction (LEED) is very suitable for the investigation of the two dimensional structures. The results have indicated that prior to the formation of the oxide, many intermediate structures of "oxygen nickel" or "O-Ni" may be observed. The number and type of structure vary with metal crystallographic orientation.

(1) The intermediate structures. The "O-Ni" Structures found on the (001) nickel face. Farnsworth and co-workers (47,48) found that a gradual exposure of the (001) face of nickel to oxygen at a pressure of  $10^{-6}$  torr or less gives rise to two intermediate structures. The first intermediate struc-

ture is the Ni (001) (2x2) which is shown in figure 2.3.1(i) (a). The (2x2) designation indicates twice the dimension of the unit mesh of the (001) nickel surface. (For reference, the unit mesh is drawn in dashed line). With further exposure the Ni(001) $\underline{c}$ (2x2) was observed. The  $\underline{c}$  stands for the centered unit mesh. This is shown in (b). The final structure is the formation of the oxide with its cube face, (001), parallel to the metal. These two structures are believed to have evolved from the exchange between the oxygen and nickel atoms. Germer et al<sup>(49)</sup> later confirmed these findings but argued that the two types of structures are essentially undisturbed nickel surfaces.

The "O-Ni" structures found on the (011) face. The (011) face of a FCC system has a more "open structure" since each nickel atom has only seven nearest neighbors compared to eight and nine for the (100) and (111) face. Up to six intermediate structures have been observed and investigators have not yet agreed on their types and the sequence of their appearance. All the six are schematically shown in figure 2.3.1.(ii).

Germer and McRae<sup>(50)</sup> have reported that the first structure to appear is the Ni(011)(2x1) shown in (b). This is followed by the (5x2)<sup>1</sup> and (3x1) shown in (c) and (d). Sometimes the (5x1) seen in (e), is also observed. Park and Farnsworth<sup>(51,52)</sup> have found the first structure to be the (2x2) seen in (a). The next two structures are the (2x1) and (3x1) shown in (b) and (c). Both groups however agreed on

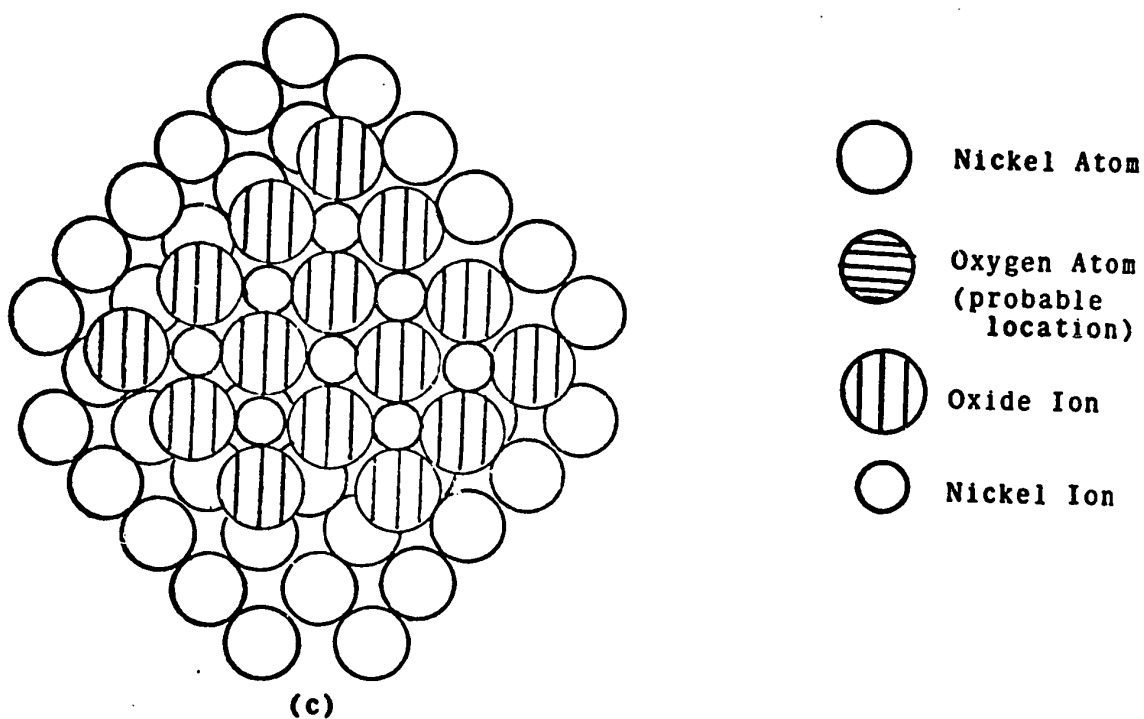
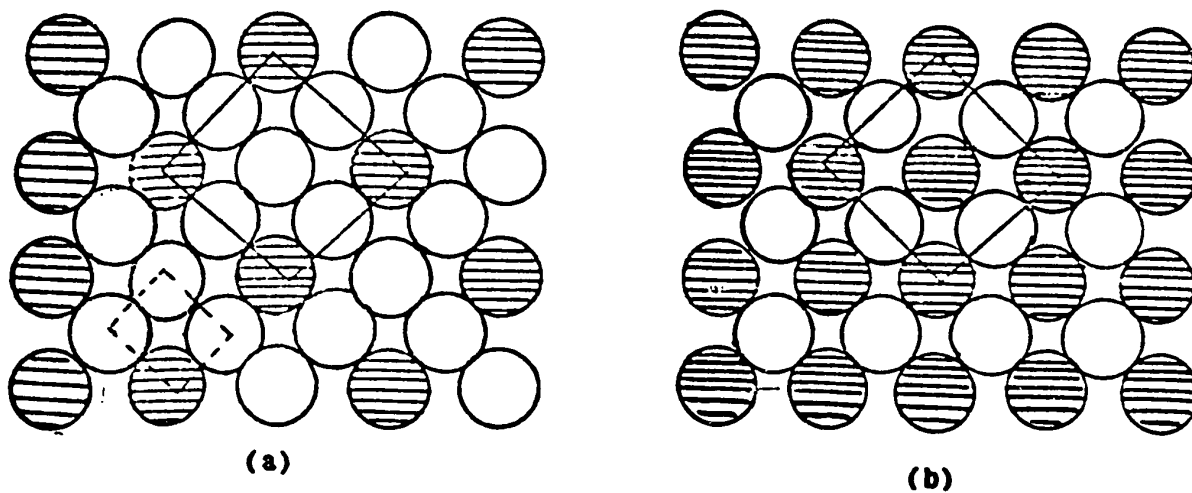


Figure 2.3.1(i) The "O-Ni" intermediate structures found on the (100) nickel face (64)

(a) Ni(001)(2x2)

(b) Ni(001)c(2x2)

(c) NiO structure

the final structure of the oxide which is the oxide having its cube face, ((001) face), parallel to the (011) face of nickel. This is a very important observation for as we shall see in the experimental results, the oxide films formed on this face sometimes exhibit perfect (100) mosaic structure. The "O-Ni" found on the (111) face. Germer<sup>(53)</sup> observed that the first transient structure was quintuple-spaced and it was designated as the "Q-structure" shown in figure 2.3.1(iii)(a). This structure is not observed at room temperature since it is believed to consist of only oxygen atoms forming an amorphous layer. Above 500°C this structure can be detected, but it is not consistently observed. More recently McRae<sup>(54)</sup> found that an exposure to oxygen in the pressure range from  $5 \times 10^{-9}$  to  $1 \times 10^{-6}$  torr-sec produced the Ni(111) (2x2) shown in (b). The (2x2) designation again refers to the mesh dimension having twice the spacing of the unit mesh of the (111) face. The unit mesh is drawn by dashed lines in (a). Additional exposure to  $20 \times 10^{-6}$  torr produced the Ni (111) ( $\sqrt{3} \times \sqrt{3}$ ) R(30°) structure. The new mesh has  $\sqrt{3}$  time the unit mesh dimension and it is rotated 30° with respect to the unit mesh. With further exposure the oxide is formed having its (111) face parallel to the metal.

In conclusion, the LEED studies have indicated that under very low oxygen pressure, the formation favored a parallel orientation for the (100) and the (111) face but for the (011) face the (100) oxide was found to be the stable orientation.

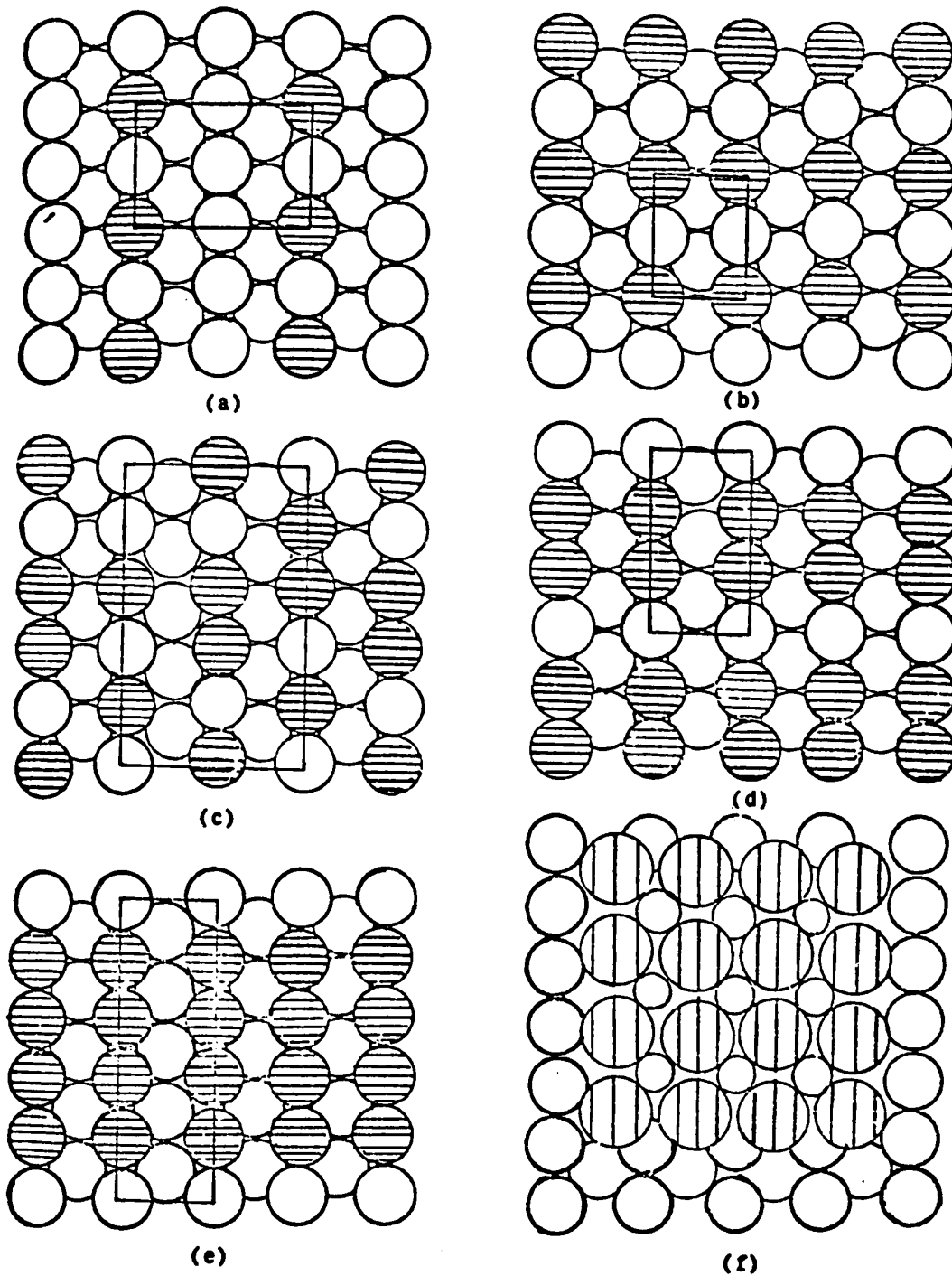


Figure 2.3.1(ii) The "O-Ni" intermediate structures found on the (110) nickel face (64)

- |     |         |                    |     |         |           |
|-----|---------|--------------------|-----|---------|-----------|
| (a) | Ni(110) | (2x2)              | (b) | Ni(110) | (2x1)     |
| (c) | Ni(110) | (5x2) <sup>1</sup> | (d) | Ni(110) | (3x1)     |
| (e) | Ni(110) | (5x1)              | (f) | NiO     | structure |

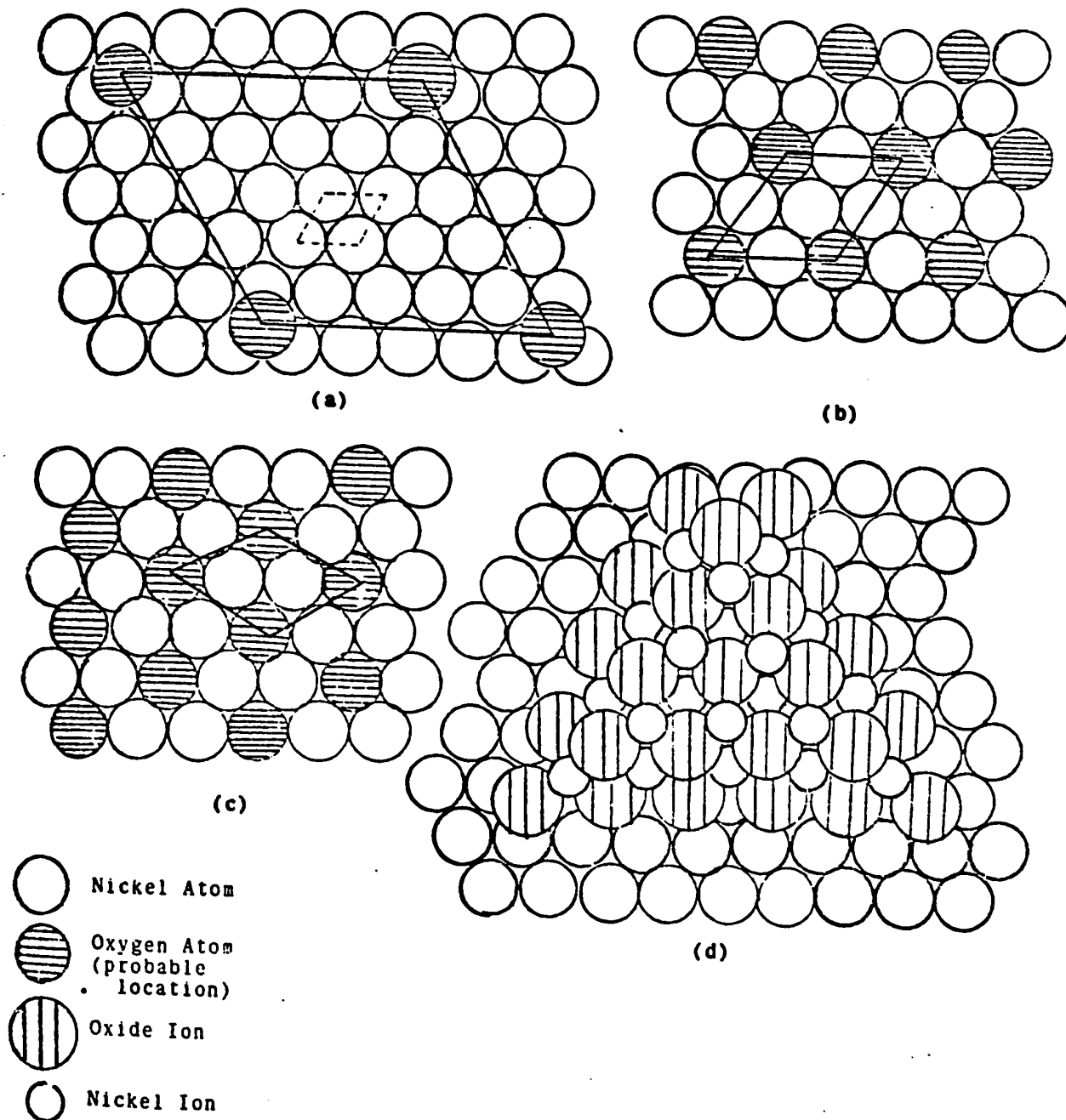


Figure 2.3.1(iii) The "O-Ni" intermediate structures found on the (111) nickel face (64)

- (a) Q-structure (b) Ni (111) (2x2)  
 (c) Ni (111) ( $\sqrt{3} \times \sqrt{3}$ ) R(30°) (d) NiO structure



(2) The structure of thin films. Thin oxide films are usually formed in air or pure oxygen on different types of substrates. These are generally spheres, thin evaporated films or flat slices. The choice of substrate is dictated by the convenience and the type of information required from the experiment. The sphere is difficult to handle but it has the distinct advantage of having many crystallographic planes present in one sample. Thin evaporated films can be easily prepared on appropriate substrates, and if thin enough, they can be directly examined in the electron microscope. Oxidation can be carried out in situ and the oxide film examined while on the metal substrate. In addition crystallographic information between the oxide and metal are readily available this way. Flat slices are easy to handle and will give a large amount of oxide on a particular face. They are suitable for X-ray and gravimetric studies.

The first comprehensive study of the formation of oxide on single crystal faces of nickel with a carefully prepared, well characterized surface has been undertaken by Lawless and co-workers<sup>(55)</sup>. The substrate was a single crystal boule metallographically polished and subjected to different treatments such as hydrogen bombardment, hydrogen reduction, vacuum degassing and vacuum annealing to  $10^{-9}$  torr. The results show that reproducibility is very difficult and only obtained after heating to 1100 °C in high vacuum. The reduction by hydrogen was found to reduce the reaction rate and also to modify the substrate structure. At one atmosphere

pressure, and in the temperature range from 78 - 178 °C, considerable anisotropy in reaction rate has been observed as deduced from interference colors. The (100) face oxidized the fastest followed by the (110) and (111) faces. Despite the lack of good reproducibility the same types of orientations were always found. On the (100) face of nickel, the (111) oxide was observed with one of its close packed directions parallel to a close packed direction in the metal. (The  $\langle 110 \rangle$  is the close packed direction in both the metal and the oxide.) Since there are two close packed directions in the metal, there are four possible orientations, two of these are "twin related". (These orientations will be clarified later.) On the (110) face, the oxide was parallel to the metal, sometimes the (411) was also present. On the (111) face, the parallel and its twin related are the usual orientations observed.

Other studies on nickel spheres by Otter<sup>(56)</sup> and Shrank<sup>(57)</sup> in the temperature range from 450-1450 °C reported similar results; however on the (011) nickel, both the (011) and the (001) oxide orientations are present.

Thin film substrates are also frequently used. Films are prepared by vacuum evaporation of nickel on a suitable substrate which is usually NaCl. Trillat et al<sup>(58)</sup> deposited nickel on the (001) NaCl substrate and oxidized the sample in a diffraction chamber with O<sub>2</sub> bombardment while the film was still on the substrate. They found the oxide to be parallel

to the metal. By simply heating an (001) foil in air, Shirai (59) observed the (111) orientation with one of the closed packed direction parallel to the one in the metal.

Pu and co-workers (60) have investigated the influence of the substrate perfection on the orientations of the oxide. The (100) and (110) films were prepared by vacuum evaporation on NaCl while the (111) was deposited on mica. In addition, the Cu/Ni double film technique was also used. This technique consists of depositing a thin layer of copper prior to the nickel and is believed to yield a better film. The orientations found appeared to be independent of the oxidation conditions. On the (100) face, both the (100) and the (111) oxide were found, but a better substrate favored a parallel orientation and for a less perfect one, the (111) dominated. On the (111) nickel face, the parallel orientation was always observed. On the (011) nickel, the "110 fibring" is the main orientation. The oxide orientations on the latter two nickel faces seem to be independent of substrate conditions and the authors have rationalized the above observations in terms of the number of the close packed directions in the metal. Since there is only one close packed direction on the (011) face, oxide can grow in any radial direction around the  $\langle 110 \rangle$  fiber axis. The (111) nickel has three close packed directions which define a plane uniquely and the parallel orientation was always found. These two planes are independent of substrate conditions. The (100) face has only two close

packed directions; there will be less restriction for the oxide to grow and perfection of the nickel has a certain influence on the oxide orientation.

Similar results on thin film substrates have been reported by Allesandrini<sup>(61)</sup>, Allesandrini and Freedman<sup>(62)</sup>, and Collins and Heavens<sup>(63)</sup>. On the (001) face, Collins and Heavens reported both the (111) and the (001) oxide with the (001) preferred at 450°C. On the (011) nickel both the (011) and the (001) oxides were found and on the (111) the parallel orientation was always present. Allesandrini found the parallel oxide on the (001) nickel but also observed several "transitional phases".

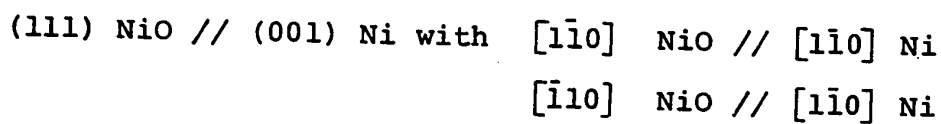
The most extensive work on oxidation of a single crystal of nickel was carried out by Garmon<sup>(64)</sup>. The studies covered the epitaxy and formation of nuclei on both thin film and bulk nickel. Thin films were prepared on a hot NaCl substrate. The bulk nickel was a sphere metallographically polished on alumina and electropolished in 50% H<sub>2</sub>SO<sub>4</sub> aqueous solution. This sample was subsequently annealed in hydrogen and high vacuum. The metal specimens were exposed in a flow of oxygen at a pressure, ranging from 10<sup>-5</sup> to 10<sup>-6</sup> torr for 5 min to an hour in the temperature range of 500-700°C, and the oxide films subsequently examined by transmission microscopy and the bulk nickel by electron reflection diffraction. The results indicated that oxide is only observed after an induction period during which oxygen is believed to dissolve

in the nickel to form a superlattice having a chemical composition of  $\text{Ni}_3\text{O}$ . When supersaturation is reached, nickel oxide is precipitated as discrete nuclei randomly distributed on the metal surface. Further exposure to oxygen does not lead to an increase in the number of nuclei, but to a growth of these nuclei. The density of the nuclei varies with the crystal face. Typical values for the density of nuclei were  $2 \times 10^{10}$  nuclei/cm<sup>2</sup> for the (001) and  $3 \times 10^9$  for the (011) for an exposure of 5 min at  $1 \times 10^{-4}$  torr at 600 °C. For the (111) face, the density was  $3 \times 10^9$  for an exposure of 1 min at the same temperature and pressure. The number of nuclei increased with the oxygen pressure and decreased with increasing temperature. Based on the appearance of oxide nuclei for the same exposure time, the (111) face oxidized the fastest followed by the (001) and the (011).

The results of Garmon<sup>(64)</sup> are sufficiently extensive and of importance to this investigation to merit detailed discussion:

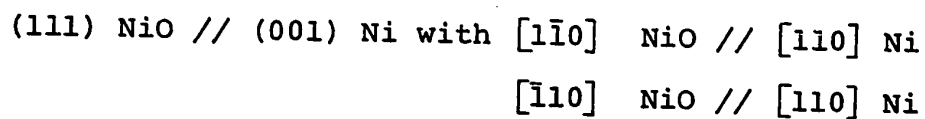
Results on the (001) nickel face. Exposure of the (001) face to an oxygen atmosphere at  $2 \times 10^{-5}$  torr for 1 min does not produce any visible oxide nuclei but diffuse rings corresponding to the oxide are observed in the diffraction pattern. The earliest oxide formed thus exists as a polycrystalline aggregate with random orientation. With further exposure at  $1 \times 10^{-4}$  torr for 5 min, discrete nuclei having distinct geometrical shape become visible. Most of these are equilateral

triangles arranged in a specific way. Sometimes they are mirror images and sometimes they are rotated  $90^\circ$  from each other. The epitaxial relationships deduced from the diffraction patterns are as follow:  $(111) \text{ NiO} // (001) \text{ Ni}$ . There are 4 possible orientations of this type. The first set of two has the specific crystallographic relation:



These two are "twin related" because they are a mirror image of each other. The two orientations are related by a rotation of  $180^\circ$  around an axis perpendicular to the film. They are crystallographically equivalent and cannot be distinguished by the diffraction pattern.

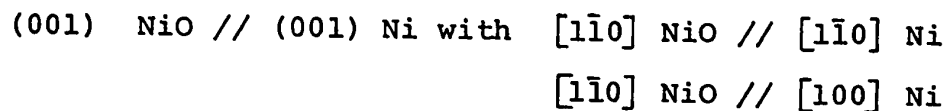
The other set is rotated  $90^\circ$  with respect to the first one. This arrangement is justified in terms of the symmetry of the (001) face of nickel which has two close packed directions  $90^\circ$  apart. The epitaxial relationship can be written as:



The two above orientations are also "twin related". Together the two sets contribute 12 diffraction spots on the (220) ring.

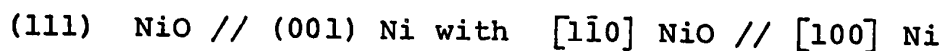
Other type of nuclei frequently observed are square shaped, most of them are arranged in a similar manner but some of them are rotated  $90^\circ$ . The diffraction patterns con-

firmed the two types of orientations:



The two above nuclei are not twinned related.

Finally, a seldomly found orientation was the



Note that this time, the close packed direction of the oxide is parallel to the cube axis of the metal. There are also 4 possible orientations of this type. All together up to 10 orientations are observed on this face. They are schematically represented in figure 2.3.1(iv).

Results on the (011) face of nickel. Only a limited number of runs have been performed on this face. Nuclei with a variety of shapes have been observed, usually after an exposure of 5 min at  $10^{-4}$  torr. The majority of the nuclei appear as isosceles triangles having an apex angle of  $70^\circ$ , some are polygonal and some exhibit rod like shape. The indexed orientations are respectively:



All the above oxide orientations possess a close packed direction parallel to the one in the metal. The (211) is always a minor orientation, the (001) is the strongest while the (011) becomes dominant as the oxide becomes thicker. One particular feature of this face was a noted degree of poly-

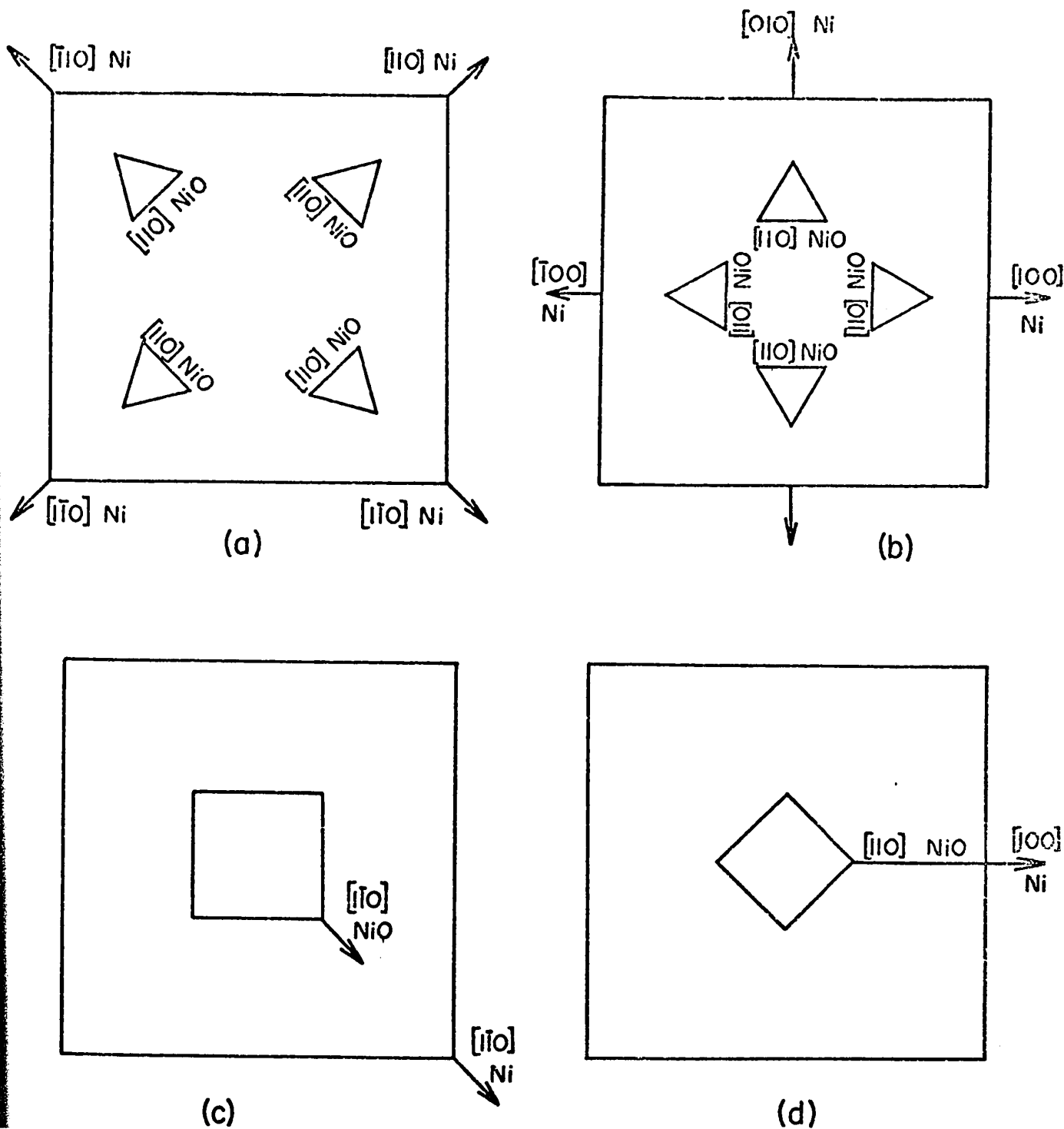


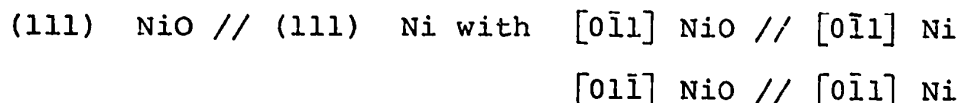
Figure 2.3.1(iv) Schematic diagram of four principal orientations of nickel oxide found on (100) nickel face. (64)

- (a) (111) oxide,  $\langle 110 \rangle$  oxide parallel to  $\langle 110 \rangle$  metal
- (b) (111) oxide,  $\langle 110 \rangle$  oxide parallel to  $\langle 100 \rangle$  metal
- (c) (001) oxide,  $\langle 110 \rangle$  oxide parallel to  $\langle 110 \rangle$  metal
- (d) (001) oxide,  $\langle 110 \rangle$  oxide parallel to  $\langle 100 \rangle$  metal

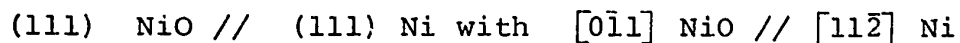


crystallinity.

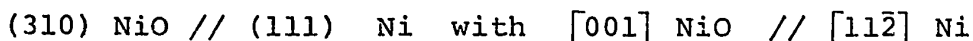
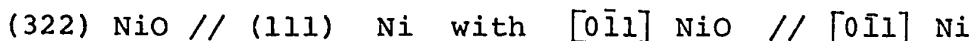
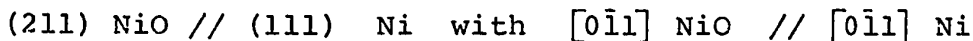
Results on the (111) face of nickel. Discrete nuclei become visible usually after an exposure of 5 min at  $10^{-4}$  torr at  $600^{\circ}\text{C}$ . The majority of the nuclei are equilateral triangles arranged as mirror images. They are twin related and cannot be differentiated in the diffraction pattern. The epitaxial relationships are:



With further exposure to oxygen, other nuclei appear. They are also equilateral triangles but are rotated  $90^{\circ}$  with respect to the first set. The epitaxial relationship deduced from the diffraction pattern gives:



The two orientations above will contribute 12 diffracted spots to the 220 ring. Some minor orientations are also present; they are:



A particular feature of the (111) nickel face is the increase in oxide polycrystallinity with the film thickness.

Similar observations have been made on the bulk nickel. The minor differences are the longer induction period and a tendency towards polycrystallinity during the early stage of oxidation.

An attempt has been made to correlate the observed epitaxy with the models of Van der Merve<sup>(65,66,67)</sup> and Cabrera<sup>(68)</sup> based upon the misfit between the oxide and the metal lattice. Both models predicted a strained overgrowth with the lattice spacing either compressed or expanded depending on whether the oxide lattice is larger or smaller than the metal. This type of information is readily available from Moire fringes. When a certain oxide plane having a different lattice spacing is parallel to the metal, periodic interferences due to the double diffraction of the electron beam gives rise to periodic fringes known as Moiré fringes<sup>(69)</sup>. The spacing of the fringes  $D$  is related to the lattice spacings by the simple formula,

$$D = \frac{d_1 d_2}{d_1 - d_2} \quad (\text{for a parallel case})$$

Thus, if the metal lattice is assumed to be unstrained, the oxide spacing can be calculated from the Moire fringes. Any positive or negative deviation from the standard value will be associated with the strain in the oxide.

The results obtained prove to be inconclusive when applied to the Van der Merve theory and even contradict the model of Cabrera. It should be borne in mind, however, that many parameters have to be assigned arbitrary values and the results should be taken accordingly.

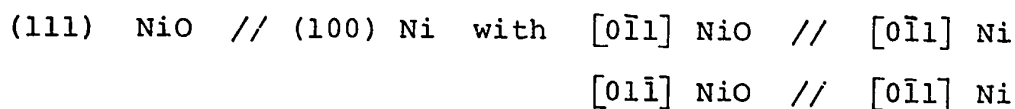
Flat nickel crystal slices have been also used. Due to

the ease of handling and large amount of oxides available, it is very suitable for X-ray studies. The application of X-ray diffraction to the investigation of thin films has been made possible by Borie and co-workers<sup>(70)</sup> who have developed a very sensitive technique capable of analysing films only 20 Å thick. This new technique, not only provides an independent check of the experimental results, but also yields additional information not readily available from electron microscopy.

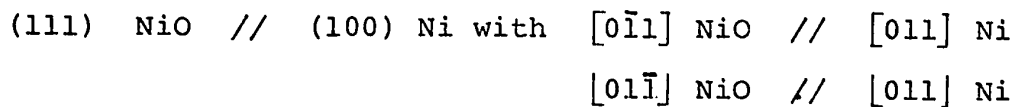
Cathcart et al<sup>(8)</sup> have used thin flat slices spark cutted from a single crystal rod. Samples were either electrolytically or chemically polished. Annealing was done in H<sub>2</sub> at an oxidation temperature in the range 400-600°C. Oxidation was carried out in oxygen at 1 atm pressure or less. The film thicknesses ranging from 25 to 500 Å were determined from X-ray intensities. They found that there is no shift in the position of the diffracted peak indicating a zero average strain, but line shape analysis has shown a broadening of the second order peak. These results can be rationalized in terms of a strain gradient model, in which part of the film is in tension and part of it is in compression. From the width at half the maximum intensity of the rocking curve, the mosaic spread of the oxide crystallites can be measured. The mosaic spread was found to be about 4° for the (111) face while it is only 2 to 3° for the (311) and (100) faces. It is also independent of the film thickness. These observations

differed markedly with those made on thin  $\text{Cu}_2\text{O}$  films formed on a copper single crystal<sup>(71)</sup>. These  $\text{Cu}_2\text{O}$  films show an expansion of the lattice on the planes parallel to the metal surface and a larger mosaic spread, which also changes with film thickness. In comparison, it can be said that NiO films show a zero average strain and have better aligned nuclei than  $\text{Cu}_2\text{O}$ .

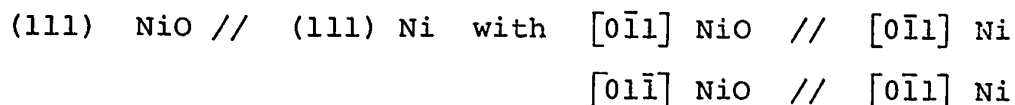
The epitaxial relationships obtained from diffraction analysis are as follows:



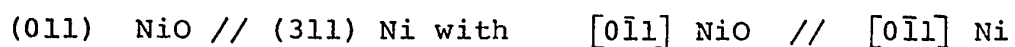
The two above orientations are called parallel and anti-parallel by Cathcart. They are simply twin related. The second set of twins is:



On the (111) face of nickel, there is only one twin set:



On the (011) nickel, polycrystalline oxide was observed and on the (311) metal, the (011) oxide orientation was found. There is only one type of orientation which has the following relationship:



With the exception of polycrystalline oxide found on the (011) nickel, the observed orientations agreed with the other

workers. The oxide films were composed of very small crystallites having a size ranging from 200 to 500 Å. The size appears to be independent of substrate orientation and oxide thickness. Dark field microscopy has also revealed that crystallites of a given orientation are randomly distributed over the surface. Considerable anisotropy in reaction rate was also observed. For a typical exposure of 30 min at 500°C, the (011) face is 5 and 10 times faster than the (100) and the (311) faces.

The authors have correlated the observed anisotropy with structural defects in the oxide films. Since the films are made up of very small crystallites, the boundaries of these crystallites can act as paths of easy diffusion for the nickel ions. And since all the crystallites have the same average size, the difference in reaction rates can be attributed solely to the number of incoherent boundaries present in the films. It is thus argued, that the (110) nickel with its polycrystalline oxide would contain the largest number of incoherent boundaries and oxidize the fastest followed by the (100) face which has two sets of twins, and the (111) which has only one set of twins. The (311) is the slowest since it has only one orientation, consequently all the boundaries are low angle boundaries. Furthermore, for a given nickel orientation, the ratio of parallel to anti-parallel twins can also alter the reaction rate. For example, if the (111) nickel face is chemically polished the ratio of anti-parallel to parallel twins was found to be 1.7 while for the electropolished

specimen, the ratio was 5.1. Since the maximum number of incoherent twin boundaries is realized when the quantities of various orientations are equal, the electropolished samples were found to oxidize 3 times slower than the chemically polished ones. The important conclusion by these investigations is that, a direct correspondence between structure and kinetics has been clearly established. The study has emphasized the role of structural defects in the mechanism of oxidation.

### 2.3.2 Oxidation Kinetics

The oxidation kinetics of nickel have been extensively investigated over a wide range of temperature and pressure. Most of the studies have been made on polycrystalline nickel and excellent reviews are available on this topic (72,73,74).

Electrical and thermochemical measurements have shown that NiO is p-type semi-conductor oxide with cation vacancies (75,76). At high temperature, the oxidation kinetics have consistently exhibited parabolic behaviour but below half of the melting point ( $\approx 1000^{\circ}\text{C}$ ) many reaction rates and mechanisms have been observed and proposed.

#### (a) Reaction mechanisms at intermediate temperature.

Uhlig, Pickett and McNairn<sup>(77)</sup> studied the oxidation of nickel in the temperature range from  $307-442^{\circ}\text{C}$ , for films up to  $3400 \text{ \AA}$  thick. A two stage logarithmic behaviour was observed with a break in the oxidation curve at the Curie temperature at

353°C. The activation energies were measured to be 19.9 and 21.1 kcal below and above the Curie temperature. The authors interpret the results by a mechanism of electron transfer from metal to the oxide as being rate controlling. The observed rate change at the Curie temperature was postulated to be associated with the change in electron work function. Engell, Hauffe and Illschner<sup>(78)</sup> oxidized nickel at 400°C in oxygen at pressures within the range 30-240 mm Hg and they expressed their results in accord with the cubic law. This law was derived from the model of Mott and Cabrera<sup>(3)</sup> based on a strong chemisorption of oxygen and an electrical field in the NiO layer. Hauffe et al<sup>(79)</sup> have observed a logarithmic behaviour at the early stage of oxidation and derived a fourth power law under an assumed existence of a negative space charge caused by the distribution of nickel ion vacancies in the growing oxide layer. The fourth power law was derived under very restricted conditions and is applicable only in a small region of oxide thickness. At 500°C, for doubly ionized cations and a value of 3 for the oxide dielectric constant, the authors have shown the thickness range in which the model is applicable is only from 300 to 600 Å. Gulbransen and Andrew<sup>(80)</sup> investigated the oxidation behaviour between 400-750°C and interpret the data by the classical parabolic law based on the analysis of Wagner. Large deviations from parabolic behaviour were observed during the initial stage of reaction and smaller deviations over long periods of time.

Two reasons were proposed to explain the deviations: the concentration of impurities decreases as the oxide increases in thickness, thus decreasing the number of vacancies available for nickel diffusion, and grain boundary diffusion plays a role in causing more rapid diffusion of nickel at the early stage of oxidation. As the film thickens, oxide crystallites grow and the influence of the boundary becomes small compared with lattice diffusion.

Following the same idea, Perrow, Smeltzer and Embury<sup>(7)</sup> have proposed an oxide growth model in which an effective diffusion coefficient,  $D_{\text{eff}}$ , is weighted according to the grain size.

$$D_{\text{eff}} = D_L (1-f) + D_B f$$

where  $D_L$  and  $D_B$  are the lattice and boundary diffusion coefficients, and  $f$  is the fraction of sites lying within the low resistance boundary paths.  $f$  in this case is a time dependent parameter since its magnitude is inversely proportional to the grain size. The model has satisfactorily accounted for the non parabolic behaviour of the oxidation of nickel at 500 and 600°C up to an observed film thickness of 8000 Å.

In conclusion, there is general agreement that the oxidation of nickel in the intermediate temperature range deviated from the parabolic law. Many rate laws and mechanisms have been proposed but there is no general acceptance of an unique type. Most often confusion exists, since the same experimental results can be represented by two different



rate laws based on completely different assumptions. Thus, the data of Gulbransen have been represented by a two stage logarithmic equation by Uhlig while Hauffe succeeded to express it by a fourth power rate equation. The general drawback of these models is the lack of consideration about the structure of the film. The important observations of Cathcart<sup>(8)</sup> who has shown definite relationships between the reaction rates and the types of structural defects, and the investigation by Perrow et al<sup>(7)</sup> which extended measurements over a wide range of film thicknesses have shown that short-circuit diffusion by structural defects in the oxide must be taken into account in the analysis of oxidation behaviour at an intermediate temperature.

(b) Reaction mechanisms at high temperature. At temperatures exceeding 800 °C nickel oxidizes according to the parabolic law. Different values of the parabolic rate constant ( $K_p$ ) are summarized in reference (39). Although parabolic behaviour is generally observed, a large range of activation energies have been reported. They are listed below (Kcal/g atom) with the appropriate temperature range:

45 (400-900 °C) <sup>(81)</sup> ;	55.4 (800-1000 °C) <sup>(82)</sup>
45.1 (980-1260 °C) <sup>(83)</sup>	49.0 (1000-1400 °C) <sup>(43,38)</sup>
56.7 (900-1400 °C) <sup>(84)</sup>	67.0 (900-1200 °C) <sup>(41)</sup>

and 36.3-43.6 (900-1400 °C)<sup>(85)</sup>

Impurities such as Mn and Fe have been attributed to cause the spread in the activation energies reported, but Paidassi<sup>(86)</sup>

has definitely shown by recent work that two magnitudes for the activation energy have been observed which are dependent upon temperature. It was established that amount of impurities only changed the values of the activation energy but do not change the presence of the two stages. Below 900 °C, an activation energy of 24 k cal/g atom and above 1000 °C, a value of 49-57 kcal/g atom have been consistently observed.

(c) Calculation of the parabolic oxidation rate constant.

The large spread in the reported values of activation energy for this type of oxidation defines the need for a more precise determination of the parabolic rate constant ( $K_p$ ). These values can be measured experimentally under restricted conditions such as very pure material and good adherence of the scales. These conditions are difficult to attain at the intermediate temperatures where adherence of the oxide is difficult and extrinsic defects such as pores, boundaries and dislocations can alter the mechanism of transport of the reactant. The values of the  $K_p$  however, can be calculated from Wagner's analysis if the values of the self-diffusion coefficients of the nickel and oxygen in nickel oxide and their dependence on oxygen pressure are known.

Wagner<sup>(2)</sup> has formulated a quantitative theory for the parabolic growth rate of a thick oxide scale based on the following assumptions: (a) The oxide layer should be thick enough to be beyond region of electrical space charge.

(b) Conditions of ambipolar diffusion where the current of positive and negative charges are equal, must apply;

(c) Interfacial reactions must be fast enough for local equilibrium to be attained at the scale interfaces, and diffusion is the rate controlling mechanism.

For an ideal parallel layer of growing oxide, the rate of thickening  $\frac{dx}{dt}$  can be then expressed as:

$$\frac{dx}{dt} = V_{eq} \frac{K_R}{x} \quad (2-1)$$

where  $V_{eq}$  is the volume equivalent of the oxide;  $x$  is the thickness and  $K_R$  is the parabolic rational rate constant which can be expressed in terms of the diffusion coefficient:

$$K_R = C_{eq} \int_{a_2(i)}^{a_2(o)} \left( \frac{z_1}{|z_2|} D_1^* + D_2^* \right) d \ln a_2 \quad (2-2)$$

where  $C_{eq} = C_1 z_1 = C_2 z_2 =$  concentration in equivalent per  $\text{cm}^3$  of metal or oxygen,  $z_1 z_2$  are the valence of the metal and oxygen ions,  $D_1^*$  and  $D_2^*$  are the self diffusion coefficients, and  $a_2$  is the activity of oxygen. The subscripts (i) and (o) indicate the metal/oxide and oxide/gas interfaces. For the case of NiO, oxygen diffusion in the oxide is very small<sup>(45)</sup> and can be approximated to zero. The expression of  $K_R$  can be then written by substituting  $d \ln a_2$  by  $\frac{1}{2} d \ln P_{O_2}$ .

$$K_R = \frac{1}{2} C_{eq} \int_{P_{O_2}(i)}^{P_{O_2}(o)} \left( \frac{z_1}{|z_2|} D_{Ni}^* \right) d \ln p_{O_2} \quad (2-3)$$

From the relation  $C_1 Z_1 = C_2 Z_2$ , we can write  $\frac{Z_1}{Z_2} = \frac{C_2}{C_1} = \frac{N_2}{N_1}$   
 where the ratio  $\frac{N_2}{N_1}$  is the atomic ratio of oxygen to nickel.

This ratio can be calculated if the concentration of nickel vacancies is known. Tretyakov and Rapp<sup>(87)</sup> have determined the concentration of nickel vacancies by coulometric titration. They arrived to the following expression:

$$[V_{Ni}^{''}] = .51(PO_2)^{1/6} \exp\left(-\frac{19000 \pm 8700}{RT}\right) \quad (2-4)$$

At 1245°C, the concentration of vacancies varies from  $7.5 \times 10^{-4}$  to  $9.38 \times 10^{-5}$  when the oxygen pressure changes from .21 atmosphere to  $10^{-6}$  atmosphere. Thus the variation of  $\frac{N_2}{N_1}$  is very small and the ratio can be assumed to be equal to  $\frac{N_2}{N_1}$

1. The expression for  $K_R$  is then:

$$K_R = \frac{1}{2} C_{eq} \int_{PO_2(i)}^{PO_2(o)} D_{Ni}^* d \ln PO_2 \quad (2-5)$$

From the above expression, if the values for the self diffusion of nickel and its dependence on oxygen pressure are known,  $K_R$  can be calculated by carrying out a simple integration. Values for the self diffusion coefficient have been measured by the tracer technique using the Ni<sup>63</sup> isotope deposited on the oxide surface. Values of  $D_{Ni}^*$  determined from this method are given in the reference (88). The latest and also the most precise measurements were done by Volpe and Reddy<sup>(89)</sup> who obtained the following expression for  $D_{Ni}^*$

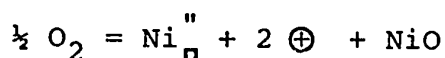
$$D_{Ni}^* \text{ (in NiO)} = 4.77 \pm 1.3 \times 10^{-2} \exp \left( \frac{-60,800 \pm 600}{RT} \right) \quad (2-6)$$

in the temperature range from 1181-1762°C. The dependence of the diffusion coefficient on oxygen pressure was found to be  $(P_{O_2})^{1/2}$  at the highest temperature and  $(P_{O_2})^{1/6}$  at the lowest temperature. The values of  $D_{Ni}^*$  and its dependence on oxygen pressure have been experimentally measured at two temperatures of 1245 and 1380°C<sup>(89)</sup>. By carrying out a simple graphical integration of equation (2-5) between the dissociation pressure for nickel oxide and the outside pressure of one atmosphere the following values for  $K_p$  are obtained ( $K_p$  and  $K_R$  are related by equation (2-11):

$$K_p = 1.56 \times 10^{-9} \text{ (g}^2 \text{ cm}^{-4} \text{ sec}^{-1}\text{) at 1245°C}$$

$$K_p = 5.5 \times 10^{-9} \text{ (g}^2 \text{ cm}^{-4} \text{ sec}^{-1}\text{) at 1380°C}$$

An analytical evaluation is possible if the coefficient for the pressure dependence is known. Mitoff<sup>(76)</sup>, Tretyakov and Rapp<sup>(87)</sup> have shown that the coefficient is equal to 1/6 at about 1000°C. This value simply means that the cation vacancies are doubly charged according to the defect equation;



The concentration of nickel vacancies  $[C_{\square}]$  can be expressed in terms of the oxygen pressure and the equilibrium constant  $K$ .

$$[C_{\square}] = K P_{O_2}^{1/6} \quad (2-7)$$

For the oxide, the diffusion coefficient of the metal can be

replaced by the diffusion coefficient of the vacancies:

$$D_{Ni}^* = D_{\square}^* C_{\square} = D_{\square}^* K PO_2^{1/6}$$

By substituting in the above values to the expression for  $K_R$  we have:

$$K_R = \frac{1}{2} C_{eq} \int_{PO_2(i)}^{PO_2(o)} D_{\square}^* K PO_2^{1/6} d \ln PO_2 \quad (2-8)$$

Integration yields:

$$K_R = 3 C_{eq} D_{Ni}^* (o) \left[ 1 - \frac{PO_2^{1/6}(i)}{PO_2^{1/6}(o)} \right] \quad (2-9)$$

Due to the 1/6 power, the factor  $\frac{PO_2^{1/6}(i)}{PO_2^{1/6}(o)}$  can be neglected.

The simplified expression for  $K_R$  is then

$$K_R = 3 C_{eq} D_{Ni}^* \quad (2-10)$$

For NiO, the value for  $C_{eq} = \frac{2p NiO}{M_{NiO}}$  where  $p$  is the density

of nickel oxide (6.85 g/cm<sup>3</sup>).  $M_{NiO}$  is the molecular

weight (74.7). The rational rate constant is accordingly

related to the parabolic rate constant by the expression:

$$K_R = \frac{M_{NiO}}{M_O^2 p NiO} K_p \quad (2-11)$$

and  $K_p$  can be expressed in terms of the self diffusion coefficient

$$K_p = 6p^2 \frac{M_o}{M_{NiO}} D_{Ni}^* \quad (2-12)$$

where  $M_o$  is the molecular weight of oxygen.

By substituting in the values for the density and the molecular weight of NiO, we have:

$$K_p = 12.91 D_{Ni}^* \quad (2-13)$$

The values of the  $K_p$  calculated from tracer diffusion data in the temperature range from 1000-1400°C are plotted in figure 2.3.2 along with the values determined from the oxidation measurements. The agreement is very good above 1100°C. Large deviations are observed at lower temperatures which are possibly due to the influence of impurities and grain boundary diffusion of both oxygen and nickel in the nickel oxide scale. Evaluation of the  $K_p$  at 500, 600, 700, and 800°C has also been carried out. These values which are recorded in Table 2.3.2 will be used later in the analysis of the oxidation mechanism.

TABLE 2.3.2

PARABOLIC RATE CONSTANT  
(calculated from tracer diffusion data from ref.(89))

<u>Temperature (°C)</u>	<u><math>K_p</math> (<math>g^2 cm^{-4} sec^{-1}</math>)</u>
500	$2.69 \times 10^{-19}$
600	$2.52 \times 10^{-17}$
700	$9.42 \times 10^{-16}$
800	$1.78 \times 10^{-14}$

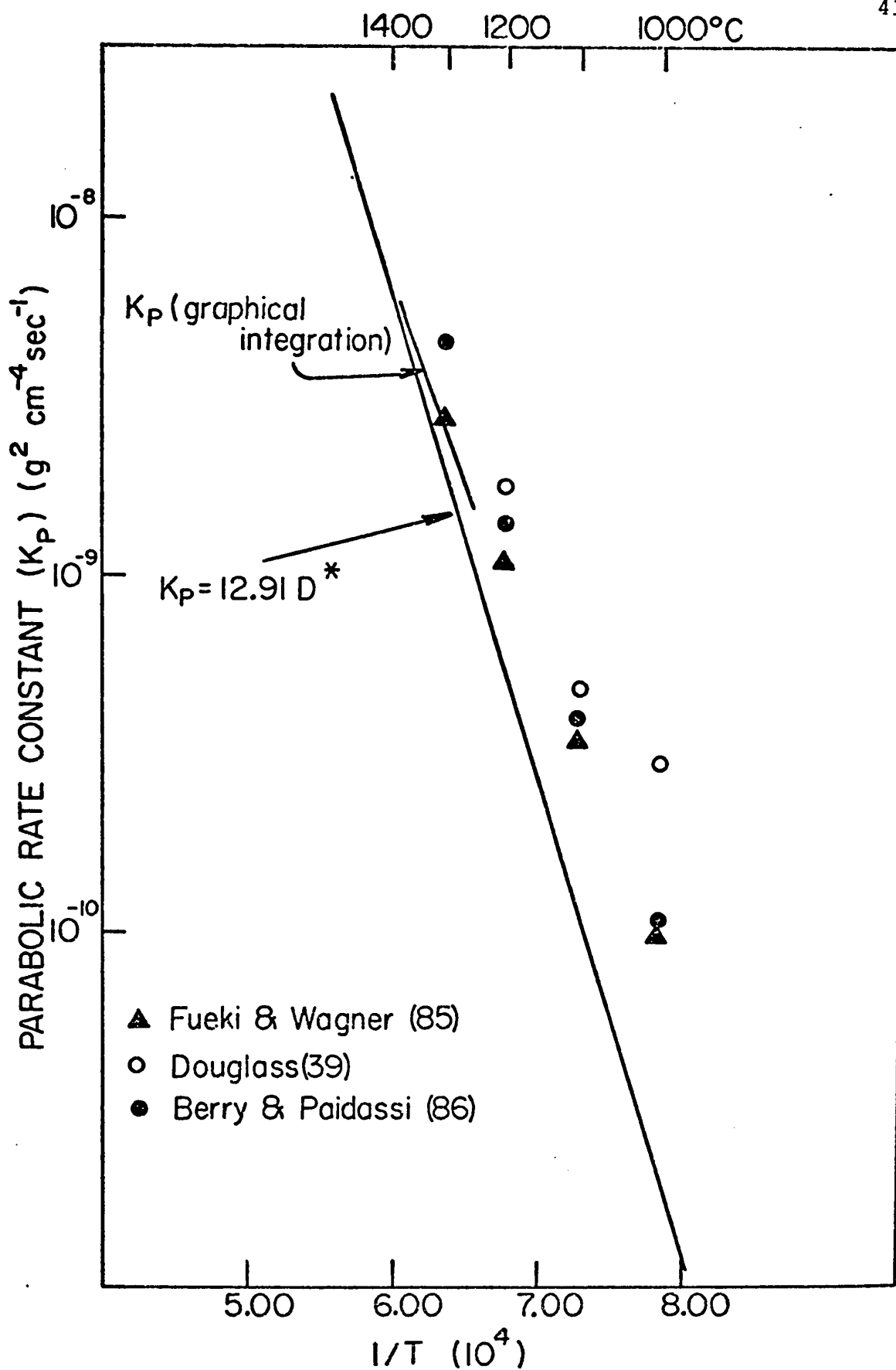


Figure 2.3.2 Parabolic Rate constant for nickel versus reciprocal temperature



## CHAPTER 3

### EXPERIMENTAL PROCEDURE AND OXIDATION APPARATUS

#### 3.1 Sample Preparation

The importance of careful sample preparation and its influence on the subsequent development of the oxide structure, has been emphasized by many authors<sup>(90,91)</sup>. A technique has been thus developed to produce a flat, strain free and relatively clean surface.

The nickel single crystals of 99.999 wt % purity were purchased as rods from Research Crystal Inc. Thin slices of about 1 mm were cut from the rods with a Servomet spark cutter using a 5 mil Molybdenum wire. The samples when cut were in the form of thin wafers 1.5 cm in diameter. A small hole was spark drilled in each specimen to enable its suspension in the reaction chamber. The specimen was then hot mounted in bakelite and metallographically polished on 240, 320, 400, and 600 grit silicon carbide papers using water as lubricant. It was removed from the mount by taking away most of the surrounding bakelite with a lathe. The remaining bakelite was peeled off taking care not to bend the specimen because slip lines arise when bending occurs. To avoid the damage due to the hot mounting process, samples were mounted on masking tape over a flat surface and final polishing was

done on 6 $\mu$  and 1 $\mu$  diamond paste lubricated with kerosene.

A deformed layer is usually produced by mechanical polishing and can be removed by electropolishing. The recurrent problem in electropolishing of nickel is the formation of pits. Different solutions have been tried and their effectiveness have been assessed. A 80% glacial acetic 20% perchloric acid solution was found to produce a very high density of pits and an uneven surface. The 60% sulfuric aqueous solution with a current density of .6 amps per cm<sup>2</sup> gave best results. The temperature of the bath should be kept near 0°C and vigorous agitation during polishing is necessary to reduce the formation of pits. Up to 40 $\mu$  of nickel was removed during the process.

Annealing of specimens was carried out at 800°C in a vacuum of  $3 \times 10^{-6}$  torr for a period up to 18 hrs. The influences of hydrogen treatment and ultra high vacuum anneals were also studied. For this purpose specimens were transferred after the conventional anneal to a high vacuum unit where they were heated in research grade hydrogen at  $10^{-1}$  torr for 15 min and subjected to an anneal at  $10^{-10}$  torr for 24 hr. No detectable difference in the surface structure was found between the two types of surface treatment (91). The conventional anneal, accordingly, was adopted as a standard annealing procedure.

The surface after each preparation stage was studied by X-rays, electron diffraction and replica techniques.

The results of these studies are given in chapter IV.

### 3.2 Oxidation apparatus

A schematic diagram of the oxidation apparatus is shown in figure 3.2. The vacuum system which consists of an oil pump backed by a mechanical pump can achieve a vacuum of  $2 \times 10^{-6}$  torr as measured by Balzers ionization gauge. The reaction tube of 3.5 cm diameter was made out of quartz. It was fitted with a removable head which contained 4 head winches. A liquid nitrogen trap was inserted between the reaction tube and the diffusion pump to prevent any back flow of oil into the system. Samples were suspended by a platinum wire to a small quartz rod connected to the winches by a 5 mil platinum wire. This arrangement allowed individual samples to be lowered or raised into the hot zone of the reaction tube. Heating was provided by a movable nichrome furnace. The temperature was controlled to  $\pm 2^\circ\text{C}$  by a Pyrovane Honeywell controller with a chromel-alumel thermocouple, in contact with the outside of the reaction tube. A two liter flask was connected to the reaction system to prevent any significant change in volume during oxidation. Ultra high purity oxygen containing less than 2 ppm of  $\text{H}_2\text{O}$  was used. All oxidation runs were carried out at the oxygen pressure of 400 torr as measured by a mercury manometer. A sample was oxidized immediately after annealing to prevent any further contamination due to the handling.

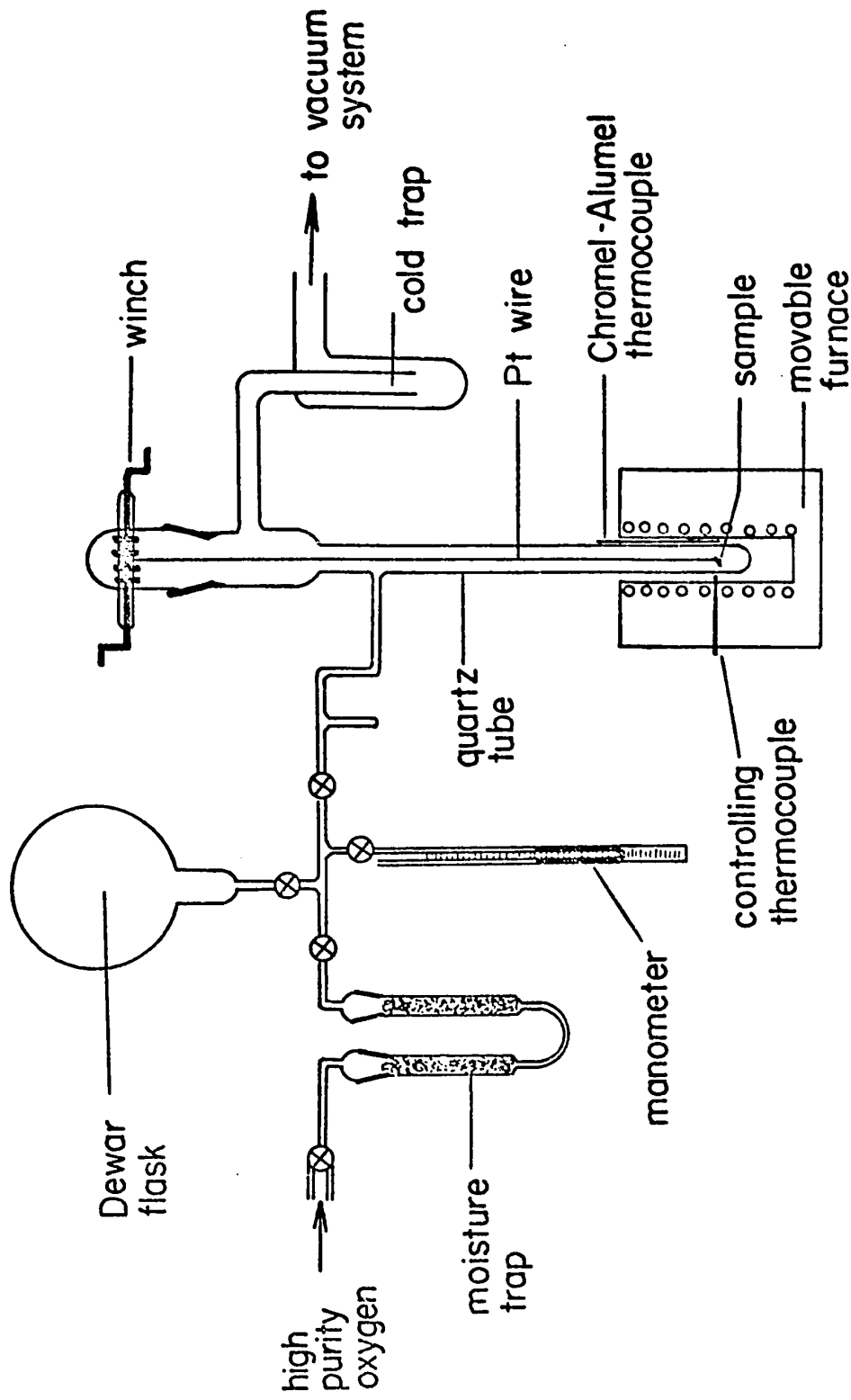


**Figure 3.2** Schematic diagram of the oxidation apparatus

### 3.3 Oxidation procedure

The oxidation apparatus was evacuated to  $3 \times 10^{-6}$  torr. The furnace was heated to the reaction temperature and raised up around the reaction tube so that the center of the hot zone correspond to the position of the samples. The time required for the temperature to stabilize was about 30 min. Oxygen was admitted to the desired pressure and the samples lowered into the hot zone. This procedure was adopted because the alternative of raising the furnace around the reaction tube caused considerable temperature fluctuations for at least 15 min. Since several of the oxidation runs lasted only 5 to 10 min. the second alternative is obviously inadequate. After oxidation the samples were slowly raised from the hot zone and oxygen was pumped out. Weighing was done immediately after cooling on a Mettler microbalance to an accuracy of  $\pm 2$  ug. They were then stored in a dessicator until examination.

### 3.4 Stripping the oxide

The film has to be removed from the metal for examination of the oxide by transmission microscopy. The very thin films (200-500 Å) tend to break into small pieces when stripped from the metal. The following techniques were tried to obtain large pieces of oxide suitable for microscopic examination.

#### (a) Anodic stripping

An oxidized sample was ground at the edges with silicon carbide papers and made the anode in an electrolytic cell

containing a saturated solution of KCl. The cell was filled in the middle with glass beads to prevent contamination by the reaction products. A potential of 1-2 volts was applied across the electrodes. The underlying nickel dissolved into the solution and the oxide film floated in the solution. Good size sections of the film could be obtained this way but contamination was heavy and the film was not suitable for examination.

(b) Acidic stripping. An acid solution was made in the following proportions: 30 ml of nitric acid, 10 ml of sulfuric acid, 10 ml of orthophosphoric acid and 50 ml of glacial acetic acid. Near 80°C, this solution readily dissolves nickel leaving the oxide film attached to the metal. The specimen is then transferred to a beaker filled with water and the oxide film shaken off; however, microscopic examination showed that the film was severely damaged.

(c) Iodine methanol stripping. This method proved to be most successful for obtaining suitable sections of the films. The oxidized samples were scored with a scalpel into 2 mm squares and left in a saturated solution of iodine in methanol. The solution is freshly prepared and kept near 50°C. About half an hour later the oxide films begin to flake off. The specimens are then removed and shaken vigorously in a beaker containing pure methanol. The oxide flakes are carefully washed and floated in distilled water. They are collected on folding microscopic grits of 150 or 100 mesh and washed in

acetone. This technique gives very good films in the thickness range of 500 to 4000 Å.

### 3.5 Examination of the oxide film by transmission electron microscopy.

The oxide films after being removed from the metal substrate were examined in the electron microscope. Bright field, dark field along with selected area diffraction techniques were employed. The information concerning these operation modes of the microscope is given in reference (92).

### 3.6 Examination of the oxide cross section by scanning electron microscopy

Due to its high resolution and the great depth of field, the scanning electron microscope is very suitable for the study of relatively thin oxide cross sections. Samples are prepared by embedding them in wax before cutting in half by a diamond wheel. They are then mounted in cold setting resin with two strips of stainless steel arranged parallel to the oxide surfaces. This set up yields good retention of the oxide edges. Polishing was carried through the usual sequence of silicon carbide papers using kerosene as lubricant. This was followed by lapping on wax containing a suspension of 40 $\mu$  alumina and final polishing was done on 6 and 1 $\mu$  diamond paste. The structure of the oxide can be revealed by etching in a 1:1:4 solution of hydrofluoric acid, glacial acetic acid and water. A potential of 3 to 5 volts is applied across the electrodes for a period ranging from 1 to 5 min. depending on

the oxide thickness. Specimens are washed in water and acetone and can be directly examined in the scanning electron microscope. The oxide grain size could be determined and the morphological development of the scale structure could be studied by this technique.

### 3.7 X-ray studies of the oxide scales.

Transmission electron microscopy cannot be used for oxide exceeding 5000 Å in thickness due to adsorption effects. Electron reflection diffraction can give some information about the oxide structure but quantitative measurement is difficult if not impossible. Oxide scales thicker than 1 μ can be readily studied by X-ray diffraction. Preliminary observations indicated that the oxidized samples showed marked preferred orientation, thus an evaluation of the texture coefficients is necessary to follow the structural development of the oxides. The inverse pole figure technique proposed by Harris<sup>(93)</sup> is adopted. This method consists of comparing the integrated intensity of a textured sample with the intensity of a random sample. The integrated intensity was measured by counting the pulses at the peak maximum for a fixed time and subtracting the background count. For this purpose the counter was equipped with a large receiving slit set at the peak maximum. To compensate for the surface irregularities samples are rotated during measurement. A copper tube was used without a filter, since the counter is provided with a LiF monochromator.



## CHAPTER 4

### EXPERIMENTAL RESULTS

The experimental results can be conveniently divided into two parts. Part I deals with the structural studies which consisted of results from electron microscopy, scanning electron microscopy and X-ray diffraction. Most results from transmission microscopy are from samples oxidized at 500°C since limited information can only be obtained at higher temperature due to the thick films formed. The oxide film thicknesses quoted are average values calculated from weight gain data. It was assumed that the film thickness is uniform covering the entire metal specimen and that  $1\mu\text{g}/\text{cm}^2$  of oxide was equivalent to  $62.9 \text{ \AA}^{(94)}$ . Part II deals with studies of the oxidation kinetics. The oxidation curves have been kindly supplied by Dr. Herchl, former postdoctorate fellow of the Institute for Materials Research.

#### 4.1 Surface preparation investigations.

The need for careful surface preparation can now be substantiated by considering the following results. Often mechanical polishing is the only way to prepare a flat surface and this usually leads to a deformed layer. Figure 4.1.1 is a typical X-ray Laue back reflection pattern from the (100) nickel face after diamond polishing. The pattern is as

expected from the (100) single crystal; however, the spots show considerable asterism indicating an extensive deformed layer. Since the depth of X-ray penetration is in the order of 10 to 15 $\mu$  the same surface was examined under reflection diffraction where the penetration depth of the electron beam was confined to less than 50 Å. A typical diffraction pattern is shown in figure 4.1.2. The continuous Debye rings can be identified as polycrystalline nickel; diamond polishing has thus produced a thin polycrystalline layer on the surface of a single crystal. It is believed that this polycrystalline layer can be formed by the rotating effect of the diamond wheel which randomized the subgrains produced during mechanical polishing. The oxide film formed on this surface is polycrystalline as expected and is shown in figure 4.1.3.

The deformed layer can be removed by electropolishing when up to 40 $\mu$  of metal are removed. Laue photographs then exhibited sharp, well defined spots. The surface is strain free and it can be concluded that the depth of the deformed layer is confined to less than 40 $\mu$ . Electron reflection diffraction of this surface shows the presence of a thin, oriented polycrystalline oxide film, figure 4.1.4. Electropolishing with subsequent washing in water has thus left a residual oxide layer which must be very thin (<20Å) since the diffracted nickel spots are also present. It can be established that the oxide film comes from the electropolishing since exposure of nickel to dry laboratory air requires at

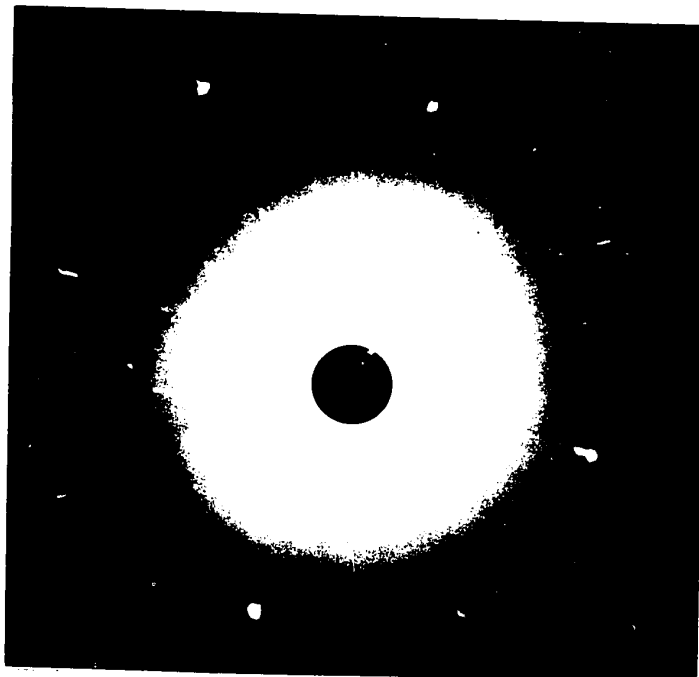


Figure 4.1.1 Laue pattern of (100) face of nickel after mechanical polishing.



Figure 4.1.2 Reflection diffraction pattern of (100) face of nickel after mechanical polishing.

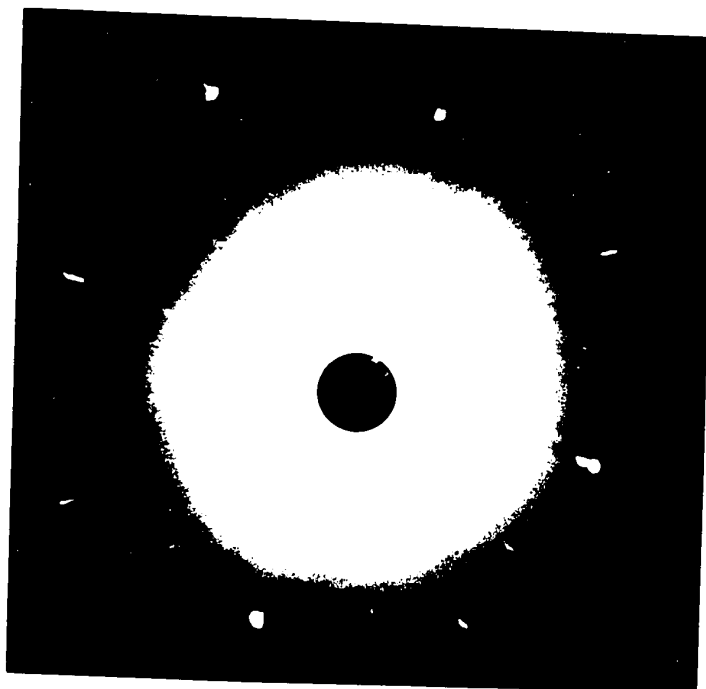


Figure 4.1.1 Laue pattern of (100) face of nickel after mechanical polishing.



Figure 4.1.2 Reflection diffraction pattern of (100) face of nickel after mechanical polishing.

least one week before the presence of oxide can be detected. This oxide film is usually reduced by annealing in hydrogen. Figure 4.1.5 is the reflection diffraction pattern of an electropolished specimen after reduction in hydrogen for 10 min. at 700 °C. The pattern is typical of a smooth single face of nickel and oxide was not detected. The same result can be obtained, however, by simply annealing a sample in a vacuum of  $3 \times 10^{-6}$  at 800 °C for 18 hrs. The reduction of the film by this simple vacuum anneal has been attributed to the carbon in the nickel which diffuses out to react with nickel oxide during the annealing process. May and Germer<sup>(95)</sup> have suggested another explanation. Since oxygen diffuses rapidly in FCC metals such as nickel, film removal by a vacuum anneal is probably associated with oxide dissociation due to the high driving force and rate for oxygen solution into the metal. Mass spectrometer analysis failed to detect the presence of any CO or CO<sub>2</sub> and this finding tends to support this view.

The influence of thermal faceting was also studied. Facets were only observed for a misorientation of more than 5°<sup>(91)</sup>. Laue orientation demonstrated that the majority of the samples were prepared to a misorientation of less than 3°.

#### 4.2 Transmission electron microscopy results for the (100) nickel face.

Transmission microscopy results of the oxide films formed on the (100) nickel face are presented in the following section

Figure 4.1.3 Oxide formed at 500 °C on mechanically polished surface. Oxidation time 5 min.

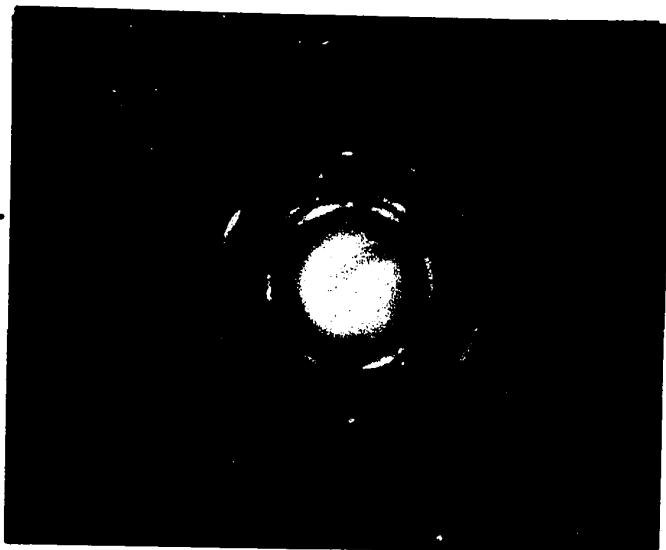


Figure 4.1.4 Reflection diffraction of (100) face of nickel after electro-polishing

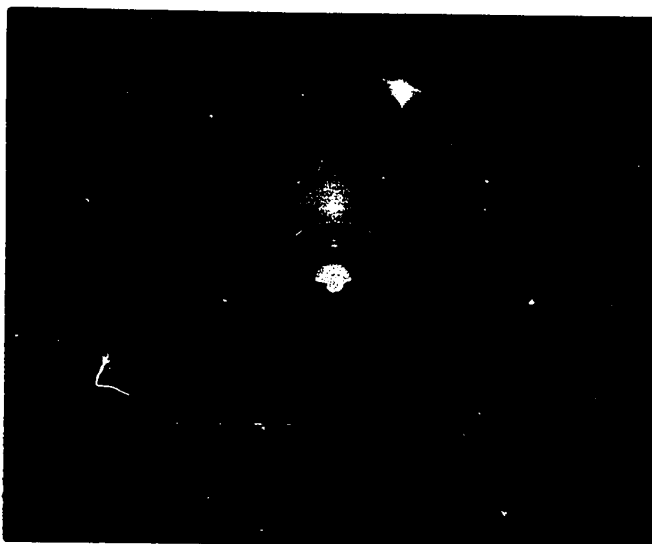
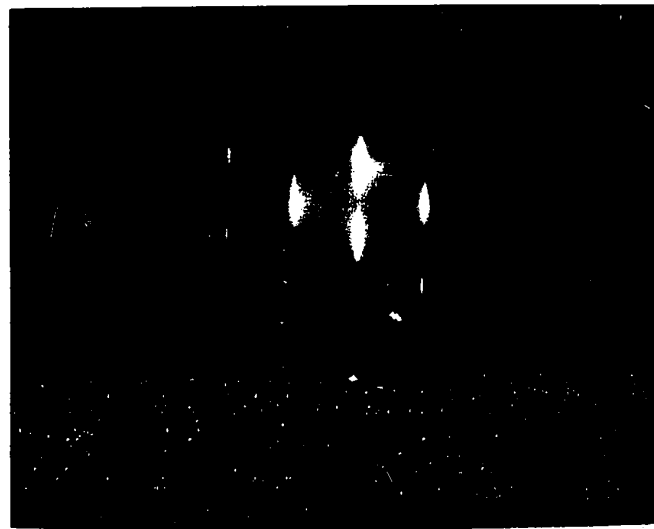
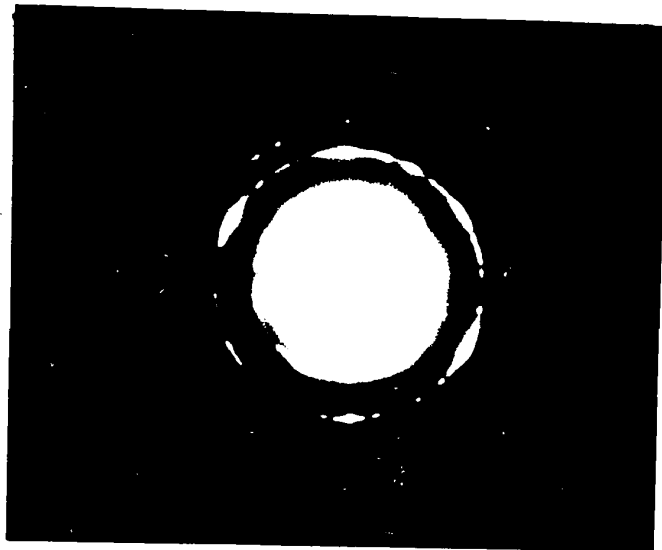


Figure 4.1.5 Reflection diffraction of surface after reduction in H<sub>2</sub> or vacuum anneal. Beam in <110> azimuth of nickel





1. The first image shows a bright, circular object centered in a dark field. The object has a distinct, bright core and a darker, textured outer ring. The overall appearance is that of a lens or a ring with a central light source.

2. The second image shows a bright, irregular shape centered in a dark field. The shape is bright and somewhat jagged, with a dark, shadowed base. It resembles a flame or a light source that is not perfectly circular.

3. The third image shows a bright, irregular shape centered in a dark field. The shape is bright and somewhat jagged, with a dark, shadowed base. It resembles a flame or a light source that is not perfectly circular.

as bright field, dark field and selected area diffraction micrographs. They are presented in chronological order of increasing exposure time to give a continuity in the study of the development of the oxide structure.

#### 4.2.1 Specimen exposure: 5 min

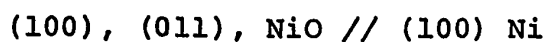
Figure 4.2.1(a) is a bright field (BF) picture of the film from a sample which has been oxidized for 5 min. (film thickness  $\approx 350$  A). General features of the film are immediately evident upon close inspection. The film is uniformly thick. It is composed of small grains or crystallites as evidenced by the diffraction contrast. The crystallite size is uniform since the film does not exhibit an island structure. The orientation relationship between the film and the metal can be deduced by a selected area diffraction (SAD) mode. A large diffraction aperture covering about 2/3 of the BF area was used to get a good portion of the film.

Since the electron beam is perpendicular to the oxide film the diffraction conditions are set up so that a parallel orientation between the oxide and the metal is obtained. The interpretation of the diffraction pattern can be resolved in terms of the reciprocal lattice planes (Relp). The construction of these reciprocal lattice planes is explained in detail in reference (92). The most commonly found reciprocal lattice planes of the oxide are given in appendix (A) along with the



3 faces of nickel. They are drawn to scales so that the interplanar spacings between the oxide and the metal can be visually estimated.

Figure 4.2.1 (b) is a SAD of (a). Superimposed on the spot patterns is a set of incomplete rings having the same spacing as the spots. From the camera constant, these rings can be identified as belonging to NiO. The spot pattern can be indexed by considering the (100) and the (011) Refls of the oxide given in appendix (A). By superimposing the two patterns with matching their common {022} reciprocal lattice points, the composite pattern obtained accounts for most of the observed spots (fig. (c)). From this pattern, the following information concerning the structure of the oxide film can be obtained: The film is composed of small crystallites; some of the crystallites are randomly oriented with respect to the metal and they contributed to the faint ring pattern but most of the crystallites have their (100) and (011) planes parallel to the metal, i.e.:



The coincidence of their {022} reciprocal lattice points indicated that both the (100) and the (011) planes of the oxide have a common  $[0\bar{1}1]$  direction, since a vector from the origin to the reciprocal lattice point represents the direction of this plane. Inspection of the diffracted spots shows that they are well defined and slightly elongated in the direction of the ring to an angular width less than  $5^\circ$ .



Figure 4.2.1 (a) Bright field (BF) micrograph of oxide film formed on the (100) face of nickel.  
x 13,500

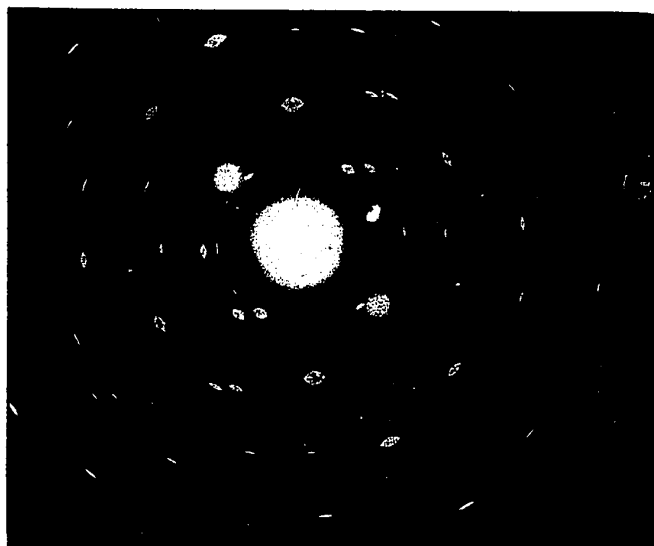
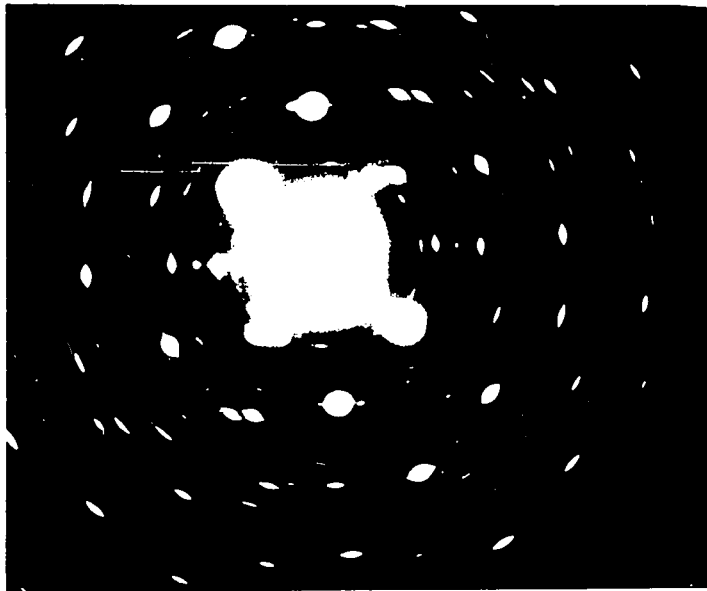
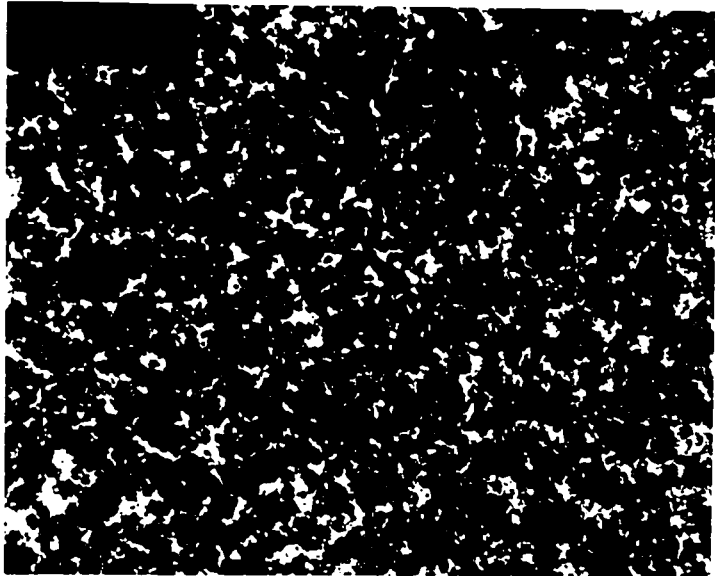


Figure 4.2.1 (b) Selected area diffraction (SAD) pattern of (a).



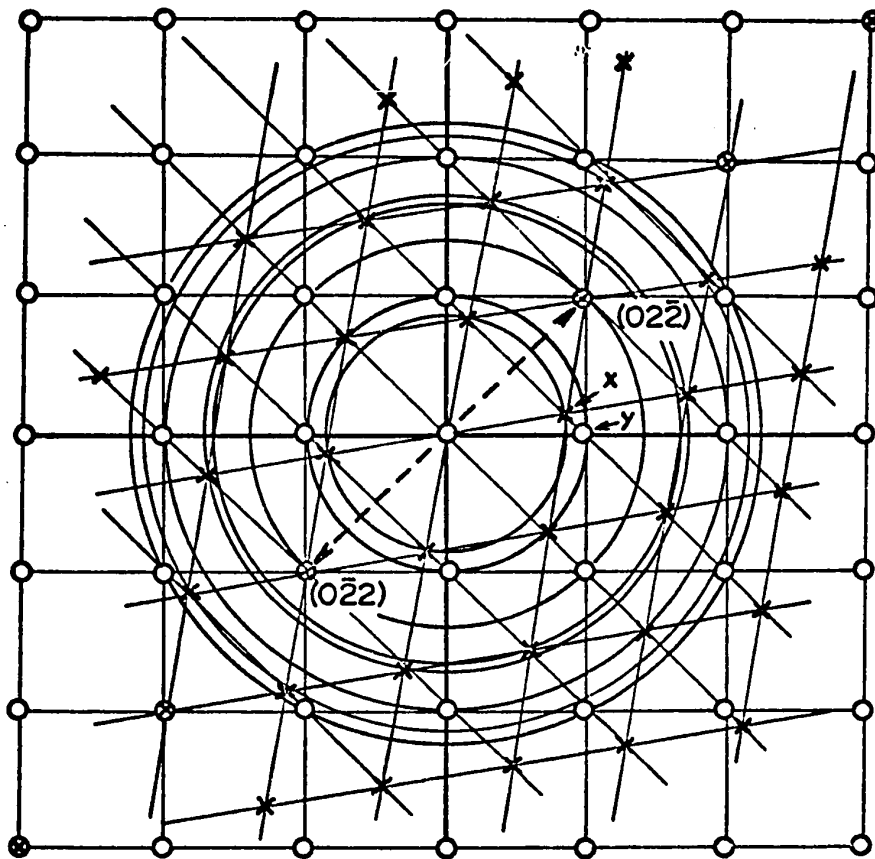


Figure 4.2.1(c)

Schematic drawing of the (100) and (011) reciprocal lattice planes of NiO. Pattern is obtained after matching the (022) reciprocal lattice points of the two Relps.

Consequently, nuclei of given orientation are misaligned from a given direction within  $5^\circ$ .

Although diffraction contrast in a BF picture yields an estimate of the crystallite size, accurate measurement is difficult. By using the dark field technique in which the crystallites contributing to a chosen diffracted beam can be imaged, crystallites count and measurement are easily possible. Additional information can also be obtained from the DF mode. When the objective aperture is set at a diffracted spot belonging, viz. to the (100) Refl, the number of crystallites having this orientation can be semi-qualitatively estimated. Figures (d) and (e) are DF pictures taken with the objective aperture set at spot "x" or "y" of figure (c) respectively. We can see that the number of crystallites having the (100) orientation as shown in (d) is much larger than the number of crystallites having the (110) orientation. Visual inspection also indicates that the average sizes of these two types of crystallites are almost the same. Exact quantitative measurement is not possible, however, since many crystallites of a given orientation may deviate slightly from Bragg's conditions and their reciprocal lattice points would not intersect the Ewald sphere. These crystallites will not be seen in the DF picture.

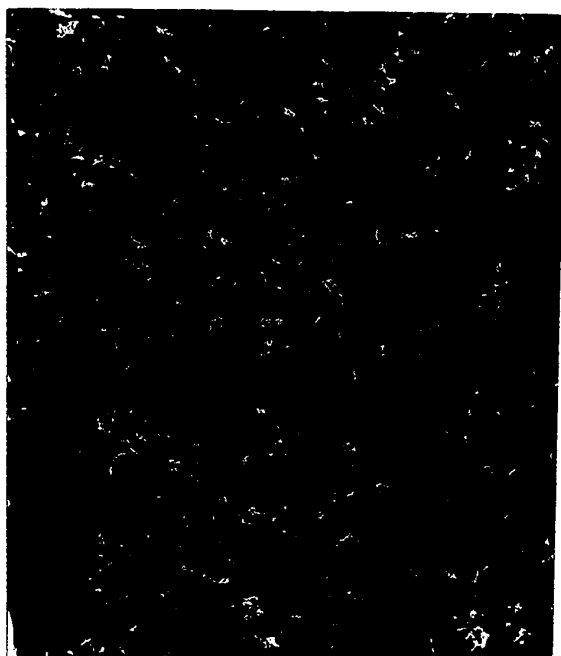
The film uniformity can now be investigated by examining another section of the film from the same sample. Figures (f), (g) are the BF and SAD of this section. No



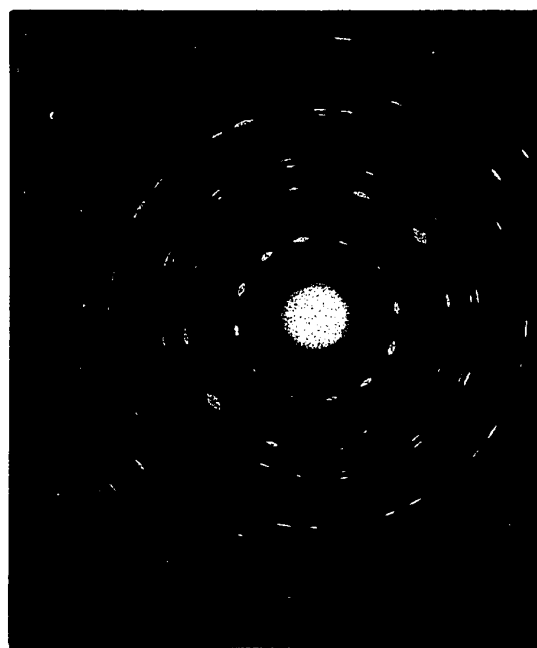
(d)



(e)



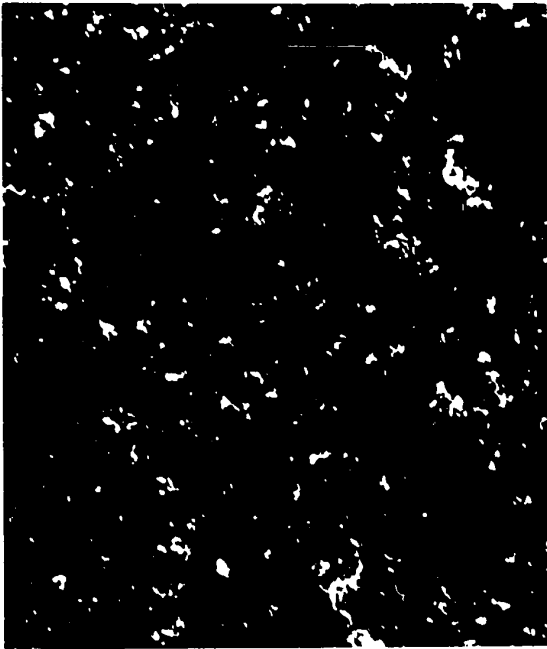
(f)



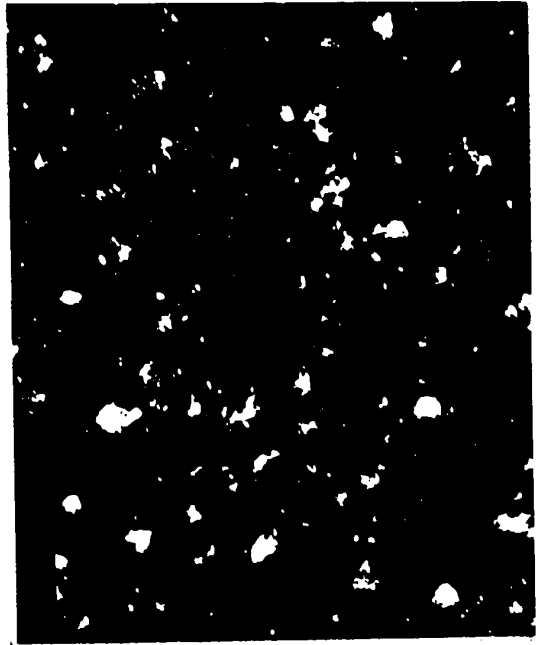
(g)

Figure 4.2.1

- (d) Dark field picture taken with aperture at "x" x 34,400
- (e) Dark field picture taken with aperture at "y" x 34,400
- (f) Bright field x 17,000
- (g) Selected area diffraction of (f)



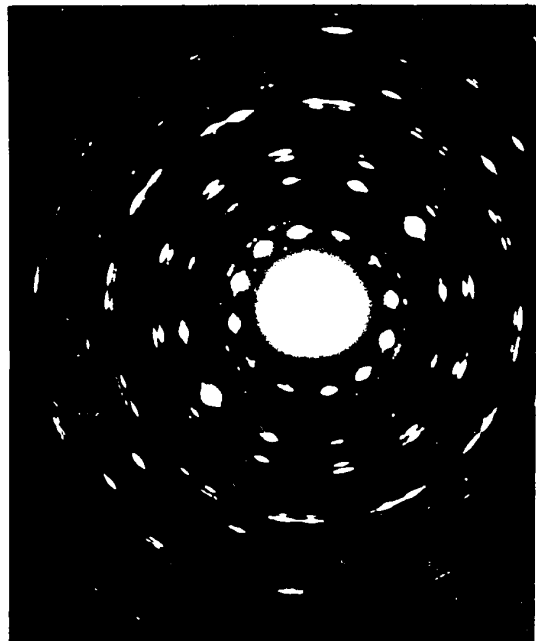
(a)



(b)



(c)

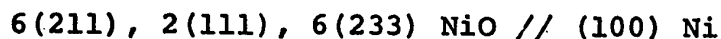


(d)

Figure 1.3.3

- (a)  $100\times$  magnification,  $10\mu\text{m}$  scale bar,  $1000\times$  magnification
- (b)  $100\times$  magnification,  $10\mu\text{m}$  scale bar,  $1000\times$  magnification
- (c)  $100\times$  magnification,  $10\mu\text{m}$  scale bar,  $1000\times$  magnification
- (d)  $100\times$  magnification,  $10\mu\text{m}$  scale bar,  $1000\times$  magnification

visible difference in the general features can be detected in the BF micrograph. The diffraction pattern however is different. The detailed interpretation of this pattern is given in appendix B(3). The following orientations have been found



The crystallographic information from transmission microscopy only gives the parallel orientation between the oxide and the metal, for example the (100) plane of NiO is parallel to the (100) plane of nickel. There is still one degree of freedom since the (100) plane can be rotated around an axis perpendicular to the plane. If this is the case then the diffraction pattern can be generated by rotating the (100) reciprocal lattice plane around its normal axis. The resulting pattern is a set of continuous rings with some missing rings. The condition for the missing rings can be set as:

$$[100] \cdot [hkl] \neq 0$$

where  $hkl$  are the Miller indices of the diffracting plane subjected to the structure factor consideration<sup>(96)</sup>. Another complication may arise when the rotation axis is not quite parallel to the electron beam. This will result in a set of arcs instead of the continuous rings. The length of an arc will depend on the degree of tilt of the axis with respect to the electron beam. Examination of all the diffraction patterns shows that is not the case since patterns with well defined spots were obtained.



The orientation relationship between the oxide and the metal cannot be obtained from a film removed from the metal. Nevertheless, some of the results from reflection diffraction<sup>(91)</sup> and from the literature have reported the common [110] close packed direction between the metal and oxide. This condition will determine an unique crystallographic relationship and is generally known as the epitaxial relationship. It has been reported in the oxidation studies of single crystal faces of copper that the degree of orientation changed with exposure time<sup>(97)</sup>; the morphological development of the film can then be followed by examining the film structure at different exposure times.

#### 4.2.2 Specimen exposure: 10 min.

Figures 4.2.2 (a)-(f) are the typical BF, SAD and DF micrographs of a sample oxidized for 10 min (film thickness  $\approx 420 \text{ \AA}$ ). The BF picture (a), still exhibits the same general features previously observed. The SAD patterns have the following orientations:

Figure (b) can be indexed as:

$$(100) \text{ NiO} // (100) \text{ Ni}$$

Figure (c):

$$(110), (100) \text{ NiO} // (100) \text{ Ni}$$

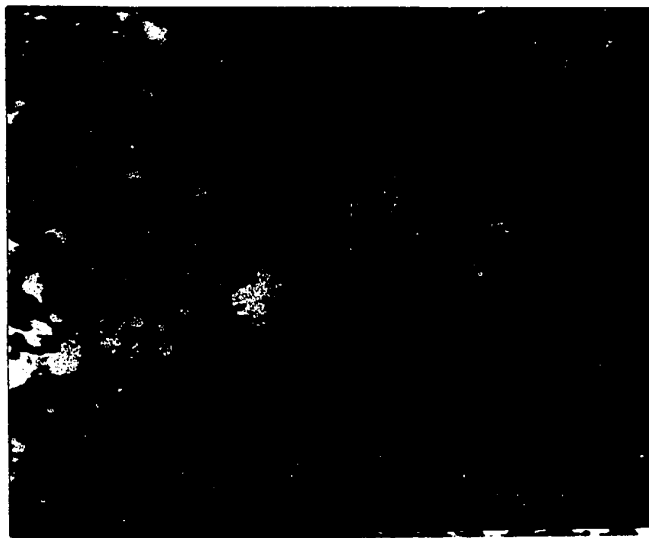
Figure (d):

$$(111), (211) \text{ NiO} // (100) \text{ Ni}$$

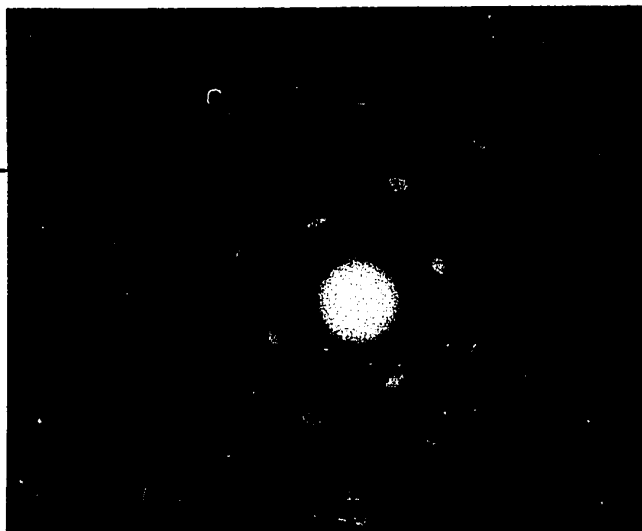
Note the elongation of the diffracted spots on the 3rd (220) ring. This elongation corresponds to a mosaic spread of at

Figures 4.2.2

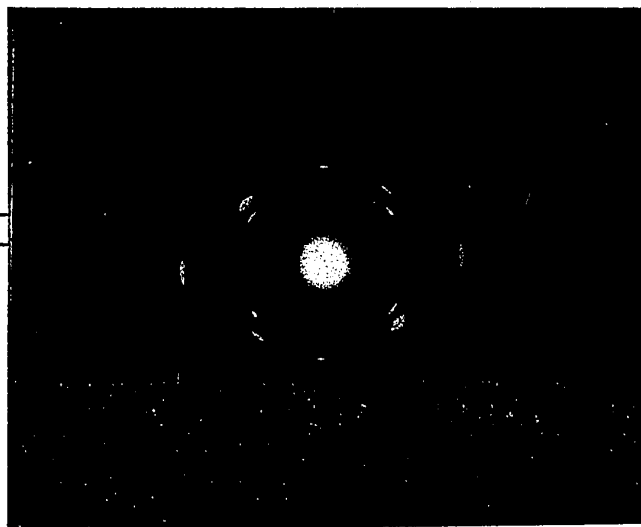
(a) BF micrograph  
x 22,000



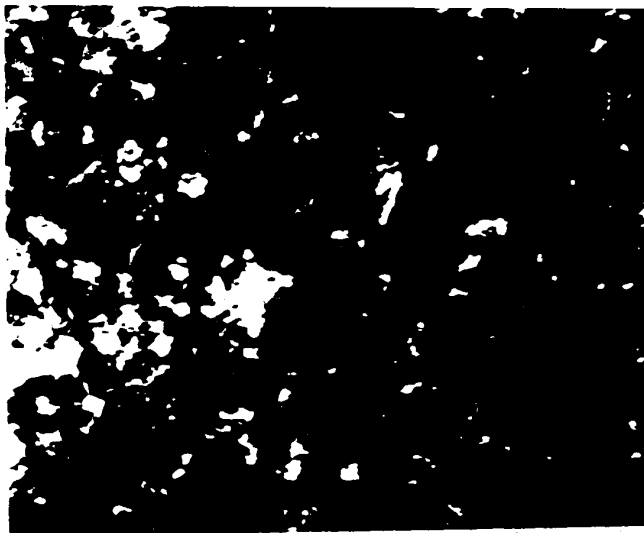
(b) Selected area diffraction pattern of (a)



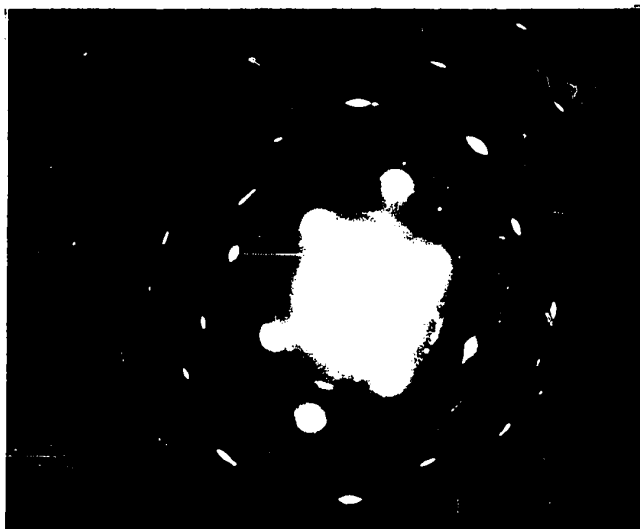
(c) Selected area diffraction pattern of different region of film



(a)  $100\times$  magnification



(b)  $100\times$  magnification  
Flow pattern at  $100\times$  magnification



(c)  $100\times$  magnification  
Flow pattern at  $100\times$  magnification  
post-removal of particles

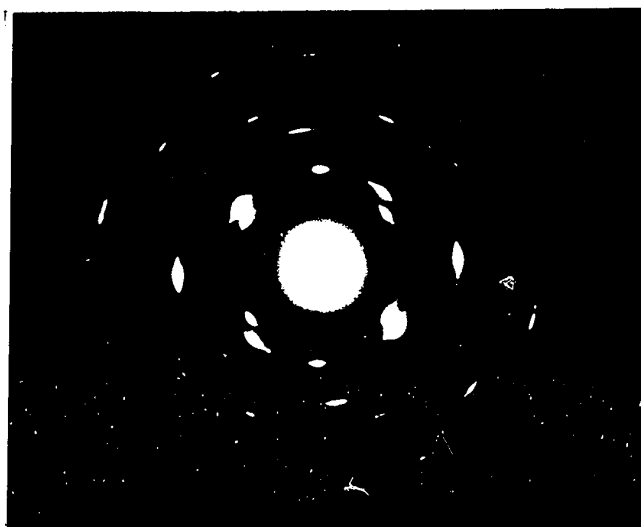


Figure 4.2.2

(d) Selected area dif-  
fraction pattern

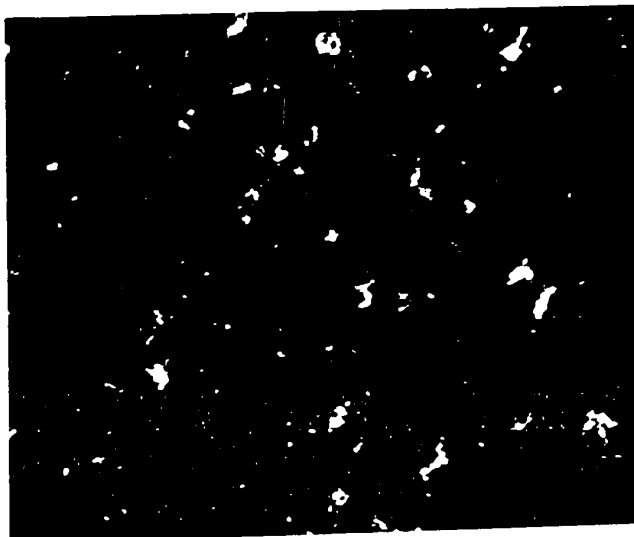
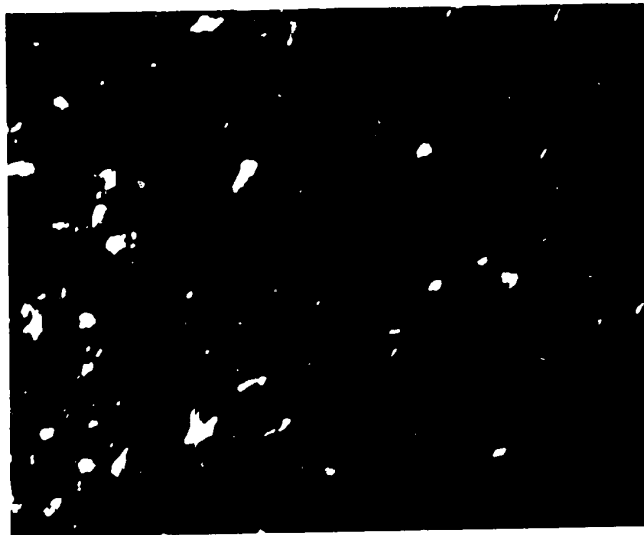
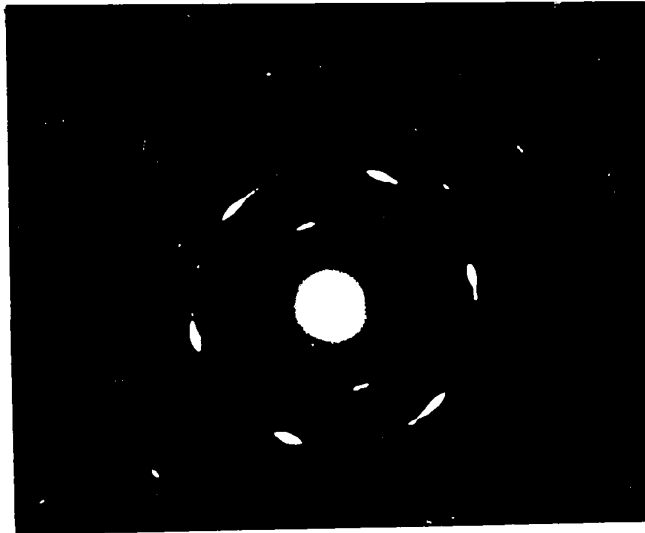


(e) Dark field picture  
taken with reflection  
from (111) Relp  
x 28,000



(f) Dark field picture  
taken with reflection  
from (211) Relp  
x 28,000





least  $15^\circ$  for the (111) oriented crystallites. Figures (e) and (f) are the dark field pictures taken with the objective aperture set at the diffracted spot belonging to the (111) and (211) Relp. It can be seen that the number of crystallites having the (111) orientation are much larger than the (211). Examination of many other parts of the film leads to the following conclusions:

- the complex pattern previously observed in figure 4.2.1(g) is no more present,
- the background diffracted rings are more continuous and better defined.
- the (100) and the (111) orientations are the most commonly observed.

#### 4.2.3 Specimen exposure: 20 min.

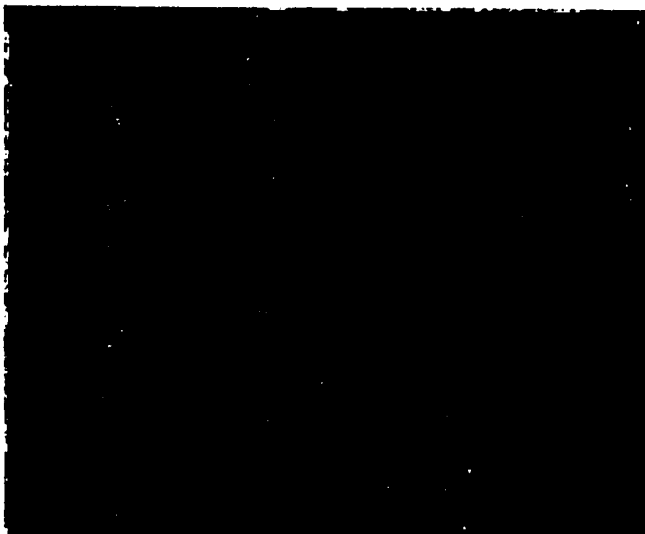
Further exposure to oxygen does not lead to any drastic change in the structure of the oxide film. Figures 4.2.3 (a)-(e) are the sequence of micrographs of a sample oxidized for 20 min (film thickness  $\approx 700 \text{ \AA}$ ). There is no marked change in the general features of the film as shown in the BF picture (a). The diffraction patterns are now composed of continuous rings with superimposed spots patterns. The (100) is shown in figure (b), the mixed (211) and (100) in (c) and the (110) in (d). The DF micrograph taken with the (220) reflection of figure (d) is shown in (e).

#### 4.2.4 Specimen exposure: 30 min. and 40 min.

Micrographs from samples exposed to oxygen from

Figure 4.2.3

(a) Bright field micrograph x 21,000

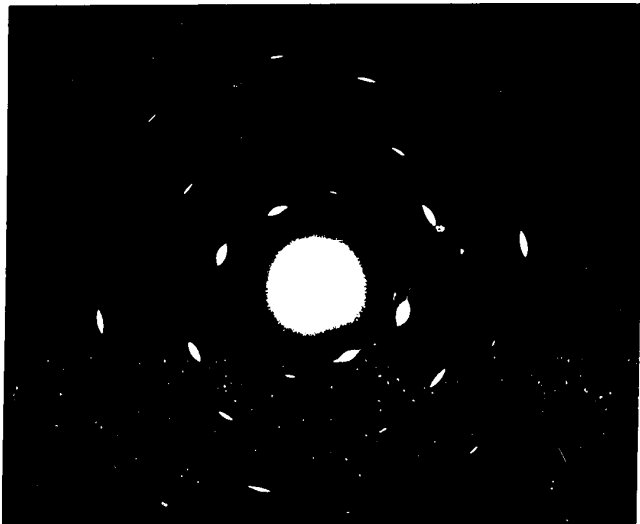
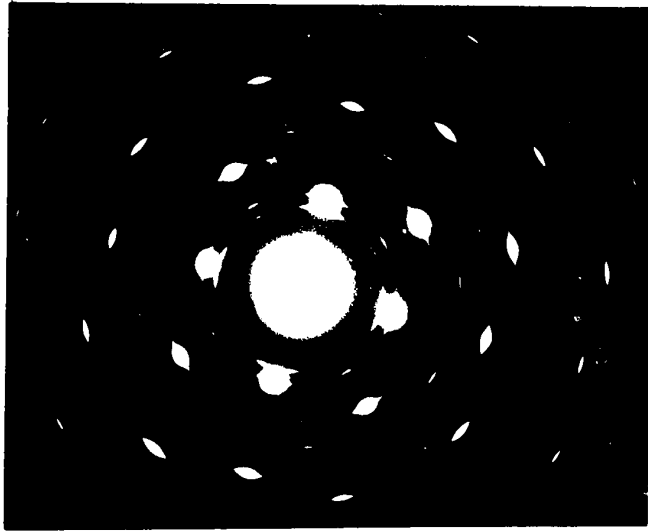
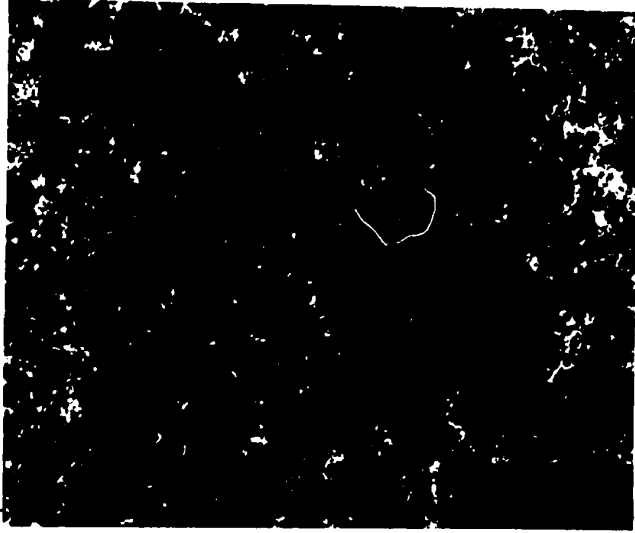


(b) Selected area diffraction pattern of (a)



(c) Selected area diffraction pattern of different region of film







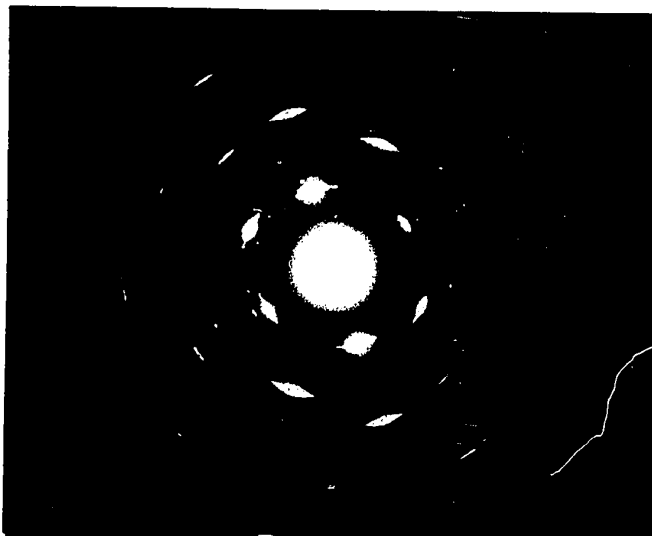


Figure 4.2.3 (d) Selected area diffraction pattern of other section of the film



Figure 4.2.3 (e) Dark field micrograph taken with (220) reflection of (d) x 50,000

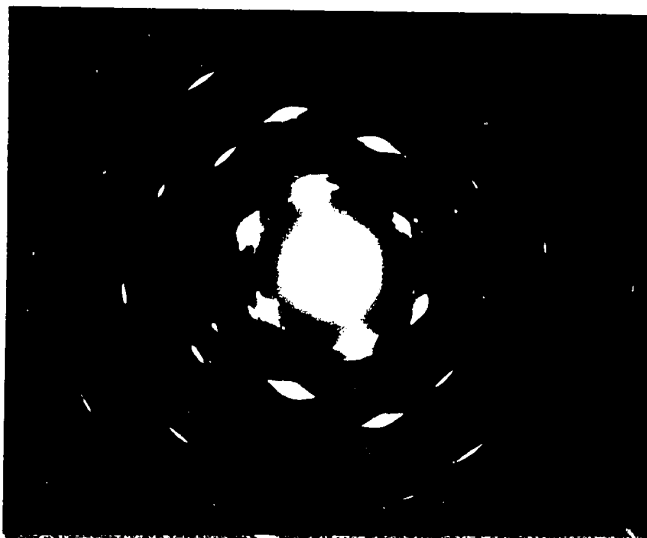


Figure 4.2.3 (d) Selected area diffraction pattern of other section of the film

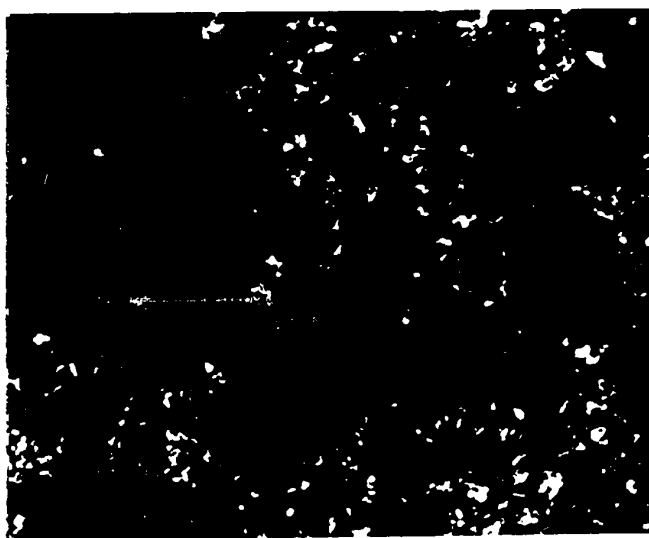


Figure 4.2.3 (e) Dark field micrograph taken with (220) reflection of (d)  $\times 50,000$

30 to 40 min (film thickness  $\approx 820, 900 \text{ \AA}$ ) are given in this section. The structure of the thicker films are rather uniform. The diffraction patterns yield mostly the (100) orientation superimposed on the rather continuous and well defined polycrystalline oxide rings. This observation can be confirmed by the following micrographs.

Figures 4.2.4 (a)-(c) are from sample oxidized for 30 min. The BF begins to show dark and light regions indicating that the thickness is not quite uniform, however no abnormally large grains are observed. The diffraction pattern (b) shows considerable amount of polycrystallinity; the (100) spot pattern is however much in evidence. The DF picture taken with the (200) reflection confirms that the crystallite size has not increased to any large extent.

Figures 4.2.4 (d)-(f) belong to a sample oxidized for 40 min. The features are much the same as the previous sample.

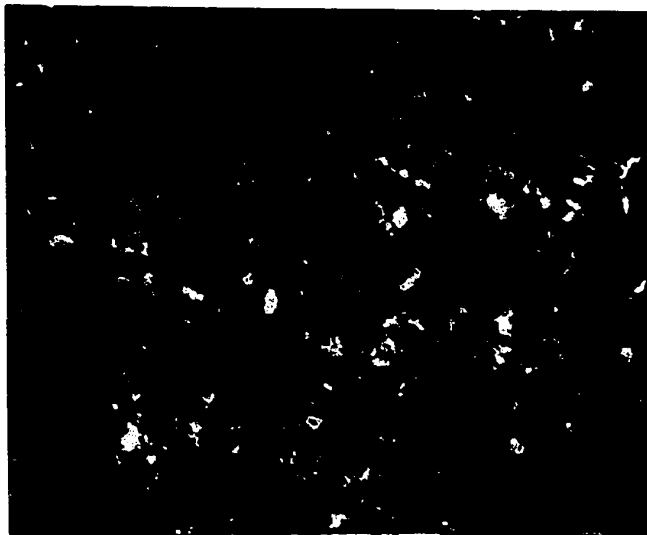
#### 4.2.5 Specimen exposures: 70 min and 120 min.

Micrographs from samples oxidized for 70 min and 120 min (film thicknesses  $\approx 1200, 1500 \text{ \AA}$ ) are presented in figures 4.2.5(a)-(c) and (d)-(f). The BF pictures now show regions of uneven thickness. The diffraction patterns consistently yield the (100) pattern along with the continuous rings. Dark field micrographs now exhibit noticeable grain growth with large spread in size distribution.

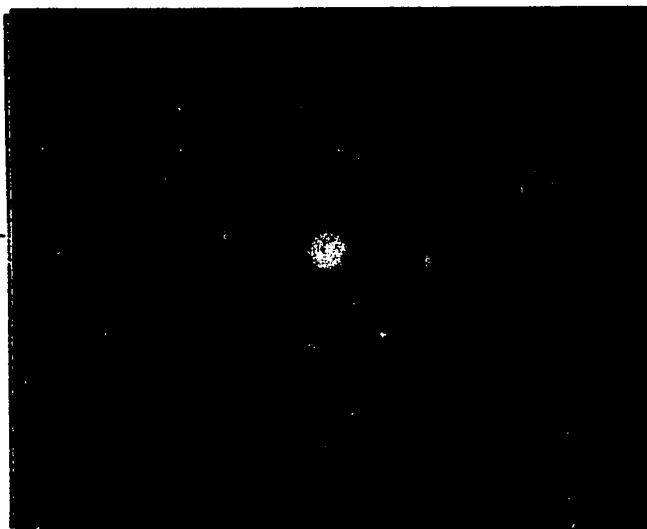
#### 4.2.6 Specimen exposures: 180 min and 300 min.

Figure 4.2.4

(a) Bright field micrograph x 42,000



(b) Selected area diffraction pattern



(c) Dark field picture taken with (200) reflection x 50,000



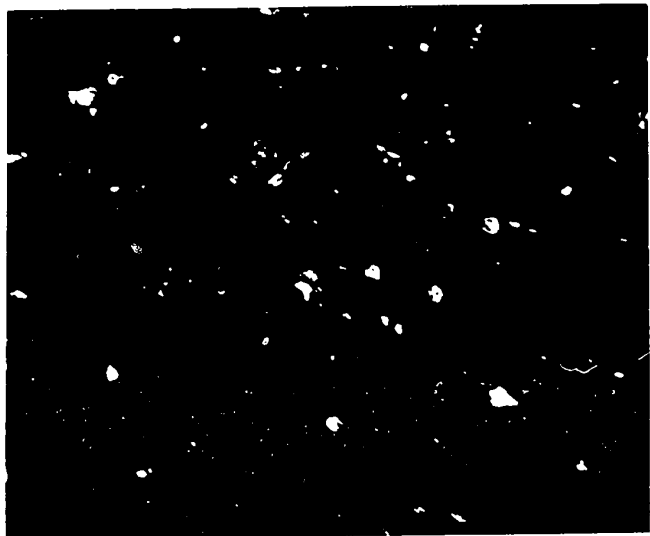
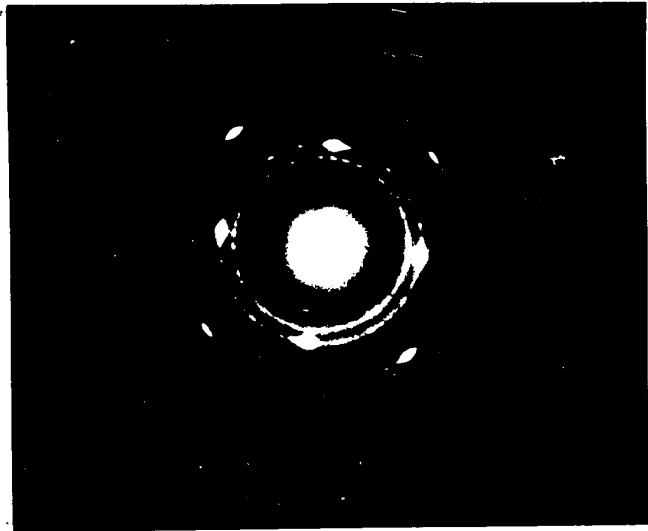
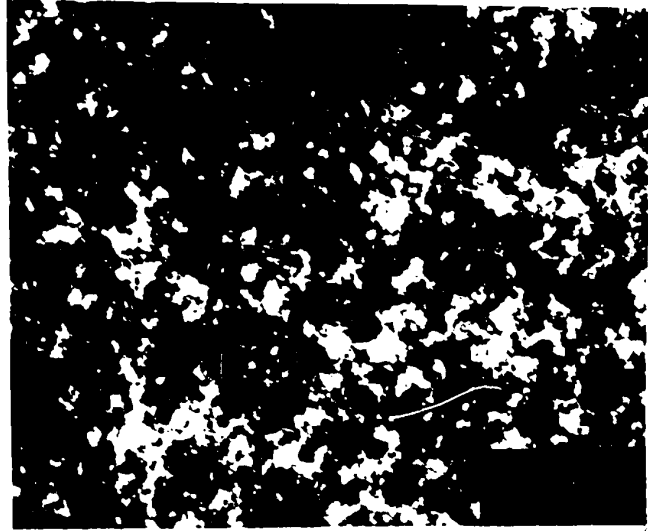
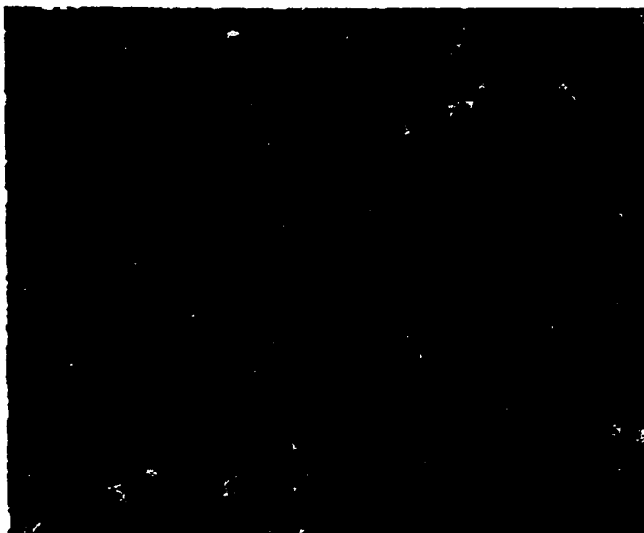


Figure 4.2.4

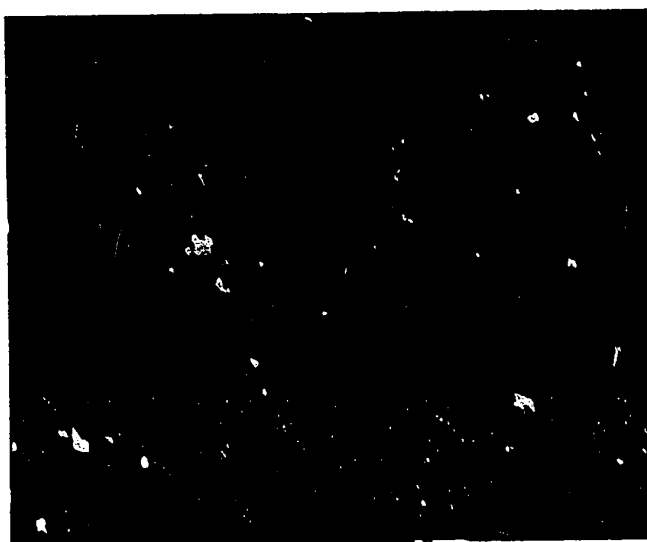
(d) Bright field micrograph x 22,000



(e) Selected area diffraction pattern



(f) Dark field picture taken with (200) reflection x 50,000



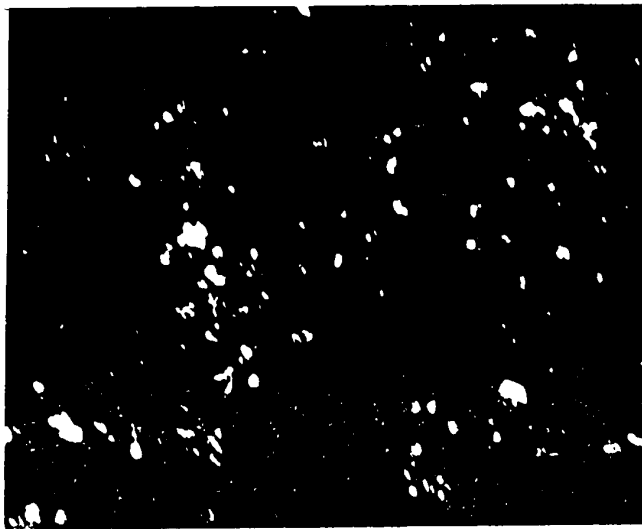
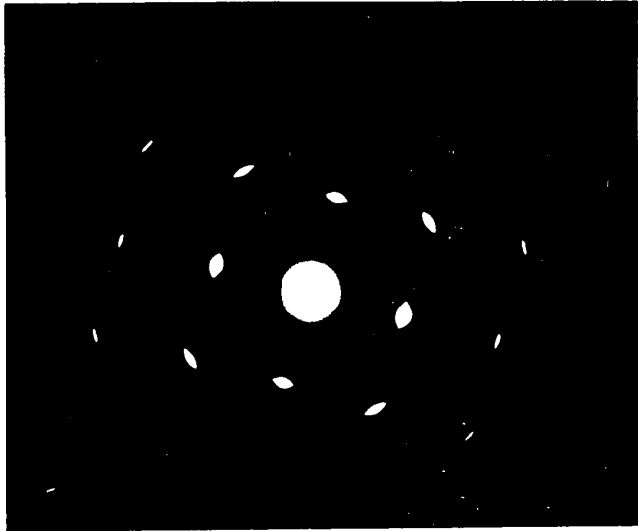
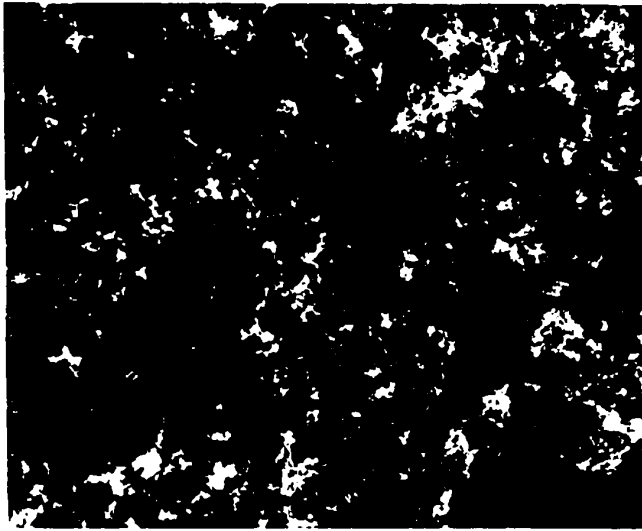
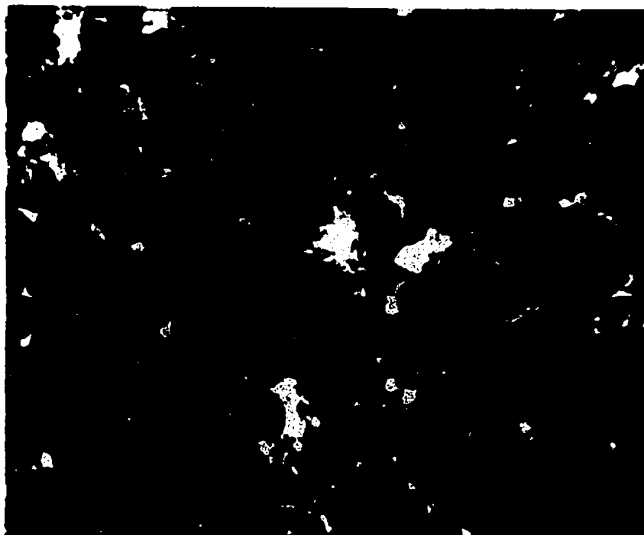
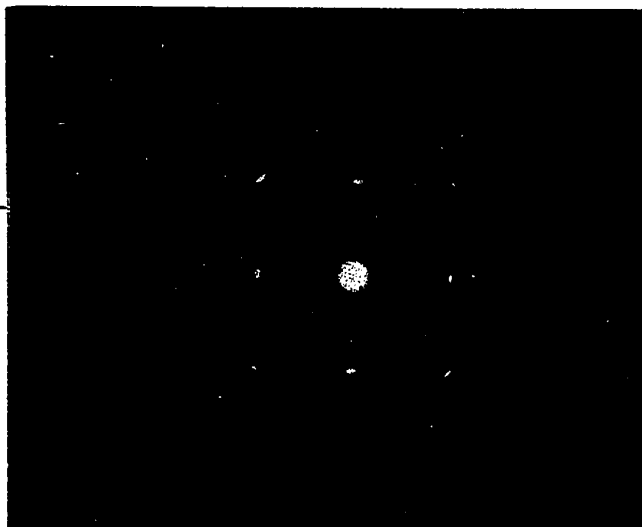


Figure 4.2.5

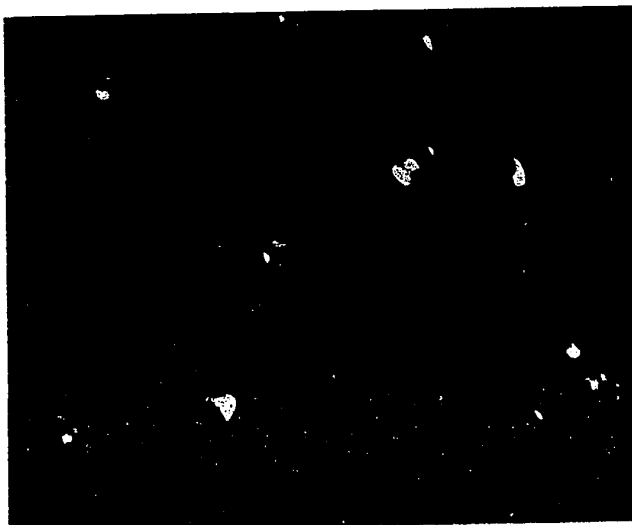
(a) Bright field micrograph x 13,500



(b) Selected area diffraction pattern



(c) Dark field picture taken with (200) reflection x 18,000





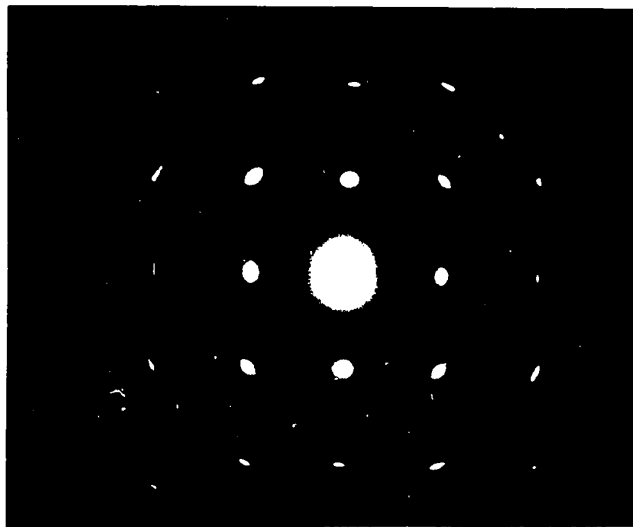
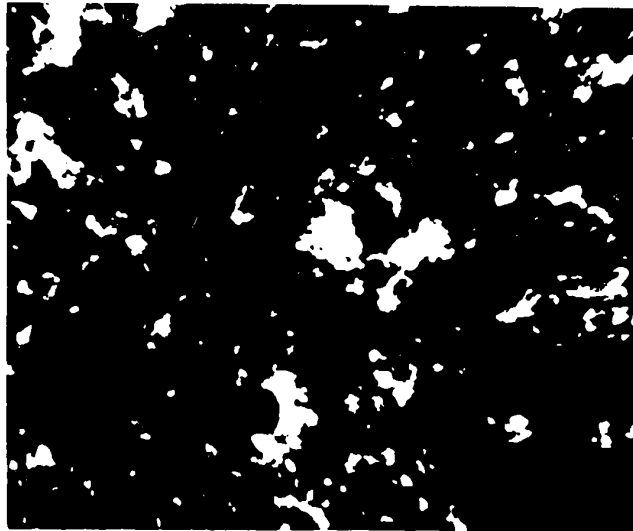
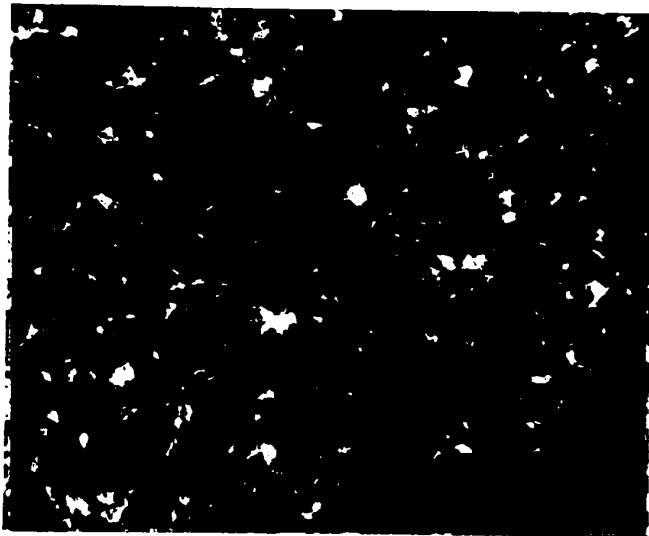


Figure 4.2.5

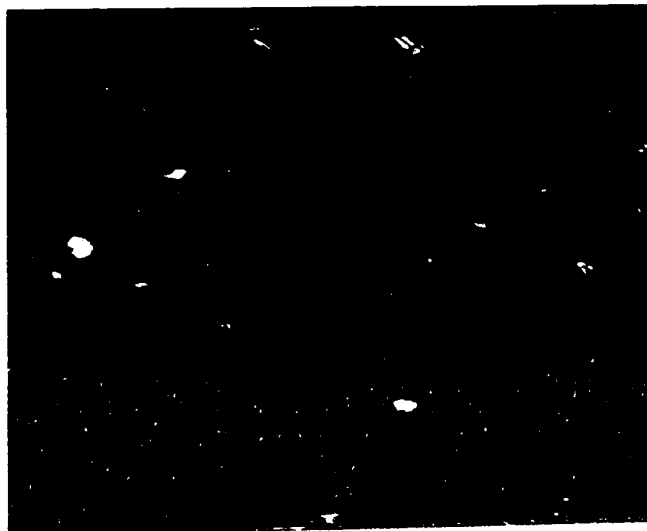
(d) Bright field micrograph x 18,000

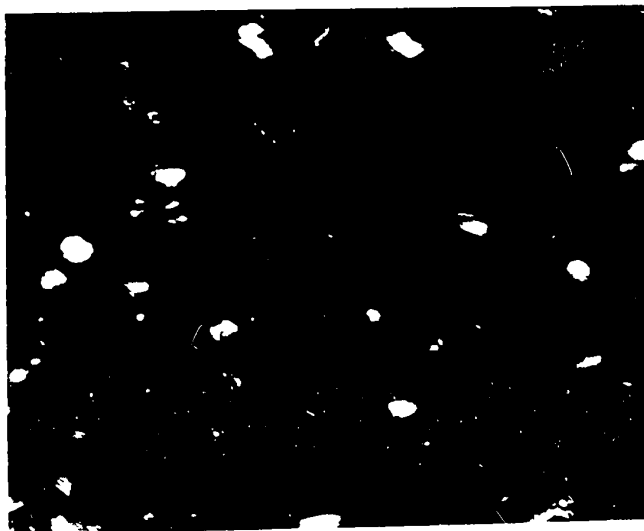
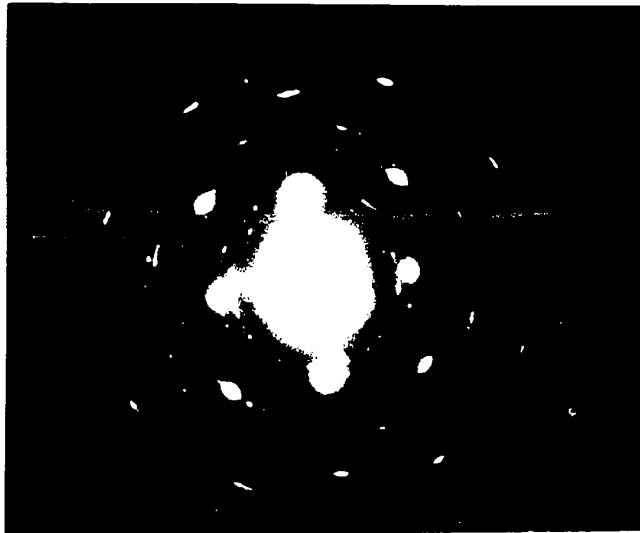
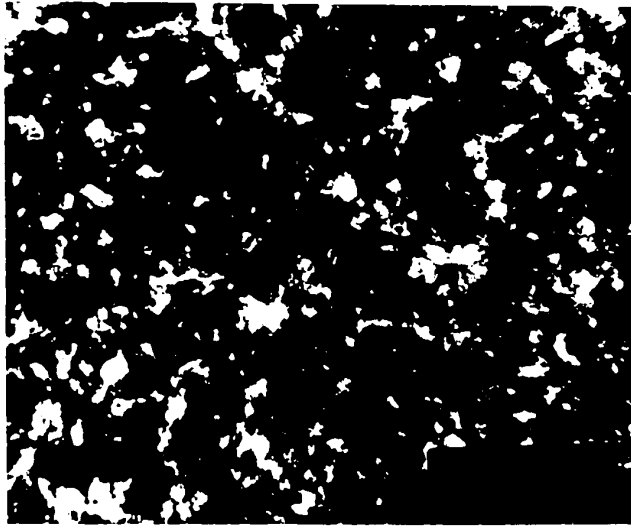


(e) Selected area diffraction pattern



(f) Dark field picture taken with (200) reflection x 28,000





Figures 4.2.6 (a)-(c) represent features of a sample which has been oxidized for 3 hr. (film thickness  $\approx 2200\text{\AA}$ ). The general features of the film can be represented by the diffraction pattern shown in figure (b) which is very typical for the film in this thickness range; however in some other sections of the film the type of pattern shown in figure (c) was found. It is essentially polycrystalline with some evidence of preferred orientation on the (111) as shown by the arcs on the 3rd (220) ring.

Figures (d)-(f) are the micrographs from a sample oxidized for 5 hr. The film average thickness is about  $3500\text{\AA}$ . Some sections of the film were too thick for the electron beam to pass through, but for most part, it was thin enough for some information to be obtained by electron transmission. The BF picture now shows dark patches of thick oxide. Selected area diffraction of these regions yield the familiar (100) spot pattern along with the continuous rings. The DF picture taken with the (200) reflection is shown in (f). Compared with the BF micrograph the crystallite size can be estimated more easily in the DF micrograph.

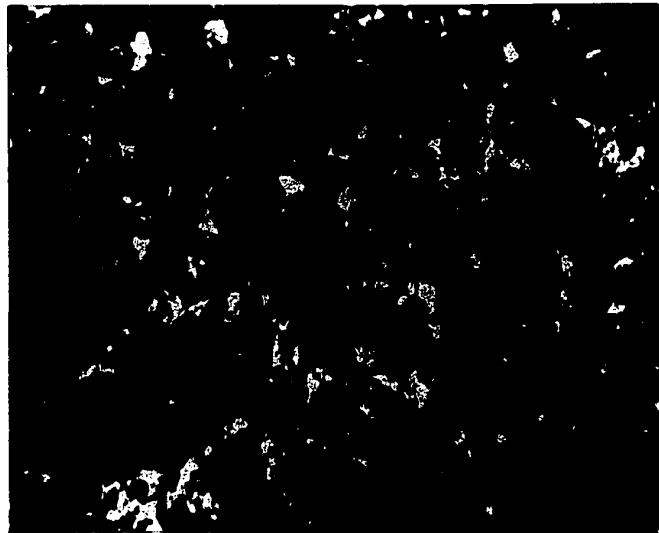
For samples oxidized up to 8 hr., the films were too thick over most regions for the electron beam to pass through. Some BF pictures were taken, nevertheless, for the purpose of measuring the grain size.

#### 4.2.7 Crystallite size and distribution.

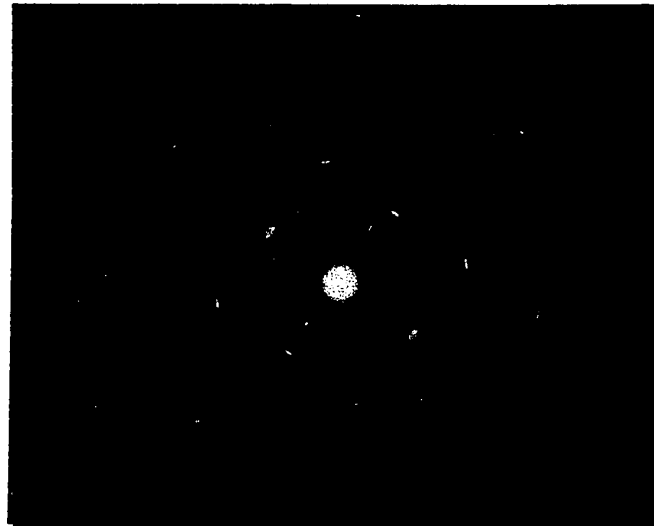
From the DF micrographs the size and distribution of the crystallites can be determined. (Up to 500 crystallites

Figure 4.2.6

(a) Bright field micrograph x 18,500



(b) Selected area diffraction pattern



(c) Selected area diffraction pattern of different region



Figure 1

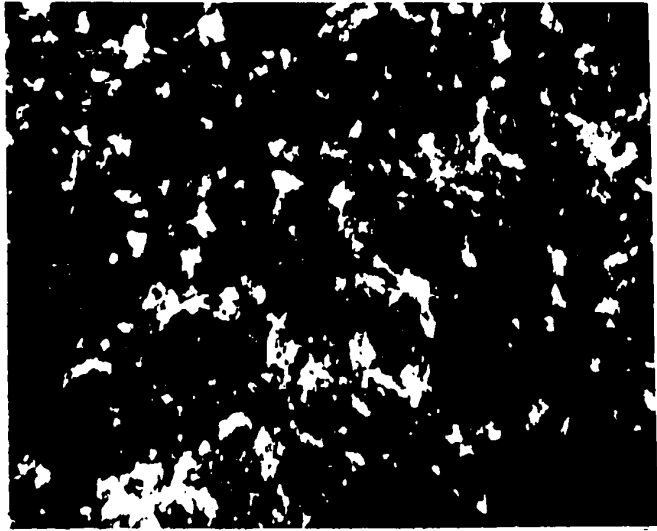


Figure 2

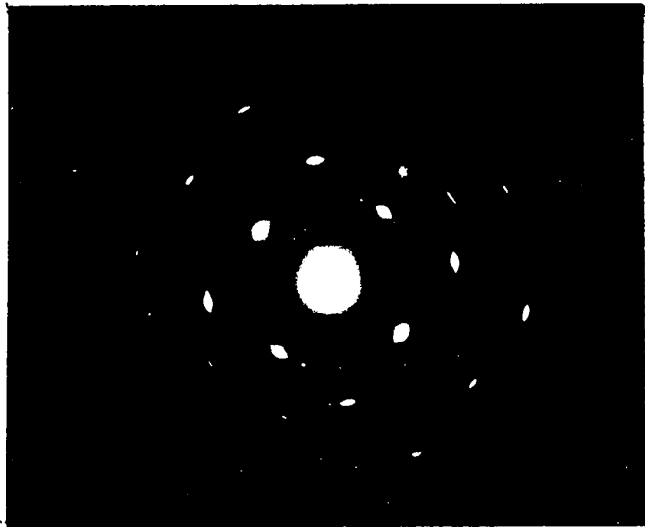
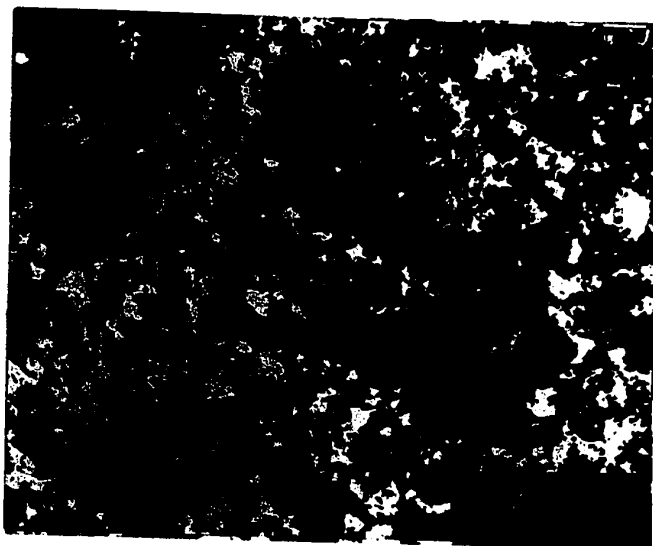


Figure 3

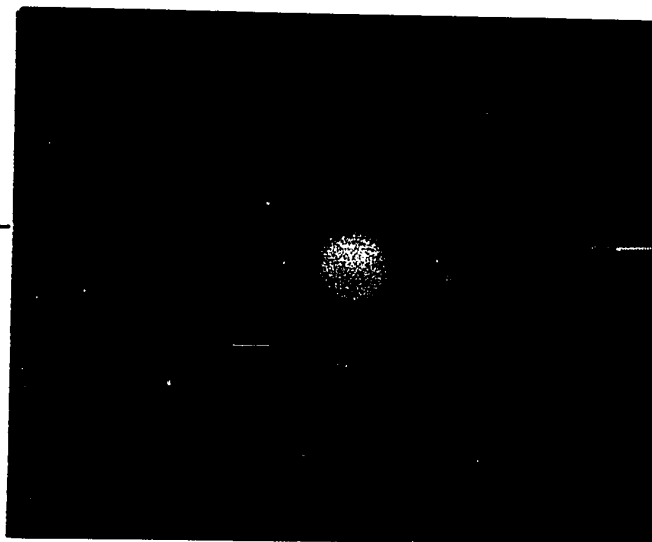


Figure 4.2.6

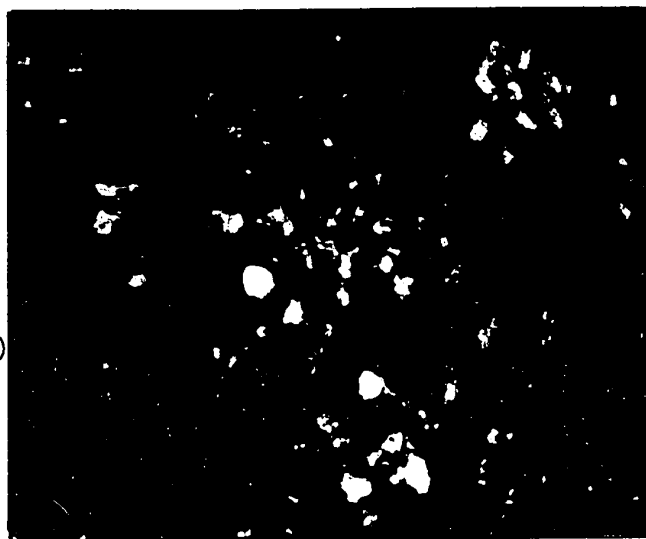
(d) Bright field micrograph x 22,000



(e) Selected area diffraction pattern



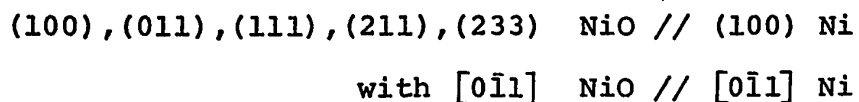
(f) Dark field micrograph taken with (200) reflection of (e) x 28,000



having different orientations from each sample were measured to .5 mm accuracy with a ruler.) The distribution of the crystallites is plotted as fraction of crystallites vs crystallite size and it is shown in figure 4.2.7 (a). Note the change in the shape of the distribution curve with exposure time. The average size is calculated from the distribution curve for each sample and is plotted vs time. The results are given in figure (b). The crystallites size remains essentially constant during a period up to 40 min; they then quickly increase in size, the growth rate decreasing with increasing exposure time.

#### 4.2.8 Summary of the results of the (100) face.

In the thickness range investigated (300-5000Å), the structure of the oxide films formed on the (100) face is relatively homogeneous and dislocations, twins or pores were not observed. The films are composed of small crystallites ranging in size from 300-400Å in the early stage of oxidation to 700-900Å after 8 hours of exposure to oxygen. These crystallites exhibit different crystallographic orientations; some of them are randomly oriented, and some of them are related to the metal substrate by the following epitaxial relationships:



All together five different orientations have been observed. They all share a common close packed direction with the metal.



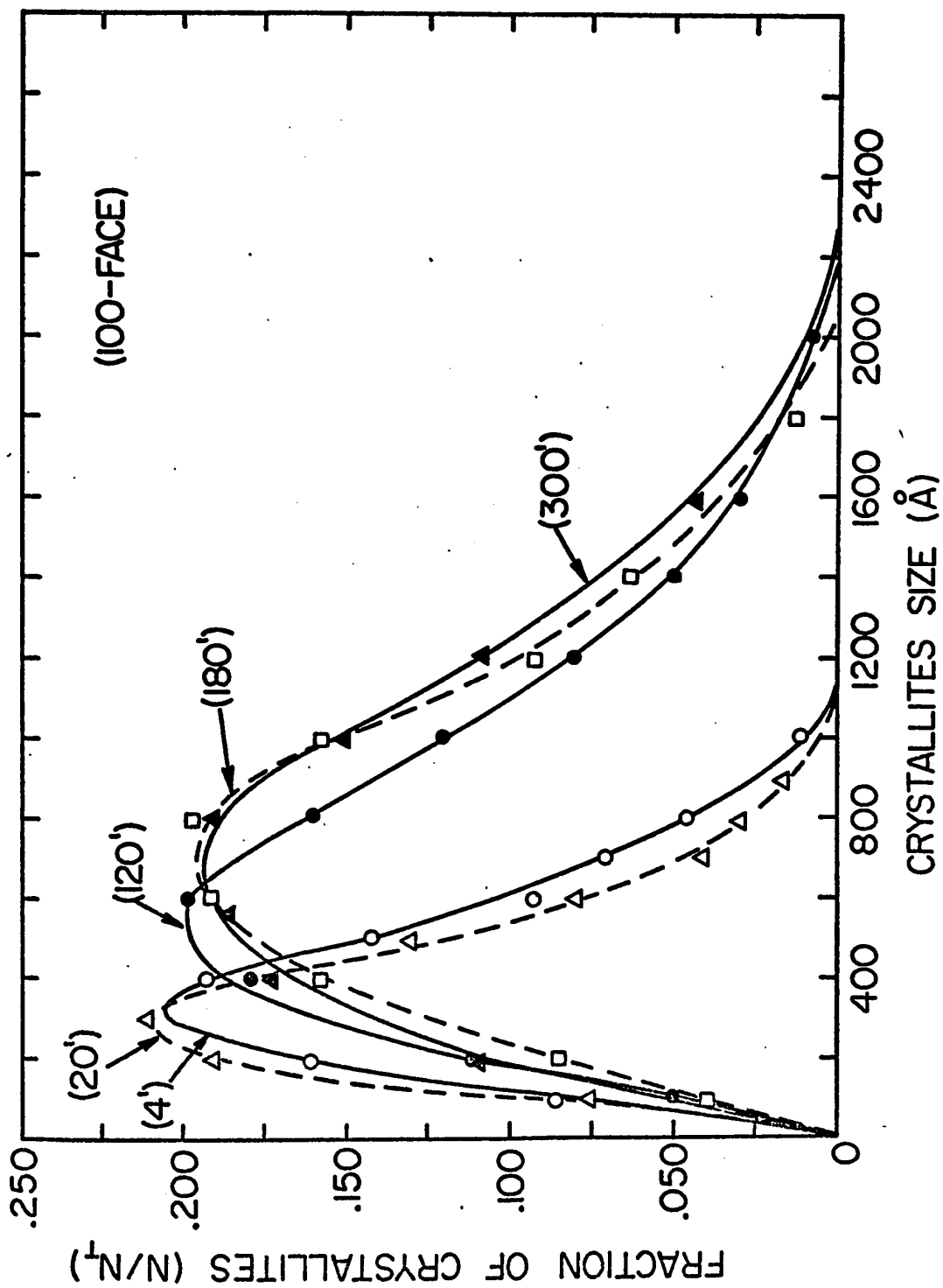


Figure 4.2.7(a) Crystallite size distribution for oxide films formed on the (100) nickel face at  $500^\circ\text{C}$

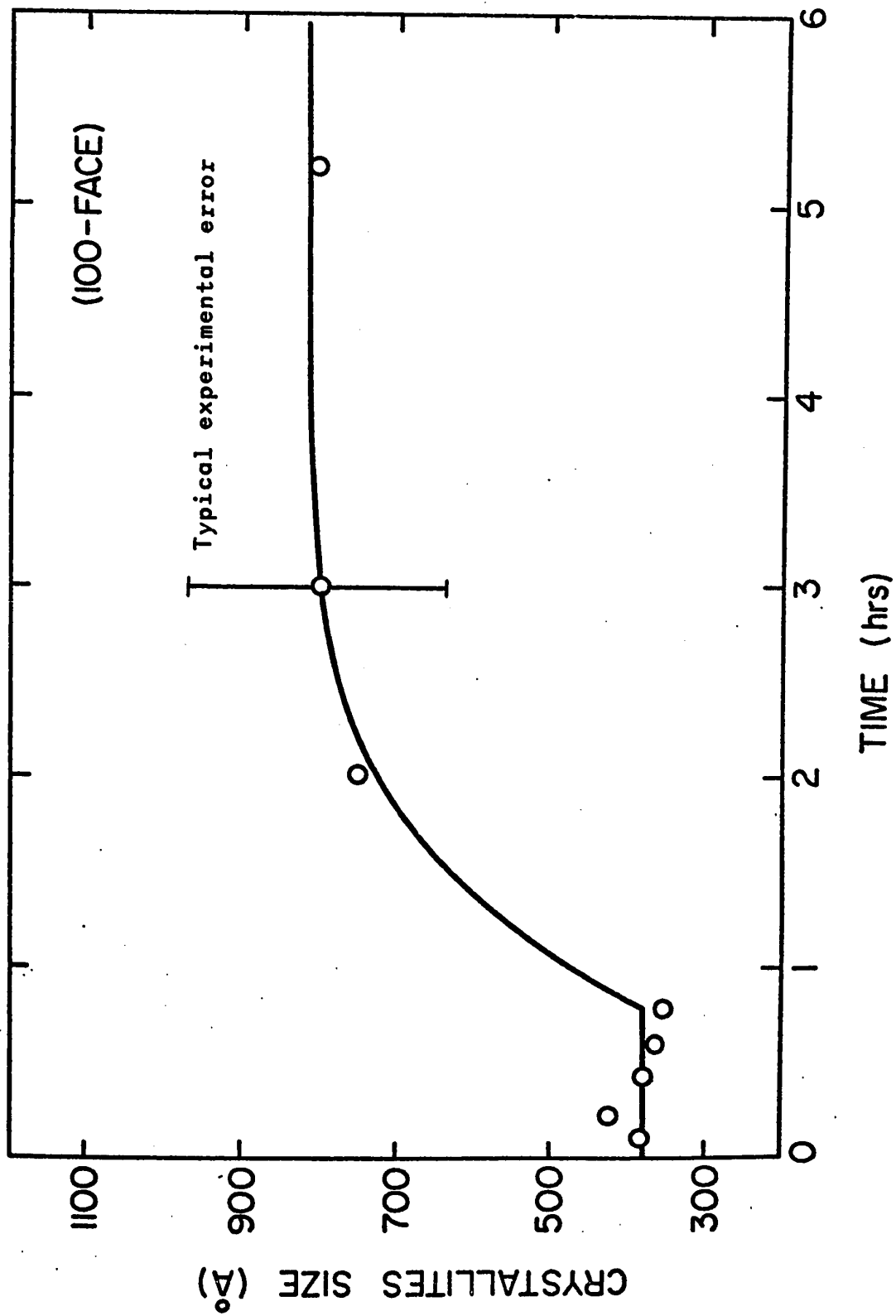


Figure 4.2.7 (b) Average crystallite size versus oxidation time

The (211) and (233) orientations have been found to occur in multiple of six. Two of the six orientations can have their  $[0\bar{1}1]$  direction parallel to the  $[011]$  direction in the metal and the remaining four have their  $\langle 011 \rangle$  directions at  $\pm 30^\circ$  from the close packed direction of the nickel. The latter four orientations were only observed in the very thin film range.

The above orientations changed with exposure time and a trend could be established. In the very thin films, crystallites with many orientations are present. The crystallites are well aligned with the metal substrate and the diffraction patterns are thus composed of many superimposed spot patterns without continuous rings. With continued exposure to oxygen, spots from the low index planes and continuous rings become more apparent. Finally, the (100) and to the much lesser extent, the (111) orientations dominate the final stage of film growth.

In conclusion, it can be said that the structure of the films formed on the (100) face are relatively uniform. This statement will be clarified and confirmed later when the results are compared with the other two nickel faces. A detailed discussion concerning the structural development of the oxide will be given in chapter 5.

#### 4.3 Transmission electron microscopy results for the (110) nickel face

The results for the (110) face will be presented in the same chronological order as the (100) face. All the relevant observations concerning the interpretation of the micrographs explained in section 4.2.1 can be directly applied to this section. It should be mentioned that the results from the investigation on the kinetics given in section 4.7 show that this is the slowest oxidizing face at 500 °C with poor reproducibility and frequent breaks in the oxidation curves.

4.3.1 Specimen Exposure: 15 min. Electron micrographs of a sample oxidized for 15 min. are given in figures 4.3.1 (a)-(n). The film thickness is about 500 to 600 Å. It is uniform with no abnormally large crystallites as shown in the BF picture (a). The diffraction pattern in (b) reveals complex orientation relationships. The detailed interpretation of this pattern with the appropriate comments are given in appendix B(4). The following orientations have been found:

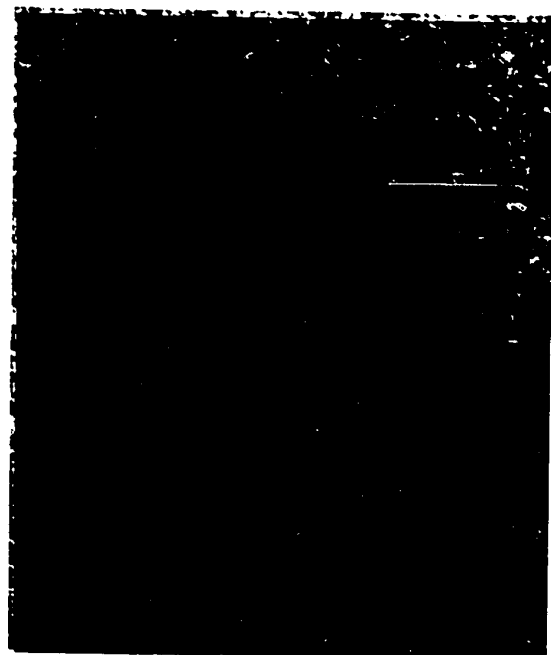
(111), (211), (311), (322), (411), (433) and (123) NiO // (110) Ni  
Note that all these planes with the exception of the (123) plane contain the  $[0\bar{1}1]$  close packed direction. The (123) plane does not contain a close packed direction but it is one of the most densely populated Relp of the FCC system.

The diffraction pattern of another section of the film is shown in (c). This pattern contains the previously

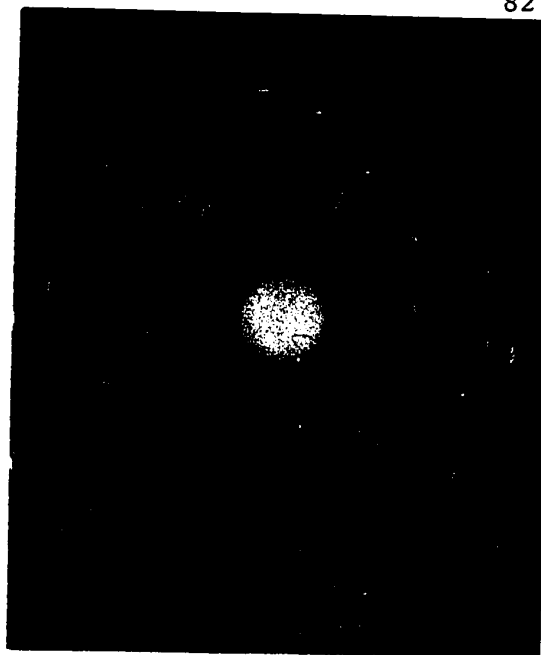
indexed orientations but the intensity of the diffracted spots from the (211) Relp is very strong indicating a highly oriented film section. The DF picture taken with the (111) reflection fig. (d), confirms this observation.

Very often twins are observed. The BF micrograph seen in (e) does not reveal any twin plates, however the SAD of the section of the film shows that twinning has occurred. The pattern in (f) can be indexed as the (011) Relp of NiO which has been twinned on the  $(11\bar{1})$  plane. The composite pattern can be obtained by rotating the (011) Relp  $180^\circ$  around the  $[11\bar{1}]$  direction. The rotation around the twin axis perpendicular to the electron beam indicated that the twinning plane hence the twin boundary is parallel to the electron beam. The schematic drawing of this pattern is shown in figure (g). The DF pictures taken with the objective aperture set at the main and its twinned diffracted spots are given in (h) and (k). The DF taken with both spots is shown in (l). It can be inferred from these observations that twinning must have occurred on individual crystallites since evidence of macroscopic twins cannot be observed.

Along with twinning, another feature particular to the films formed on the (011) face is that in certain sections of the films very strong (100) single crystal patterns are often observed. The BF and SAD are shown in (n) and (m). The strong single crystal pattern indicated a perfect mosaic structure in which the crystallites differed one from each



(a)



(b)



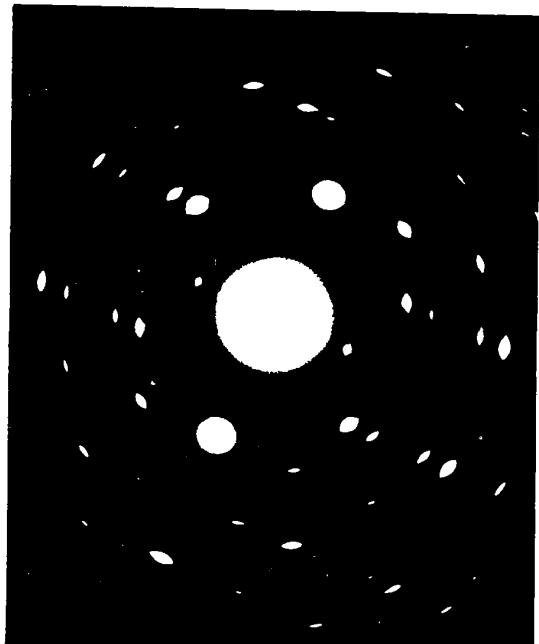
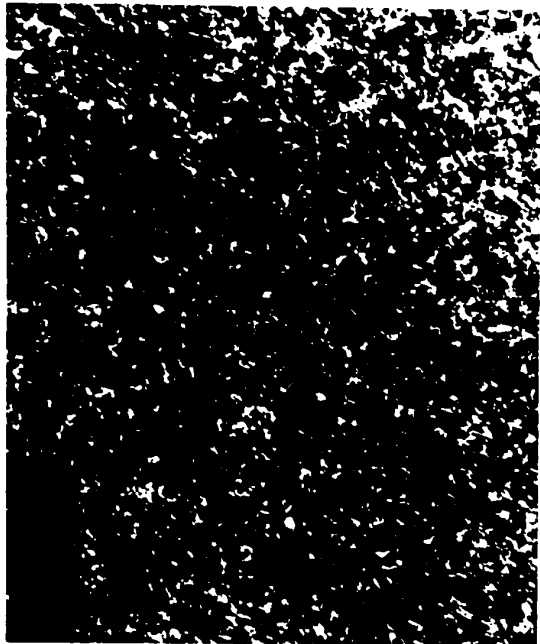
(c)



(d)

Figure 4.3.1

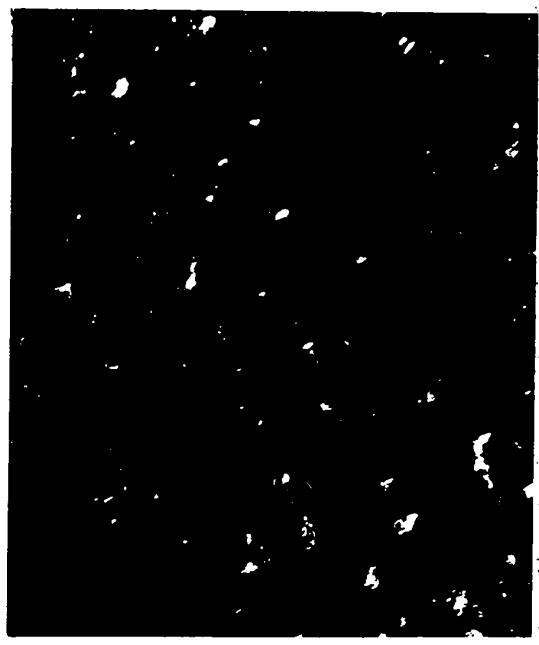
- (a) Bright field micrograph x 18,000
- (b) Selected area diffraction pattern of (a)
- (c) Selected area diffraction pattern of other region of the film
- (d) Dark field taken with the (111) reflection of (c) x 35,000



(10)



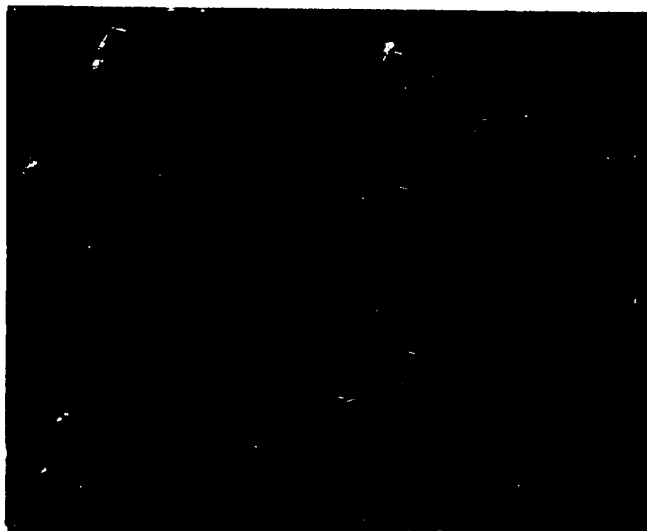
(11)



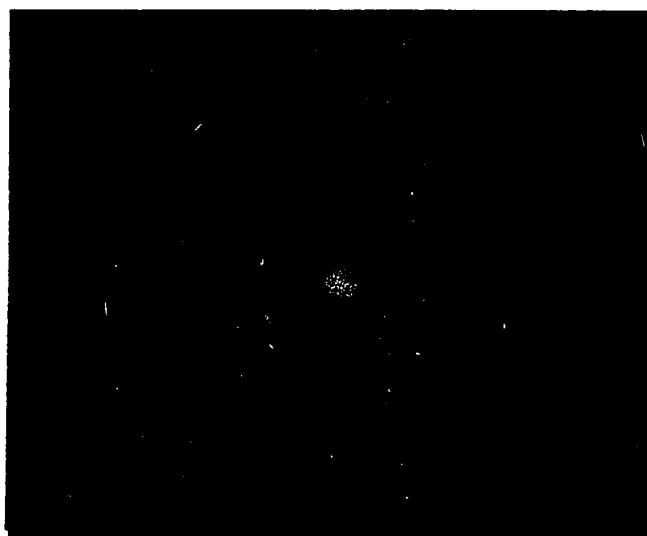
(12)

Figure 4.3.1

(e) Bright field micrograph x 42,000



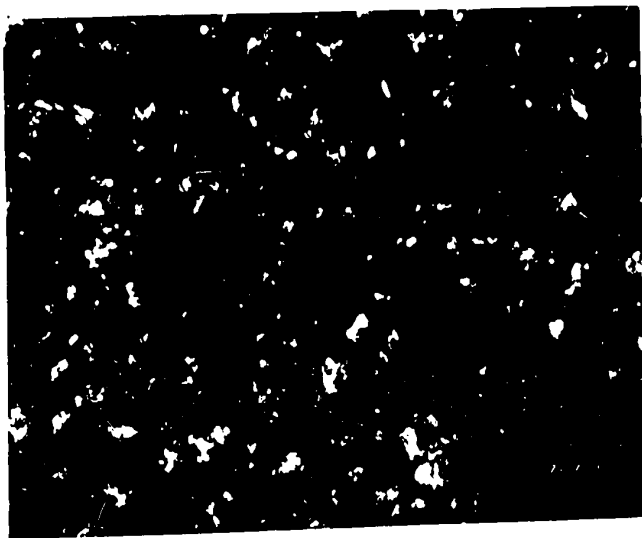
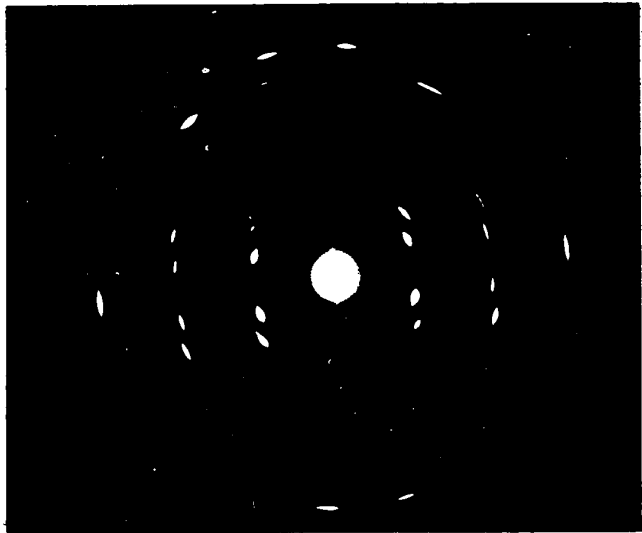
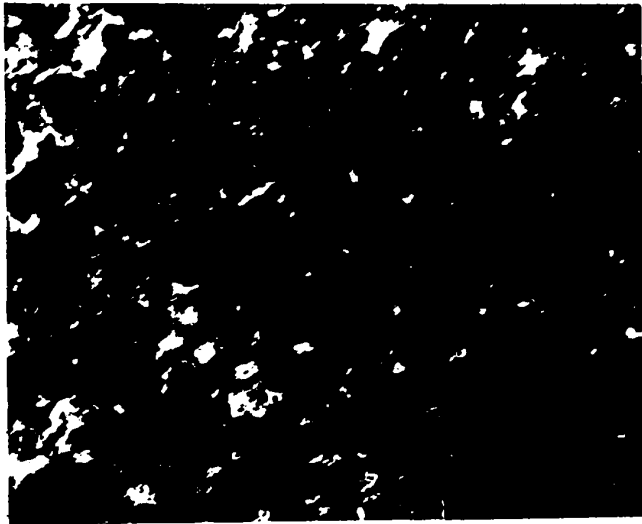
(f) Selected area diffraction pattern showing the presence of twins (schematic drawing is shown in (g)).



(h) Dark field micrograph taken with the objective aperture set at the main diffracted spot (see (g)) x 42,000







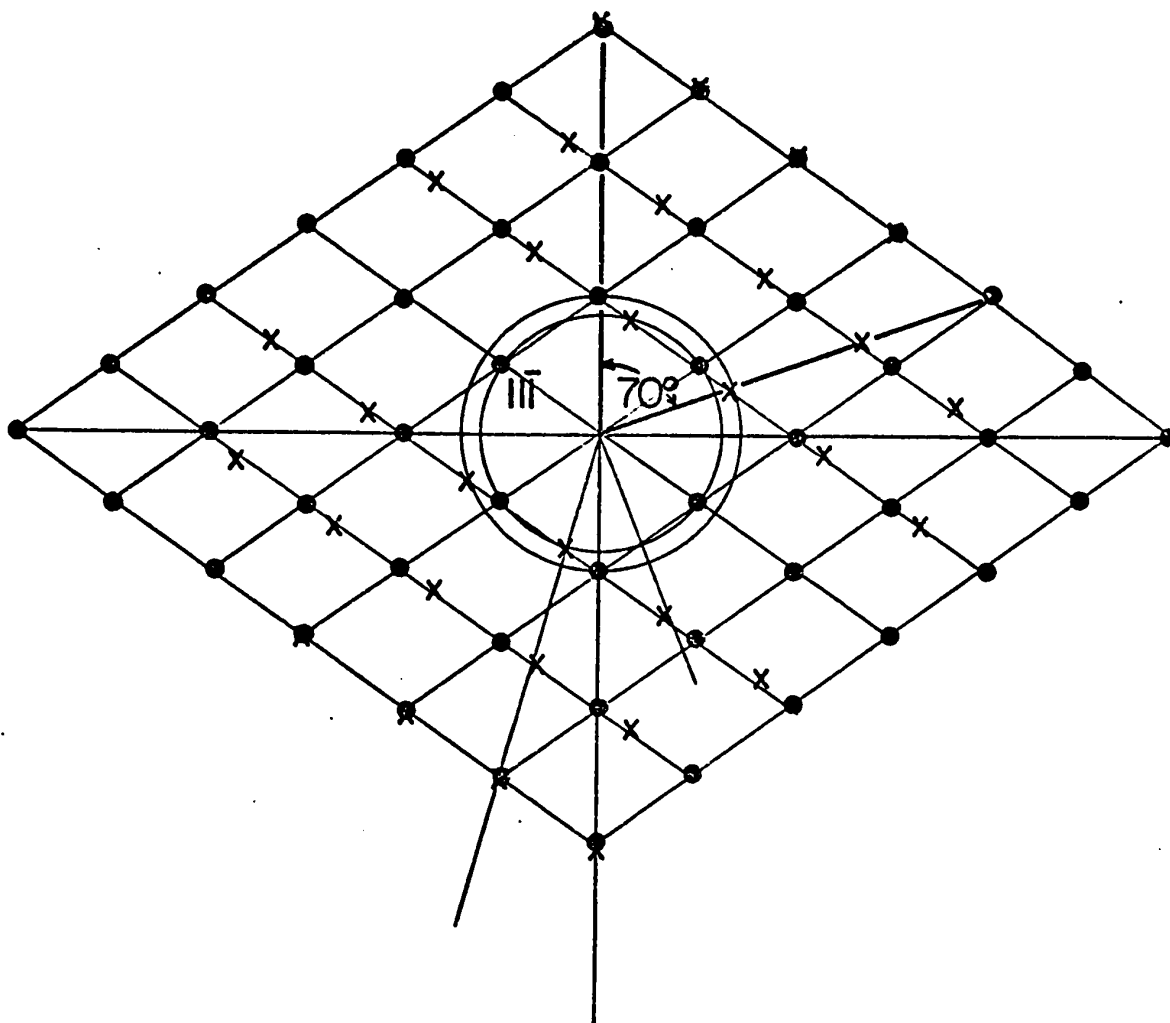
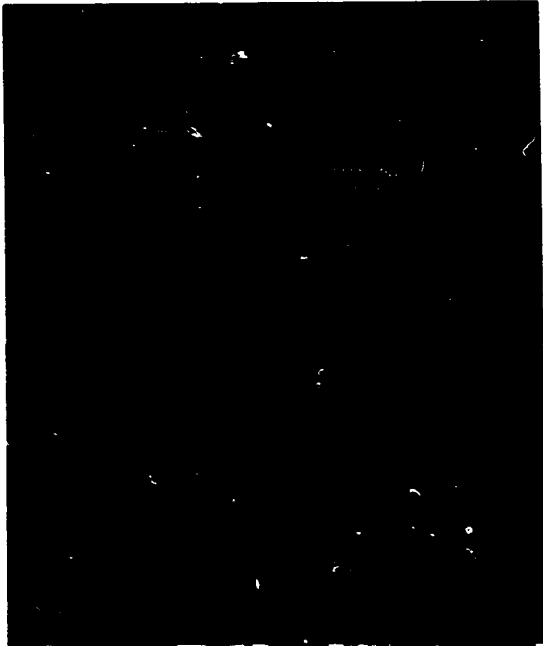


Figure 4.3.1 (g)

Schematic drawing of the (011) reciprocal lattice plane of NiO which has been twinned on the  $(11\bar{1})$  plane. The main diffracted spots are represented by (•) and the twinned spots by (x)

(\* Figure added for the purpose of indexing pattern 4.3.1(f)



(k)



(l)



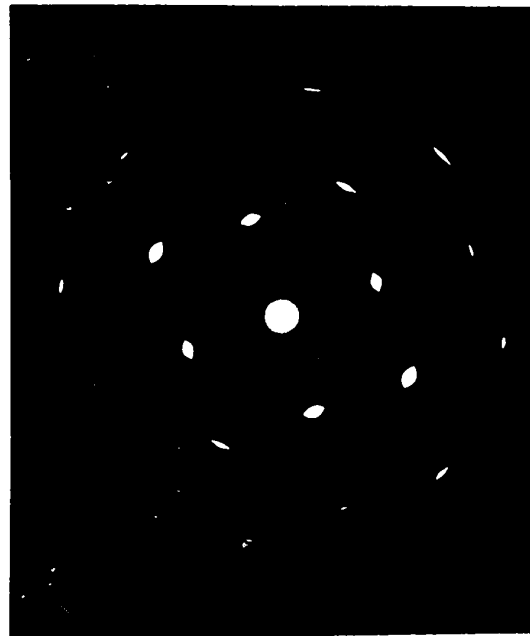
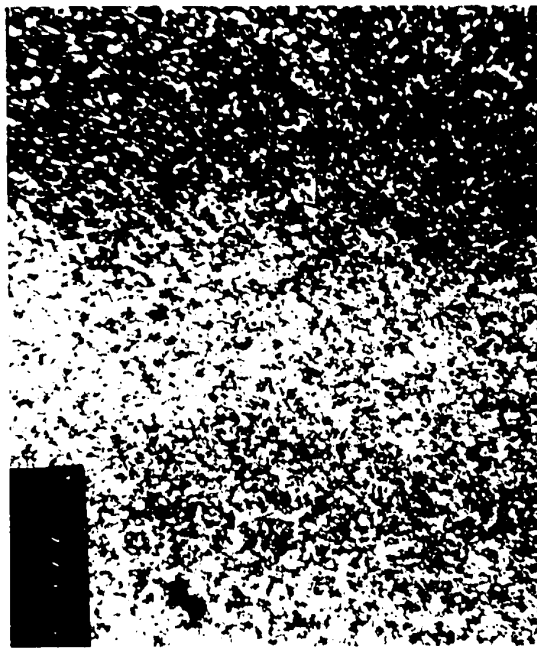
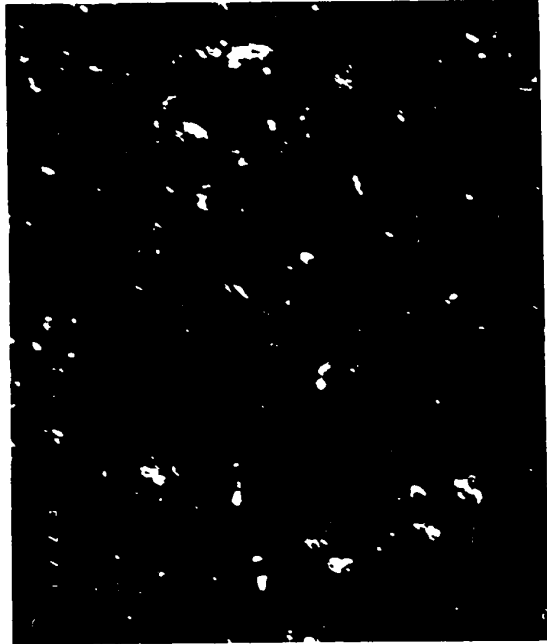
(m)



(n)

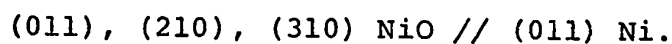
Figure 4.3.1

- (k) Dark field taken with the twinned diffracted spots x 42,000  
 (l) Dark field taken with both diffracted spots x 42,000  
 (m) Bright field micrograph of different section of the film x 13,500  
 (n) Selected area diffraction pattern of (m) showing (100)  
 Relp of NiO



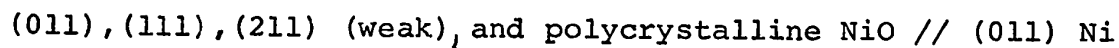
other by a very small angular misorientation.

4.3.2 Specimen exposure: 30 min. The structure of the film from a sample oxidized for 30 min. (film thickness  $\approx 700 \text{ \AA}$ ) are represented by the micrographs in figure 4.3.2 (a)-(k). The series of SAD patterns show a great number of orientations present in the film. The pattern (b) can be indexed as:

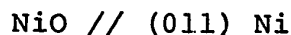
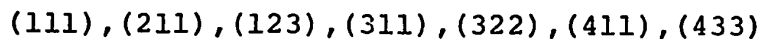


(See appendix B (5) for detailed interpretation.)

The pattern (c) corresponds to:



The pattern (d) corresponds to:

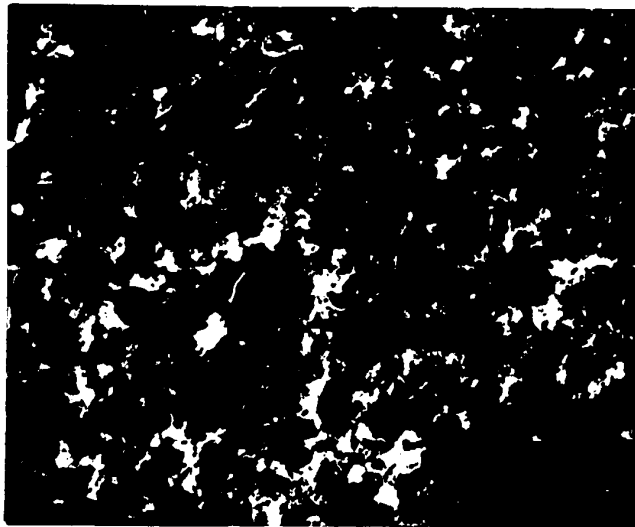


The pattern (e) contains the same orientations as the previous one in addition the (210) is also present. This plane can be recognized by the two diffracted spots on the (200) ring. (see appendix B(6)). Again the previously observed perfect (100) mosaic structure is present. The respective BF and SAD are shown in (f) and (g). The DF pictures taken with the (200) and the (220) reflection, (h) and (k), confirm the perfect mosaic structure of this portion of the film.

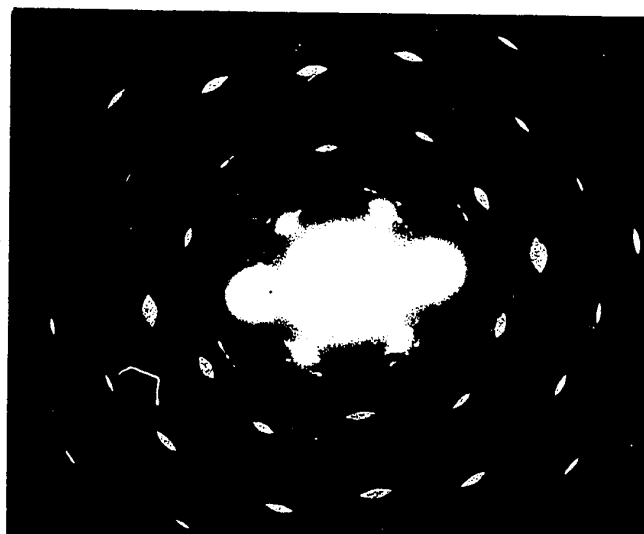
4.3.3 Specimen exposure: 60 min. A sample which has been oxidized for 60 min (film thickness  $\approx 1200 \text{ \AA}$ ) shows structure irregularities. The dark and light patches of the BF micrograph (a), indicated that the film thickness has

Figure 4.3.2

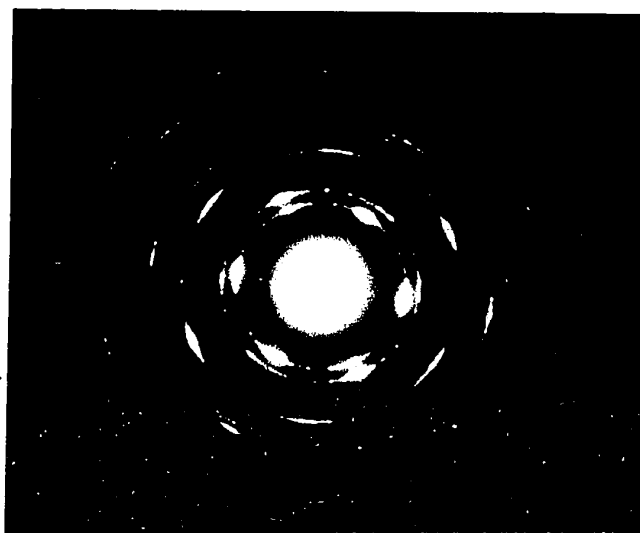
(a) Bright field micro-  
graph x 28,000



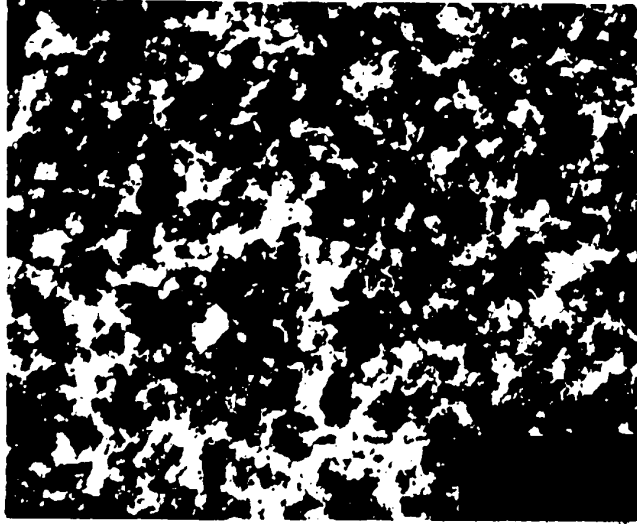
(b) Selected area diffrac-  
tion pattern of (a)



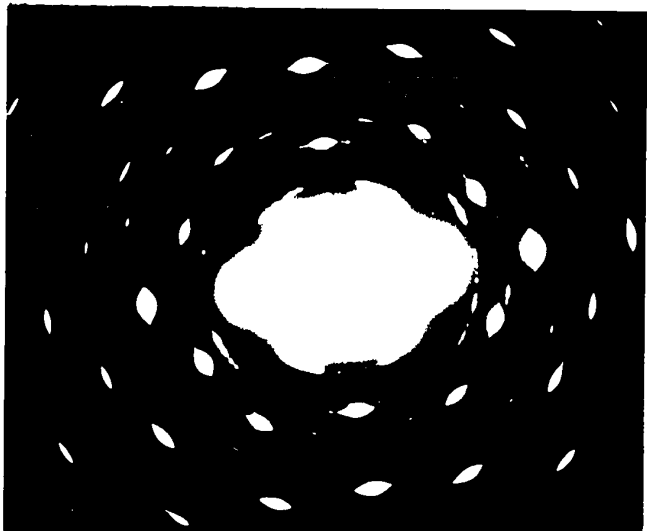
(c) Selected area diffrac-  
tion pattern of other  
section of film



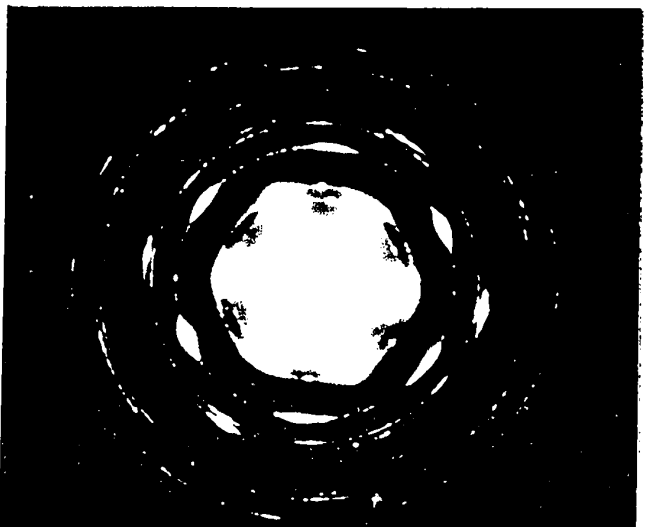
(a) Original image



(b) Original image with  
mean filter



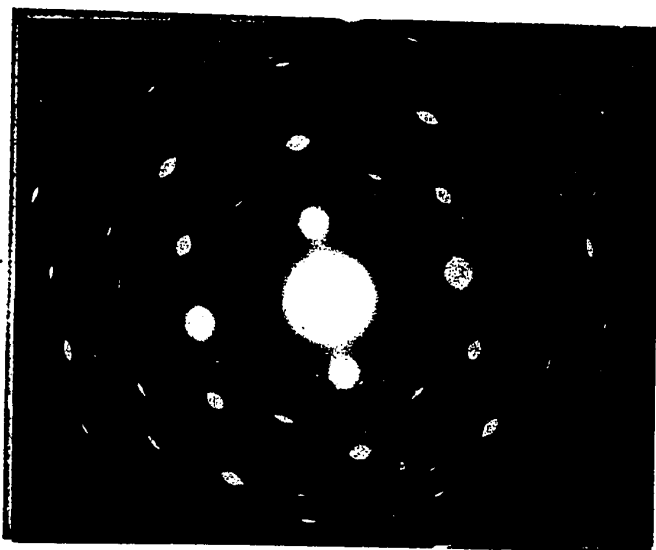
(c) Color image with  
mean filter



(d) Color image with  
mean filter and  
post-filtering

Figure 4.3.2

- (d) Selected area diffraction pattern of other section of the film



- (e) Selected area diffraction pattern of other region



- (f) Bright field micrograph x 9,000





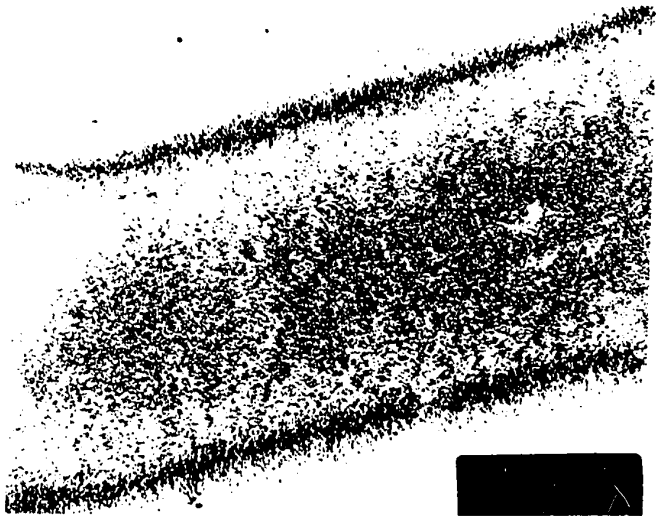
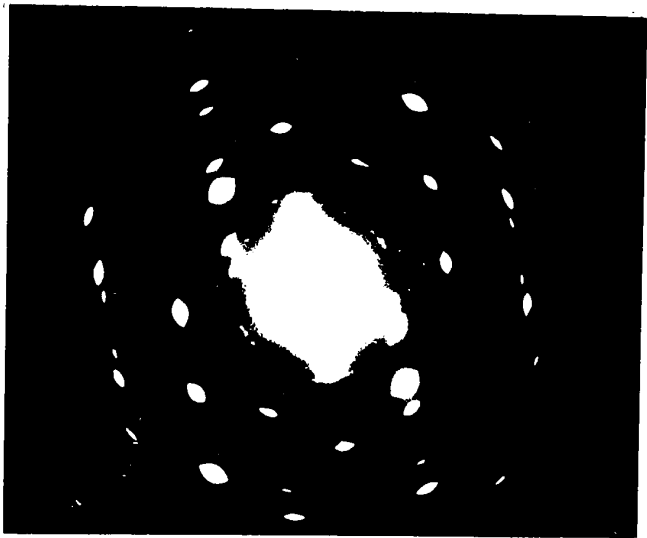
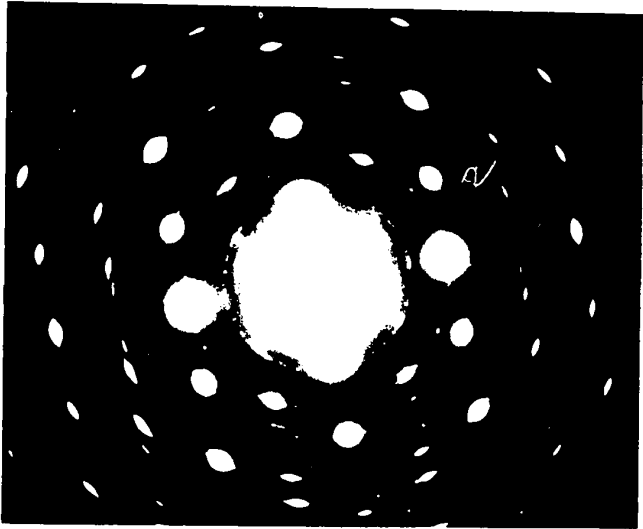
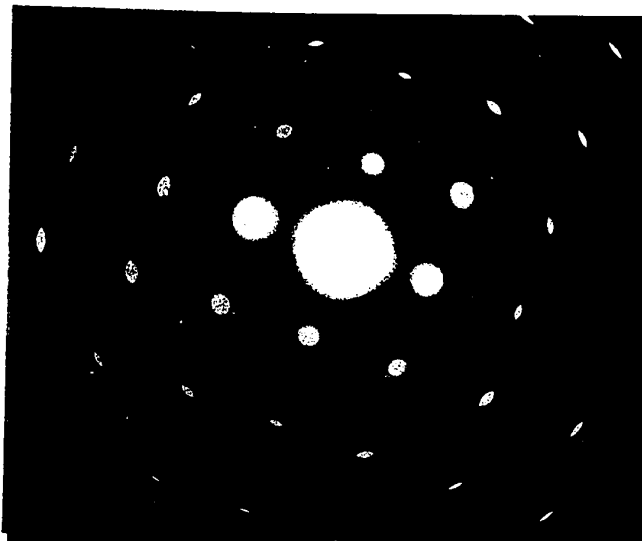


Figure 4.3.2

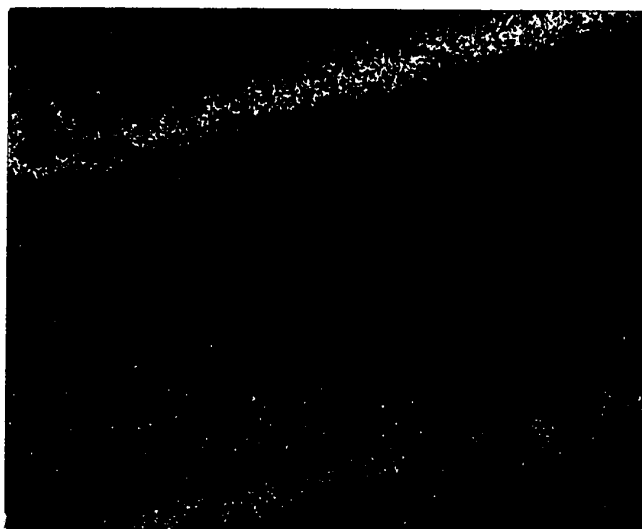
- (g) Selected area diffraction pattern of (f) showing (100) single crystal pattern



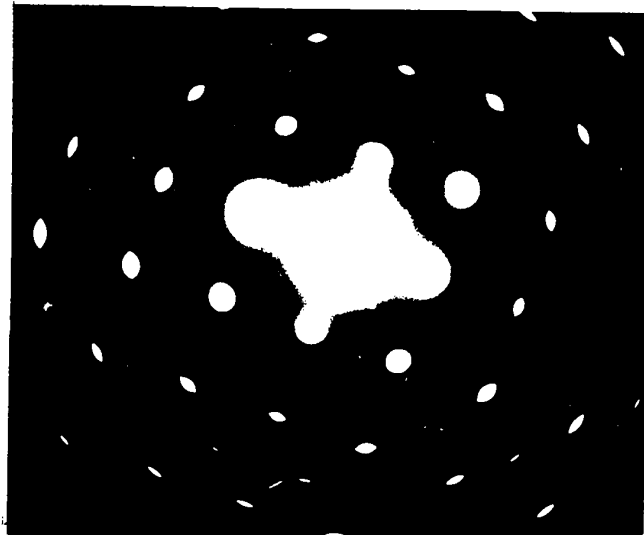
- (h) Dark field micrograph taken with (200) reflection of (g) x 9,000



- (k) Dark field micrograph taken with the (220) reflection of (g) x 9,000

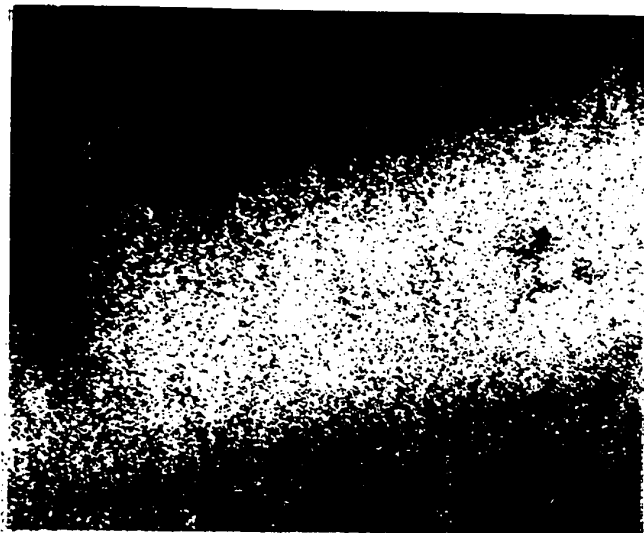


(a) *Styela* sp.

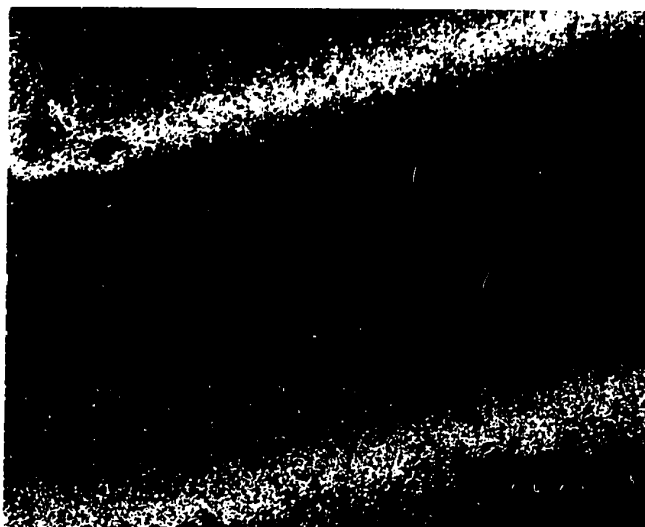


(b) *Styela* sp. showing the internal structure of the arms and the central disk.

(c) Dark field of view showing the internal structure of the arms and the central disk.



(d) Dark field of view showing the internal structure of the arms and the central disk.



become less uniform. In addition dislocations are also observed. (See region in circle.) The diffraction results now show some degree of polycrystallinity along with the following orientations, fig. (b):

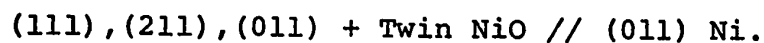


Figure (c) shows a very strong (211) orientation. The DF (d) taken with the (220) reflection indicated that the crystallites have grown to an irregular shape. Diffraction patterns of different sections of the film are given in (e) and (f). The pattern (e) contains the same orientations as the pattern 4.3.2(e). As we have seen, this type of pattern is fairly typical in this thickness range. In (f) the almost (211) fiber texture is found. It should be mentioned that the (100) perfect mosaic structure is also observed in this sample. The micrographs are similar to the previously shown and will not be presented here.

4.3.4 Specimen exposure: 120 min. For samples oxidized up to 2 hr. corresponding to a film thickness of about 2000 Å, the structure begins to show some evidence of polycrystallinity and complex diffraction patterns containing the high index planes are no longer observed. The BF micrograph is shown in (a). The most representative diffraction patterns given below confirmed these observations.

The pattern in (b) contains the following orientations:

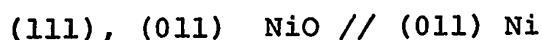
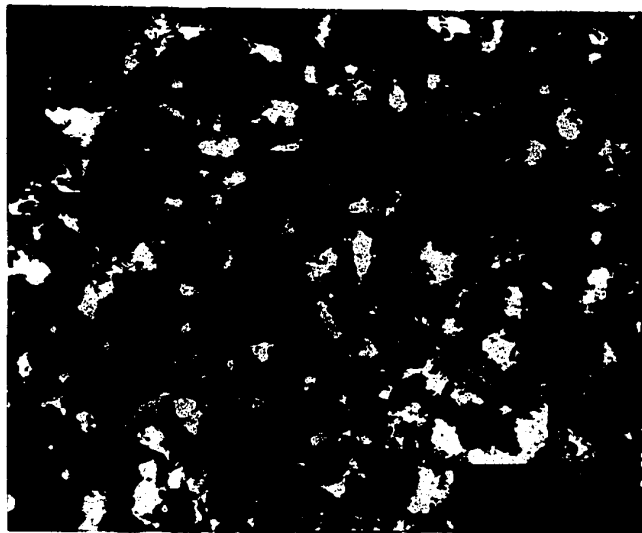
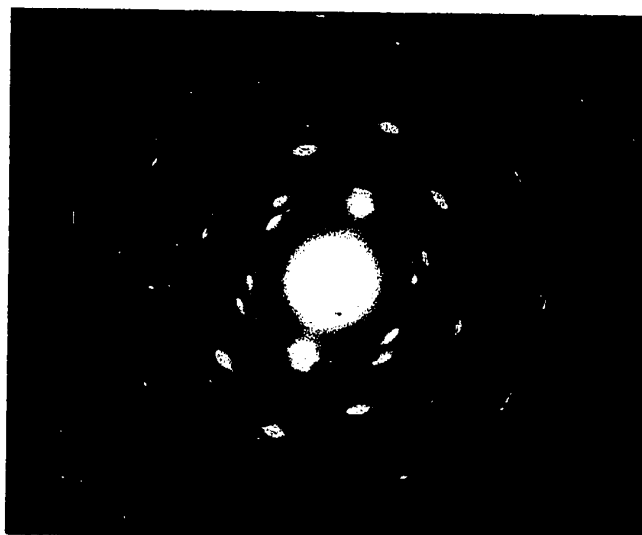


Figure 4.3.3

(a) Bright field micrograph x 35,000



(b) Selected area diffraction pattern of (a)



(c) Selected area diffraction pattern of other section of the film

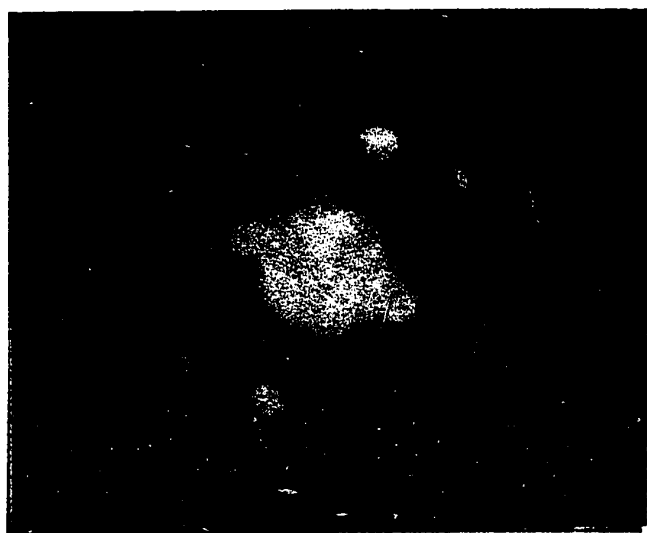
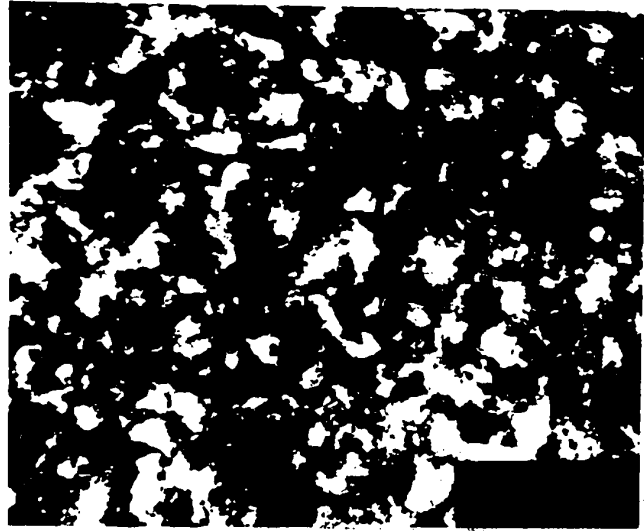
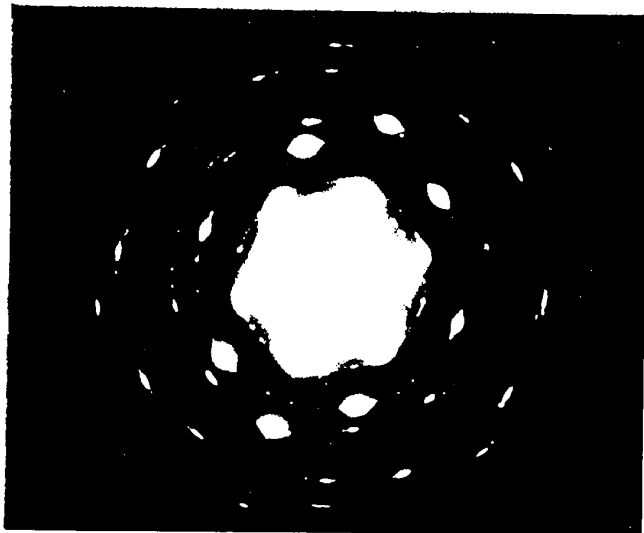


Figure 10.1

(a) Slight deformation graph of  $\alpha$ -Fe



(b) Selected area diffraction pattern of (a)



(c) Selected area diffraction pattern of other section of the film

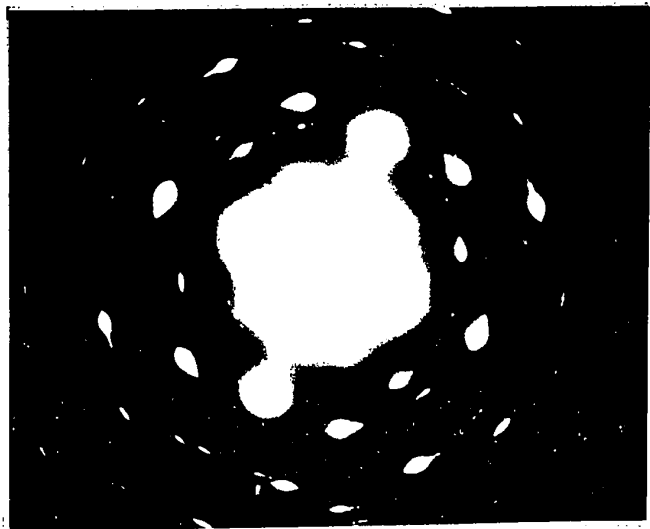
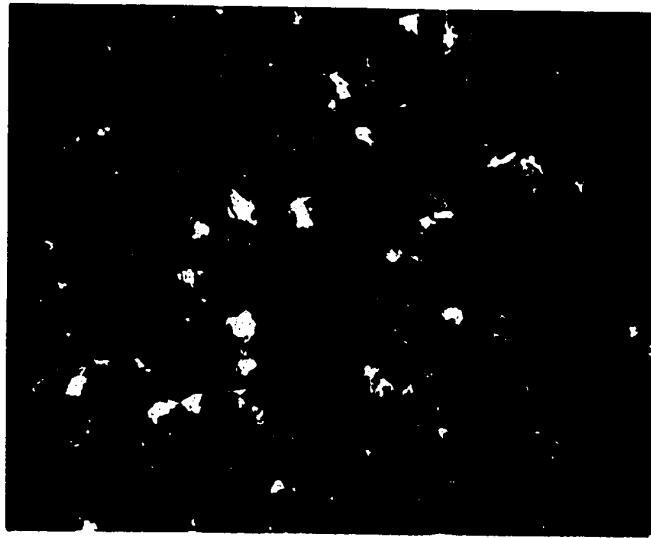
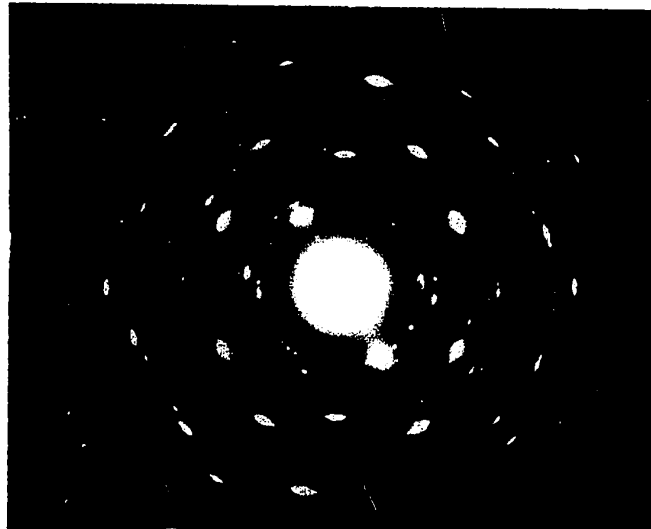


Figure 4.3.3

- (d) Dark field micrograph  
taken with (220)  
reflection x 42,000

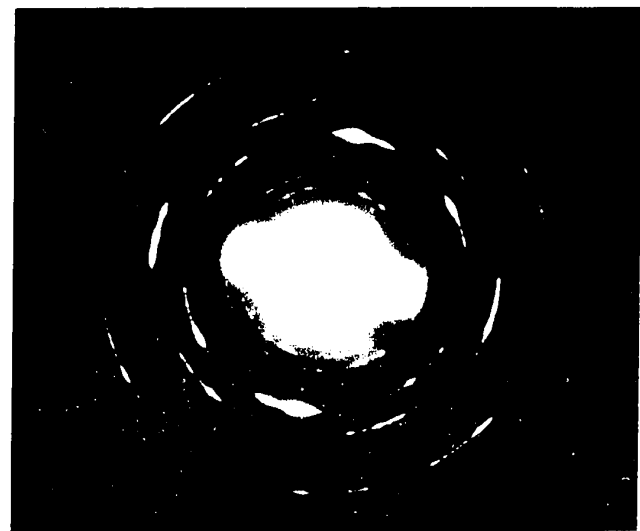
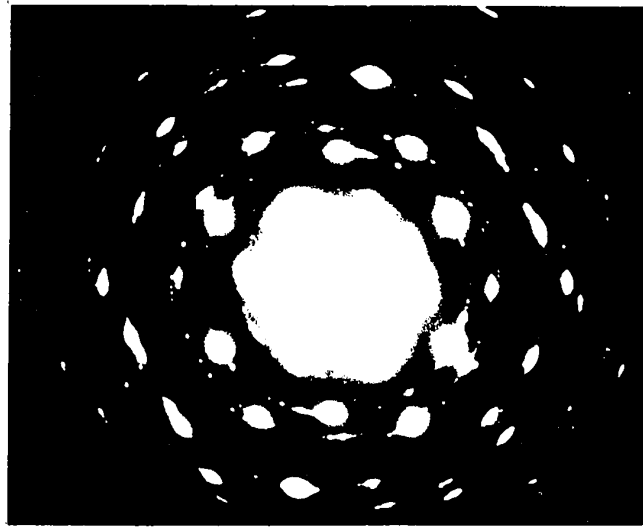
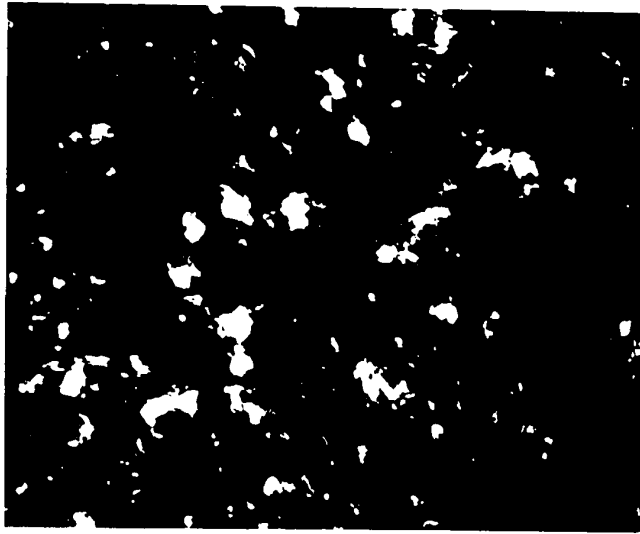


- (e) Selected area diffraction  
pattern of other  
region



- (f) Selected area diffraction  
pattern of other  
film section







The pattern in (c):

(211), (111) NiO // (011) Ni

The pattern in (d):

(011), (100) NiO // (011) Ni

The DF pictures taken with the reflections belonging to the three Relps (111), (211), (100) are shown in (e), (f) and (g). It can be seen from the DF that the crystallites having these three orientations have approximately the same size distribution.

4.3.5 Specimen exposure: 180 min. The results from a sample exposed to oxygen for 3 hr. are shown in this section. The film thickness is only 2000 Å which is about the same as the previous sample. The BF micrograph (a) shows regions of uneven thickness and the presence of dislocations. The SAD patterns show the familiar (011) twinned pattern, seen in (b), and a strong (211) along with the previous orientations shown in (c). (see for example fig. 4.3.1(b)) The results from another sample oxidized for 3 hr. show, however, regions of considerable polycrystallinity and "single crystal-mosaic" region as indicated by the two patterns seen in (d) and (e). Note that the degree of orientation or polycrystallinity may vary from sample to sample but the same type of orientations are usually found. The DF micrograph in (f) shows a large spread in size distribution of the crystallites.

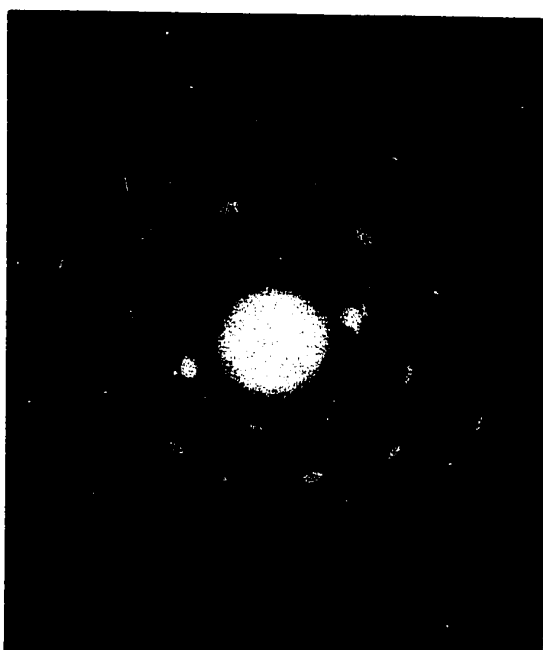
4.3.6 Specimen exposure: 240 min. Figures 4.3.6(a)-(d) are from a sample oxidized for 4 hr. (film thickness



(a)



(b)



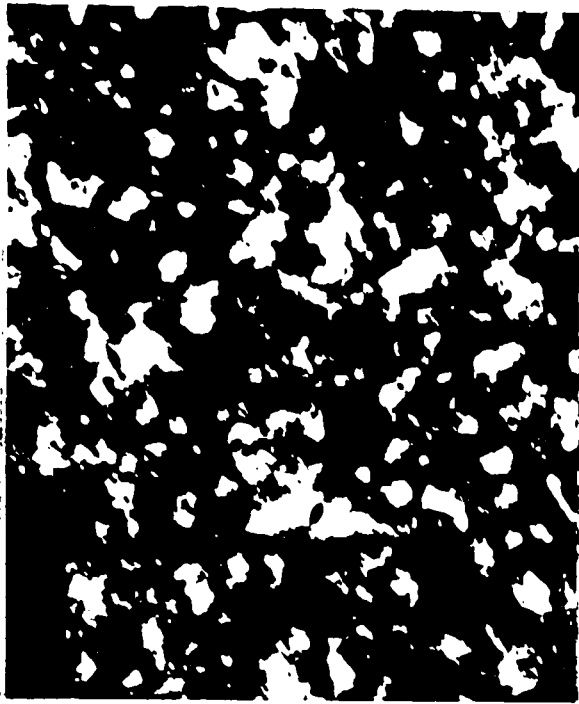
(c)



(d)

Figure 4.3.4

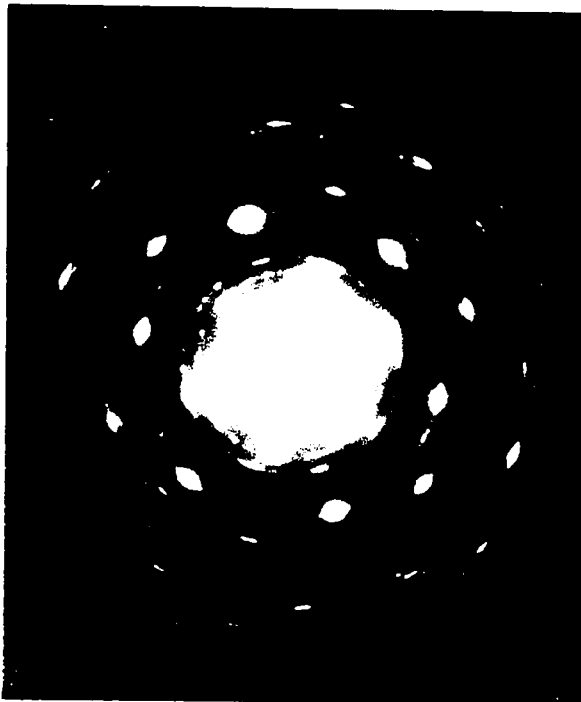
- (a) Bright field micrograph x 35,000
- (b) Selected area diffraction pattern of (a)
- (c) Selected area diffraction pattern of other section
- (d) Selected area diffraction pattern of other film section



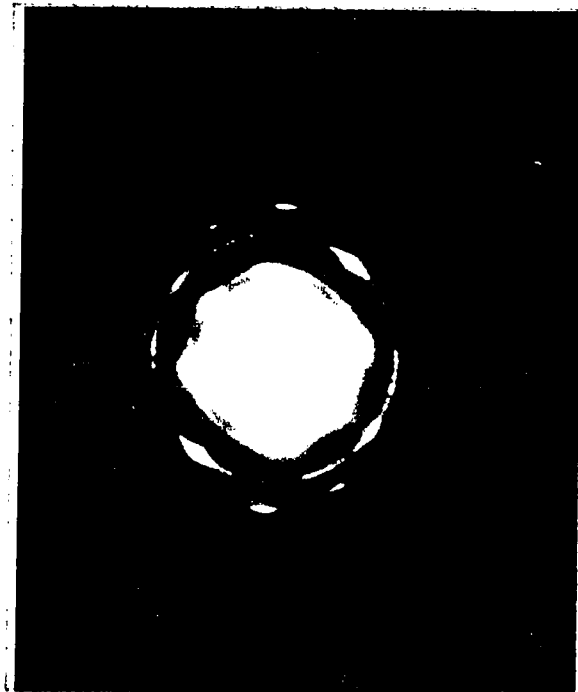
(a)



(b)



(c)



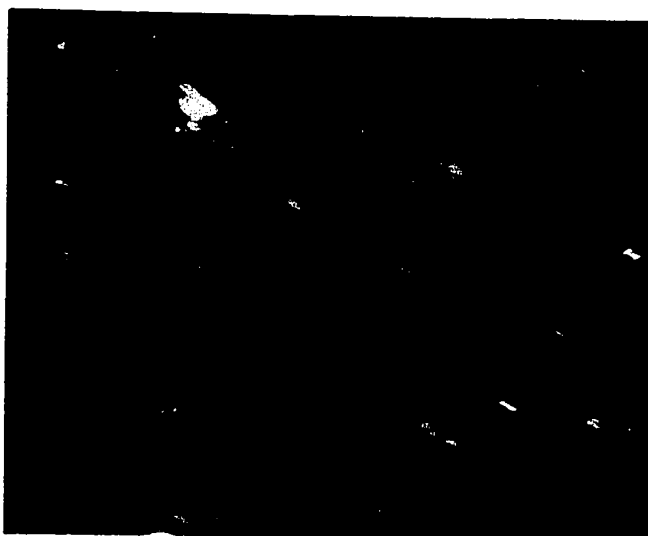
(d)

Figure 4.3.4

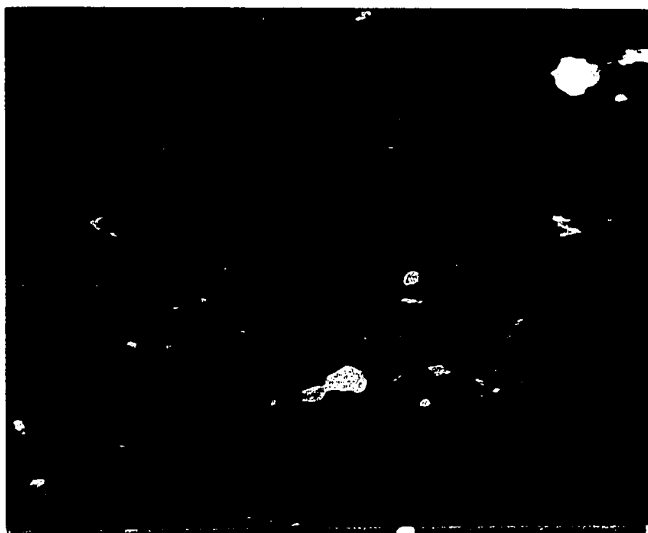
- (a) Bright field micrograph  $\times 35,000$
- (b) Selected area diffraction pattern of (a)
- (c) Selected area diffraction pattern of other section
- (d) Selected area diffraction pattern of other film section

Figure 4.3.4

- (e) Dark field picture  
taken with reflection from the (111)  
reciprocal lattice  
plane x 42,000



- (f) Dark field picture  
taken with reflection from the (211)  
Recp x 50,000



- (g) Dark field picture  
taken with reflection from the (100)  
Recp x 50,000



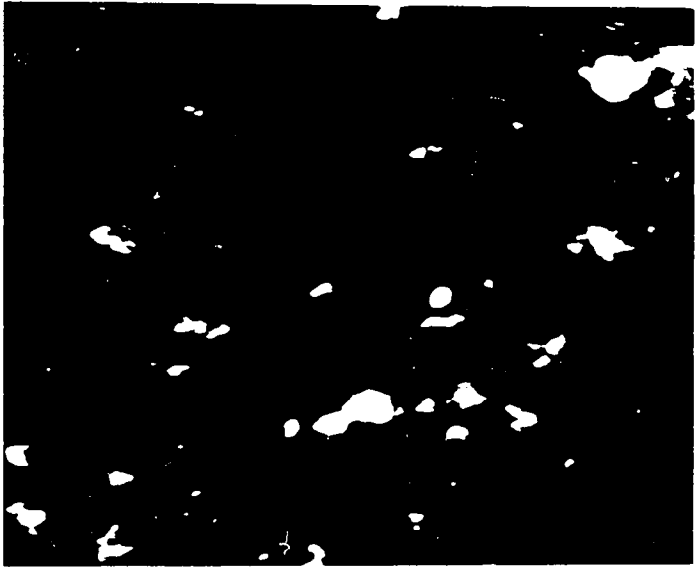
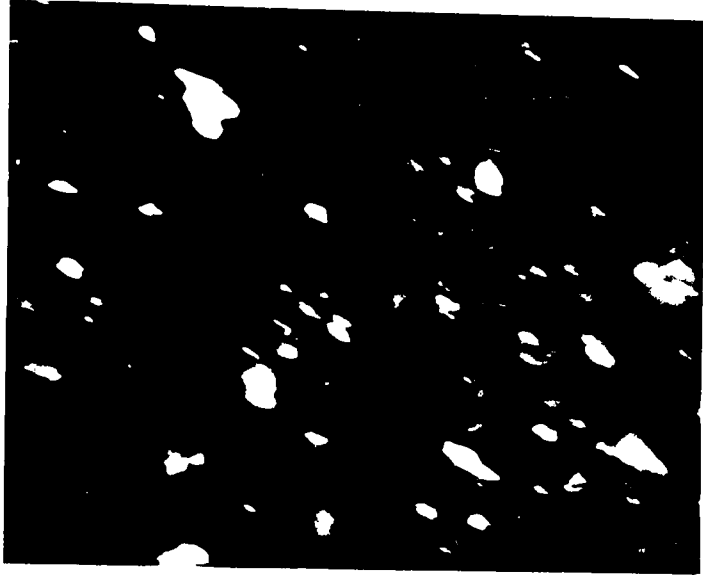
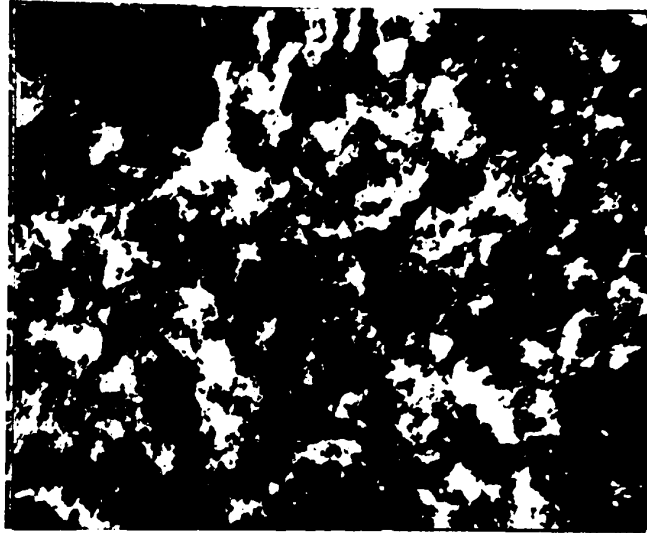
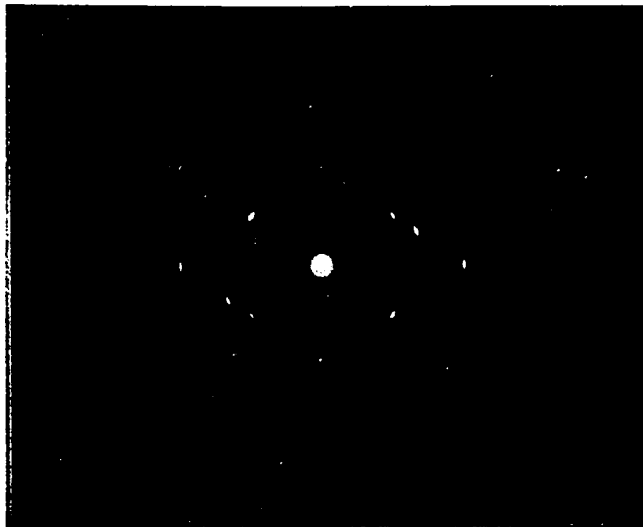


Figure 4.3.5

(a) Bright field micrograph x 35,000



(b) Selected area diffraction pattern showing the (011) Relp with twinning on the (111) plane

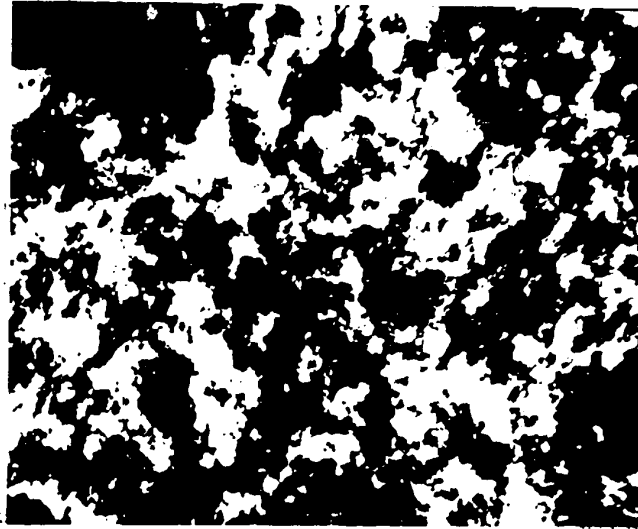


(c) Selected area diffraction pattern of other section of the film

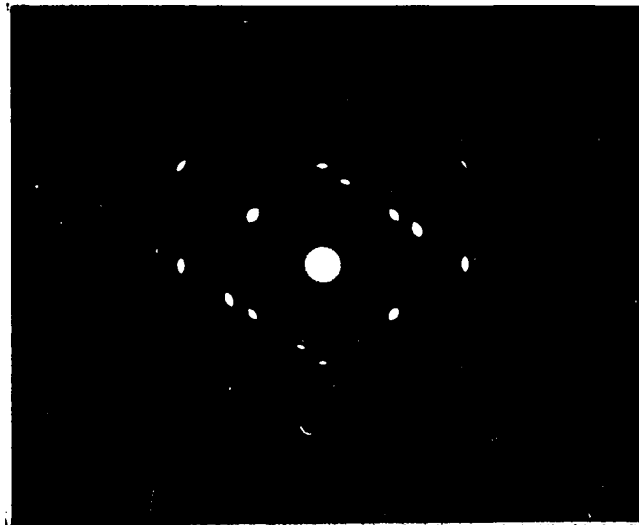


Figure 10

(a) Diffraction pattern  
of a single crystal



(b) Selected area electron  
diffraction pattern showing  
the (010) reflection with  
twinning on the (110)  
plane



(c) Selected area electron  
diffraction pattern of other  
section of the film

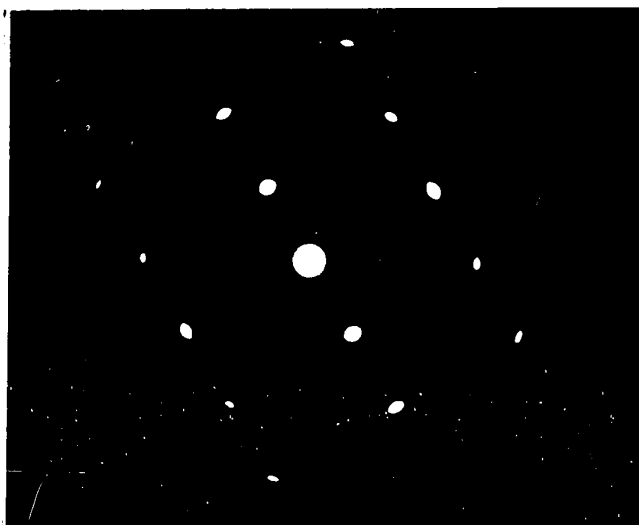
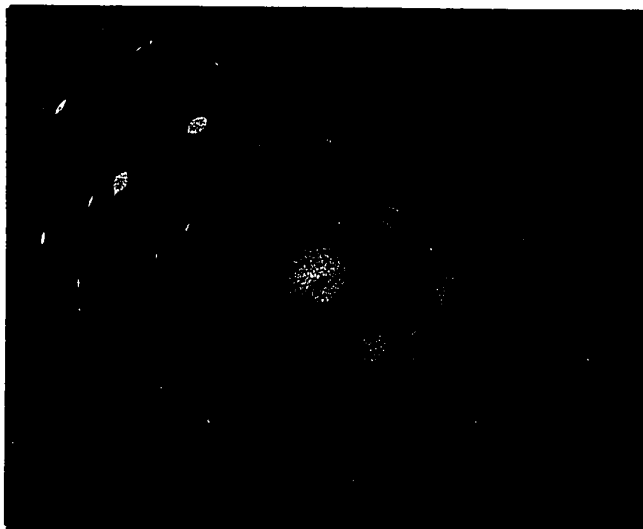


Figure 4.3.5

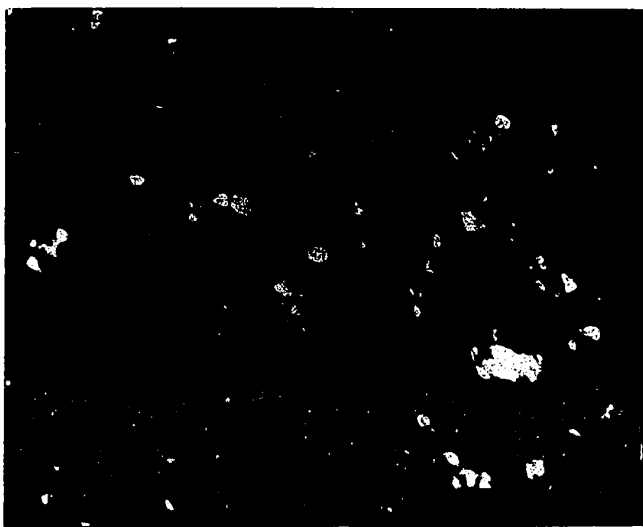
- (d) Selected area diffraction pattern of different sample oxidized for 3 hr.



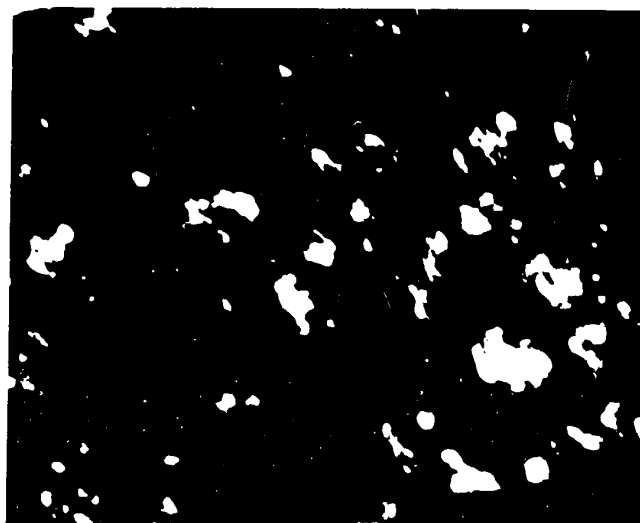
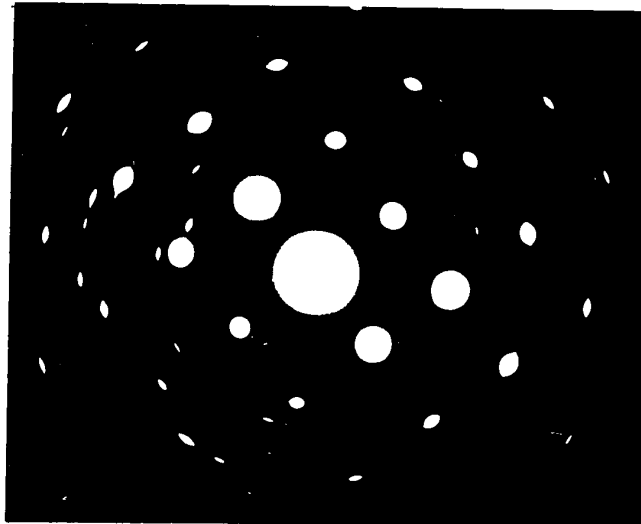
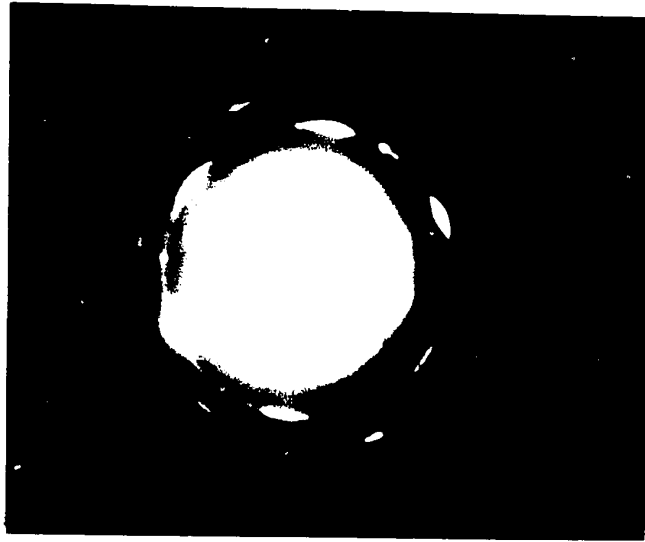
- (e) Selected area diffraction pattern of other section of the film



- (f) Dark field micrograph taken with reflection from (e) x 50,000







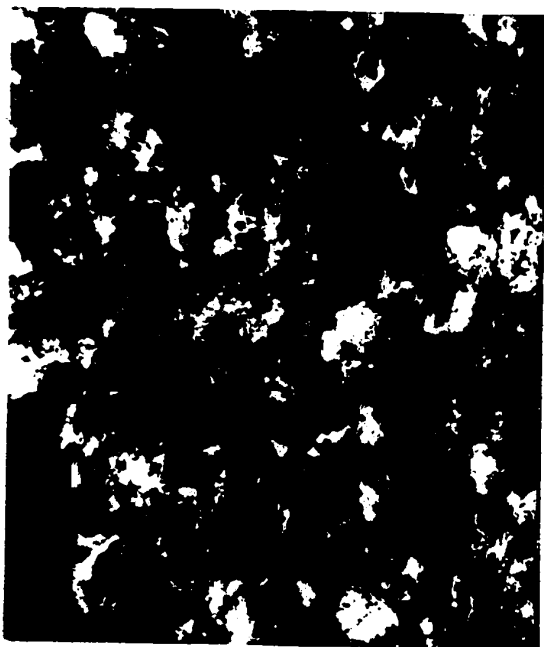
$\approx 3000 \text{ \AA}$ ). Dislocations contrast can be seen clearly from the BF micrograph (a). The single crystal patterns are usually obtained from different sections of the film. The (211) and (100) are shown in (b) and (c). DF micrographs taken with the (200) reflection seen in (d) indicated that the crystallites have grown to an irregular shape. Note that the complex diffraction patterns containing the high index planes are not observed.

4.3.7 Specimen exposure: 360 min. Further exposure in oxygen to 6 hr. resulted in an oxide film too thick for electron transmission; however in some rare thin sections or at the edges of the film the SAD patterns are very similar to the previous sample. They are not given here since the structure of the film has been amply illustrated in the previous sections.

4.3.8 Crystallite size and distribution. Plots for the size distribution and average sizes of the crystallites are given in figures 4.3.8(a), (b). Their average size remains essentially constant at 300  $\text{\AA}$  for approximately 40 min and then increases in size at a continuously decreasing rate. Their size after 6 hr. of exposure was approximately 800  $\text{\AA}$ .

4.3.9 Summary of the results of the (110) face.

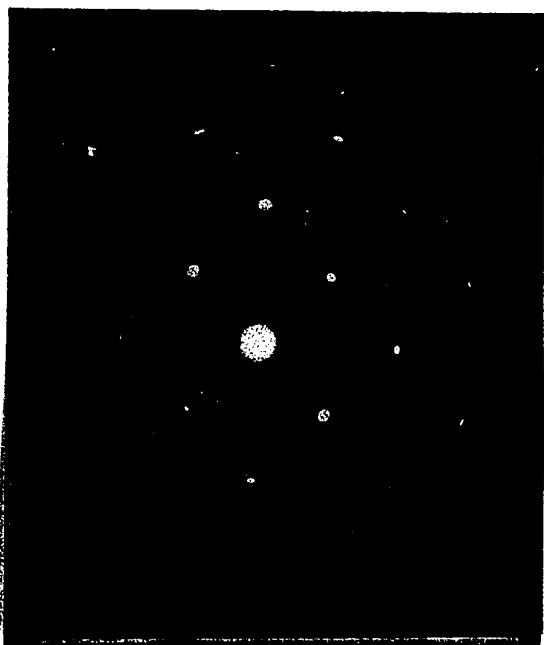
The most striking features of the oxide films formed on the (110) face are the large varieties in structure



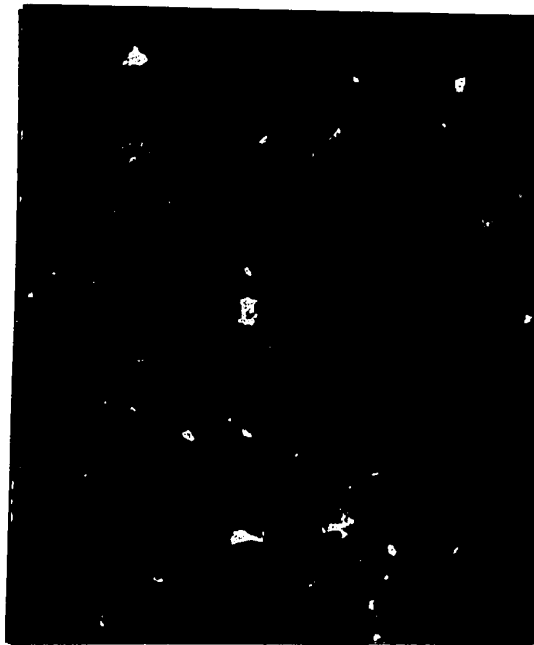
(a)



(b)



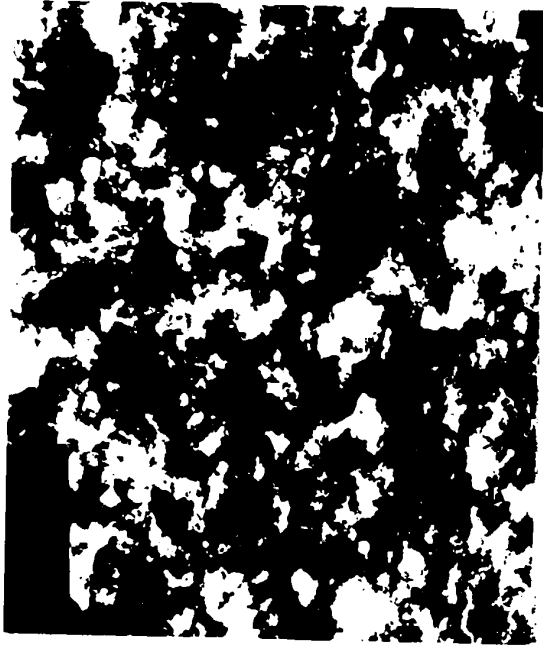
(c)



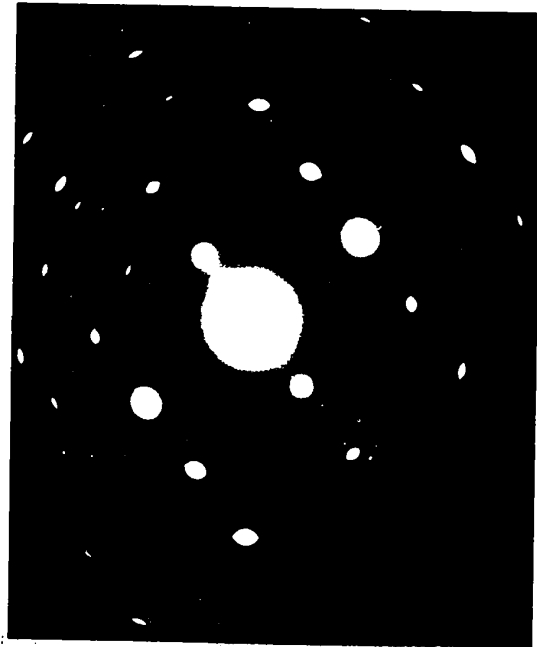
(d)

Figure 4.3.6

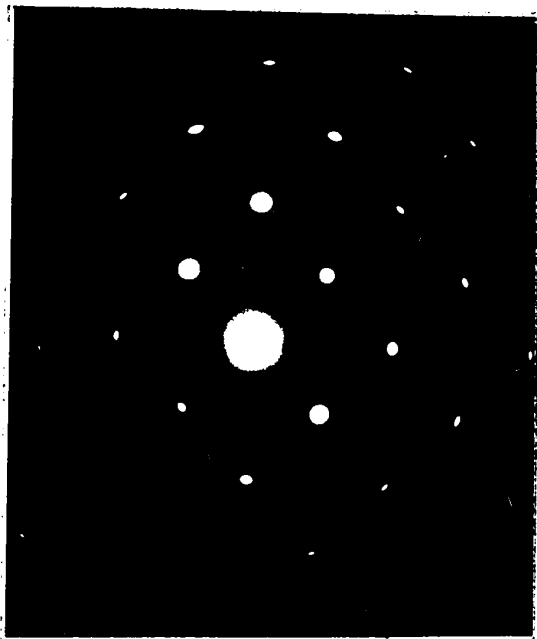
- (a) Bright field micrograph x 35,000  
 (b) Selected area diffraction pattern of (a) showing the (211) Relp  
 (c) Selected area diffraction pattern of other section of the film  
 (d) Dark field picture taken with the (200) reflection of (c) x 35,000



(a)



(b)



(c)



(d)

Figure 4.3.6

- (a) Bright field micrograph  $\times 35,000$
- (b) Selected area diffraction pattern of (a) showing the (211) spot
- (c) Selected area diffraction pattern at other section of the (111)
- (d) Dark field picture taken with the (200) reflection of (1)  $\times 35,000$

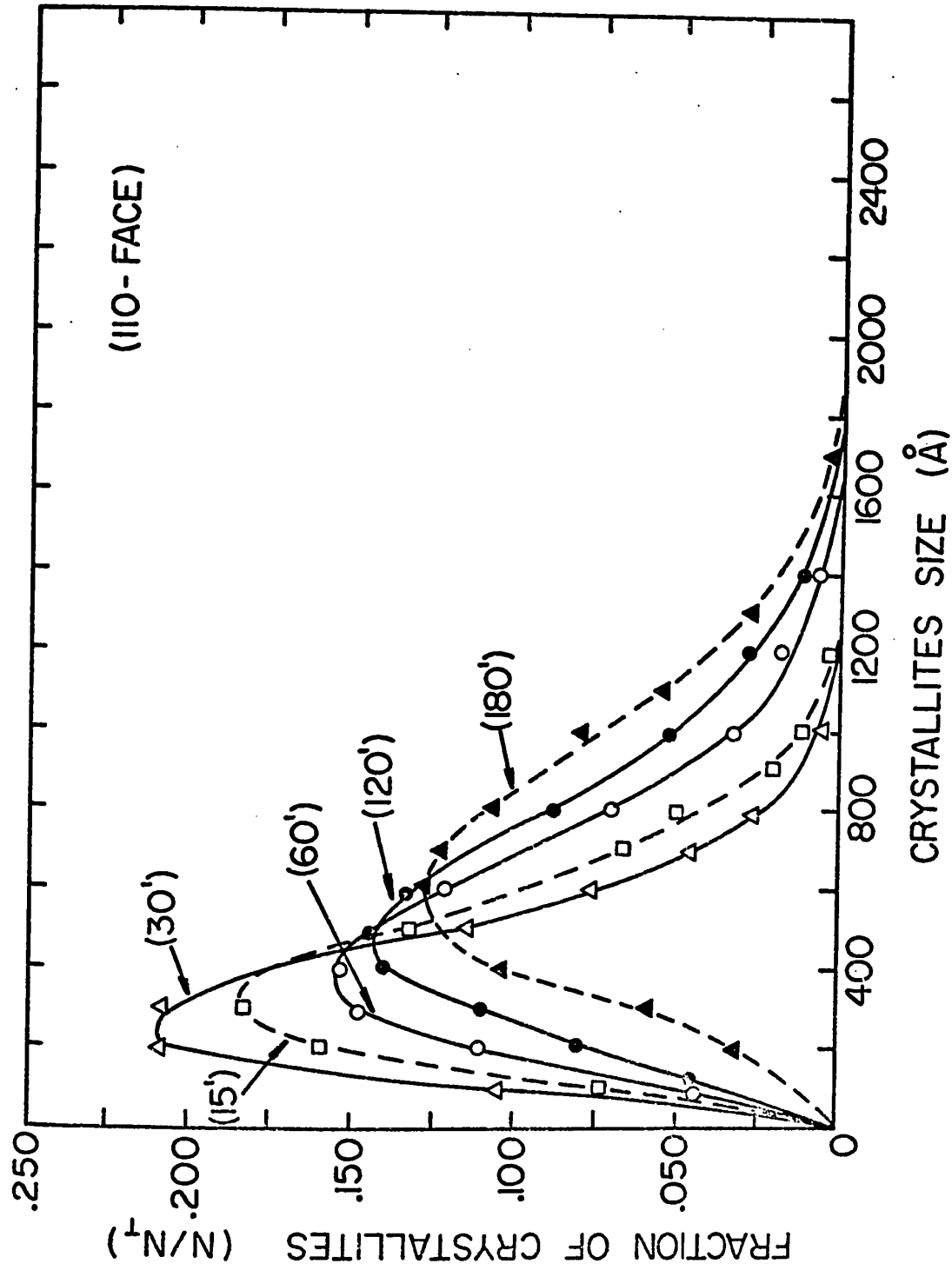


Figure 4.3.8 (a) Crystallite size distribution for oxide films formed on the (110) nickel face at 500°C

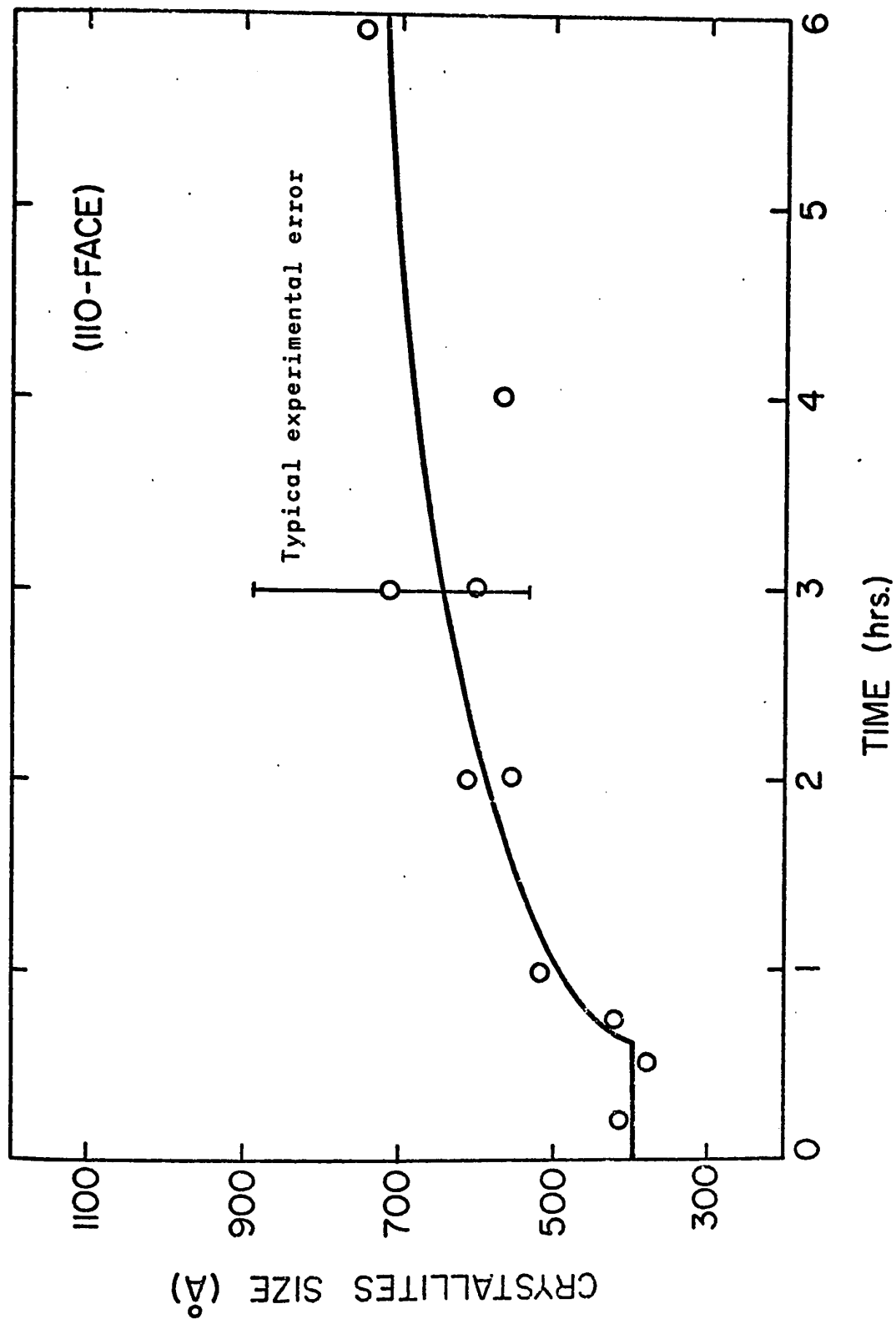


Figure 4.3.8 (b) Average crystallite size versus oxidation time

along with the presence of twins and dislocations. The differences in the film structure are evidenced by a large number of diffraction patterns having completely different orientations. For example, within a single sample, a pattern showing perfect mosaic structure, a pattern containing mainly twins and patterns exhibiting up to six orientations have been found.

The large number of orientations can be divided into two sets. The first set is characterized by a common closed packed direction between the oxide and the metal and is made up of the following orientations:

(100), (011), (111), (211), (311), (322), (411), (433) NiO // (011) Ni  
 with  $[0\bar{1}1]$  NiO //  $[0\bar{1}1]$  Ni

The second set has the following orientations:

(210), (310) NiO // (011) Ni  
 with  $[001]$  NiO //  $[100]$  Ni

Note that the  $[100]$  direction can be the coincident direction between the metal and the oxide. This direction is also a close packed direction in a NaCl crystal system. The latter orientations are very seldom observed. Finally the (123) orientation is also present. It does not belong to either set and has one of the  $[111]$  direction parallel to the  $[100]$  direction in the metal.

All together, eleven orientations have been identified. These orientations changed with the oxide thickness and a trend similar to the (100) face can be established. In the

early stage of oxide growth to film thickness of 700 Å, a large number of orientations were found including the high index planes such as the (433), (411) and (322). In this thickness range, crystallites were well aligned and the diffraction patterns were composed of superimposed spot patterns with no evidence of continuous rings. As the oxide becomes thicker, the high index planes disappear and after 3 to 4 hr. of exposure, only the low index planes such as the (100), (011), (111) and the (211) are commonly observed. With the increase in thickness some dislocations become visible and an apparent polycrystallinity is more in evidence.

#### 4.4 Transmission electron microscopy results from the (111) nickel face

Compared to the (110) face, the (111) face of nickel oxidized slightly faster at 500°C but still much slower than the (100) face. The reproducibility in the oxidation curves is better than that for the (110) face although some irregularities have been observed.

4.4.1 Specimen exposure: 10 min. Electron micrographs for a sample oxidized for 10 min. are given in fig. 4.4.1 (a)-(g). The film thickness is about 500-600 Å. It is uniform and is composed of small crystallites having different orientations as evidenced by the diffraction contrast in the BF picture shown in (a). The orientation of these crystallites can be revealed by the diffraction patterns. The pattern in (b) can be indexed as:



(111), (211), (233) NiO // (111) Ni.

All the above orientations occurred in multiple. The (111) oxide has 3 close packed directions and only two types of orientations have been observed. The first orientation is characterized by one of the close packed direction of the oxide being parallel to one of the  $\langle 110 \rangle$  directions in the metal. The other orientation by one of the close packed directions of the oxide being parallel to the  $\langle 112 \rangle$  directions in the metal. The (211) orientation has only one close packed direction; there are three possible equivalent orientations according to the symmetry of the (111) face of the metal. However, a total of six orientations are possible if the  $\langle 112 \rangle$  directions of the metal is parallel to the closed packed direction of the oxide. Indeed, close examination of the pattern shows that there are 6 (211) orientations, 3 of these orientations have their  $\langle 110 \rangle$  directions parallel to the  $\langle 110 \rangle$  in the metal while the other 3 have their  $\langle 110 \rangle$  directions parallel to the  $\langle 112 \rangle$  in the metal. Two of the latter orientations are not readily recognizable due to the faintness of the diffracted spots. The (233) orientation has also one close packed direction and like the (211) up to six orientations have been observed.

The type of the pattern above is fairly typical of this sample but other orientations are also present. The SAD pattern of other section of the film is seen in (c). It has the following orientations:

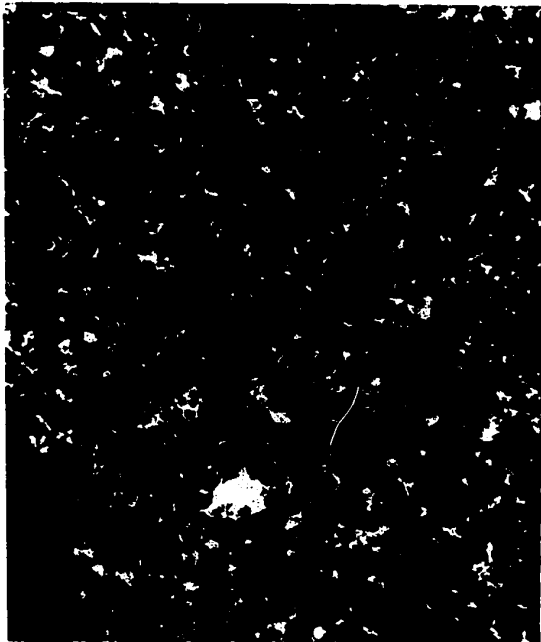
(011), (211) NiO // (111) Ni

There is only one (011) and two (211) oxide orientations. Some faint reflections which seem to belong to the (310) NiO are also present. The first (211) shares a common close packed direction with the (110) oxide while the other (211) is rotated  $30^\circ$  with respect to the first one. Thus one of the (211) orientations must have its close packed direction parallel to the  $[110]$  in the metal and the other has its close packed direction parallel to the  $[112]$  direction in the metal. The schematic drawing of the 3 above orientations is shown in fig. 4.4.1(e).

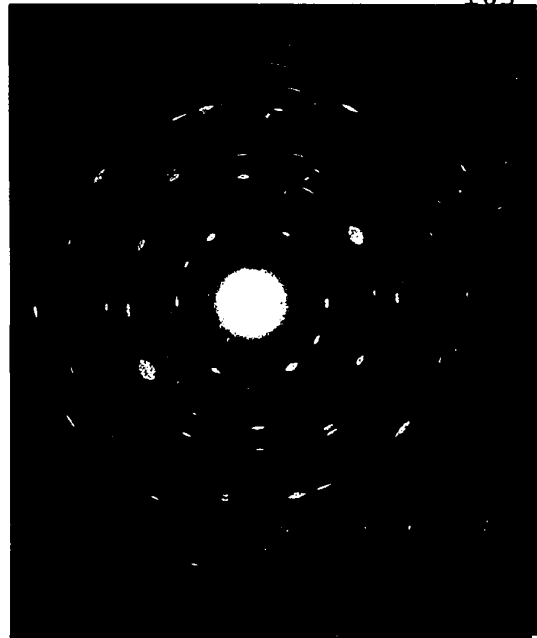
Another type of pattern observed is shown in (d). In this pattern there are four (211) orientations, three of those are arranged  $60^\circ$  apart thus correspond to the 3  $\langle 110 \rangle$  directions in the nickel. The fourth one must have its close packed direction parallel to the  $\langle 112 \rangle$  in the metal.

The three above patterns are fairly representative for this sample. Although they are different the same type of orientations were found. The crystallites size and their distribution are represented by the two DF pictures shown in (f) and (g). It can be seen from these pictures that the crystallites have very irregular shape and exhibit a large spread in size distribution.

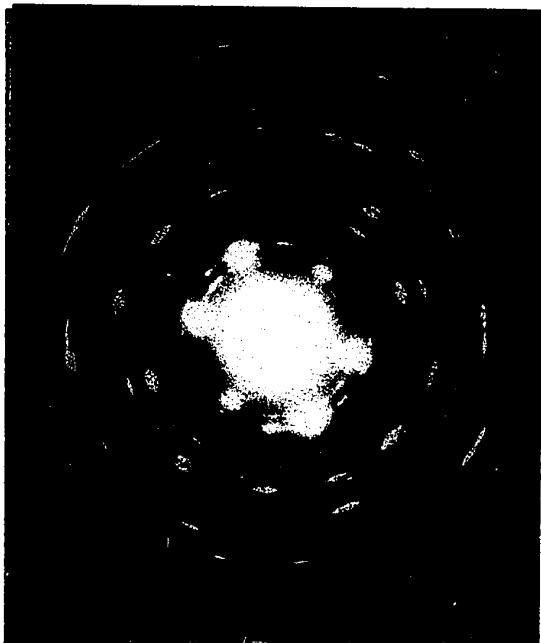
4.4.2 Specimen exposure: 35 min. Figures 4.4.2(a)-(e) are the usual sequence of micrographs from a sample oxidized for 35 min. The film thickness is about 700-800 Å. The



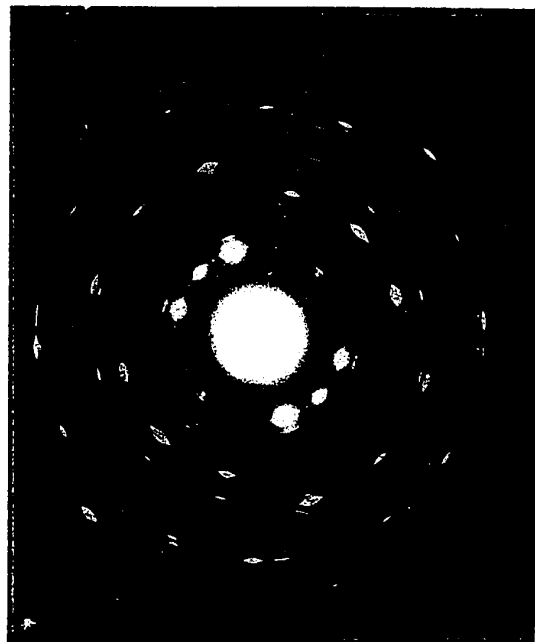
(a)



(b)



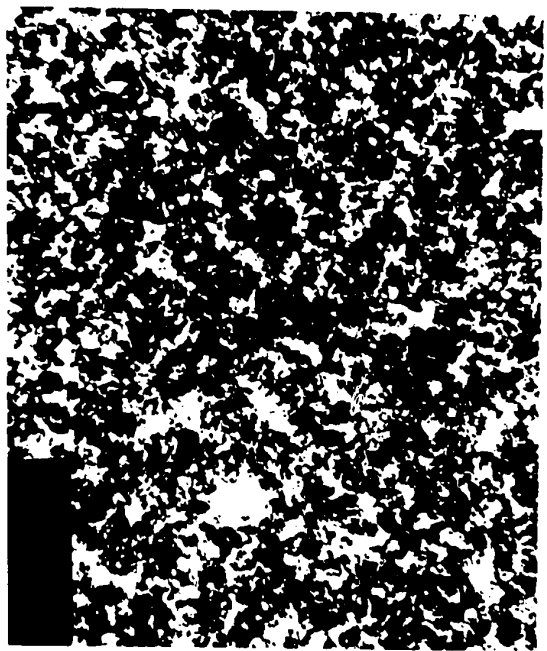
(c)



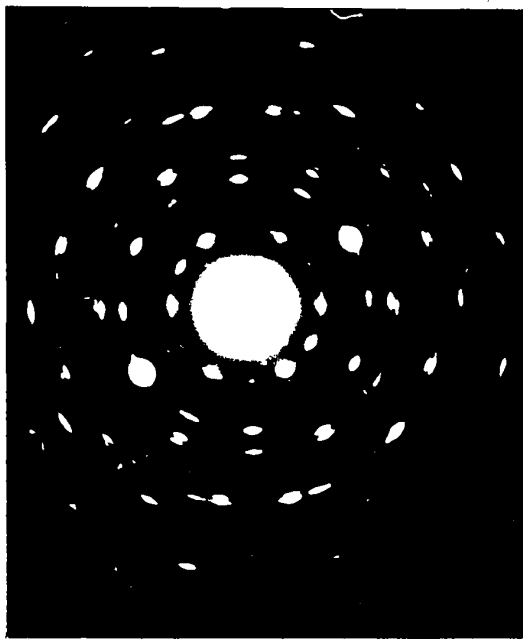
(d)

Figure 4.4.1

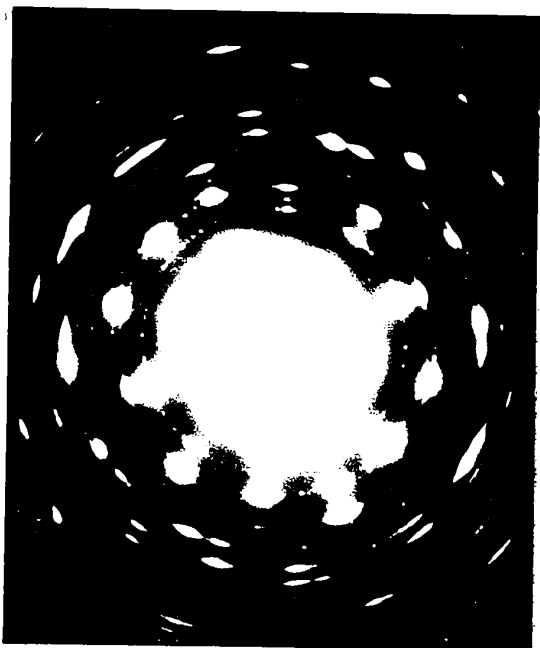
- (a) Bright field micrograph x 15,000
- (b) Selected area diffraction pattern of (a)
- (c) Selected area diffraction pattern of other section of film
- (d) Selected area diffraction pattern of other section of film



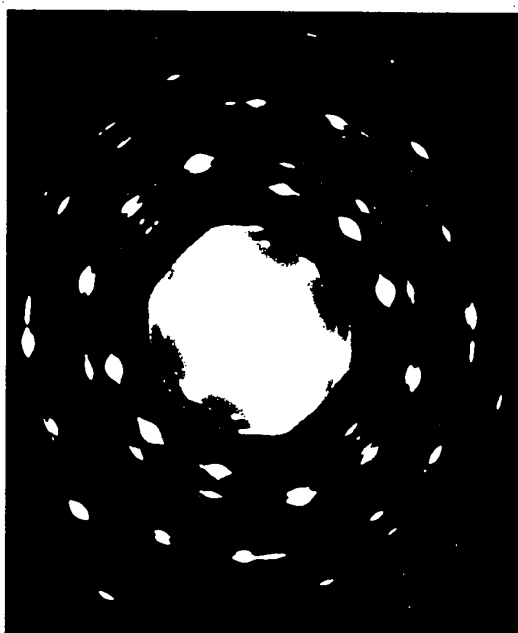
(a)



(b)



(c)



(d)

### Figure 10

- (a) original image
- (b) original image with a circular mask
- (c) original image with a circular mask and a central region
- (d) original image with a circular mask and a central region

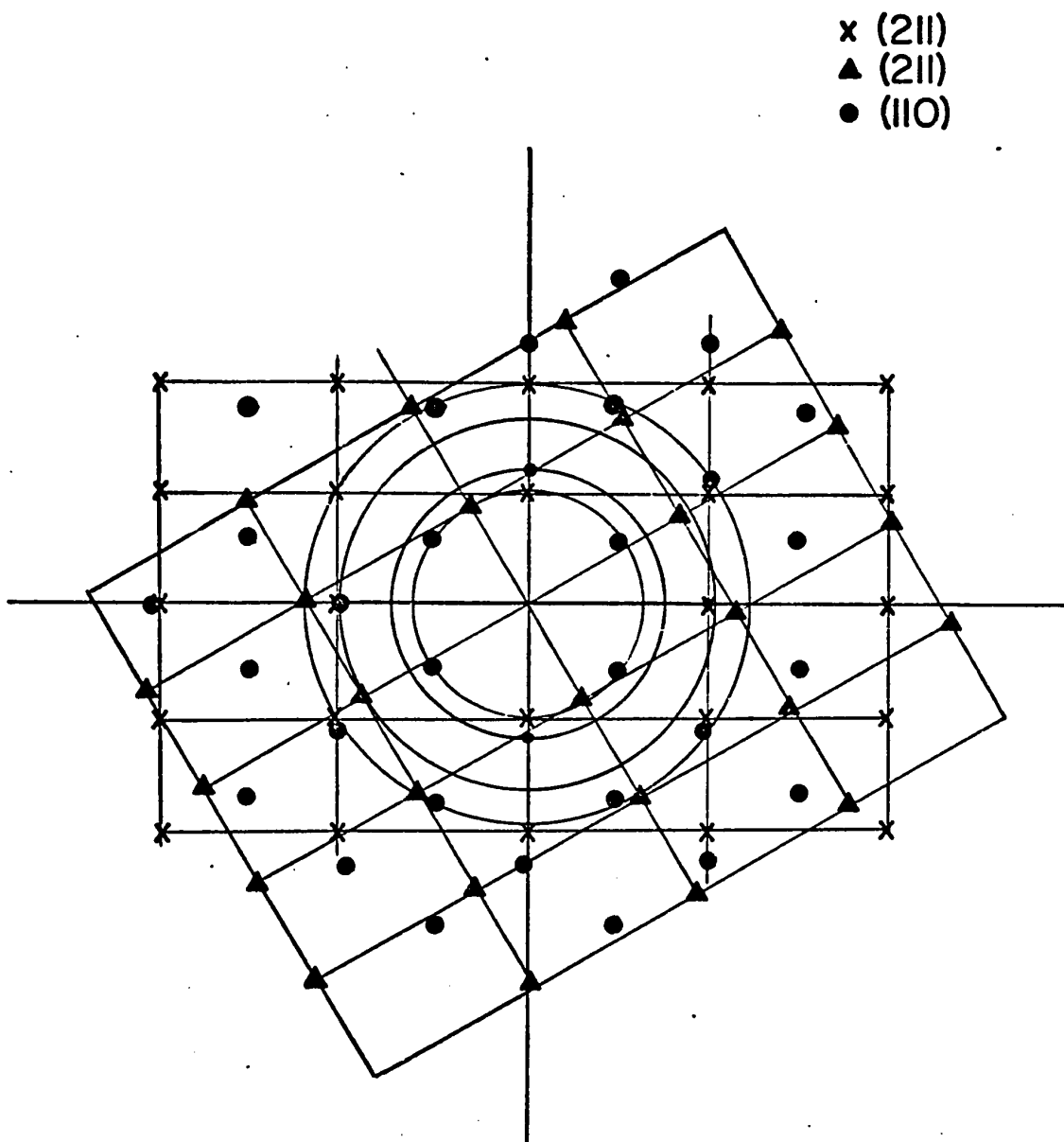


Figure 4.4.1 (e)

Schematic drawing of the diffraction pattern (c) showing the (011) reciprocal lattice plane represented by (•) and the two (211) reciprocal lattice planes represented by (+) (▲). Note the common closed packed direction between the (011) and one of the (211) Relp.



Figure 4.4.1(f) Dark field micrograph taken with the (220) reflection. x 50,000

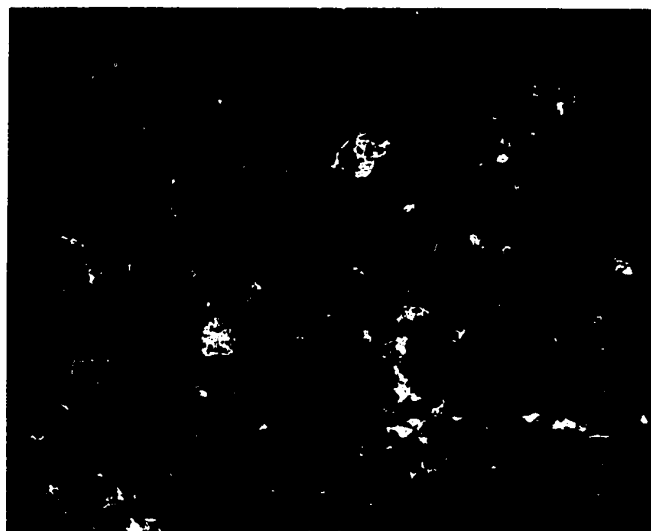


Figure 4.4.1 (g) Dark field micrograph taken with (111) reflection from (d). x 42,000

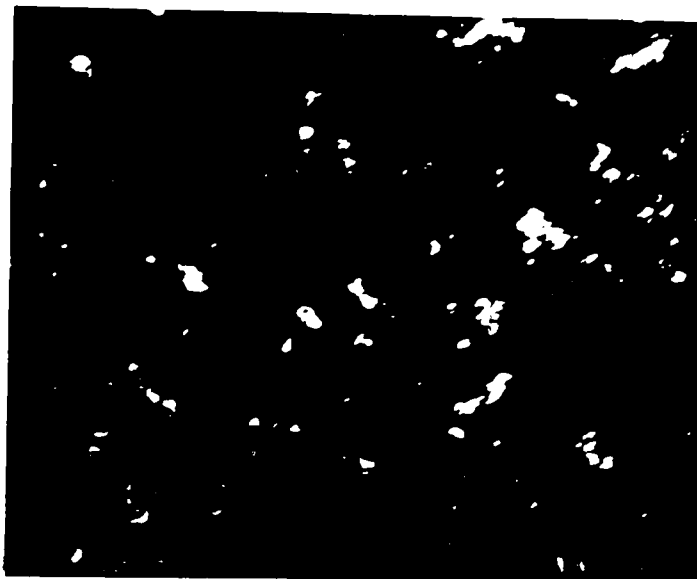


Figure 4.4.1 (1) Dark field electron micrograph taken with the (200) reflection.  $\times 40,000$

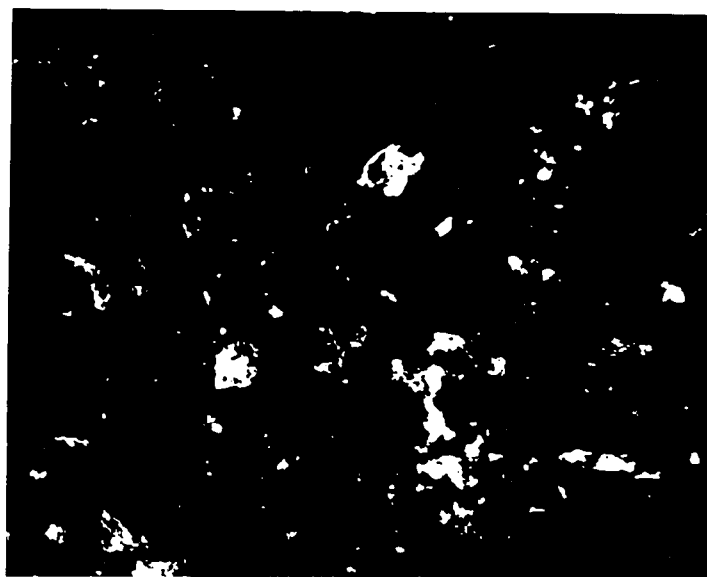
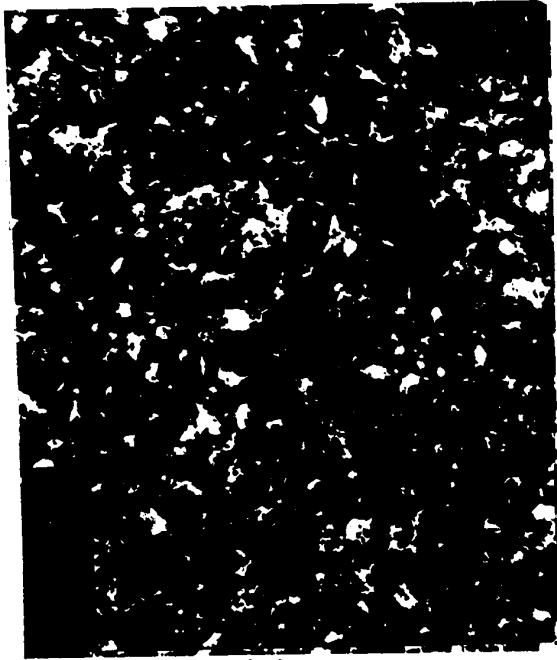
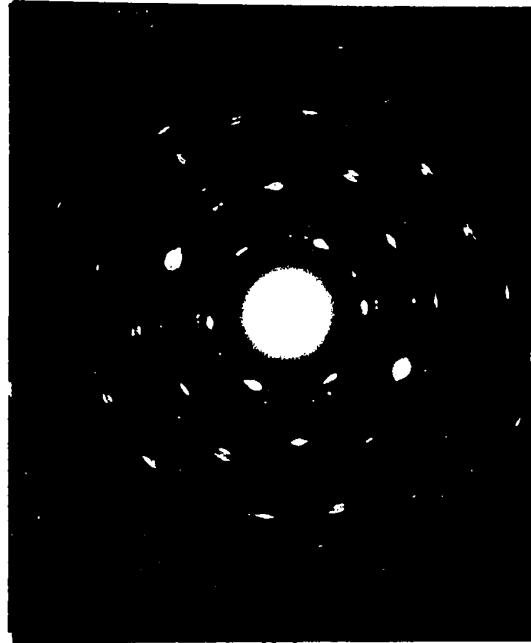


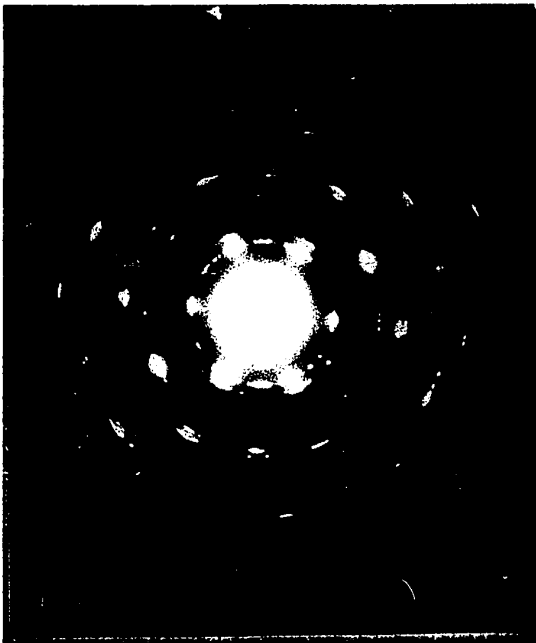
Figure 4.4.1 (2) Dark field electron micrograph taken with the (111) reflection.  $\times 47,000$



(a)



(b)



(c)



(d)

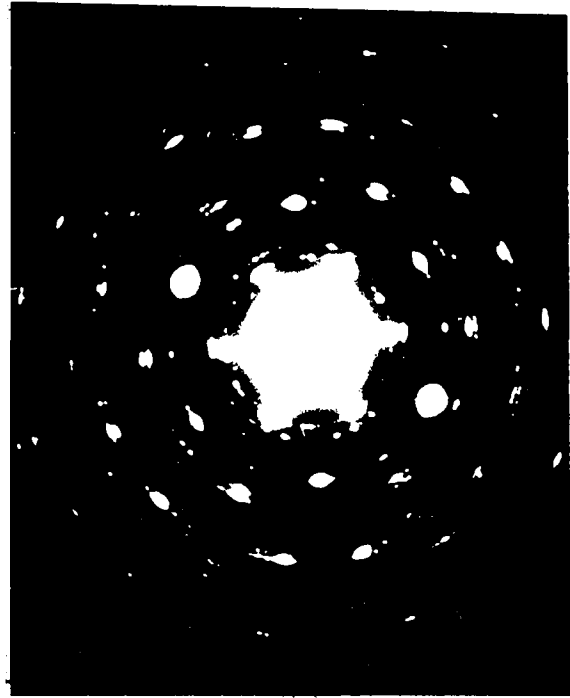
Figure 4.4.2

- (a) Bright field micrograph x 23,000  
 (b) Selected area diffraction pattern of (a)  
 (c) Selected area diffraction pattern of another section of film  
 (d) Dark field micrograph taken with the (220) reflection  
 x 42,000

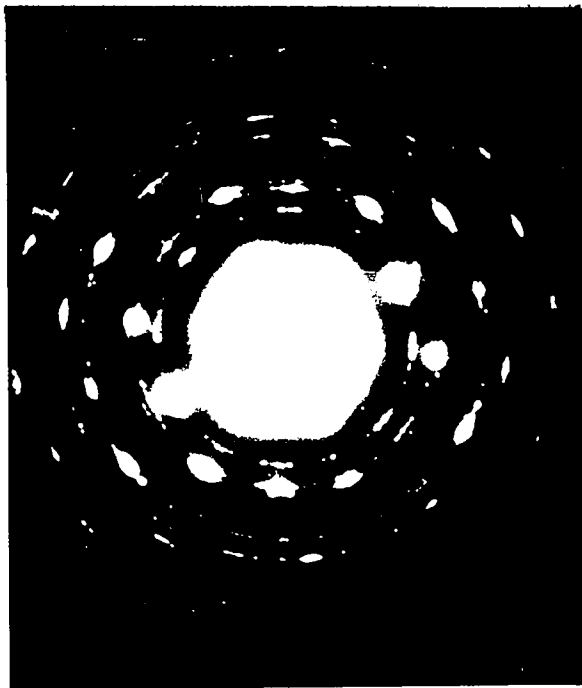




(a)



(b)



(c)

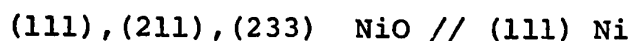


(d)

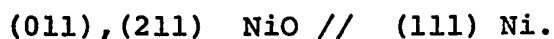
Figure 2 (cont)

(A) original image of the sample surface  
(B) original image of the sample surface  
(C) original image of the sample surface  
(D) original image of the sample surface

BF micrograph in (a) shows the usual features previously observed. The diffraction patterns still show the same types of orientations but some recrystallization has occurred in the film. The evidence is indicated in the following SAD patterns. Figure (b) can be indexed as:



Note that the same types of orientations are observed but the number of orientations has now decreased. There is only one (111) oxide orientation and three (211) and (233) instead of six. It can be inferred from the pattern that the oxide orientations having one of the  $\langle 110 \rangle$  directions parallel to the  $\langle 112 \rangle$  direction in the metal may not be a stable orientation; consequently it is not observed after the oxide reaches a certain thickness. Figure (c) is the SAD pattern of another section of the film. The following orientations are present:



These two orientations share a common close packed direction. Again, the multiple orientations are not observed.

A DF micrograph taken with the (220) reflection shown in (d) indicated that the crystallites have very irregular shape and exhibit a large spread in size distribution.

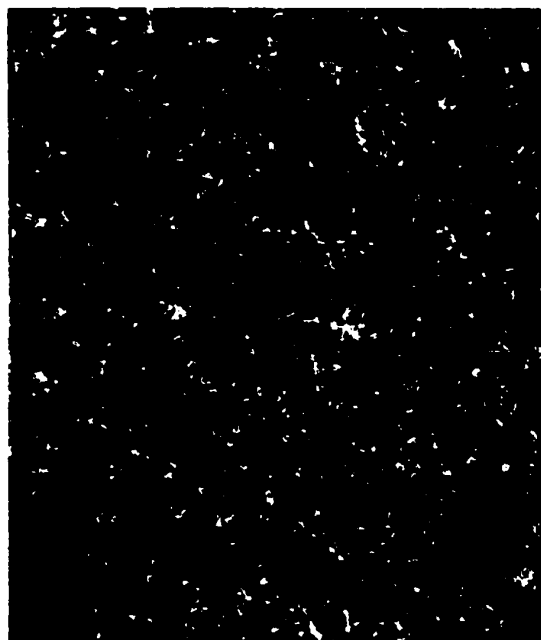
4.4.3 Specimen exposure: 60 min. There is no drastic change in the structure of the oxide film when a sample is oxidized for 60 min. The BF picture seen in (a) begins to show regions of uneven thickness as indicated by the dark

patches in the film. The diffraction pattern of the same section of the film is in fig. (b). The following orientations have been indexed:

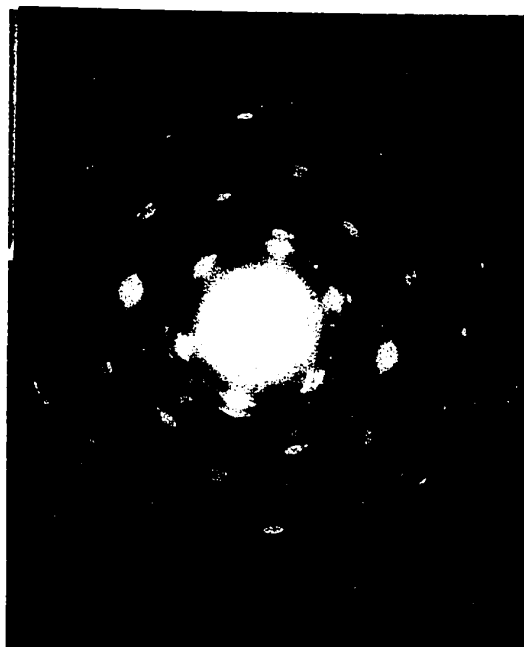
(111), (211), (233) NiO // (111) Ni.

Note that there are only one (111) orientation and three (211) and (233); the (233) orientation seems to disappear as evidenced by the faintness of the reflections on the 331 ring. Some faint spots which belong to the (011) Relp are also observed. The SAD pattern of another section of the film is shown in (c). The pattern is very similar to the previous one but the reflections from the (111) orientation are now very strong. The same features are observed in the pattern (d) with some evidence of polycrystallinity as indicated by the almost continuous rings. It can be concluded from the three patterns that the film structure is fairly uniform. The DF micrographs taken with the 220 reflections are given in (e) and (f). Again, note the irregular shape and the large spread in size of the crystallites. In some instances, dislocations were also observed; they are shown in the micrograph (g).

4.4.4 Specimen exposure: 120 min. Some change in the structure is now noticed in the film of the sample oxidized for 120 min. (film thickness  $\approx 1300 \text{ \AA}$ ). The most evident feature is the frequent observation of the dislocations as seen in the BF picture. (a). The diffraction patterns now show very strong single crystal properties. The (111) is seen in (b), the mixed (011) and (211) in (c). Irregular shaped crystallites are seen in the DF micrograph (d).



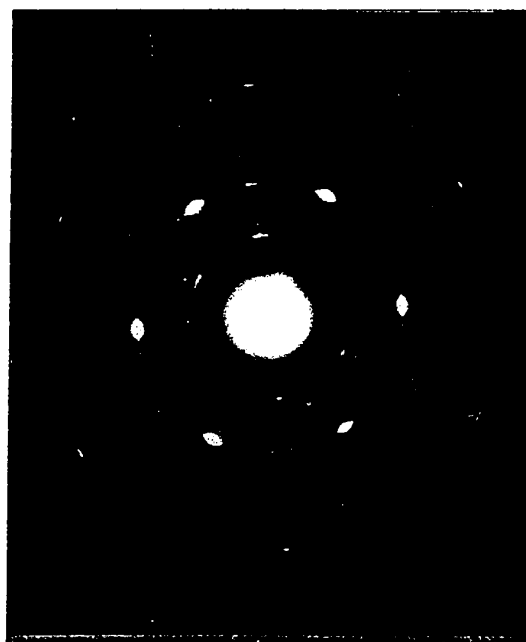
(a)



(b)



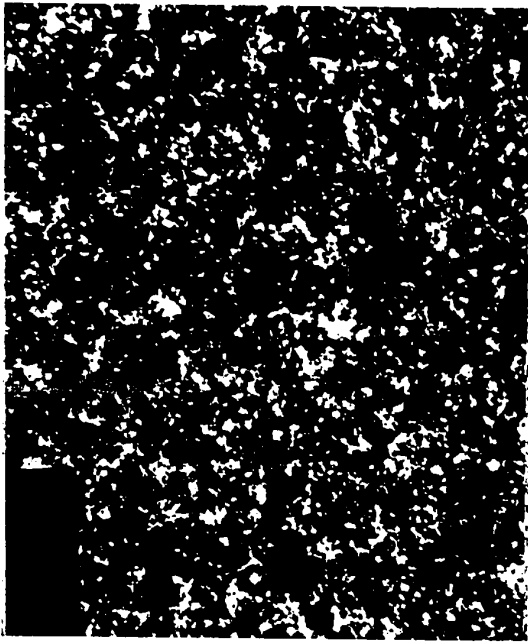
(c)



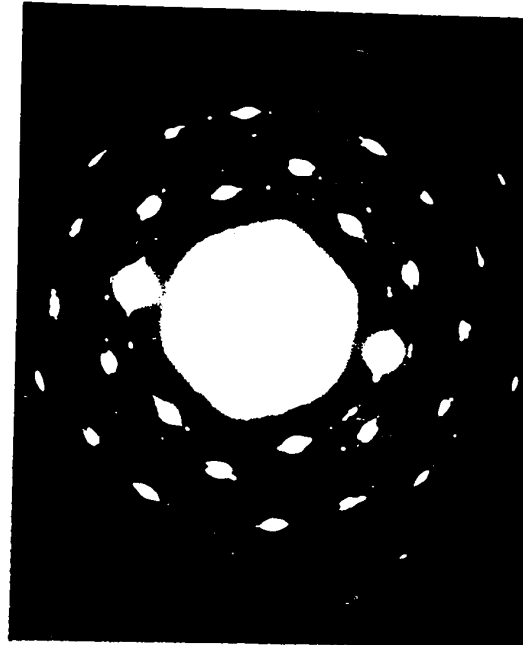
(d)

Figure 4.4.3

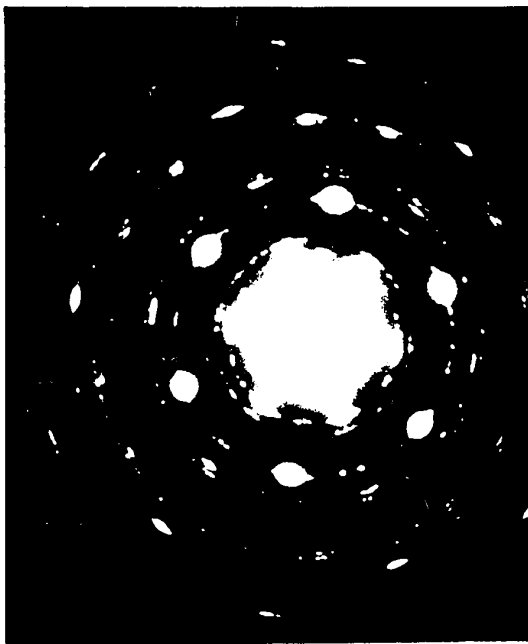
- (a) Bright field micrograph. x 15,000
- (b) Selected area diffraction pattern of the same region as (a)
- (c) Selected area diffraction pattern of different region of film
- (d) Selected area diffraction pattern of other region of film



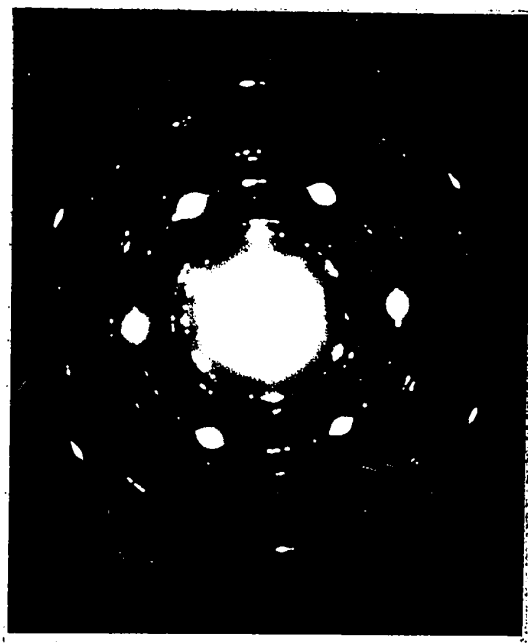
(a)



(b)



(c)



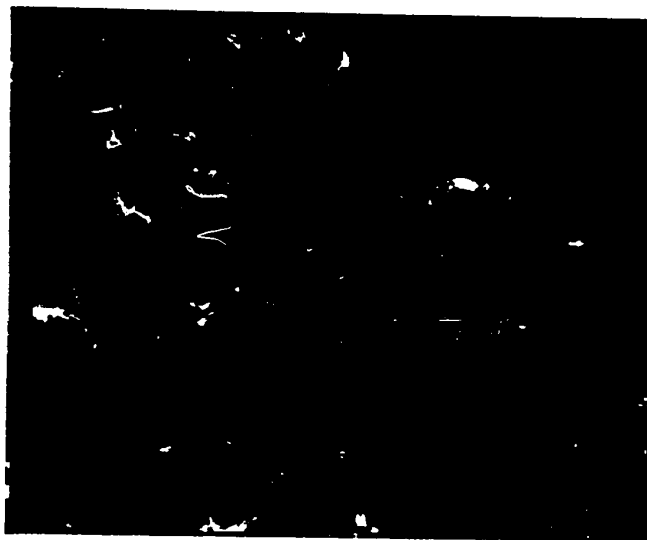
(d)

Figure 4.4.3

- (a) Infrared film surface,  $\times 15,000$   
 (b) Polystyrene interference pattern at the core position as (a)  
 (c) Polystyrene interference pattern at different position as (a)  
 (d) Polystyrene interference pattern at different position as (a)

Figure 4.4.3

- (e) DF micrograph taken with one of the 220 reflection. x 42,000

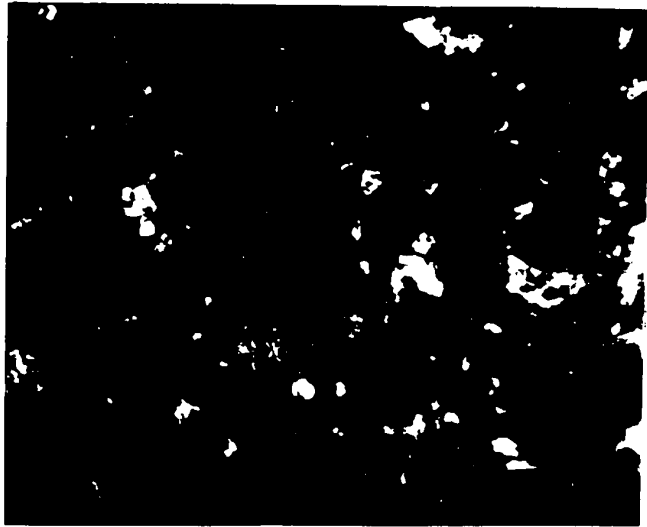


- (f) DF micrograph taken at different film section. x 42,000



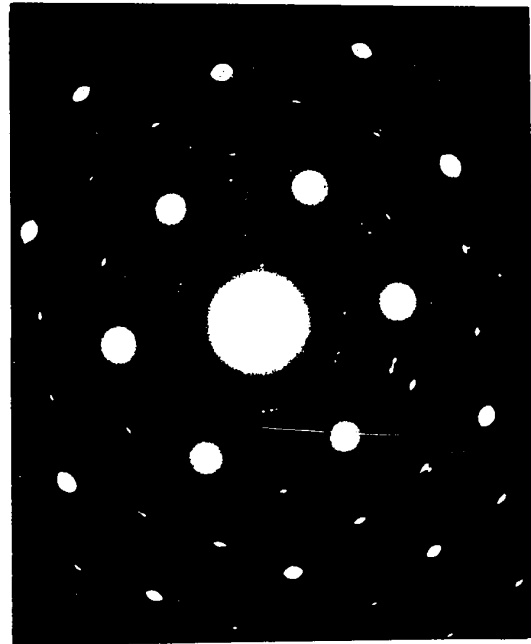
- (g) BF micrograph showing the presence of dislocations x 80,000







(a)



(b)



(c)



(d)

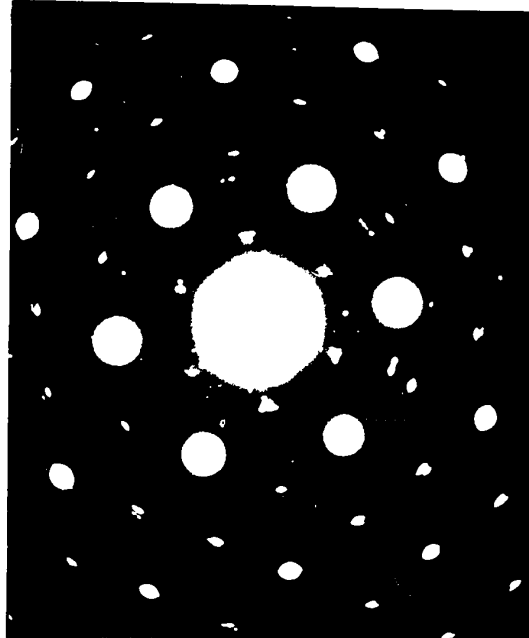
Figure 4.4.4

- (a) Bright field micrograph. x 42,000
- (b) Selected area diffraction pattern showing strong reflections from the (111) Relp.
- (c) Selected area diffraction pattern showing the mixed (011) and (211) Relps.
- (d) Dark field micrograph taken from the (220) reflection. Note the irregular shape crystallites. x 42,000

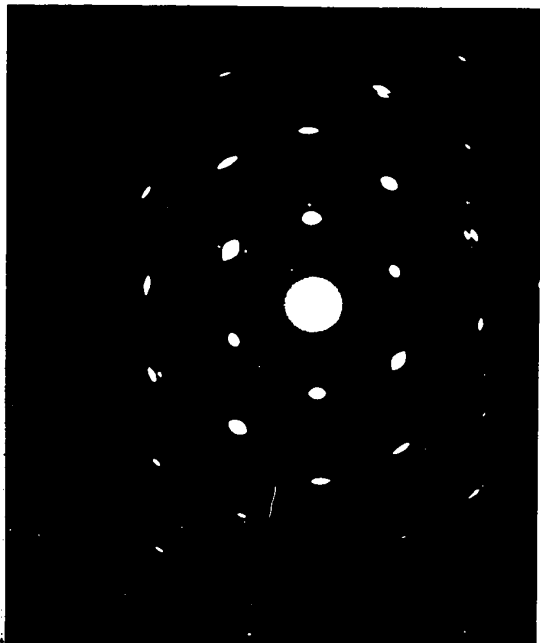




(a)



(b)



(c)



(d)

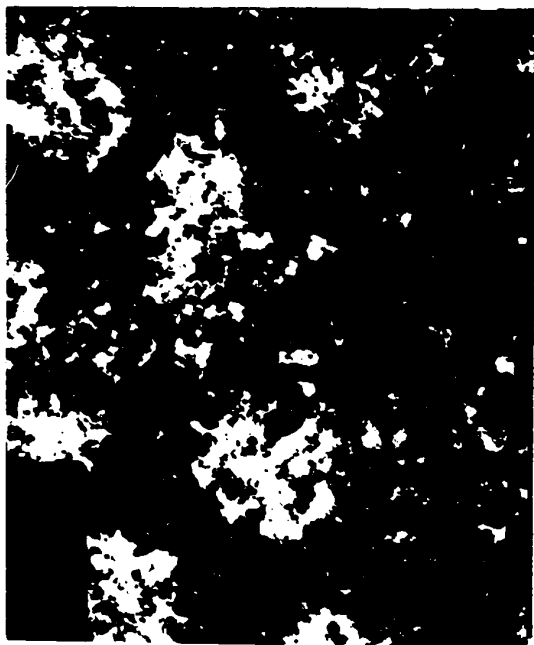
Figure 3.4.4

- (a) Bright field micrograph.  $\times 42,000$
- (b) Selected area electron pattern showing strong reflections from the (111) plane.
- (c) Selected area electron pattern showing the mixed (011) and (211) planes.
- (d) Dark field micrograph taken from the (220) reflection. Note the presence of the mixed (111) plane.  $\times 42,000$

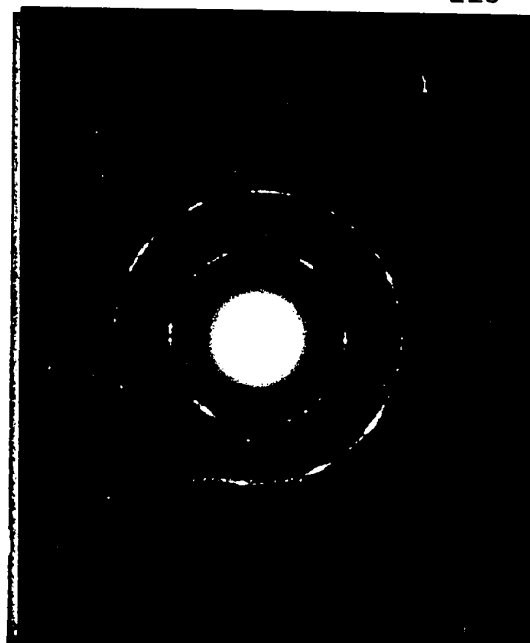
4.4.5 Specimen exposure: 240 min. Exposure to oxygen for 240 min. (film thickness  $\approx 2500 \text{ \AA}$ ) resulted in some drastic change in the oxide structure. The BF picture in (a) now definitely shows regions of very uneven thickness. The diffraction patterns consistently yield polycrystalline rings with some preferred orientation on the (111) as indicated by the arcs on the 220 (3rd) ring. Some other orientations may be present as evidenced by some faint arcs in the (111) ring. However, positive identification is not possible due to the considerable polycrystallinity in the higher rings. The structure is essentially uniform since SAD of other sections of the film gave similar results. The two diffraction patterns are given in (b) and (c). A DF micrograph taken with the objective aperture set at the first two rings is shown in (d).

The polycrystalline nature of the film in the thickness range was confirmed by the examination of another sample oxidized at the same temperature and exposure time. The results indicated that the film structure is polycrystalline with some preferred orientation as previously observed.

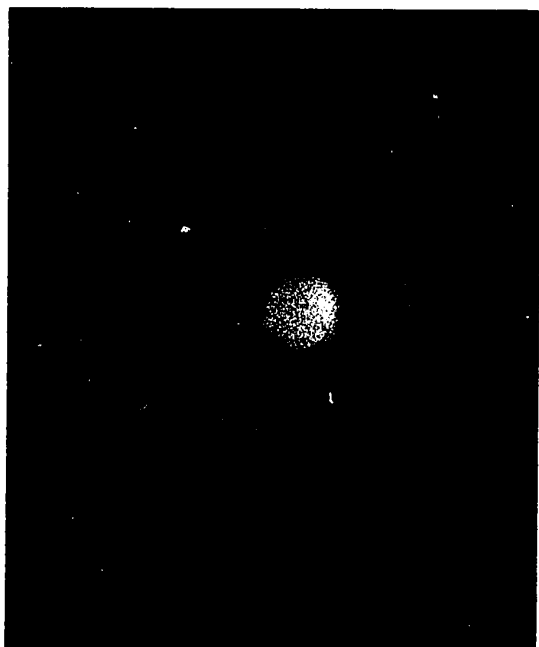
4.4.6 Specimen exposure: 360 min. The structure of the film from a sample oxidized for 6 hr. (film thickness  $\approx 3500 \text{ \AA}$ ) is very similar to the previous sample. The bright field micrograph seen in (a) indicated that the film is very thick. The diffraction patterns from the thin sections of the film yielded the familiar polycrystalline rings with some preferred



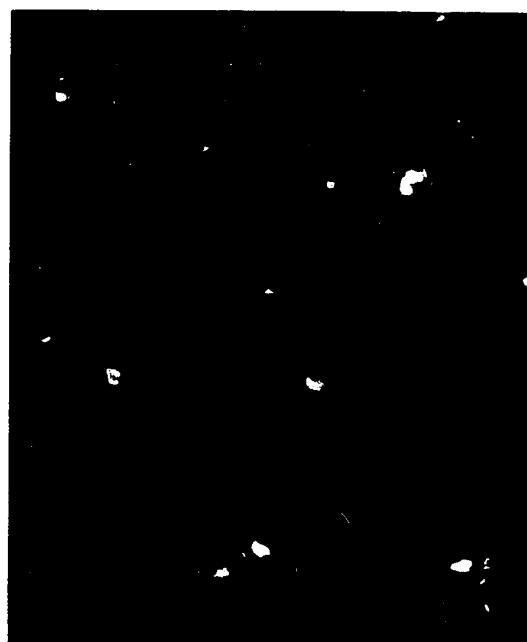
(a)



(b)



(c)



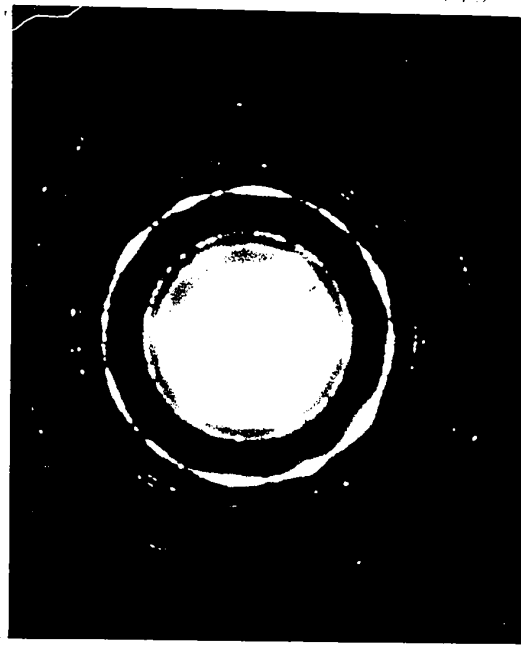
(d)

Figure 4.4.5

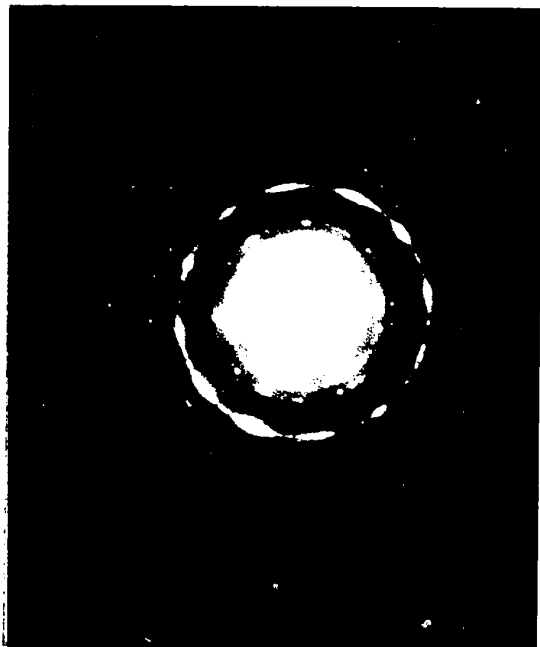
- (a) Bright field micrograph. x 42,000
- (b) Selected area diffraction pattern showing polycrystalline oxide with preferred orientation.
- (c) Selected area diffraction pattern of other section of film
- (d) Dark field micrograph taken with objective aperture set at the first two rings. x 42,000



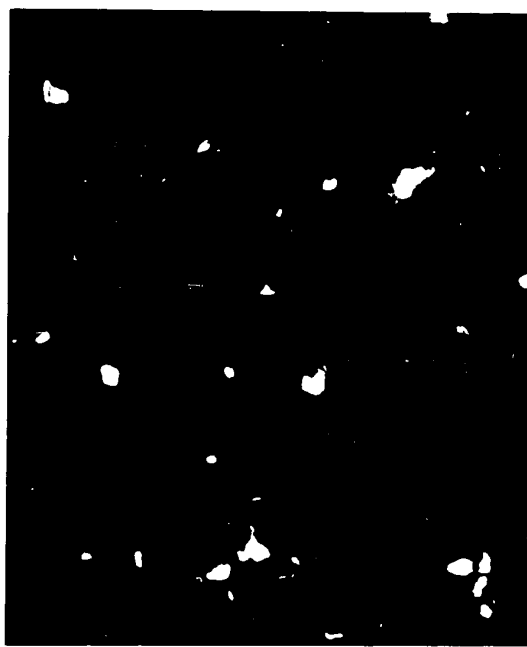
(a)



(b)



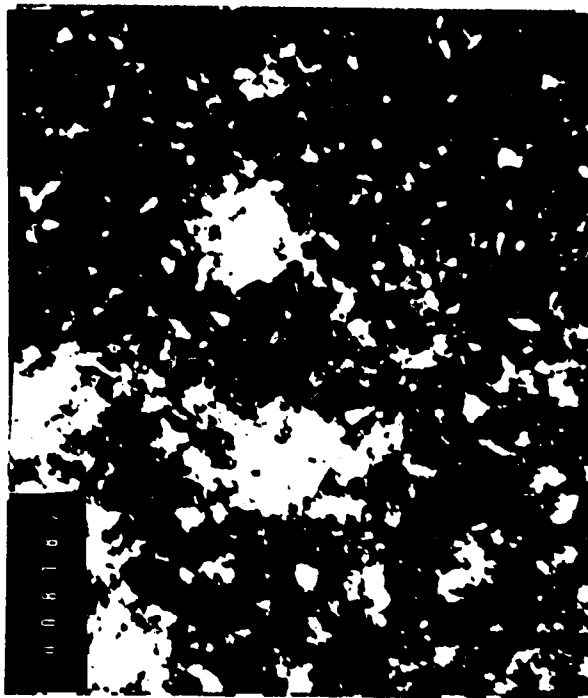
(c)



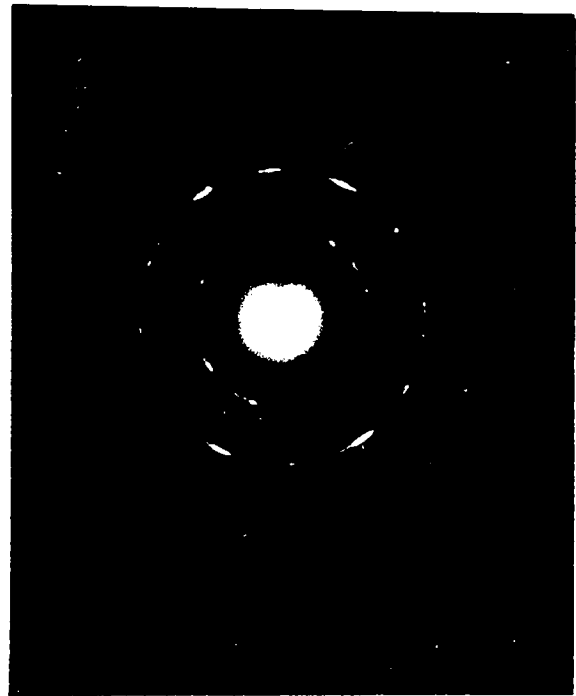
(d)

Figure 4.1.5

- (a) Bright field micrograph.  $\times 42,000$
- (b) Selected area diffraction pattern showing polycrystalline oxide with preferred orientation.
- (c) Selected area diffraction pattern of other section of film
- (d) Dark field micrograph taken with objective aperture set at the first two rings.  $\times 42,000$



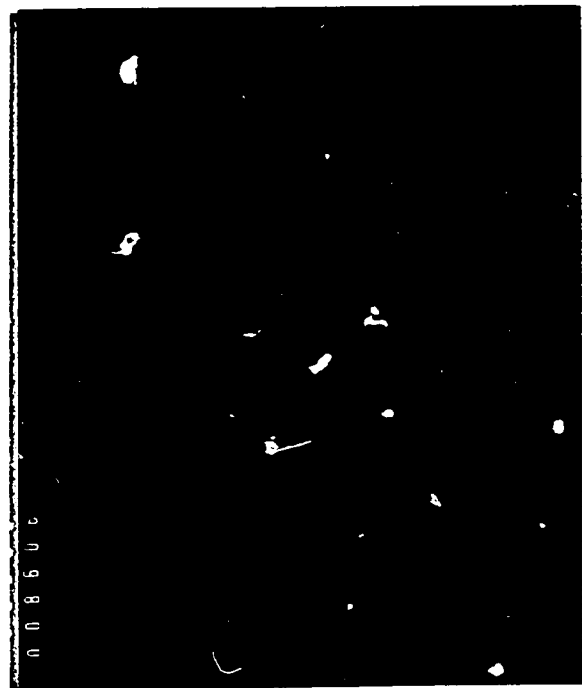
(a)



(b)



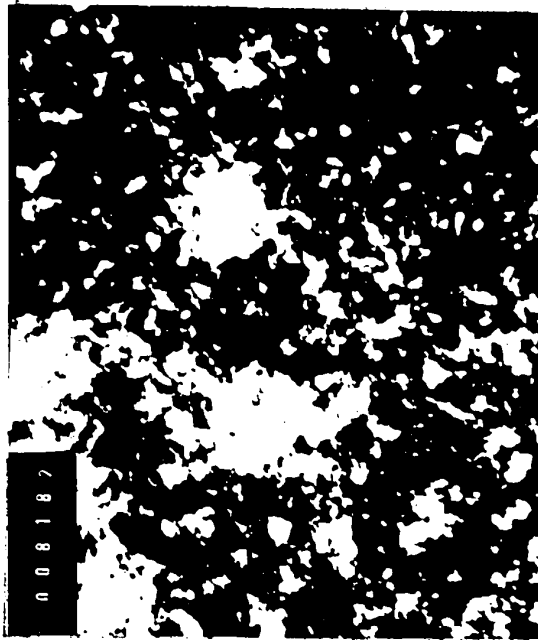
(c)



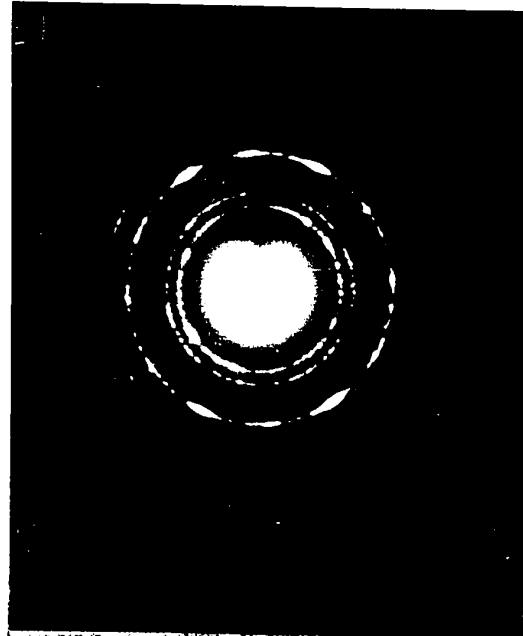
(d)

Figure 4.4.6

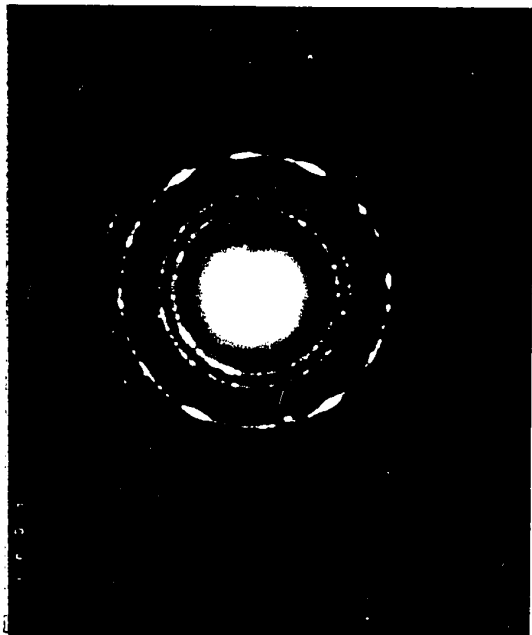
- (a) Bright field micrograph. x 28,000  
 (b) Selected area diffraction pattern of (a)  
 (c) Selected area diffraction pattern of different section of the film  
 (d) Dark field micrograph taken with aperture set at the first two rings. x 35,000



(a)



(b)



(c)



(d)

Figure 4.4.6

- (a) Bright field micrograph.  $\times 26,000$
- (b) Selected area diffraction pattern of (a)
- (c) Selected area diffraction pattern of different section of the film
- (d) Dark field micrograph taken with aperture set at the first two rings.  $\times 26,000$

orientation as evidenced by the arcs on the 220 (3rd) ring. This type of structure is observed everywhere across the whole sample indicating the uniformity of the film. The two SAD patterns are shown in (b) and (c). A DF micrograph taken with the aperture set at the first two rings is given in (d).

4.4.7 Crystallite size and distribution. From the dark field micrographs the size and the distribution of the crystallites were measured. The results are graphically shown in figures 4.4.7(a) and (b).

4.4.8 Summary of the results of the (111) face.

Compared with the (110) face of nickel, the structure of the oxide films formed on the (111) face is relatively uniform. Only five orientations have been observed and no perfect mosaic structure and twinning could be found.

The most interesting features of the oxide are the multiple occurrence of the same orientation indicating the strong influence of the metal substrate. For example up to six of the (211) and (233) planes have been identified within a single SAD pattern. These multiple orientations are only present at the very early stage of film growth and they can be divided into two types. The first type is characterized by a common  $\langle 110 \rangle$  close packed direction between the metal and the oxide parallel to the  $\langle 112 \rangle$  directions in the metal.

The mentioned orientations are given below:

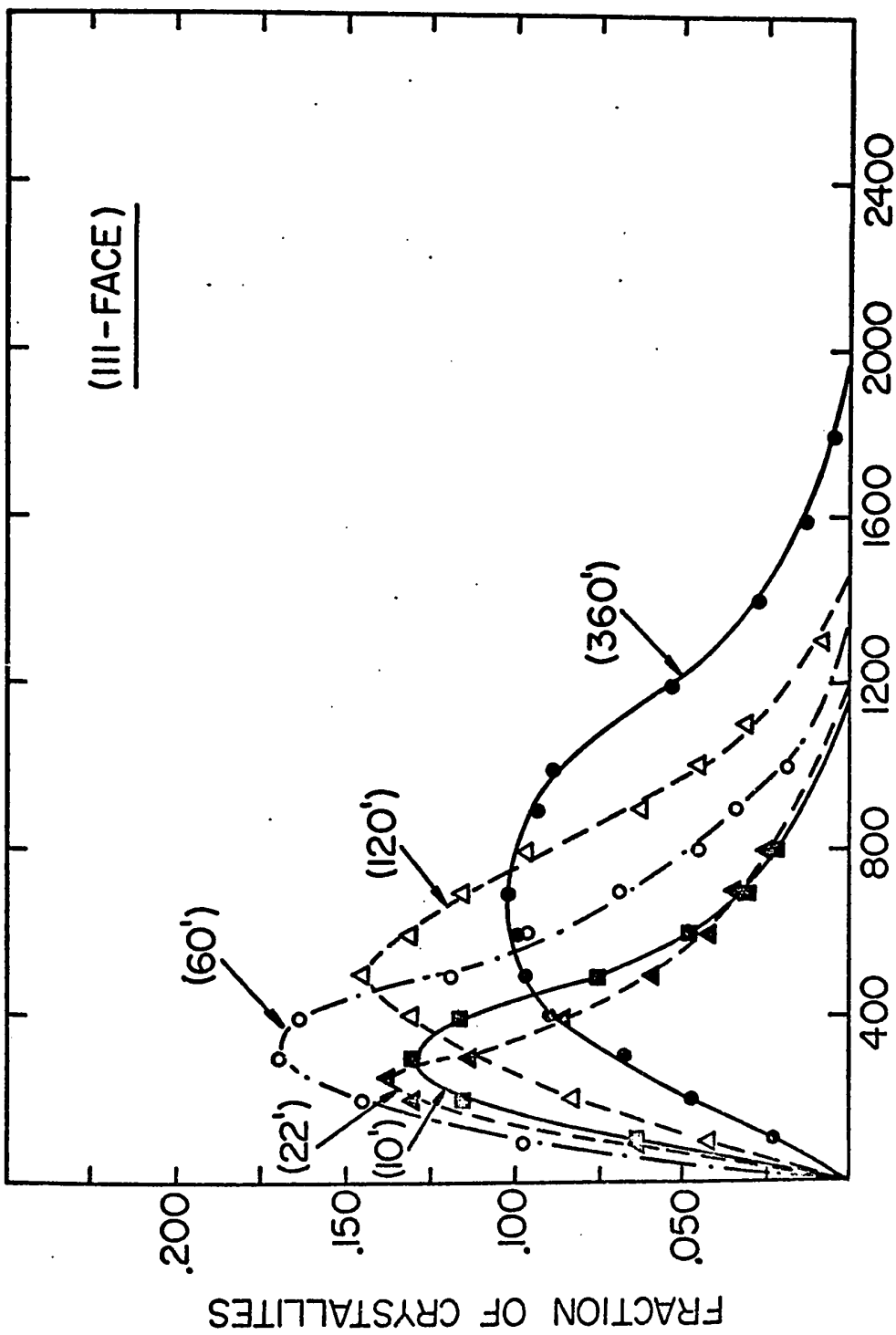


Figure 4.4.7 (a) Crystallite size distribution for oxide films formed on the (111) nickel face at 500°C



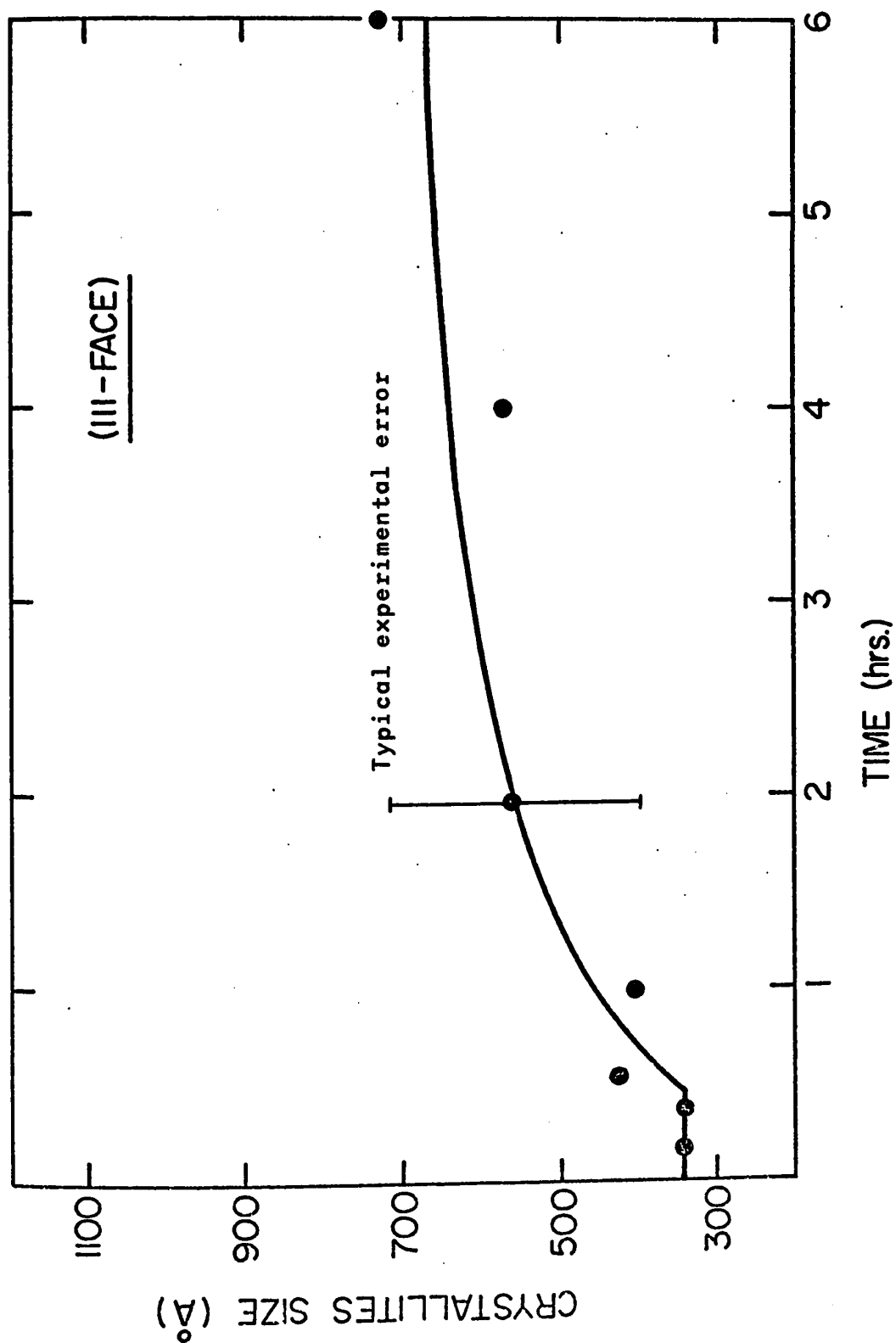


Figure 4.4.7 (b) Average crystallite size versus oxidation time

<u>TYPE A</u>	<u>TYPE B</u>
(111) NiO // (111) Ni	(111) NiO // (111) Ni
3(211) NiO // (111) Ni	3(211) NiO // (111) Ni
3(233) NiO // (111) Ni	3(233) NiO // (111) Ni
with $[0\bar{1}1]$ NiO // $[0\bar{1}1]$ Ni	$[0\bar{1}1]$ NiO // $[\bar{1}1\bar{2}]$ Ni

The orientation: (011) NiO // (111) Ni with  $[0\bar{1}1]$  NiO //  $[0\bar{1}1]$  Ni is also present but multiple orientations have not been observed.

With longer exposure to oxygen the second set disappears which indicates that some structural rearrangement has occurred in the oxide. The remaining multiple orientations of the first type are all equivalent and they continued to be observed for some time. Finally with much longer exposure (from 4-6 hrs), the (233) disappears and the (211) is very seldom observed. Polycrystalline rings with some evidence of preferred orientation are the usual features encountered during the final stage of film growth.

#### 4.5 X-ray diffraction results of the thick oxide films.

We have seen from transmission electron microscopy that when the oxide film thickness is greater than 5000-6000 Å, the electron beam can not penetrate and another means of investigation is needed to follow the structural development of the oxide in a scale. Electron reflection diffraction, which can be used at any film thickness, will give some information about structure but it is confined to a very small portion of the sample and to a very thin superficial layer. In addition, quantitative measurement is difficult because of the

difficulty in measuring the diffracted intensity.

X-ray diffraction is very suitable for the study of the structure of the oxide scales due to its large penetrating power (a beam will go through  $20\mu$  of oxide) and a large cross-section of the oxide is sampled by the beam. Also the possibility exists for accurate measurements of diffracted beam intensities. Two types of information readily obtainable are the strain in the oxide and the texture of the preferred orientation of the oxide.

The origin of the strain in the oxide is generally associated with the change in volume when the metal is transformed into its oxide. The magnitude of the change is often related to the Pilling Bedworth<sup>(98)</sup> ratio defined as:

$$\text{PBR} = \frac{\text{Volume per metal ion in the oxide}}{\text{Volume per metal ion in the metal}}$$

The PBR of NiO is 1.65<sup>(4)</sup>. Thus the oxide could be under a lateral compression which would lead to an expansion of the lattice planes perpendicular to the metal surface. The expansion of the lattice planes will cause a shift in the position of the diffracted peak to a lower value of  $\theta$ , since from the Bragg law, the d-spacing is inversely proportional to  $\sin\theta$ . The continuous variation of the lattice spacing with the film thickness will also cause a broadening of the peak due to the gradual loss in periodicity. This type of information can be deduced from Fourier analysis of the peak profile as Borie and Spark<sup>(99)</sup> have shown for the case of  $\text{Cu}_2\text{O}$  film.

Line broadening can also be due to the particle size effect and care should be taken to distinguish the two components<sup>(100)</sup>. Broadening due to the strain will affect more the second order peak since by differentiating the Bragg's law one obtains the relation:

$$-\left(\frac{\Delta d}{d}\right) \tan\theta = \Delta\theta$$

Thus for a given  $\frac{\Delta d}{d}$ , the line broadening  $\Delta\theta$  is proportional to  $\tan\theta$ , and the second order peak will show larger broadening due to the strain. Broadening associated with particle size will not affect the second order peak and the two components can be separated.

The results from the X-ray investigation are for samples which have been oxidized in a microbalance assembly at the oxygen pressure of 400 mm Hg (same pressure as for samples used for E.M). The temperature range is from 500-800°C and the exposure time varied from 25-100 hr. corresponding to oxide thicknesses from 1 $\mu$  to 15 $\mu$ .

The measurements have shown that for oxide greater than 1 $\mu$  thick, there is no appreciable shift in the position of the diffracted peak. This observation is in agreement with the findings of Cathcart<sup>(8)</sup> and Sartrell and Li<sup>(41)</sup> who reported little or no shift in the diffraction peak. Broadening due to the crystallite size is also not noticeable when compared with a silicon standard of known crystallite size. This finding is not surprising since the amount of

broadening given by the expression<sup>(101)</sup>:

$$t = \frac{.9\lambda}{B\cos\theta}$$

where  $t$  is the crystallite width,  $\lambda$  is the wavelength,  $B$  is the width at half peak height and  $\theta$  is the Bragg angle, is negligible when  $t \approx 1000 \text{ \AA}$ . Results from electron transmission and scanning microscopy have shown that the crystallites size is approximately 800-1000  $\text{\AA}$  after an exposure time of 10-25 hours at 500 °C.

Another type of information easily obtainable is the texture of the oxide or preferred orientation of the crystallites. A complete characterization of the oxide texture can be described by means of a pole figure which gives the variation in pole density with the pole orientation for a selected set of crystal planes<sup>(102)</sup>. A combined reflection and transmission method will give a complete 180° angular distribution of the selected pole within the sample. However, we are only interested in the parallel orientation of certain oxide planes with the metal. Thus a simple inverse pole figure<sup>(103)</sup> is very suitable for this purpose. This method also allows the oxide to be studied without being removed from the metal substrate.

A parallel orientation can be obtained from the diffractometer measurement since the diffraction conditions are set up so that only the planes parallel to the surface satisfy Bragg's condition. The type of preferred orientation is

obtained simply by comparing the integrated intensity of an (hkl) plane of the textured sample with the intensity of a similar plane of a random sample. The degree of preferred orientation can be expressed by the texture coefficient defined by Harris<sup>(93)</sup> as:

$$P_{hkl} = \frac{\frac{I_{hkl}}{I_{r,hkl}}}{\frac{1}{n} \sum \frac{I_{hkl}}{I_{r,hkl}}}$$

where  $P_{hkl}$  is the texture coefficient of the (hkl) plane,  $I_{hkl}$  is the integrated intensity of the textured sample,  $I_{r,hkl}$  is the integrated intensity of a random sample given by the ASTM index card,  $n$  is the number of peaks investigated.  $N$  should be large in order to minimize the error inherent in the definition of the formula. Clearly,  $P_{hkl}$  is equal to one for a random sample.

It has been found during measurement that the integrated intensity changed with a simple rotation of the sample. This means that some of the diffracting planes are not exactly parallel to the surface and to reduce this type of error, samples are continuously spinned during observation. The degree of preferred orientation was also found to be different on different faces of the same sample and thus an average value based on the intensities obtained for the two faces is used to give a representative texture coefficient for the particular sample.

The texture coefficients of all the samples from the three faces of nickel are given in the tables 4.5.1-3.

The highest values for the texture coefficients are represented graphically in figures 4.5.1-3. The texture coefficients are plotted against the oxide thickness instead of the usual stereographic projection. This representation allows the morphological development of the oxide structure to be followed graphically. A line simply joins all the points belonging to the same (hkl) plane. No attempt has been tried to smooth out the experimental points.

From the graphs we can see that the oxide on the (100) face of nickel exhibits a strong preferred orientation on either the (100) or the (111) or sometimes on both. The frequency of occurrence of either orientation is about 50%. Other reflections are present but only to a very small extent. Their respective texture coefficients are usually less than 0.5. The degree or type of preferred orientation appears to be independent of oxide thickness and are quite scattered across the thickness range. No definite trend could be established. The two major orientations, the (100) and the (111) are the same major orientations observed in the thin film range. Thus there seems to be no change in the type of preferred orientation during the growth of the oxide scales.

This type of behaviour was not observed on the (110) nickel face (fig. 4.5.2) which shows a definite (100) preferred orientation. This is not expected since the (100) orientation,

TABLE 4.5.1

## TEXTURE COEFFICIENTS OF THE (100) FACE

Sample number	Thickness Temperature	(111)	(200)	(220)	(311)	(331)	(420)	(422)
20	1.5 $\mu$ (53 hr) (500 °C)	4.85	0.76	0.03	0.09	<.01	0.19	0.02
19	2.2 $\mu$ (104hr) (500 °C)	1.86	3.00	0.01	<.01	<.01	<.01	<.01
18	4.0 $\mu$ (50hr) (600 °C)	1.04	3.88	0.01	<.01	<.01	<.01	0.05
5	4.5 $\mu$ (106hr) (600 °C)	3.57	2.00	0.02	0.51	0.31	0.14	0.41
10	5.8 $\mu$ (10 hr) (800 °C)	3.25	1.14	0.31	0.50	0.70	0.33	0.68
16	6.8 $\mu$ (50 hr) (700 °C)	3.11	3.40	0.05	0.16	0.09	0.03	0.16
8	7.8 $\mu$ (135hr) (800 °C)	0.97	5.80	0.03	0.04	0.04	0.02	0.04
15	10.0 $\mu$ (110hr) (700 °C)	4.43	1.12	0.20	0.41	0.31	0.22	0.32
14	11.3 $\mu$ (48 hr) (800 °C)	5.78	0.38	0.16	0.24	0.18	0.06	0.21
12	14.0 $\mu$ (120hr)	3.12	2.96	0.08	0.26	0.20	0.15	0.26



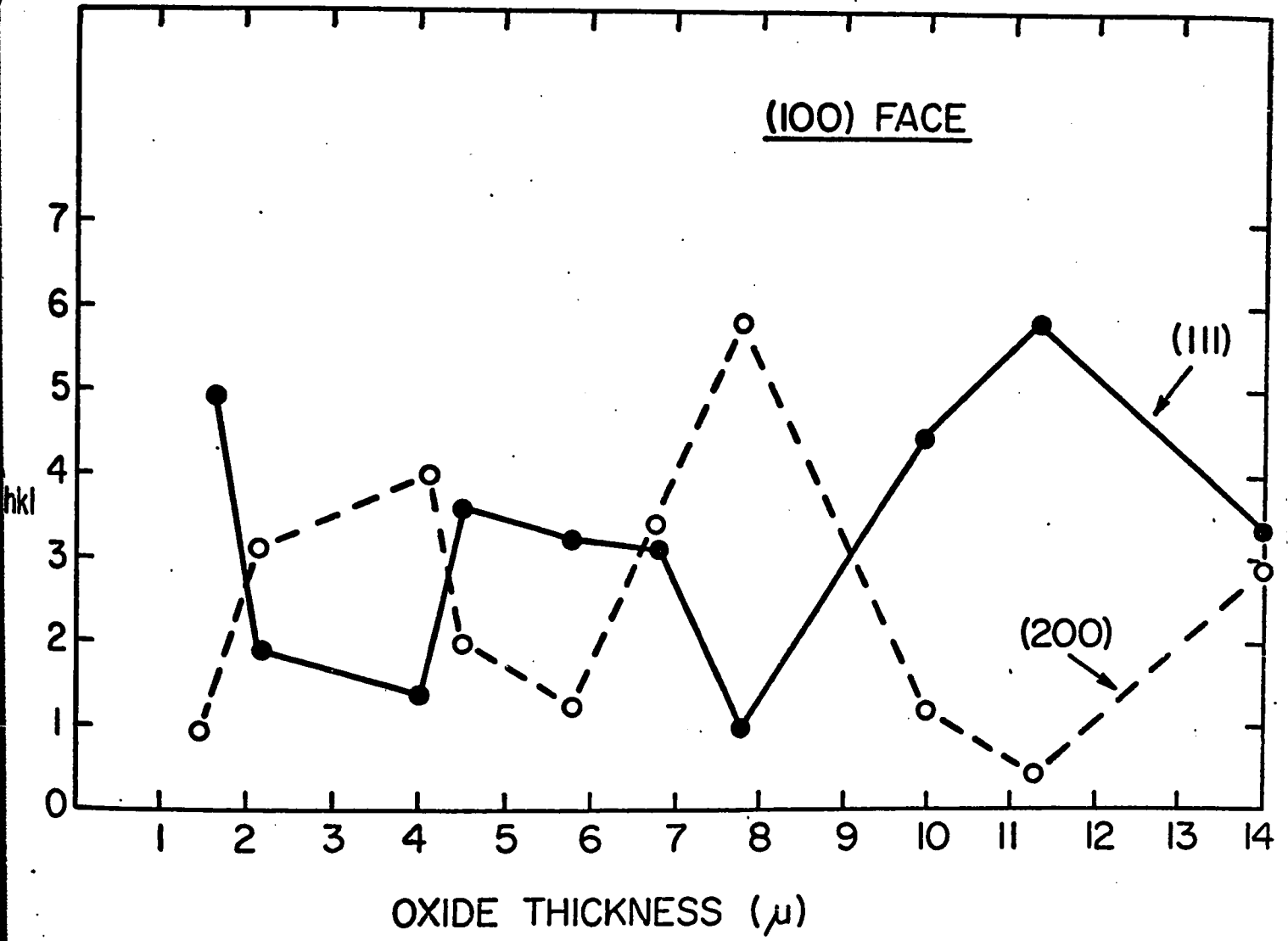


Figure 4.5.1 Texture coefficients of the oxide formed on the (100) nickel face

TABLE 4.5.2

## TEXTURE COEFFICIENT OF THE (110) FACE

Sample number	Thickness Temperature	(111)	(200)	(220)	(311)	(331)	(420)	(422)
50	1.2 $\mu$ (100 hr) (600 °C)	0.67	2.64	1.29	1.90	0.01	0.46	0.20
51	2.2 $\mu$ (50 hr) (600 °C)	0.46	2.74	1.19	1.03	0.71	0.52	0.33
49	2.9 $\mu$ (100hr) (600 °C)	0.32	3.56	1.05	0.97	0.67	0.39	<.01
42	3.3 $\mu$ (50 hr) (800 °C)	0.38	3.55	0.76	1.14	0.56	0.60	<.01
45	5.1 $\mu$ (100 hr) (700 °C)	0.21	3.68	1.12	1.04	0.37	0.32	0.24
44	5.6 $\mu$ (50 hr) (700 °C)	0.32	2.96	1.00	0.98	0.38	0.57	0.25
41	6.2 $\mu$ (67 hr) (800 °C)	0.41	2.77	0.86	1.17	0.75	0.55	0.46
43	7.2 $\mu$ (100 hr) (800 °C)	0.35	4.5	0.69	0.59	0.28	0.17	0.16

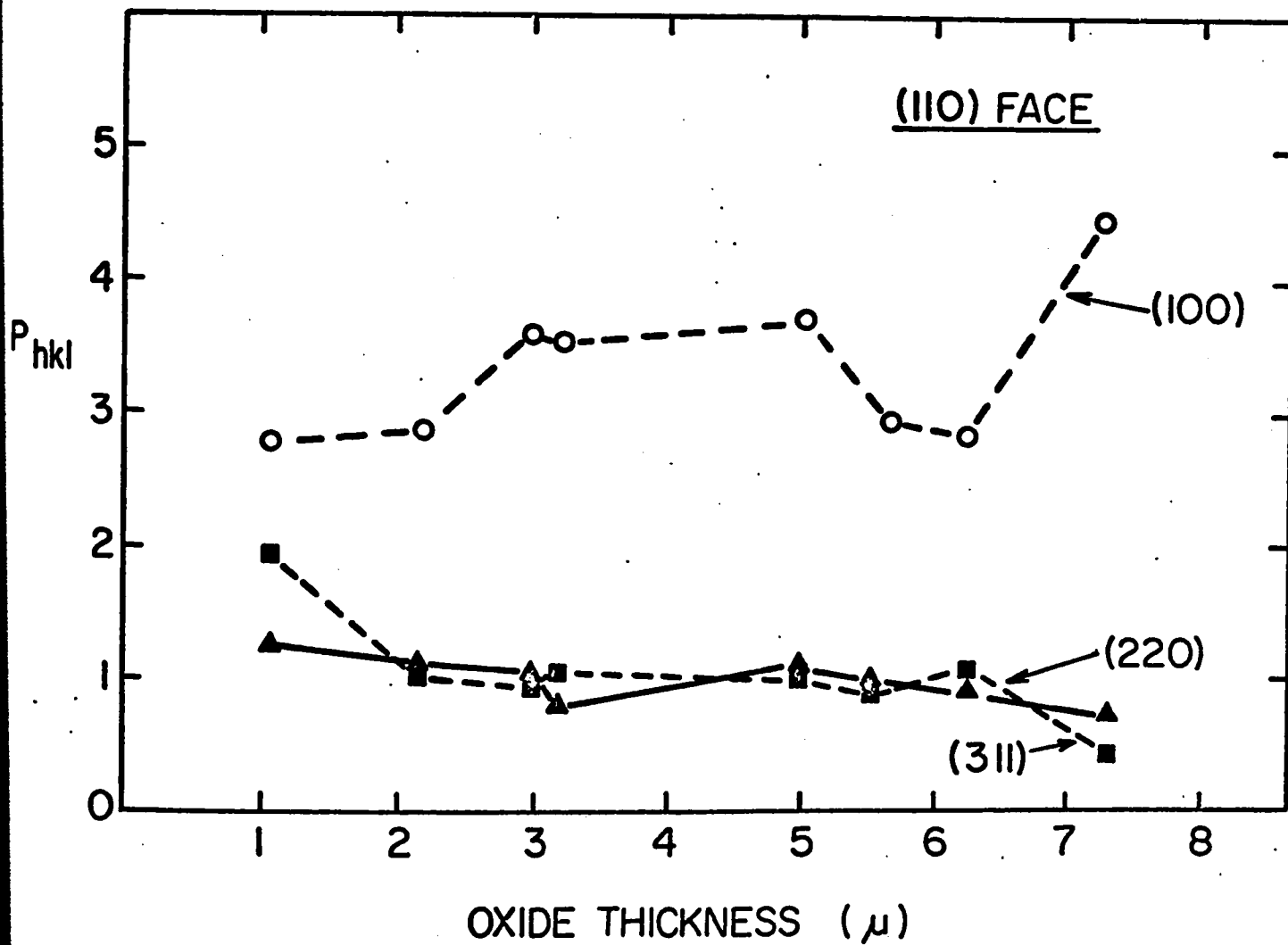


Figure 4.5.2 Texture coefficient of the oxide formed on the (110) nickel face

although it has been observed in the thin film range was not a major orientation. The degree of preferred orientation is however not very strong. The (100) texture coefficient is about 2-4. In addition other reflections are also present to a larger extent, especially the (220) and the (311) planes. From the above observation it can be said that the oxide on this face exhibits a more polycrystalline nature in spite of a definite (100) preferred orientation. Note that the texture seems to increase with the oxide thickness, a trend not observed on the (100) face. The important feature of the oxide on this nickel face is that the preferred orientation in the thick scale is not a major orientation in the thin film range. This development must be due to an oriented overgrowth process in which the (100) is the preferred growth plane.

The behaviour of the oxide on the (111) face is shown in figure 4.5.3. This oxide shows a definite preferred (111) orientation. The texture coefficients are relatively higher than the (110) nickel and seem to increase with the oxide thickness. These two features are similarly observed on the (110) face. The (111) preferred orientation in the scale is the same major orientation observed in the thin film range and the preferred growth is simply extended from the already existing orientation in the thin film. To this extent, the behaviour is very similar to that for the (100) face of nickel.

TABLE 4.5.3  
TEXTURE COEFFICIENT OF THE (111) FACE

Sample number	Thickness Temperature	(111)	(200)	(220)	(311)	(331)	(420)	(422)
37	0.5 $\mu$ (116hr) (500 °C)	2.44	1.02	0.69	0.46	.01	.01	.01
39	0.9 $\mu$ (114hr) (500 °C)	3.07	0.41	0.09	0.43	.01	.01	.01
38	1.5 $\mu$ (69 hr) (500 °C)	3.07	1.50	0.43	0.90	0.95	0.31	0.25
33	2.7 $\mu$ (114hr) (600 °C)	3.50	0.45	0.29	0.78	0.42	0.50	0.55
34	4.6 $\mu$ (53 hr) (600 °C)	4.50	0.64	0.27	0.74	0.23	0.22	0.33
25	5.5 $\mu$ (130hr) (700 °C)	3.86	0.73	0.27	0.86	0.41	0.21	0.65
24	7.9 $\mu$ (103hr) (700 °C)	4.05	0.25	0.35	0.74	0.34	0.11	0.57
28	8.26 $\mu$ (70hr) (700 °C)	4.00	0.43	0.39	0.84	0.50	0.26	0.54
29	10.7 $\mu$ (68hr) (700 °C)	4.10	0.43	0.34	0.83	0.54	0.24	0.43

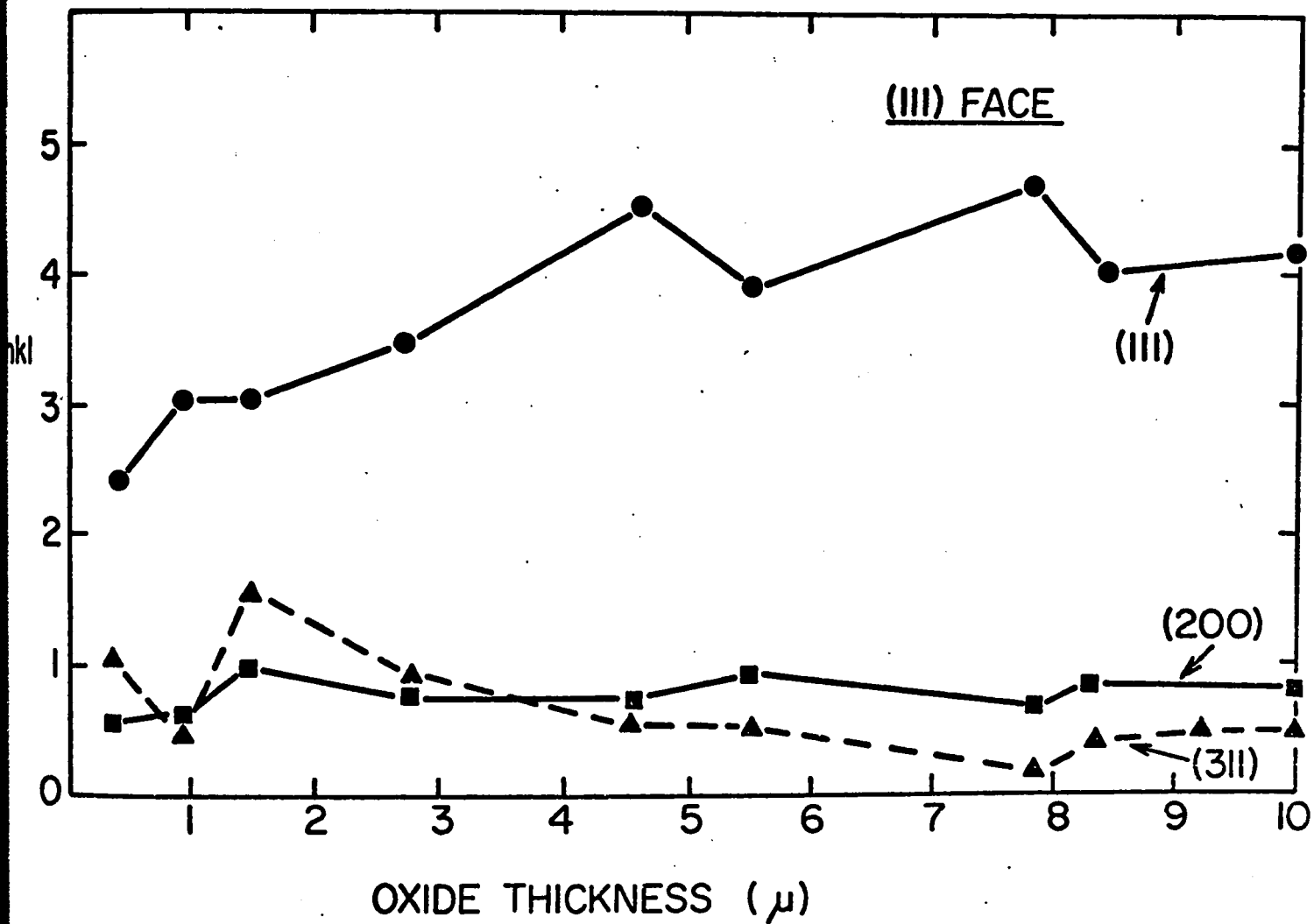


Figure 4.5.3 Texture coefficients of the oxide formed on the (111) nickel face

From the observations made on the three faces of nickel, the following conclusions can be made. The oxide formed on these three nickel planes show a preferred (100) or (111) orientation. These planes are parallel to the surface of the metal, and in a NaCl-type crystal structure, they are the most densely packed and contain the highest number of close packed directions. In spite of the presence of many other orientations in the thin films including the low index planes such as the (110) and the (211), only two major orientations are observed. The (100) and the (111) are the preferred growth planes in the Ni-NiO system due to their being densely packed and/or their large number of close packed directions.

#### 4.6 Scanning electron microscope results of the thick oxide films

A study of the structure of the thick oxide films by X-ray diffraction gave information about the strain and the texture of the oxide but the growth morphologies such as grain size and the scale microstructure cannot be obtained by this technique.

The scanning electron microscope (SEM) is very suitable for the study of the microstructure of the scale due to its high resolution and depth of field<sup>(104)</sup>. These observations will complement those obtained by X-ray diffraction and give a more complete description of the oxide structure in the thick film range. Surface oxide topography is obtained directly without special preparation. The sample cross-sections are prepared by cutting the sample in half, mounting in room-setting plastic and polishing. The microstructure can be revealed by a suitable etch previously described in this thesis.

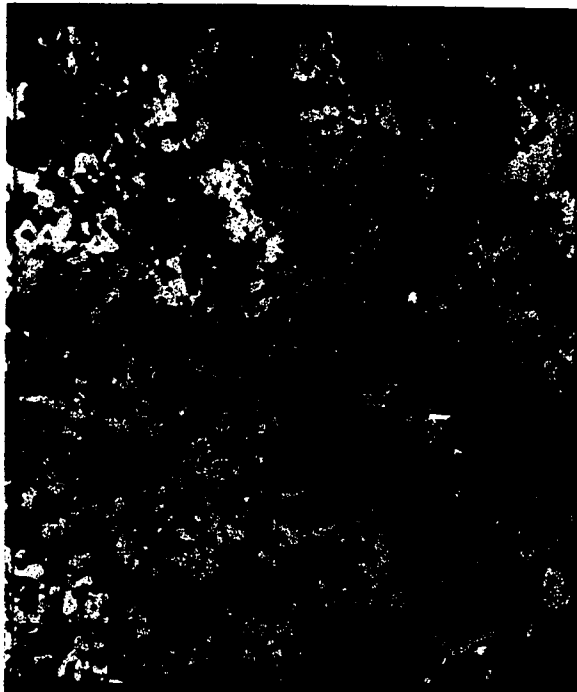
##### 4.6.1 Results for the (100 nickel face).

The oxidized samples upon examination by the naked eye exhibit a uniform greenish color. At low magnification the surface has a "sandy finish" appearance. The high magnification micrographs taken with the SEM are shown below. Fig. 4.6.1(a) is a surface view of a sample oxidized for 100 hr at 500 °C. The picture clearly shows grains with a uniform distribution in size. No abnormally large grains, terraces or ledges are observed. The surface view of another



sample exposed for the same period at 700°C is shown in fig. (b). The general features are similar to the previous sample. Exposure at 800°C for 25 hr lead to some growth irregularities as shown in fig. (c). Regions of uneven thickness and differences in grain structure are seen in the micrograph. Exposure to 50 hr at the same temperature does not lead to any drastic change in the microstructure but after 100 hr, well defined geometrical grains are seen extending from the surface, fig. (d). Most of the grains exhibit a rectangular shape which is probably defined by low indices crystallographic planes.

The oxide cross-sections of the samples oxidized for 100 to 120 hr are shown in fig. 4.6.1(e)-(h). The most noticeable feature common to all these cross-sections is the presence of two distinct oxide layers in the scales. The outer layer is characterized by relatively columnar grains and the inner layer by equiaxed grains. Close examination of these two layers revealed that there exist significant differences depending on whether the oxide is formed at high or low temperature. Fig. 4.6.1(h) is a micrograph of a sample oxidized at 800°C. Note that the boundary between the two layers is rather diffuse and that the average grain size of the two layers is not much different. If one compares this with the micrograph of a sample oxidized at 600°C, shown in (f), one immediately sees that a very well defined boundary and a large difference in grain size exist between the two



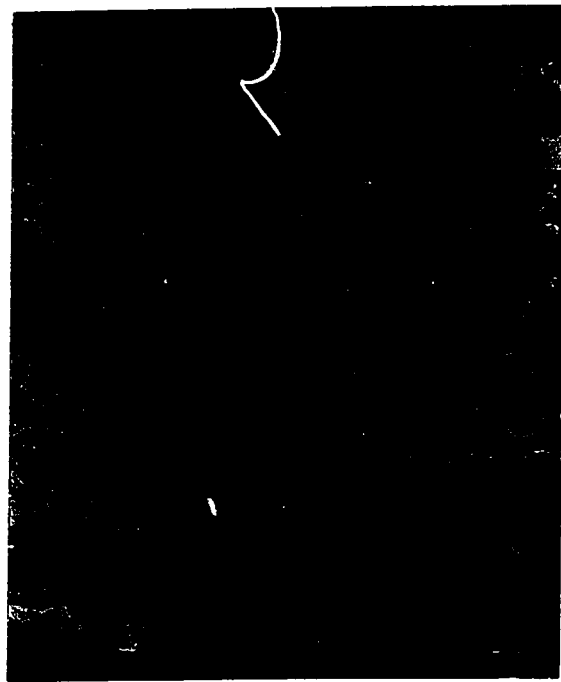
(a)



(b)



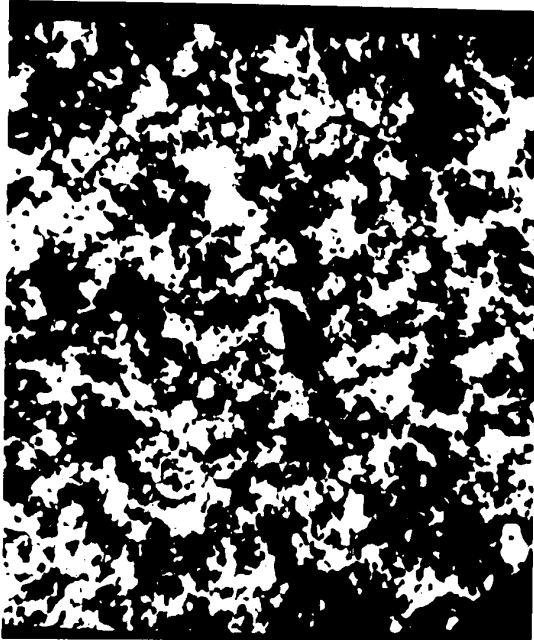
(c)



(d)

Figure 4.6.1

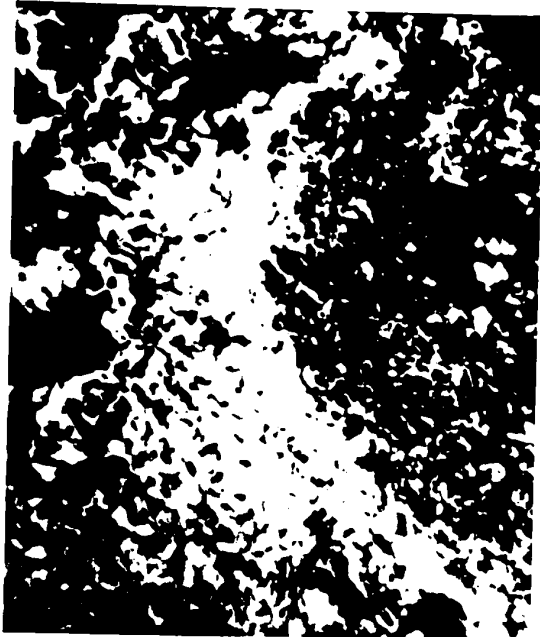
- (a) Surface view of a sample oxidized at 500 °C for 100 hr x 3800  
(b) Surface view of a sample oxidized at 700 °C for 110 hr x 2100  
(c) Surface view of a sample oxidized at 800 °C for 25 hr x 2000  
(d) Surface view of a sample oxidized at 800 °C for 120 hr x 1800



(a)



(b)



(c)



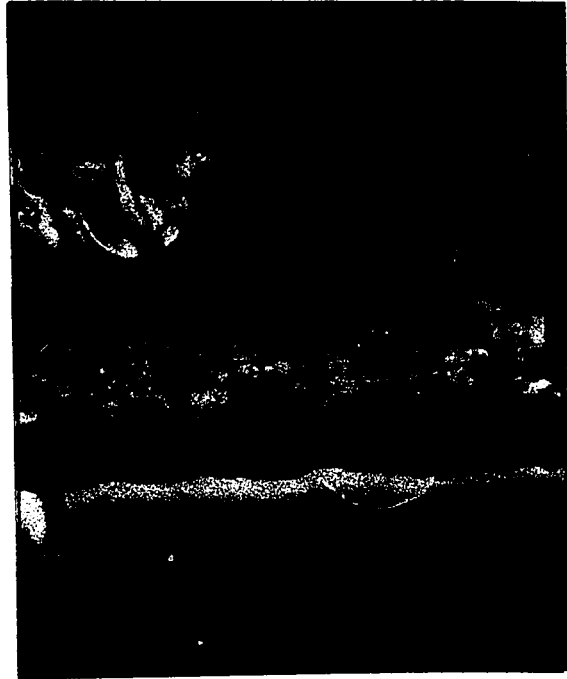
(d)

Figure 4.6.1

- (a) Surface view of a sample oxidized at 500 °C for 100 hr x 3800
- (b) Surface view of a sample oxidized at 700 °C for 110 hr x 2100
- (c) Surface view of a sample oxidized at 800 °C for 25 hr x 2000
- (d) Surface view of a sample oxidized at 800 °C for 120 hr x 1800



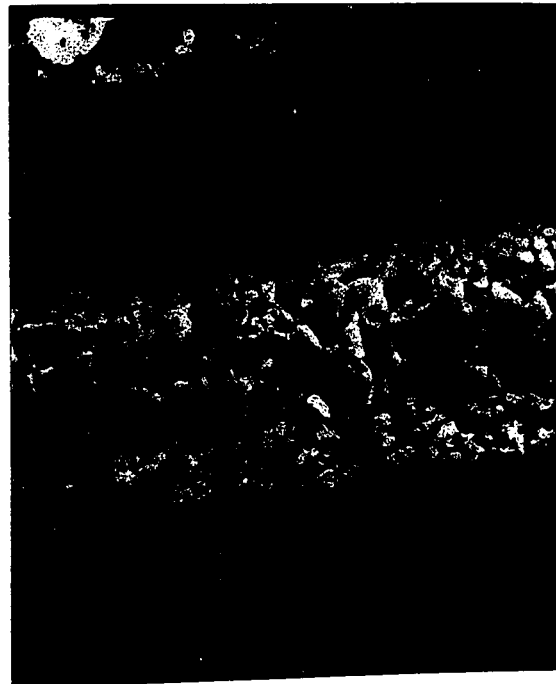
(e)



(f)



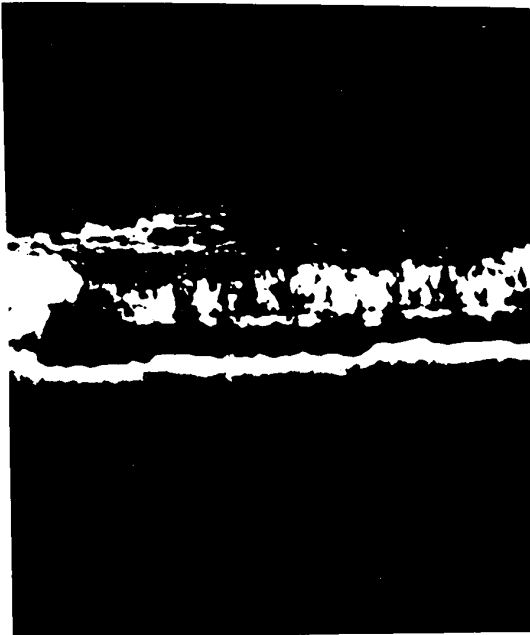
(g)



(h)

Figure 4.6.1. Cross section view

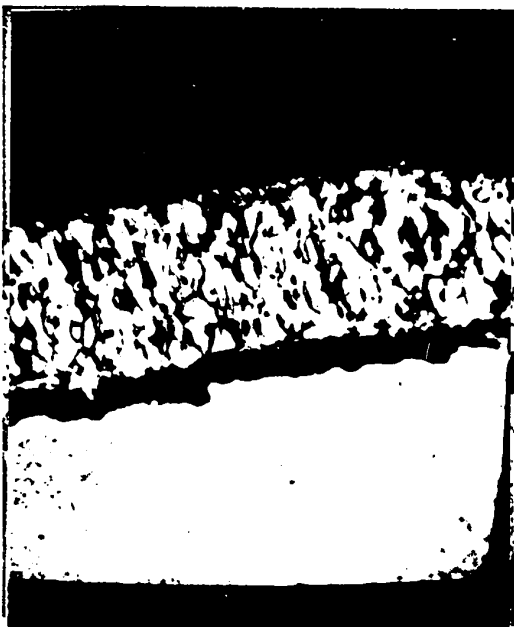
- |     |                                     |        |
|-----|-------------------------------------|--------|
| (e) | Sample oxidized at 500°C for 100 hr | x 6300 |
| (f) | Sample oxidized at 600°C for 115 hr | x 4300 |
| (g) | Sample oxidized at 700°C for 110 hr | x 2100 |
| (h) | Sample oxidized at 800°C for 120 hr | x 2000 |



(e)



(f)



(g)



(h)

Figure 4.6.1. Cross section view

- (e) Sample oxidized at 500 °C for 100 hr x 6300  
 (f) Sample oxidized at 600 °C for 115 hr x 4300  
 (g) Sample oxidized at 700 °C for 110 hr x 2100  
 (h) Sample oxidized at 800 °C for 120 hr x 2000

layers. In addition considerable porosity is observed in the inner layer. From the micrographs of these cross-sections an average grain size in the outer oxide layer and an average ratio of the thicknesses of the two layers can be determined. The values obtained are summarized in Table 4.6.1.

TABLE 4.6.1

SEM RESULTS FOR THE (100) NICKEL FACE

Sample number	Temperature (°C)	Oxidation time (hr)	Oxide thickness (μ)	Average grain size in outer layer (μ) *	Average ratio of outer/inner layers
5	800	16	4.7	1.13	0.8 ± 0.1
7	800	25	7.8	1.28	1.0 ± 0.1
14	800	48	11.4	1.76	1.2 ± 0.2
12	800	120	14.2	1.87	2.1 ± 0.5
16	700	50	6.8	0.92	3.0 ± 1.0
15	700	110	10.7	0.78	3.2 ± 1.1
18	600	50	3.5	0.63	1.2 ± 0.3
17	600	115	5.9	1.03	1.9 ± 0.8
19	500	104	2.1	0.25	1.2 ± 0.4

The following conclusions can be made in view of the above observations.

(a) The average grain size of the oxide increases with temperature and exposure time.

\* grain size determined by linear intercepts

(b) The oxide cross-sections show the presence of two distinct layers at all temperatures and thicknesses investigated. The ratio of the thicknesses (outer/inner) increases with exposure time but seems to be independent of temperature. The ratio was not constant within a given sample and the maximum variation was found at 700 °C.

(c) From the examination of many micrographs, it can be said that the structure of oxide on the (100) face is very uniform; i.e. the same type of microstructure was found at all temperatures and across the whole thickness range.

#### 4.6.2 Results for the (110) nickel face.

Similar results obtained for the (110) face are presented in the following micrographs. Fig. 4.6.2(a) is a surface view of a sample oxidized at 600 °C for 100 hr. The micrograph clearly shows regions of uneven thicknesses with different grain structures in each region. The structure of a sample exposed at 700 °C for 100 hr is shown in fig. (b). Growth features such as nodules, regions of uneven thickness and noticeable difference in grain size are seen in the micrograph. The same types of features are observed on a sample oxidized at 800 °C which are seen in fig. (c). These observations are illustrated by two micrographs taken at different sections of (c). Fig. (d) is a magnified picture of the thin region. Well defined geometrical shaped grains are seen extending from the surface forming a sort of stepped structure. Fig. (e) is a magnified view of the

thicker region. Grains with a variety of shapes forming a rather flat surface are observed in this region. In addition, a marked difference in grain size exists between the two regions.

The cross-sectional views of the oxide from the same samples are shown in fig. 4.6.2(f)-(l). The sample at 600 °C is seen in (f). A very diffuse boundary deliniating two layers could be distinguished at several areas; however, no marked difference in the grain structure is seen between the two layers. The cross-section at 700 °C is shown in (g). Note the fine grained and slightly porous region near the metal interface. The outer region shows some elongated grains but at the same time very large and equiaxed grains are also present. The structural varieties of this sample are illustrated by another micrograph shown in (h) taken at the same magnification. Note the difference in thickness and grain structure in the two micrographs. The structural varieties are also observed in a sample oxidized at 800 °C shown in fig. (k) and (l). Note again the difference in thickness, grain morphology and the lack of a two-layer structure. In spite of the large spread in size distribution, an average grain size was determined from many micrographs. The results are summarized in table 4.6.2.



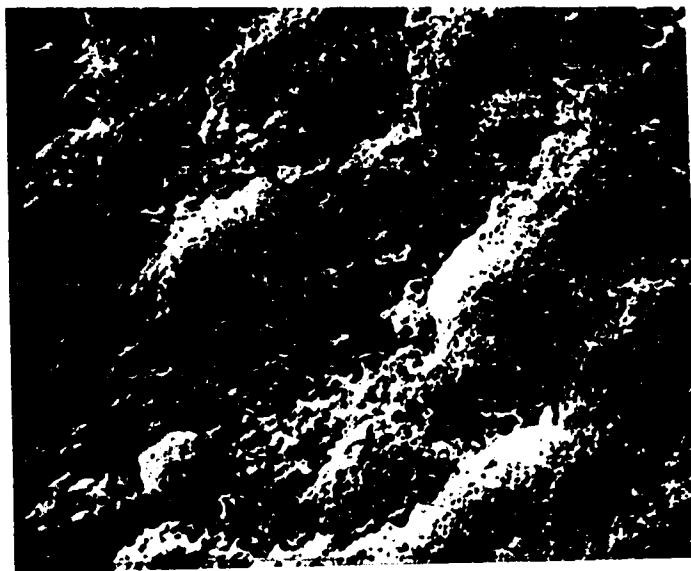


Figure 4.6.2 (a) Surface view of a sample oxidized at 600°C for 100 hr x 1200

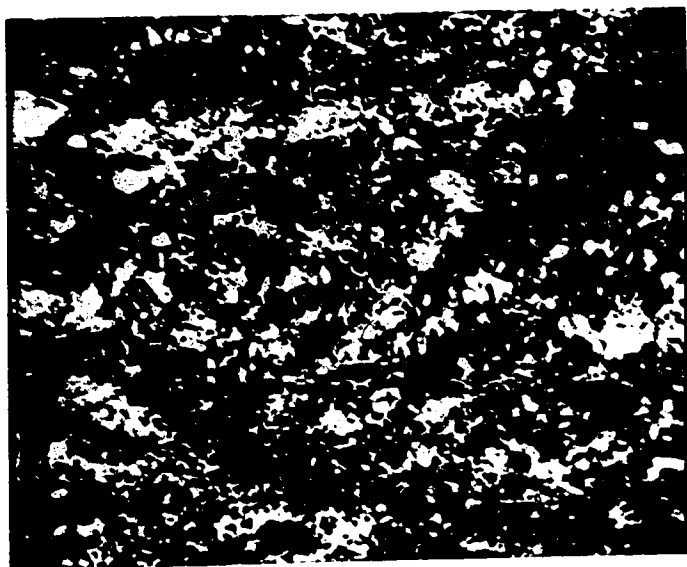


Figure 4.6.2 (b) Surface view of a sample oxidized at 700°C for 100 hr x 600

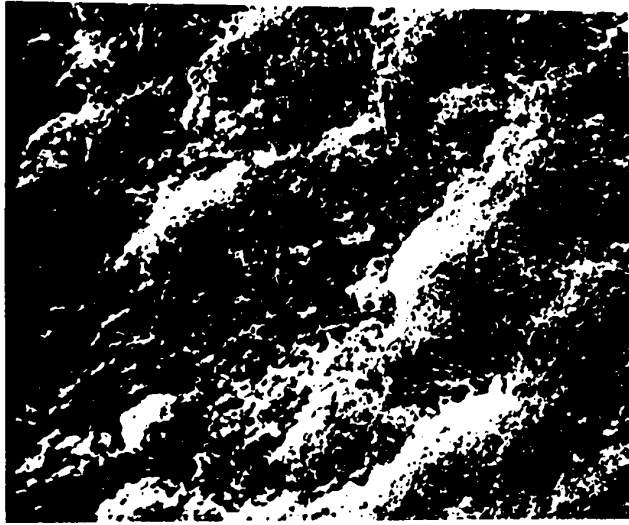


Figure 4.6.2 (a) Surface view of a sample oxidized at 600°C  
for 100 hr x 1200

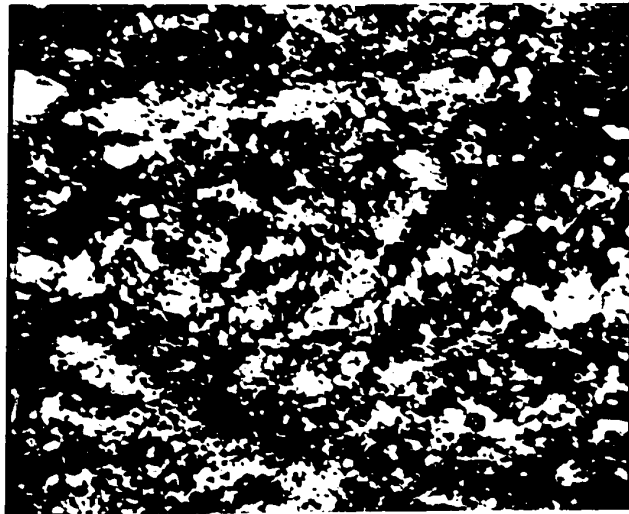
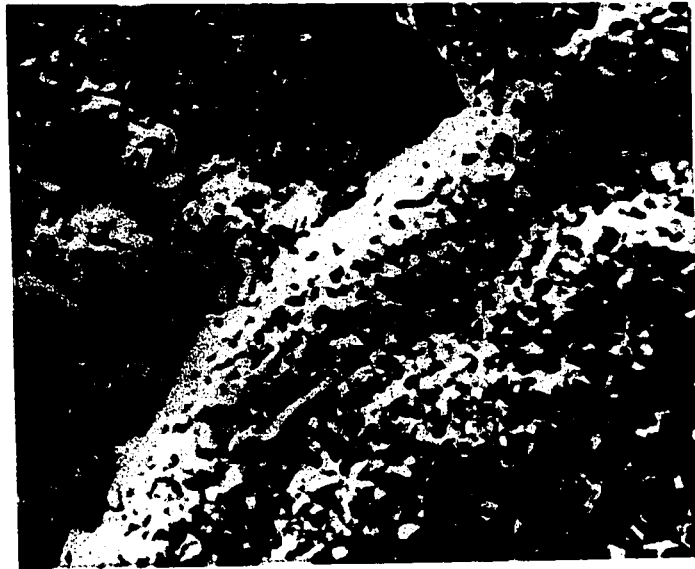


Figure 4.6.2 (b) Surface view of a sample oxidized at 700°C  
for 100 hr x 600



(c)



(d)



(e)

Figure 4.6.2

- (c) Surface view of a sample oxidized at 800°C x 1100  
 (d) Magnified view of the thin region of (c) x 2200  
 (e) Magnified view of the thick region of (c) x 2200



(c)



(d)



(e)

Figure 4.6.2

- (c) Surface view of a sample oxidized at 800°C x 1100  
 (d) Magnified view of the thin region of (c) x 2200  
 (e) Magnified view of the thick region of (c) x 2200

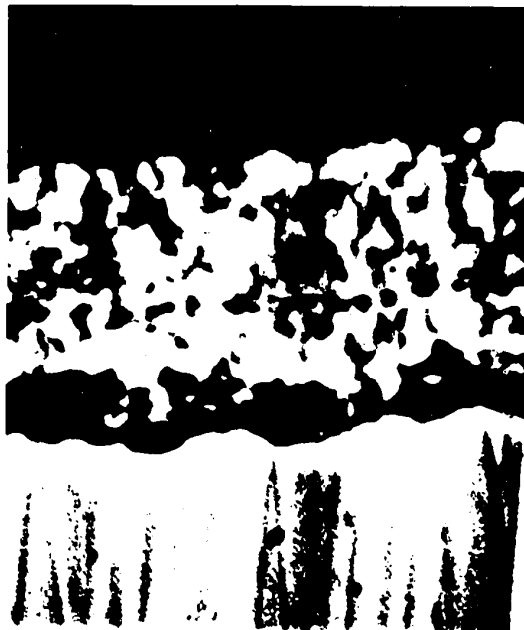
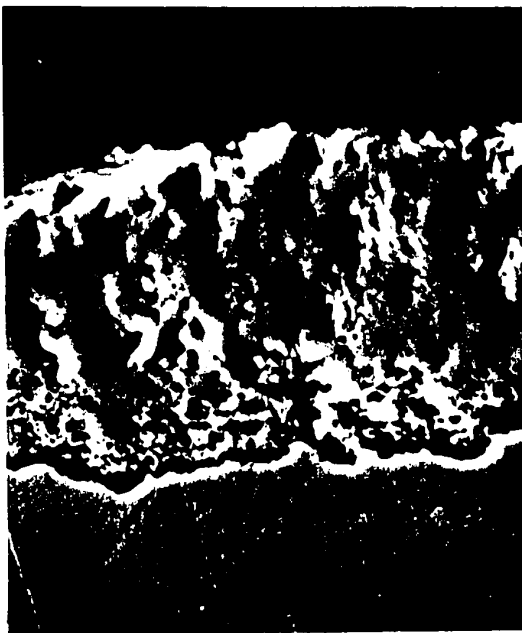


Figure 4.6.2 (f) Cross section of a sample oxidized at 600°C for 100 hr x 4600



(g)



(h)

Figure 4.6.2 Cross section view

(g) Sample oxidized at 700°C for 100 hr x 1900

(h) Same sample as (g) but at different film section x 1900

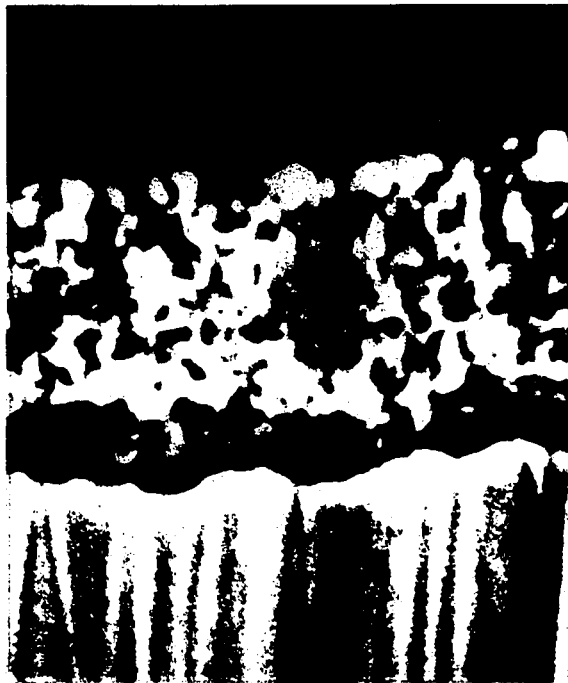
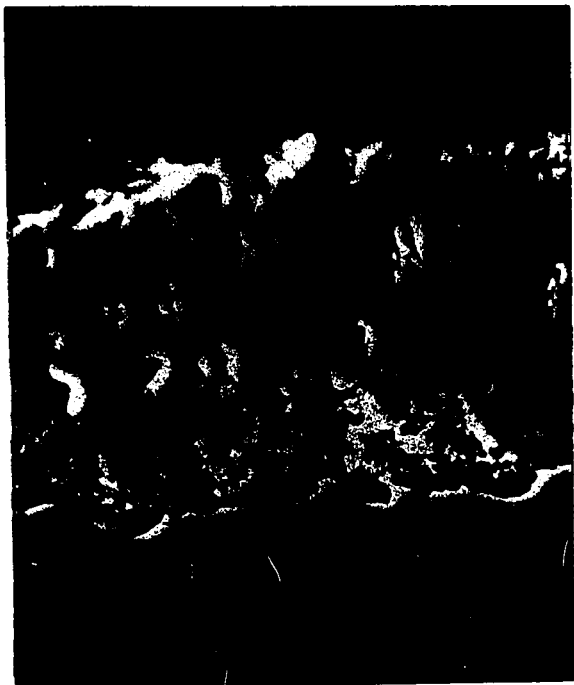


Figure 4.6.2 (f) Cross section of a sample oxidized at 600°C for 100 hr x 4600



(g)



(h)

Figure 4.6.2 Cross section view

- (g) Sample oxidized at 700°C for 100 hr x 1900  
 (h) Same sample as (g) but at different film section x 1900



Figure 4.6.2 (f) Cross section of a sample oxidized at 600°C for 100 hr x 4600



(g)



(h)

Figure 4.6.2 Cross section view

- (g) Sample oxidized at 700°C for 100 hr x 1900  
 (h) Same sample as (g) but at different film section x 1900

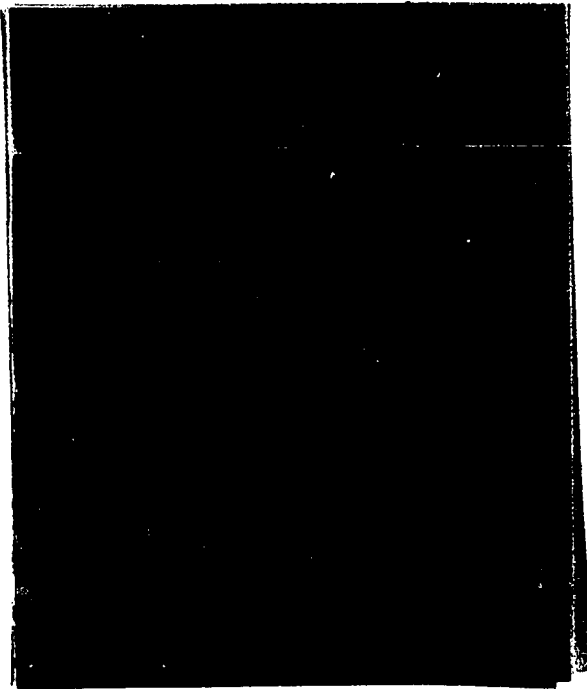
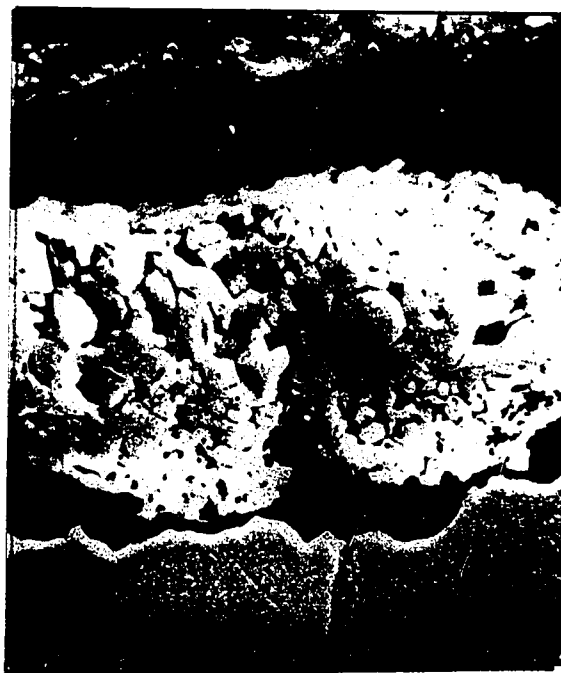


Figure 4.6.2 (k) Cross  
section of sample oxidized  
at 800°C for 100 hr x 1800

Figure 4.6.2 (l) Cross  
section of same sample  
as in (k) but at different  
film section x 1800





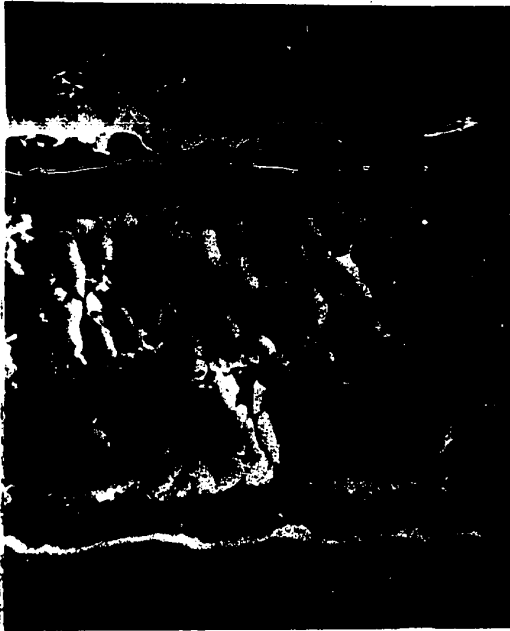


Figure 4.6.2 (k) Cross section of sample oxidized at 800°C for 100 hr x 1800

Figure 4.6.2 (l) Cross section of same sample as in (k) but at different film section x 1800



TABLE 4.6.2

## SEM RESULTS FOR THE (110) NICKEL FACE

Sample number	Temperature (°C)	Oxidation time (hr)	Oxide thickness (μ)	Average grain size of oxide gas interface (μ)	Ratio of two layers
41	800	67	6.4	1.90	single layer
43	800	100	7.0	2.48	single layer
44	700	50	5.5	.94	single layer
45	700	100	5.3	1.62	single layer
51	600	50	2.2	.40*	?
49	600	100	2.7	0.71	Two layers (not always observed)

\* grain size determined from top view

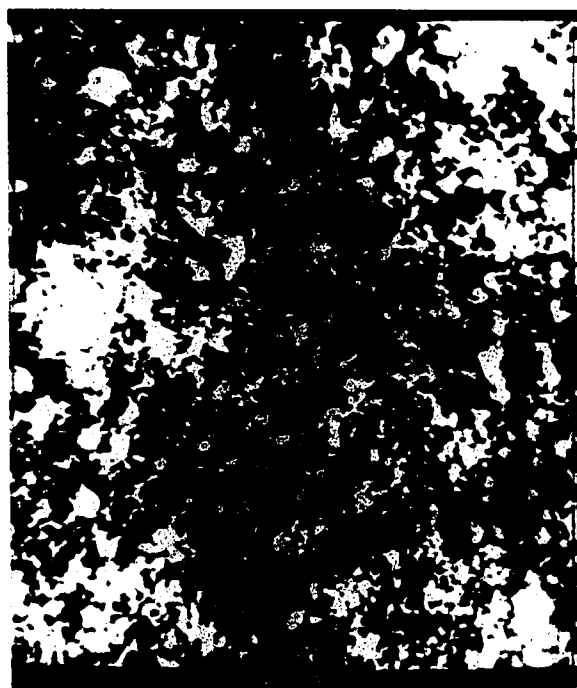
The following comments can be made concerning the structure of the oxide film of the (110) face:

- (a) The average grain size of the oxide increases with temperature and exposure time but the grain size is 10-40% larger than the oxide on the (100) nickel face at 700 and 800 °C.
- (b) The presence of a duplex scale is not observed at any temperature and oxide thickness.
- (c) The structure of the oxide is not uniform when compared to the (100) face. Growth nodules, differences in thicknesses and in grain structure are frequently observed.

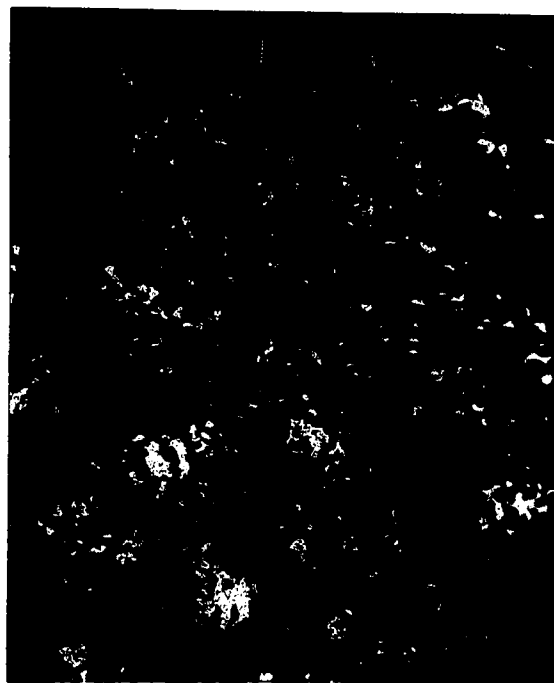
#### 4.6.3 Results for the (111) nickel face.

The surface view of an oxide formed on the (111) face at 500 °C for 116 hr is shown in fig. 4.6.3(a). The picture exhibits light and dark regions indicating some variations in film thickness. In addition marked differences in grain size are also observed. The same general features are present in a sample oxidized at 600 °C. The micrograph shown in (b) is from a sample oxidized at 700 °C for 130 hr. Some growth "nodules" are seen on the lower left of the micrograph but the remaining grain structure is rather uniform. Exposure to 48 hr at 800 °C results in some growth irregularities as shown in fig. (c). The micrograph exhibits regions of different thickness and microstructure. Note that the shape of the grains although well defined still does not show a regular geometrical shape. The simple geometrically shaped grains become however visible after 100 hrs exposure. This is seen in fig. (d). Note that a variety of shapes are present. They are not overwhelmingly rectangular as in the case for the (100) face.

The oxide cross-sections are shown in the following micrographs. Fig. 4.6.3(e) and (f) are from a sample oxidized at 600 °C. The presence of two layers is clearly in evidence. The outer layer shows the familiar columnar grains and the inner layer the equiaxed grains. Note however that the difference in grain size is not large. This feature is quite different from the (100) sample oxidized at the same tempera-



(a)



(b)



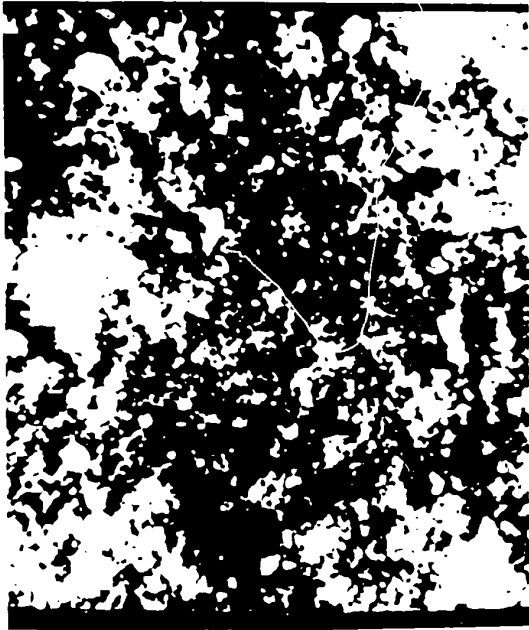
(c)



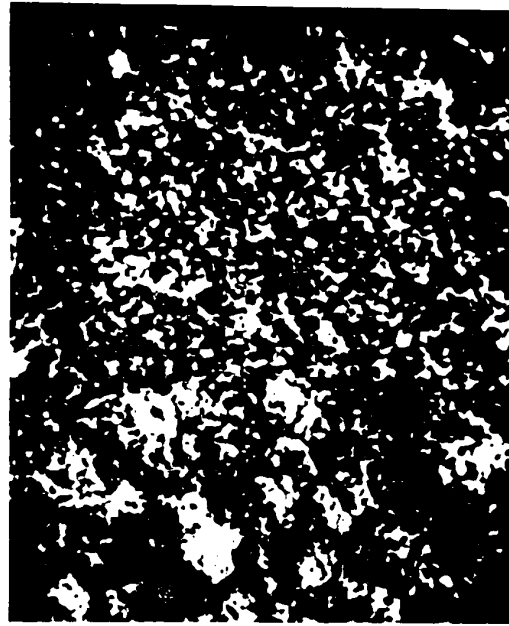
(d)

Figure 4.6.3

- |     |   |        |
|-----|---|--------|
| (a) | Surface view of a sample oxidized at 500°C for 116 hr | x 1500 |
| (b) | Surface view of a sample oxidized at 700°C for 130 hr | x 1000 |
| (c) | Surface view of a sample oxidized at 800°C for 48 hr  | x 750  |
| (d) | Surface view of a sample oxidized at 800°C for 100 hr | x 1800 |



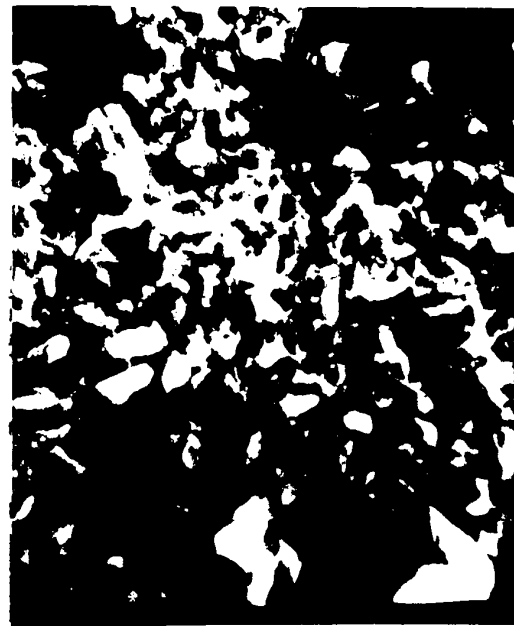
(a)



(b)



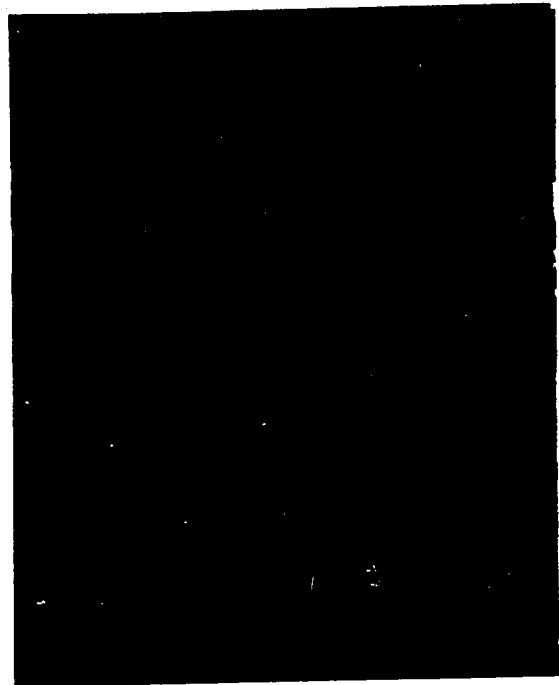
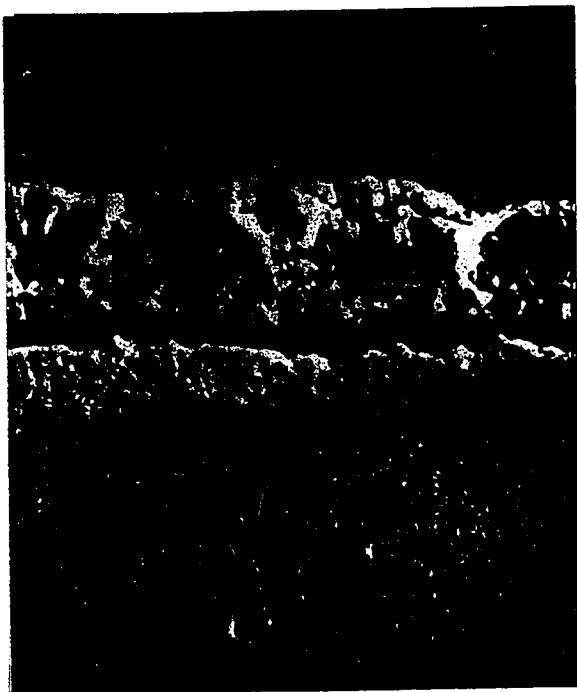
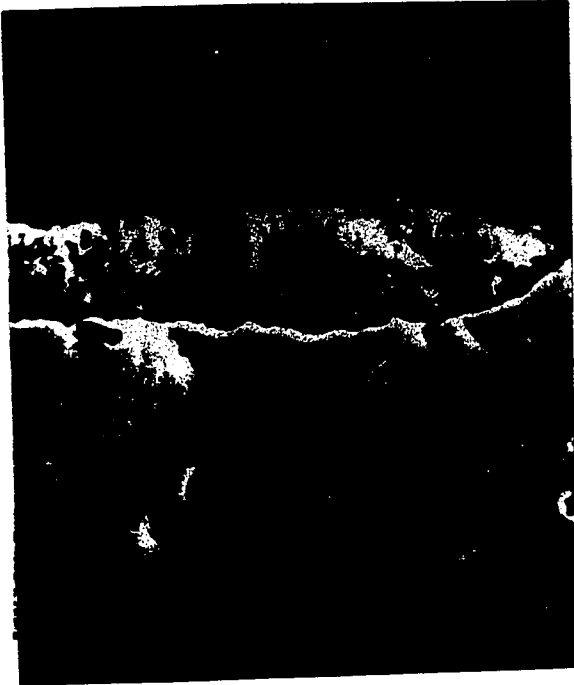
(c)



(d)

Figure 4.6.3

- |     |   |        |
|-----|---|--------|
| (a) | Surface view of a sample oxidized at 500°C for 116 hr | x 1500 |
| (b) | Surface view of a sample oxidized at 700°C for 130 hr | x 1000 |
| (c) | Surface view of a sample oxidized at 800°C for 48 hr  | x 750  |
| (d) | Surface view of a sample oxidized at 800°C for 100 hr | x 1800 |

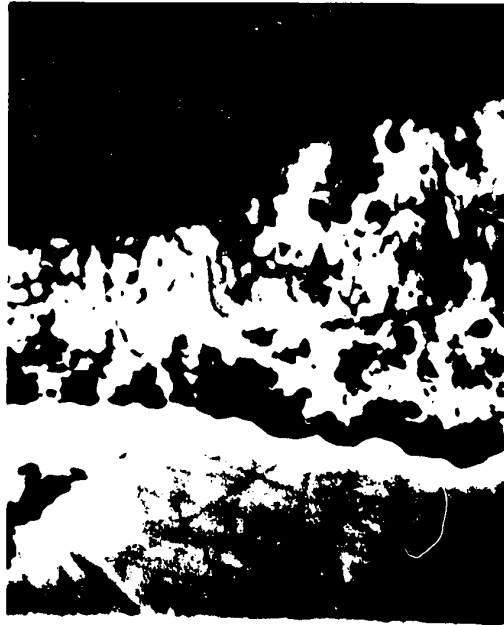


(g)

(h)

Figure 4.6.3 Cross section view

- (e) Sample oxidized at 600°C for 114 hr x 1400  
 (f) Same sample as in (e) x 4400  
 (g) Sample oxidized at 700°C for 50 hr x 1700  
 (h) Sample oxidized at 800°C for 115 hr x 1800



(g)

(h)

Figure 4.6.3 Cross section view

- (e) Sample oxidized at 600°C for 114 hr x 1400  
 (f) Same sample as in (e) x 4400  
 (g) Sample oxidized at 700°C for 50 hr x 1700  
 (h) Sample oxidized at 800°C for 115 hr x 1800

ture and exposure time. (see fig. 4.6.1(f)). The cross-sectional view at 700 °C is shown in (g). Again note the presence of two layers and the difference in grain size. At 800 °C the boundary between the two layers becomes more diffuse and a difference in grain size is less evident. This is illustrated in fig. (h). As before, the average grain size of the oxide in the outer layer and the ratios of the two layers were determined from these micrographs and the results are summarized in table 4.6.3.

TABLE 4.6.3

SEM RESULTS FOR THE (111) NICKEL FACE

Sample number	Temperature (°C)	Oxidation time (hr)	Oxide thickness	Average grain size of outer layer	Average ratio of outer/inner layers
22	800	48	6.4	1.60	2.0 ± 0.2
23	800	115	8.0	1.91	1.3 ± 0.3
26	700	50	5.0	1.23	1.4 ± 0.5
28	700	70	8.3	1.32	1.5 ± 0.3
36	600	53	5.6	0.59	1.2 ± 0.2
33	600	114	2.7	0.66	1.3 ± 0.4
37	500	116	0.7	0.47*	n.a.

\* Grain size determined from top view of sample.

In view of the previous observations made on the (100) and the (110) faces and the results obtained above the following



conclusions can be made:

(a) The oxide formed on the three single faces of nickel in the temperature and thickness ranges investigated are composed of small grains which grow during the oxidation process. The growth rate of the oxide grains on the (111) face is smaller than the (110) but slightly larger than the (100). The difference in growth rates is more noticeable at 700 and 800 °C.

(b) The cross-sections of the oxide on the (100) and (111) metal faces show a distinct two-layer structure characterized by columnar grains at the oxide/gas interface and by usually smaller equiaxed grains at the oxide/metal interface. The ratio of the thicknesses of these layers increases with exposure time but on the (100) face it seems to be independent of temperature while on the (111) face it shows an apparent small increase with temperature. The structure of the oxide formed on the (100) face is most homogeneous. It also has the highest thicknesses ratio (outer/inner) at all temperatures (except one run at 800 °C for 48 hr.) The structure of the oxide on the (110) face does not exhibit a two-layer structure and at the same time shows large difference in film structure.

#### 4.7 Oxidation kinetics. Results from a gravimetric investigation.

We have reported from our structural investigations of the oxide films that there exist significant differences in the structure and growth morphology associated with the

difference in crystallographic orientation of the three crystal faces of nickel.

Parallel to these differences, a marked anisotropy in reaction rate and oxidation behaviour of the three crystal faces have also been observed. These differences are illustrated by the graphs shown in figures 4.7.1(a)-(c). In these graphs, the weight gains of the metal faces in pure oxygen at 400 torr pressure and at the temperature of 500 , 600 , 700 and 800 °C, as recorded by a Cahn microbalance, are plotted versus time. These results were obtained by Dr. R. Herchl (\*).

The following conclusions are immediately evident upon examination of these graphs:

- a) The (100) crystal face exhibits the largest rate at all temperatures. Typical values for the weight gain are  $1.7 \frac{\text{mgO}}{\text{cm}^2}$  for the (100),  $0.5 \frac{\text{mgO}}{\text{cm}^2}$  for the (110) and  $0.8 \frac{\text{mgO}}{\text{cm}^2}$  for the (111) after an exposure of 100 hours at 700 °C. In addition the oxidation curves for this face are smooth and exhibit continuously decreasing slopes with exposure time.
- b) The (111) and (110) faces oxidized much slower than the (100) nickel face with the (110) more rapid at 500 and 600 °C. This order was reversed at 700 and 800 °C.
- c) The oxidation curves for the latter two faces show abrupt changes in reaction rate, these changes being most frequent

(\*) Post doctoral fellow of the Institute for Materials Research

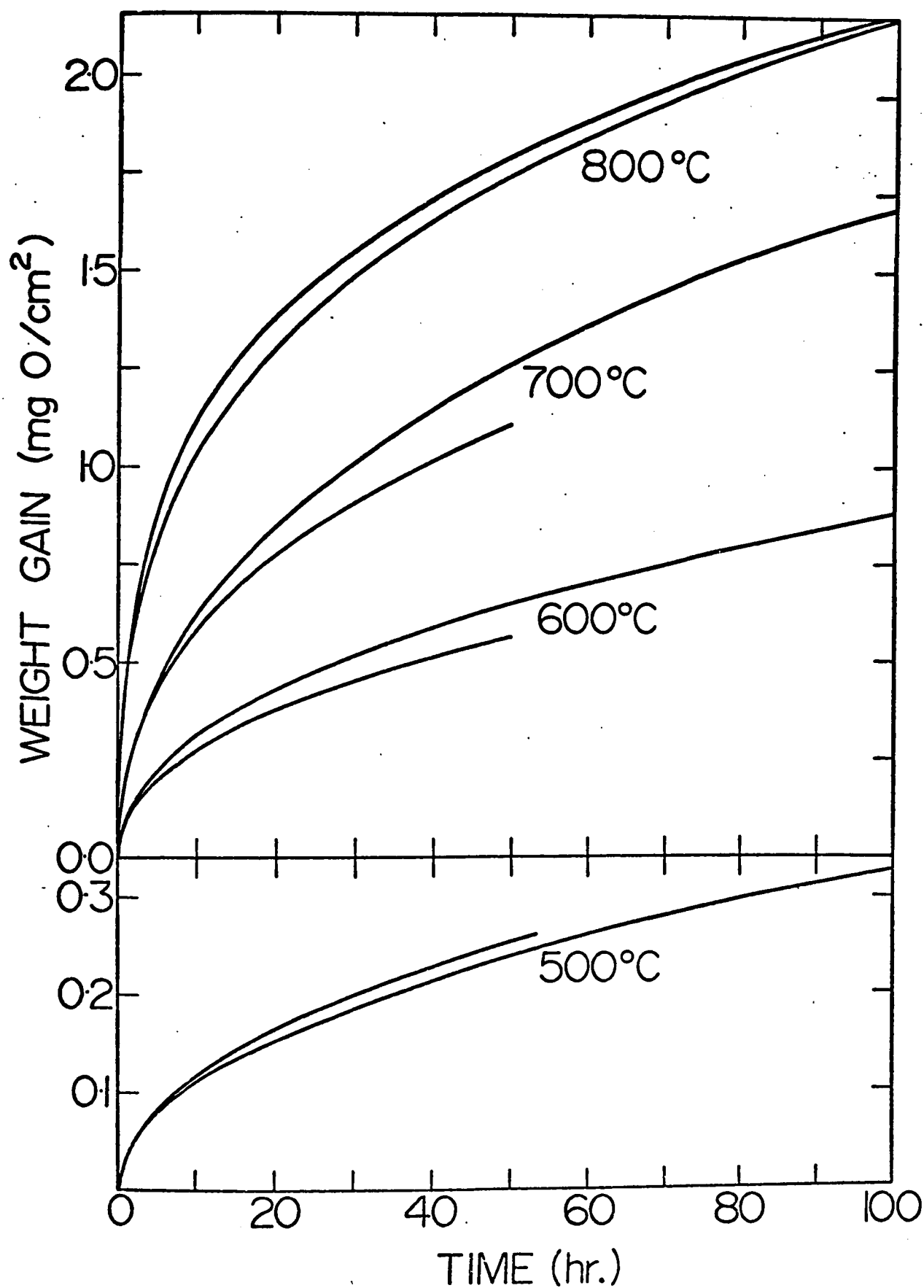


Figure 4.7.1 (a) Oxidation kinetics for the (100) nickel face

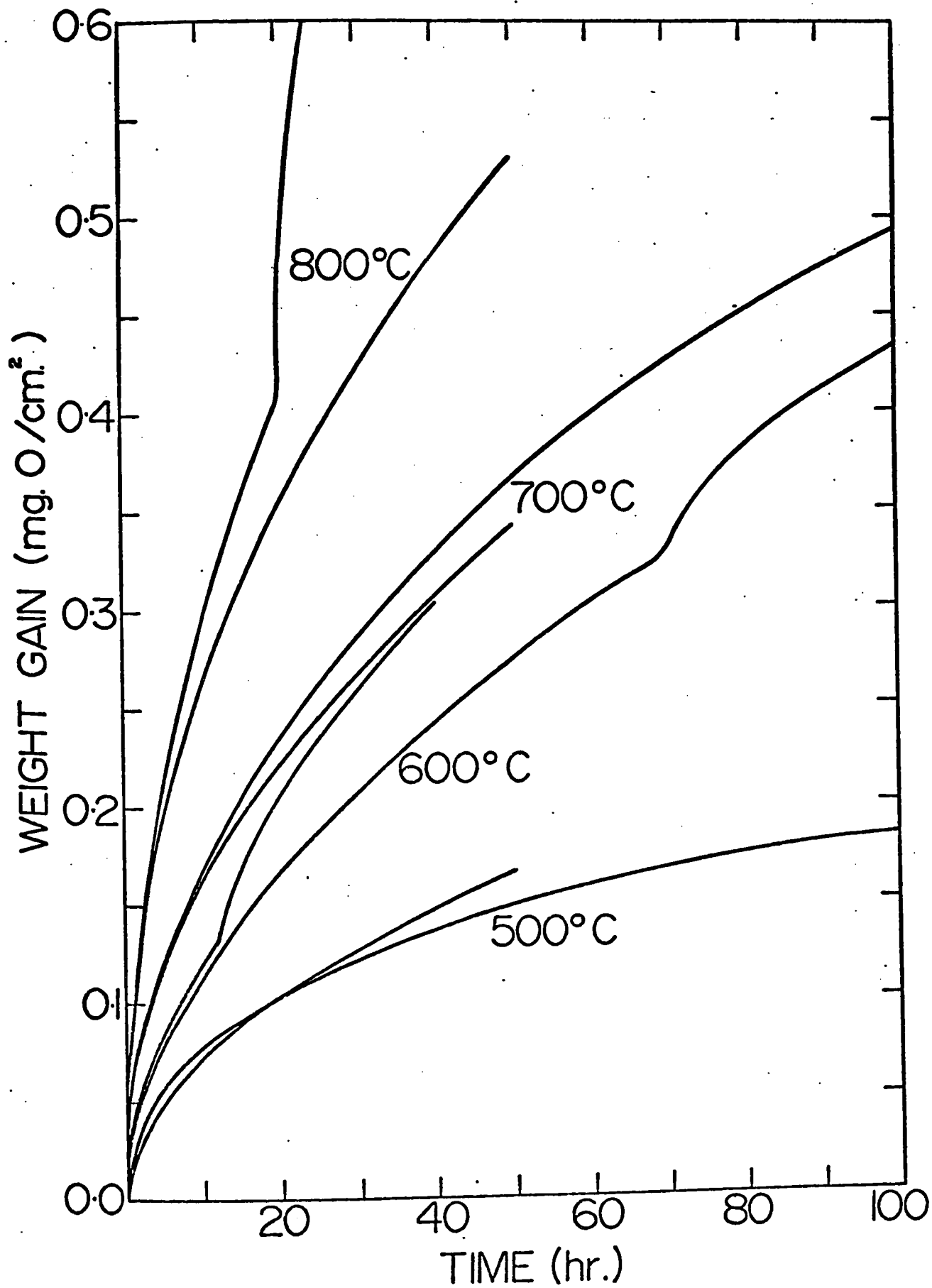


Figure 4.7.1 (b) Oxidation kinetics for the (110) nickel face

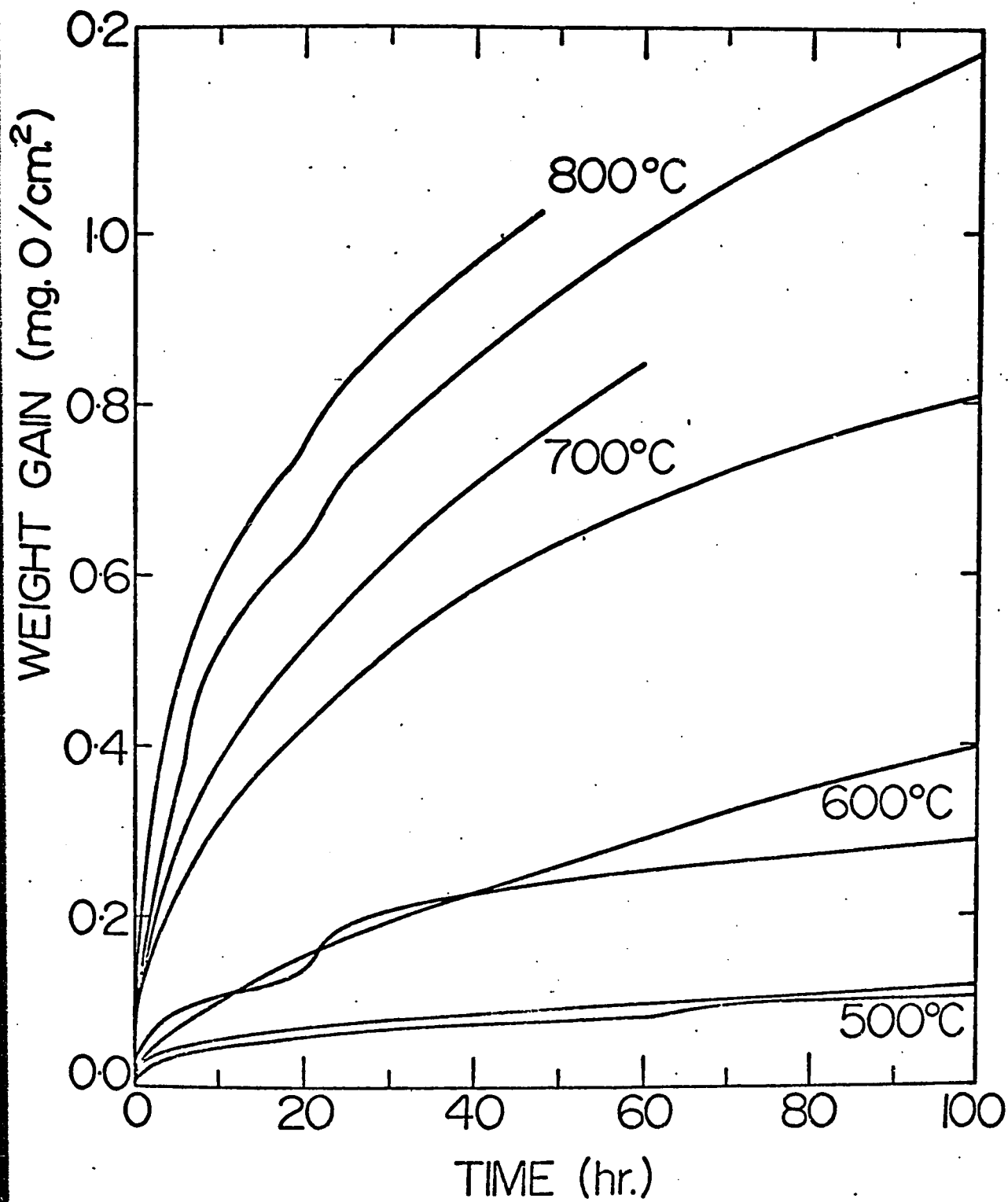


Figure 4.7.1 (c) Oxidation kinetics for the (111) nickel face

for the (110) face. Those specimens which exhibited anomalous reaction changes gave rise to oxide scales containing blisters or cracks when examined under the SEM<sup>(105)</sup>.

It would appear that besides having large differences in weight gain, these crystal faces also exhibit differences in oxidation behaviour. These differences will be discussed and correlated to the structure in the next chapter.

## CHAPTER 5

### DISCUSSIONS OF RESULTS

#### 5.1 General Considerations

In the previous chapter the structures and growth kinetics of the superficial oxide layers formed on three crystal faces of nickel at temperatures in the range from 500 to 800 °C have been presented. The results show that differences occur in the numbers and types of orientations, in oxide grain growth, in morphology of the scales and concurrently in oxidation rates of the different metal faces. In the present chapter a structural model for growth of the oxide layers based upon these observations is advanced to seek correlations between the morphological development of the oxide on the different nickel crystal faces. This model when combined with nickel diffusional properties may then be used to account for the observed kinetics of the (100) and (111) nickel faces. Using the results obtained from the structural investigations, namely the size and the growth rate constants of the oxide crystallites, the values are calculated for the boundary diffusion coefficients of nickel in the oxide films on the above two metal faces. Finally correlations between the oxide structures and the oxidation kinetics will be presented.

## 5.2 Structural considerations

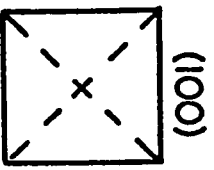
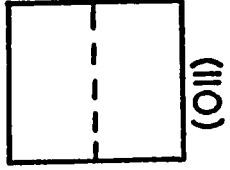
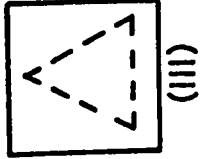
### 5.2.1 Development of the oxide structure

It has been shown that exposure of a single crystal face of nickel to oxygen results in the formation of an oxide film consisting of an aggregate of crystallites with many different orientations. The crystallites on each metal face are not however randomly distributed but exhibit definite textures which appear to be dictated by both the metal substrate and oxide growth. The orientations, moreover, are not rigidly fixed by the metal substrate but change with oxidation time. The orientations found in this investigation are summarized and illustrated in the diagram shown in figure 5.2.1.

The diagram is constructed to show the different orientations over different thicknesses of the oxide layers. The results in the thickness range 300 - 5000 Å were obtained by transmission electron microscopy; those at oxide thickness greater than 1 $\mu$  were obtained by reflection x-ray diffraction. These results are given in chapter 4, sections 2, 3 and 4. In the diagram the nickel is represented by a square and the oxide by a circle. The lines drawn across the circle or square are the close packed direction (cpd) and the number of lines represent the number of cpd present in the plane, the angle between the lines representing the angles between these directions. The family of crystallographic planes is shown in the braces (only planes which are parallel to the metal are considered). The number before a brace represents the number



MORPHOLOGICAL DEVELOPMENT OF THE STRUCTURE

NICKEL	OXIDE		X-RAY Thickness (1-14 μ)
	RESULTS FROM T.E.M.	Thickness (300 - 5000 Å)	
 <p>(001)</p>	<p>6 {233}</p> <p>6 {211}</p> <p>1 {011}</p> <p>{100}*</p> <p>2 {111}</p>	<p>{211}</p> <p>{011}</p> <p>{100}* polycrystalline</p> <p>{100}* polycrystalline</p>	<p>{100}*</p> <p>{110}*</p>
 <p>(011)</p>	<p>{433} {310}</p> <p>{411} {211}</p> <p>{322} {011} + Twin</p> <p>{100}</p> <p>{111}</p> <p>others {310} {123}</p>	<p>{433} {310}</p> <p>{411} {211}</p> <p>{322} {011} + Twin</p> <p>{100}</p> <p>{111} (A)</p>	<p>{211}</p> <p>{011}</p> <p>{100}</p> <p>{111}</p> <p>{100}*</p>
 <p>(111)</p>	<p>3 {233} (A) + 3 {233} (B)</p> <p>3 {211} (A) + 3 {211} (B)</p> <p>{011}*</p> <p>{111} (A)</p> <p>{111} (B)</p> <p>others 310</p>	<p>3 {233} (A)</p> <p>3 {211} (A)</p> <p>{011}</p> <p>{111} (A)</p> <p>{111} (B)</p>	<p>{211}</p> <p>{011}</p> <p>{111}*</p> <p>{111}*</p> <p>{100}*</p> <p>polycrystalline</p>

(x) major orientation  
 Figure 5.2.1 Schematic diagram showing the morphological development of the oxide structures.

of equivalent orientations in cases where there are more than one orientation; for example 3 {211} means there are three equivalent {211} planes. \*

The (100) nickel face. This metal face is characterized by two cpd  $90^\circ$  apart. A total of five different oxide orientations have been observed in the film approximately 300 Å thick. All these orientations contain a close packed direction which has been shown by a large amount of evidence for different substrate-film systems in the literature to be parallel to the cpd in the metal. The (211) and (233) orientations have been found to occur in multiple of six (figure 4.2.1(g)). These multiple orientations deserve to be mentioned since they have been previously reported<sup>(64)</sup>. Among the six orientations, two of them can have their cpd parallel to the two cpds in the metal, the remaining four have their cpd at  $\pm 30^\circ$  from the  $\langle 110 \rangle$  directions in the metal. These four types of arrangements are thus not compatible with the symmetry of the (100) face and comments about these orientations are given in appendix B(3). The (111) orientation has been observed to occur in a multiple of two. These two orientations are however equivalent and simply arise by matching one of its cpd to the two cpds in the metal. These types of orientations and all others have been reported in the literature.

Changes in orientations are observed with increasing exposure to oxygen. The most noticeable change was the disappearance of the multiple orientations of the (233) and

\* see Appendix B(3)

(211) planes, but the single (211) and other low index planes continue to be observed. With further increase in exposure only the (100) and to a much lesser extent the (111) planes and polycrystalline rings are found. This latter type of pattern is consistently observed over the whole exposure range from 40 min to 6 hr, which indicates a rather uniform film structure. Thus the changes in orientation of the oxide crystallites appear to occur within films less than 1000 Å thick. Results from X-ray diffraction of the thick films in the micron range (1-14μ) show a very strong preferred orientation on the (100) or (111) planes (Table 4.5.1). These orientations are parallel to the metal substrate and are the same major orientations present in the thin film. It would appear that these orientations are simply extending from the already existing major orientations of the oxide crystallites in the thin film and as a result, a strong preferred orientation, characterized by a high texture coefficient has been observed in the scale. The microstructure of a scale when seen in cross-section in the SEM shows the presence of two oxide layers. The outer layer consisted of columnar grains and the inner layer of equiaxed grains (Fig. 4.6.1). With increasing exposure and temperature the interface between the layers became more diffuse.

There are several features particular to the oxide formed on the (100) nickel face. Only five orientations of the oxide were observed with the (100) as the most dominant orientation in the thin films and the (100) and (111) in the

thick films. An oxide scale was composed of two layers. The thickness ratio of the outer columnar to the inner equi-axed layer was the highest with respect to the layers formed on the three metal faces. A strong preferred orientation was also present. The combined (100) and (111) texture coefficients accounted for more than 80% of all the orientations observed.

The (110) nickel face This face is characterized by the presence of only one cpd and a total of eleven different oxide orientations have been found. Among the eleven orientations, the (210), (310) and (123) are minor since they were seldomly observed. The remaining eight were frequently found and all contain at least one cpd which has been confirmed by many investigations to be parallel to the cpd in the metal. The large number of orientations also include the presence of high index planes such as the (433), (411), (322) and (311). Among these high index planes only the (411) has been previously found<sup>(55)</sup>. Thus three new orientations have been identified. Cathcart<sup>(8)</sup> has reported by X-ray diffraction studies that the oxide formed on this face in the same temperature and pressure range to be polycrystalline. Since the X-ray technique is not very sensitive to minor orientations, the authors could only conclude from the large number of observed reflections that the oxide is polycrystalline. Pu and co-workers<sup>(60)</sup> have also reported the "110 fibring" type structure for the oxide formed on this face. The authors have probably referred this type of structure to the series of planes including the

very high index planes which all share a common  $\langle 110 \rangle$  direction (Fig. 4.3.1(b)) since they did not specifically attempt to identify all planes present. It would appear from the above observations that the three new orientations reported in this investigation were probably observed by other workers but they have not been reported in the literature.

With increase in exposure, changes in orientations are observed but these changes are gradual. The reflections from the high index planes gradually disappear in the polycrystalline background and only the low index planes continue to be observed. There is, however, no preference for a unique orientation like for the (100) metal face since up to four orientations were still present even after 4-5 hr of exposure. The (100) preferred orientation as shown by the X-ray diffraction studies only dominates in the scales 1-10 $\mu$  thick. This orientation, moreover, was not a major orientation in the thin film as evidenced by the low frequency of its appearance. It would thus appear that the (100) is a preferred plane which develops during the growth of the oxide. This preferred orientation is not very strong but it appears to increase with oxide thickness. The (100) preferred orientation has also been observed in the oxidation of polycrystalline nickel after long exposure to oxygen<sup>(39)</sup>.

The microstructure of the oxide scales when viewed in cross-section did not exhibit the presence of equiaxed and columnar oxide layers (Fig. 4.6.2). In addition, the oxide

crystallites showed a broad distribution of size across the scale. It would thus appear that the absence of a two-layer structure and the lack of a strong preferred orientation may be related. It is not suggested, however, that a columnar layer of oxide could not develop on this metal face at longer time since the preferred orientation was increasing gradually with the scale thickness.

The other features particular to this face which deserve to be mentioned are the presence of oxide twins (Fig. 4.3.1(f)) and regions of the oxide where a (100) single crystal pattern is observed (Fig. 4.3.2(g)). For all cases where twins could be positively identified, twinning always occurred in the parallel orientation,  $(110) \text{ NiO} \parallel (110) \text{ Ni}$ , and on the (111) plane. The indexing of the twins indicated that the twin boundary is perpendicular to the surface. The mechanism for the formation of these twins is not known but these types of twins have been frequently observed in many vapor deposited systems<sup>(106,107,108)</sup> and probably arise during the coalescence of the nuclei. The presence of the (100) single crystal pattern in a rather "polycrystalline" film is rather surprising; however, results from LEED studies<sup>(50)</sup> have shown that this orientation was favoured on the (110) nickel face, under certain favourable conditions.

It would thus appear that the characteristic features of the oxide formed on the (110) nickel face are the occurrence of

a large number of orientations, a slow change in the structure resulting in a small degree of preferred orientation along with the lack of evidence for formation of a columnar outer layer in the scale.

The (111) nickel face. This metal face is characterized by three cpd  $60^\circ$  apart. The total number of different oxide orientations observed was five. In the thin films approximately 500 Å thick, multiple orientations were present. The (211) and (233) planes contain only one cpd and up to six equivalent orientations have been identified. Three of these orientations have their cpd  $60^\circ$  apart and they thus satisfy the condition for parallelism of cpd with the (111) metal face (type A). The remaining three orientations would possibly lie with their cpd parallel to the  $\langle 112 \rangle$  directions on the metal (Type B). Diffraction results of nickel oxide while still on the metal substrate indeed prove this to be correct<sup>(64)</sup>. The (111) oxide orientation has three cpd and only two orientations have been found. These two types of oxide arrangements can be simply explained in a manner similar to the above orientations. These latter oxide orientations have also been reported in the literature<sup>(64)</sup>.

With a slight increase in exposure time (10-15 min.) some rearrangement in the oxide did occur since the diffraction patterns then showed the presence of only  $3\{211\}$ ,  $3\{233\}$  and  $1\{111\}$  (Fig. 4.4.7(b)). It is not possible to know upon examining a film removed from the metal substrate which type of

orientation has disappeared; however, one can safely assume that the oxide having one of the cpd parallel to the  $\langle 112 \rangle$  direction in the metal (Type B) does not satisfy the close packed rule (CP-rule). Consequently, it is not stable and gradually disappears.

With increasing exposure to oxygen, the (111) orientation becomes most dominant and the reflections from the (233) plane become weak. The (211) and (011) continue to be observed for some time. Finally, after long exposures from 4-6 hr, considerable polycrystallinity is found. This polycrystallinity, which is observed on every section of the film (Fig. 4.4.5(b)) indicates that the structure is rather uniform. Some preferred orientation is however present as evidenced by the arcs on the 3rd (220) ring (Fig. 4.4.5(c)). The appearance of more than six arcs on the (220) ring indicates that the oxide can have more than one type of preferred orientation. There are possibilities for two types of (111) preferred orientation or other planes containing the 220 reciprocal lattice points. The rare occurrence of the arcs on the (111) and (200) rings, however, permits one to only conclude that some preferred orientation occurs on the (111) plane. This assumption is confirmed by the results from X-ray diffraction (Fig. 4.5.3). The large degree of polycrystallinity in the film over this thickness range has also been reported by other investigators<sup>(64)</sup>.

X-ray studies of the oxide scales in the micron thickness range show the development of a strong (111) preferred orien-



tation. The degree of preferred orientation increases with oxide thickness as indicated by the texture coefficient (Fig. 4.5.3) and it is higher than that for the oxide on the (110) metal face but lower than that for the (100) face. The microstructure of a scale when seen in cross-section also shows the presence of equi-axed and columnar oxide layers (Fig. 4.6.3). The thickness ratios (outer/inner) of these two layers are in general smaller than those for the (100) face. (Compare Tables 4.6.3 to 4.6.1) No twins have been identified, but as for the oxide on the (110) face, the presence of dislocations are sometimes observed.

The structural development of the oxide on the metal face is thus very similar to that for the (100) face. The major orientation in the thin film range corresponds to the preferred orientation in thick scales. Both scales exhibit relatively high texture coefficients and the presence of equi-axed and columnar layers.

#### 5.2.2 Morphological development of the oxide layers.

It has been shown in the previous section that the oxide undergoes structural changes during the oxidation process and that the most rapid changes seem to occur when the films are less than 3000 Å thick. These structural rearrangements of the crystallites are also accompanied by crystallite growth. The behaviour and magnitude of the growth during the first few hours of oxidation are illustrated in figures 4.2.8(b), 4.3.7(b) and 4.4.7(b). The graphs show that the average size of the

crystallites on the three metal faces remains constant during an induction period for 30-40 min. The size of the crystallites in the induction periods,  $D_0$ , is about 300-400 Å and it does not differ much from one metal face to another. These observations are in agreement with the results of Cathcart<sup>(8)</sup> who has found that the oxide films formed on the same single crystal faces over the same temperature and pressure range, also exhibit crystallites ranging from 200-500 Å in size independent of substrate orientation and film thickness. This induction period was also observed by Perrow and co-workers<sup>(7)</sup> in the oxidation of polycrystalline nickel.

The growth kinetics of the crystallites on the three metal faces as indicated by the above graphs are however different. These differences are reflected in the changes of the distribution curves with exposure time (Fig. 4.2.8(a), 4.3.7(a) and 4.4.7(a)). The (100) face shows a grain distribution which changes relatively little with exposure time (Fig. 4.2.8(a)). This behaviour reflects a normal growth process<sup>(109)</sup> which is probably due to the dominance of the (100) oriented crystallites in the films less than 5000 Å thick. The oxide on the (111) face, which was also of high preferred orientation, shows some changes in the distribution curves. The largest changes, however, were found on the (110) face (compare figures 4.3.7(a) and 4.4.7(a)). This latter face exhibits the largest number of oxide orientations.

The average crystallite sizes of the oxide on the three metal faces are approximately the same after 5-6 hr of exposure. The size range is 700-800 Å and any difference is within the range of experimental errors. The results from SEM studies, nevertheless, show that large differences in oxide grain size exist after 50-100 hr of exposure, (compare Tables 4.6.1, 4.6.2 and 4.6.3). The oxide on the (100) nickel face has the smallest rate of grain growth along with a highly columnar structure and the highest preferred orientation. All these findings are consistent with the general observations on solids that a strong preferred orientation is usually observed in materials exhibiting columnar structure and that this preferred orientation impedes grain growth<sup>(109,110)</sup>. The oxide on the (110) metal face exhibits the largest grain growth rate and also the lowest preferred orientation. The oxide on the (111) face shows a larger rate of grain growth and lesser preferred orientation than that for the oxide on the (100) metal face. It would appear that the oxide on the (111) and (110) metal faces undergoes considerable structural alteration which is reflected by the larger grain growth rates and frequent appearance of dislocations. The growth behaviour of the crystallites, as represented by the figures 4.2.8(b), 4.3.7(b) and 4.4.7(b), are similar in form to those obtained for recrystallization and grain growth in solids<sup>(111)</sup>. It will be established in the section on oxidation kinetics (section

5.3) that these general features are compatible with theory for grain growth and a proposed diffusion model. Good agreement is found between the values for the growth rates determined from structural investigations and those predicted from the analysis of the oxidation kinetics.

### 5.2.3 Oxide growth model

The morphological development of the oxide structure in the thickness range from  $300\text{\AA}$  to  $14\mu$  has been discussed in detail in the previous section. In order to present an oxide growth model from the early stage of oxygen adsorption to the growth of the scales, reference will be made to the literature extensively reviewed in chapter 2. However before discussing the model, it is important to consider the effect of sample preparation on the structure of the oxide.

Although it has been long realized that the oxidation behaviour of a metal depends upon the physical nature of its initial surface <sup>(112)</sup>, the results from this investigation yield several new findings on metal surface structure. The observations reported in section 4.1 have shown that the superficial structure of a metal single crystal can be profoundly altered by surface preparation. Mechanical abrasion leads to a surface exhibiting a polycrystalline structure (Fig. 4.1.2) which extends at least  $5-10\mu$  into the underlying metal. Electropolishing produced a smooth surface which is however covered with a residual oxide film

consisting of oriented crystallites (Fig. 4.1.4). Annealing by either a conventional anneal at  $10^{-6}$  torr or a high vacuum anneal at  $10^{-10}$  torr produced a nickel surface having identical crystallographic structures (Fig. 4.1.5). Presumably the oxide film was destroyed by dissolution of oxygen into the metal.

Nickel oxide exhibits the same structure when formed on a metal face which has been subjected to either of the two types of vacuum anneals and then exposed to oxygen at pressures in the range from  $10^{-5}$  to 400 torr at 500°C. The oxide at the early stage of oxidation was found to be polycrystalline with the crystallites randomly distributed over the surface. This finding was consistent with the results of Garmon<sup>(64)</sup> who oxidized nickel faces at the same pressure and over the same temperature range. The polycrystalline nature of the oxide film was not observed when the nickel surface was exposed to very low pressure of oxygen and for a very short time ( $10^{-9}$  torr-sec to  $10^{-5}$  torr-min). The results from LEED studies given in section 2.3.1 indicated that the intermediate "O-Ni" structures are observed which then lead to the formation of an oxide exhibiting single crystal properties. The observations from LEED and our observations are all consistent with the theory of Kenty and Hirth<sup>(33)</sup> who have applied classical heterogeneous nucleation theory to the development of epitaxy.

The basic tenets of the theory can be simply stated as follows. Atoms from a gas phase which is supersaturated

with respect to the bulk solid phase, strike the surface and either immediately rebound or are adsorbed and become thermally equilibrated with the substrate. The adsorbed atoms (adatoms) through statistical fluctuations in concentration, form small clusters which grow and decay by the addition or loss of single atoms. The formation of a cluster is energetically favorable when a critical size is reached and at which time further growth is assumed to be favored and rapid.

The driving force for the nucleation process is the volume free energy change for the transformation from adatoms to the bulk solid phase,  $\Delta G_v$ , given by the expression:

$$\Delta G_v = -\frac{kT}{v} \ln \frac{N_1}{N_{1e}} \quad (5-1)$$

where  $v$  is the atomic volume,  $N_1$  is the actual adatom concentration and  $N_{1e}$  is the equilibrium concentration with the bulk solid phase. In the usual experimental case the adatoms are in equilibrium with the gas phase, and the volume free energy change is

$$\Delta G_v = -\frac{kT}{v} \ln \frac{J_{\text{imp}} \sqrt{2\pi mkT}}{P_0} \quad (5-2)$$

where  $J_{\text{imp}}$  is the impingement flux of atoms from the beam striking the substrate (atoms/cm<sup>2</sup>sec), and  $P_0$  is the equilibrium vapor pressure of the bulk solid phase at the

substrate temperature  $T$ . For a typical spherical cap-shaped nuclei, the activation free energy for nucleation when the cluster reaches a critical size,  $R^*$ , is given by the expression:

$$\Delta G^* = \frac{16\pi\gamma^3 f(\theta)}{3\Delta G_v^2} \quad (5-3)$$

where  $\gamma$  is the surface energy of the condensing phase,  $f(\theta) = \frac{1}{4}(2 - 3 \cos \theta + \cos^3 \theta)$  and  $\theta$  is the equilibrium contact angle. The radius of the critical size nucleus,

$$R^* = \frac{-2\gamma}{\Delta G_v} \quad (5-4)$$

is independent of the contact angle. At the steady state, the nucleation rate  $J \frac{\text{nuclei}}{\text{cm}^2 \text{sec}}$  can be regarded as the product of the concentration of critical sized nuclei<sup>(113)</sup> and the frequency with which adatoms join the critical nuclei. The expression for the nucleation rate can be written as:

$$J = \frac{4\pi\gamma a N_o J_{\text{imp}}}{-\Delta G_v} \left( \frac{\Delta G^*}{3\pi k T i^{*2}} \right)^{\frac{1}{2}} \exp \left( \frac{\Delta G_{\text{des}} - \Delta G_{\text{sd}} - \Delta G^*}{kT} \right) \quad (5-5)$$

In this expression,  $a$  is the adatom jump distance,  $N_o$  is the number of nucleation sites on the surface,  $\Delta G_{\text{des}}$  and  $\Delta G_{\text{sd}}$  are the activation free energies for desorption and surface diffusion, and  $i^*$  is the number of atoms contained in the nuclei.

It is assumed that the nuclei on the surface are composed of only two types, "epitaxial" and "random" which are

identical in every aspect except for the difference in the magnitude of the interfacial free energy between the substrate and the epitaxial nuclei,  $\gamma_e$ , the interfacial free energy between the substrate and the random nuclei,  $\gamma_r$ , and the interfacial free energy between the substrate and the random nuclei,  $\gamma_r$ . The authors were then able to deduce the following expression:

$$\frac{J_e}{J_r} = \frac{\sin\theta_e}{\sin\theta_r} \left( \frac{f(\theta_r)}{f(\theta_e)} \right)^{\frac{1}{2}} \exp \left( \frac{\Delta G_r^* - \Delta G_e^*}{kT} \right) \quad (5-6)$$

The term  $\left[ \frac{f(\theta_r)}{f(\theta_e)} \right]^{\frac{1}{2}}$  originates from the weak dependence of the Zeldovitch factor <sup>(114)</sup> on the contact angle  $\theta$ , which is different for epitaxial and random nuclei ( $\gamma_e < \gamma_r$ ,  $\theta_e < \theta_r$ ).

By assigning arbitrary values for  $\gamma_e$  and  $\gamma_r$ , several qualitative aspects of epitaxy can be deduced and verified from the heterogeneous nucleation rate equation. At high temperature or low impingement flux, the supersaturation or  $\Delta G_v$  is small and from equation (5-3),  $\Delta G^*$  is large and the nucleation rate is correspondingly low. Thus epitaxy is favored. Also from relation (5-4), the nuclei are larger and thus fewer grain boundaries are formed. Conversely a large supersaturation will produce a greater number of smaller nuclei, thus favoring random nucleation.

Since the oxidation pressure ranges from  $10^{-5}$  to 400 torr, the metal is subjected to the experimental pressure  $10^{15}$  to  $10^{22}$  larger than the dissociation pressure of nickel



oxide (its value is  $2 \times 10^{-23}$  atm. at  $500^\circ\text{C}$ ). Such a large supersaturation, equations (5-1,4,6), could be expected to produce a large number of small oxide nuclei randomly distributed over the surface without any specific epitaxial relations<sup>(91,64)</sup>. After this oxidation stage, in which the metal surface would become covered with randomly oriented crystallites, considerable and rapid rearrangement could occur leading to the development of the oriented films. These considerations are consistent with the observations and the results from this investigation.

It has been shown that the oxidation of a nickel crystal face leads to the formation of an oxide film containing crystallites or grains with many different orientations. The majority of these orientations, hence the most frequently observed are usually low index planes which contain at least one cpd. The results available in the literature confirm that these cpd would lie parallel to the cpd in the metal. The "omni-presence" of this "CP-rule" or "CP-mechanism" leads to a logical question: to what extent do the number of cpd in the metal influence the type and number of oxide orientations?

Let us consider the different nickel crystal faces. The (100) and (111) faces possess two and three cpd respectively and only five oxide orientations, all of them low index planes, have been found. The most dominant and the most frequently observed was the parallel orientation. The (110) face has only one cpd and up to eleven different oxide orientations have been observed. Moreover, there are at least

four preferred planes in the thin film and the final (100) orientation only becomes observable in the scaling range. It would appear that the presence of more than one cpd in the metal substrate defines a rather rigid condition for the oxide to satisfy. This condition appears to lead to a small number of orientations and the dominance of the parallel orientation. This parallel arrangement would be energetically the most favorable since it minimizes the interfacial energy whilst it maximizes the coincidence of the cpd. This seems to be the case for the oxide on the (100) and (111) metal faces.

The presence of only one cpd of the (110) nickel face would then define a less rigid condition and the oxide has more freedom to grow. This would result in a large number of oxide orientations including the presence of the high index planes such as the (433) and the (411). These planes, however, must satisfy the less stringent condition of possessing only one cpd parallel to the cpd in the metal. This could possibly account for the relatively slow structural change in the oxide on the (110) face. There is no preference for an unique type of orientation and as a consequence, four low index planes, the (011) (001) (111) and (211) continue to be observed for long exposures. The (100) orientation only becomes noticeable when the oxide thickness reaches the micron range. The emergence of the (100) orientation in the thick scale is probably due to the growth process, since it is not

a major orientation in the thin film and it is also observed in the oxidation of polycrystalline nickel. Finally, it is possible that twinning in the oxide which is frequently observed on this face may be probably due to the less rigid condition defined by the presence of only one cpd in the metal.

It would appear from the above observations and the results from the literature that the superficial oxide layers develop as follows. Oxygen is initially adsorbed and enters into solution in the metal. Adsorption leads to two-dimensional nickel-oxygen ordered structures. At a sufficiently high concentration of oxygen, oxide is precipitated as discrete nuclei<sup>(64,36)</sup>. These nuclei, at first, are randomly distributed on the metal substrate as a consequence of the high supersaturation of oxygen in the gas phase for initiation of nucleation. The diffraction patterns at this stage therefore show complete polycrystalline rings<sup>(91)</sup>.

Rapid rearrangement along certain crystallographic direction at the metal/oxide interface could then occur as nickel diffuses outward through the oxide film but it is not however complete. The diffraction patterns accordingly yield multiple orientations and orientations which do not satisfy the "CP-rule". With increase in exposure, multiple orientations and orientations which do not satisfy the "CP-rule" disappear along with the high index planes. Finally the low index planes which have at least a cpd parallel to the cpd in the metal are

preferred and probably exist as stable orientations. At this stage the preference for a specific orientation would depend on the number of cpd in the metal. If the metal contains more than one cpd, the most stable oxide orientation would be the one which maximizes the coincidence of the cpd. This is shown to be the case of the (100) and the (111) metal faces where the parallel orientation was frequently observed. The importance of the "CP-mechanism" is not however limited only to the Ni-NiO system. In an extensive review of 3000 papers yielding 600 orientation relationships in thin-film-substrate combinations, Gerdes and Young<sup>(13)</sup> have found that 86% of these relationships can be accounted for by the "CP-mechanism" alone. This rule, however, remains as an empirical correlation of epitaxial conditions.

The influence of the metal substrate would be expected to decrease with the thickness of the oxide. Crystallites which are formed when the film thicknesses reach a few thousand Angstroms would not be strongly influenced by the substrate. They are probably randomly distributed and thus contribute to the polycrystalline rings in the diffraction patterns which are frequently observed at this thickness range. At this stage one would expect a growth mechanism to dominate and a strong preferred orientation is expected if the major orientations present in the thin films are also the preferred growth planes. This type of behaviour would then describe the growth pattern of the oxides on the (100) and (111) metal faces. The (110)

nickel does not exhibit a strong preference for a particular type of oxide orientation in the thin film range but shows a (100) preferred orientation after long exposure. It would then appear from our results that both the (100) and (111) planes can be the preferred growth planes in the Ni-NiO system. These planes could be imagined as growing preferentially parallel to the metal surface as adsorbed oxygen is incorporated into the nickel oxide layer at its outer surface by the outward flux of nickel ions.

The studies of the microstructure of the scales of the oxides formed on the (100) and (111) faces where a relatively strong preferred orientation has been observed, consistently show the presence of two distinct layers. This observation which is more than coincidental would thus lead to the conclusion that a strong preferred orientation is perhaps responsible for the formation of the duplex scale. These observations provide additional complexities to an already controversial and unsettled argument now prevailing in the literature about the origin of these oxide layers. The interface between the layers has been attributed to the position of the original metal surface, to the inward diffusion of oxygen in the lattice and grain boundaries and also to the effects of impurities and plasticity in the oxide. It would be difficult to justify these contentions since the observations in this investigation show that the oxide formed on the (110) face of nickel which contains the same amount

of impurities and is subjected to the same oxidation conditions as the other nickel faces failed to exhibit the two-layer structure. However, the association of the lack of a two-layer structure with the absence of a strong oxide preferred orientation may be perhaps incomplete. This rather limited observation coupled with the insufficient and often controversial results available in the literature would make the proposal of a single mechanism to explain the origin of this layered structure too presumptuous. The argument of Birks and Rickert<sup>(46)</sup> concerning the oxide plasticity and the possibility of dissociation of the oxide at the metal/oxide interface may play a role in the growth of the inner layer and the good adherence of the oxide scale to the continuously receding metal interface.

#### 5.2.4 Concluding remarks concerning the oxide structure.

The structure of the oxides formed on three crystal faces of nickel has been shown to be different in the number and types of orientation, in scale morphology and degree of preferred orientation. These differences are believed due to the crystallographic orientations of the metal substrate and to the growth mechanism for oxide. The oxide has been found to undergo structural changes during the oxidation process and a trend common to the development of the oxide on the different nickel crystal faces has been established. These structural changes have also been observed in many thin-film-substrate systems<sup>(115,116)</sup>. The (100) nickel face shows the most

consistent behaviour characterized by an uniform oxide film structure followed by the (111) face. The oxide on the (110) nickel face, besides having a low preferred orientation, exhibits large differences in structure. The common preferred growth plane in the oxide scales is in all cases, a low index face, the (100) or (111) face lying parallel to the surface of the nickel substrate.

The dominance of these low index planes which also contain the largest number of cpd would perhaps favor an oxide over-growth model in which the metal substrate would play little or no role in determining the final oxide orientation. The proposed mechanism, however, remains speculative since no direct observations have been made.

As it has been previously argued that due to the high supersaturation of the experimented oxygen pressure, the oxide film in the early stages of oxidation is composed of crystallites with many different orientations. These crystallites are probably highly mobile but exhibit little growth, since the size of the crystallites is in the same order of magnitude as the film thickness. This observation is substantiated by the fact that the incubation period which has been observed in both polycrystalline and single crystals of nickel, seems to be independent of the substrate orientation. Rearrangement of the oxide crystallites can occur during the growth of the film but the final orientation of the oxide grains will be determined by the crystallographic planes which contain the largest number of cpd. This is highly probable since in a NaCl structure these  $\langle 110 \rangle$  directions can contain only

nickel or oxygen atoms. The nickel atoms which diffuse out can thus align themselves along these cpd and this mechanism is perhaps responsible for the dominance of the two types of planes in the final stage of oxide growth. In addition it should be mentioned that both the (100) and (111) planes are also the most densely packed planes in a NaCl structure.

### 5.3 Oxidation kinetics

#### 5.3.1 Consideration of diffusion model

The oxidation curves given in fig. 4.7.1(a)-(c) when plotted according to the parabolic equation:

$$x^2 = K_p t + C \quad (5-7)$$

where  $x$  is the film thickness,  $K_p$  is the parabolic rate constant,  $t$  is the time and  $C$  is a parameter dependent upon the scale thickness show that parabolic behaviour is not obeyed. Accordingly, Wagner's mechanism based solely on lattice diffusion of a reactant is not satisfied. This deviation from parabolic behaviour has also been observed by other workers studying the oxidation kinetics of polycrystalline nickel at temperatures less than half of the melting point of the oxide ( $\approx 1000^\circ\text{C}$ ). The non-parabolic behaviour has led many investigators to suggest alternate mechanisms and rate laws. Thus Uhlig<sup>(77)</sup> proposed a 2-stage logarithmic; Engell and Hauffe<sup>(79)</sup> have derived the logarithmic, cubic and fourth power laws. The main drawbacks of these relationships is their limited range of applicability (for example, the 4th



power law is valid only in the thickness range from 300-600Å), and their lack of consideration to the oxide structure and mechanism for reactant transport.

We have seen from the kinetics that deviations from parabolic behaviour are extended over 100 hr of exposure even at the highest temperature investigated of 800°C. In addition, our structural investigations have shown that the oxide films are composed of small crystallites ranging from a minimum of 200-300 Å in size at 500°C to a maximum value of 2-3μ at 800°C. These observations coupled with those made by Cathcart<sup>(8)</sup> who has established a definite relationship between reaction rates and density and type of defects, define a need for a mechanism in which various types of structural defects will play a role in the transport of reactant in the growing oxide scales. Furthermore, an attempt to fit our data with the above proposed rate laws failed to give satisfactory answers.

These considerations would then lend credence to a modified parabolic equation which would take into account the presence of the defects in the film and also account for the changing rate with increasing exposure time. The proposed model thus consists of defining an effective diffusion coefficient in which both lattice diffusion and diffusion via paths of low resistance offered by these structural defects will contribute to nickel transport across the

oxide layer. The diffusion coefficient based on the random walk analysis, has been derived by Hart<sup>(117)</sup> and can be written as:

$$D_{\text{eff}} = D_1(1-f) + D_B f \quad (5-8)$$

where  $D_1$  and  $D_B$  are the diffusion coefficients in the lattice and in the line defect,  $f$  is the fraction of sites lying in the low resistance paths. The condition for the Hart's relation to hold is  $2(D_1 t)^{1/2} > l_d$ , where  $l_d$  is the spacing of line defects such as boundaries or dislocations. Perrow<sup>(13)</sup> has shown that this condition is satisfied for the case of oxidation of polycrystalline nickel at intermediate temperatures. The factor  $f$  is a time dependent function and can adopt a purely phenomenological form based upon the structural properties of the oxide.

The following forms of  $f$  have been successfully used to interpret the oxidation kinetics of some metal oxide systems. The first functional form of  $f$  is a first order rate expression:

$$f(t) = f_0 e^{-\alpha t} \quad (5-9)$$

where  $f$  and  $\alpha$  are two constants empirically determined to fit the data. This model has been successfully applied by Smeltzer and Kirkaldy<sup>(118)</sup> to the formation of oxide films on Zr, Hf and Ti. The second form of  $f$ , usually applied to a polycrystalline aggregate can be expressed as:

$$f(t) = \frac{2d}{D t} \quad (5-10)$$

where  $D_t$  is the diameter of the grain at the time  $t$ , and  $d$  is the width of the grain boundary. Clearly both forms of  $f$  are decreasing functions of time. The mathematical analysis given in the following section will test both site models. The results indicate that most of the oxidation data can be fitted to the second form of  $f$ .

### 5.3.2 Mathematical analysis\*

Referring to the derivation by Wagner previously described in section 2.3.2(c) of this thesis, the rate of thickening of an oxide layer can be written as:

$$\frac{dx}{dt} = v_{eq} \frac{K_r}{x}$$

Substituting in the value for  $K_r$  for NiO, after making the appropriate assumptions and using the proposed effective diffusion coefficient, we have:

$$\frac{dx}{dt} = \Omega D_{eff} \frac{\Delta c}{x} \quad (5-11)$$

where  $\Omega$  is the volume of the oxide per nickel ion. Replacing the  $D_{eff}$  term by its equivalent, equation (5-11) may be expressed as:

$$\frac{dx}{dt} = \Omega \frac{\Delta c}{x} [D_L(1-f) + D_B f] \quad (5-12)$$

---

\* The calculations for error limits to the evaluation of the oxidation parameters are presented in Appendix C.

Taking the value of 400 Å as the diameter of an average crystallite and 10 Å for the width of the boundary, the value for  $f$  is .05. Therefore  $f \ll 1$  and the above expression can be approximated to:

$$\frac{dx}{dt} = \Omega \frac{\Delta c}{x} D_L + \Omega \frac{\Delta c}{x} D_B f(t) \quad (5-13)$$

which yields upon integration:

$$x^2 = 2\Omega \Delta c D_L t + 2\Omega \Delta c D_B \int f(t) dt \quad (5-14)$$

By differentiating  $x^2$  with respect to  $t$ ,

$$\frac{dx^2}{dt} = 2\Omega \Delta c D_L + 2\Omega \Delta c D_B f(t) \quad (5-15)$$

The expression  $\frac{dx^2}{dt}$  is equivalent to the instantaneous effective parabolic rate constant  $K_p(t)$ , at time  $t$ . The values for  $K_p(t)$  can be obtained by taking the tangents to the oxidation curves plotted in parabolic form. These values have been evaluated by the finite difference method using a computer. The expression  $2\Omega \Delta c D_L$  is the Wagner's parabolic rate constant for lattice diffusion and is fixed for a given oxygen pressure. The term  $2\Omega \Delta c D_B$  is the line defect contribution to the overall transport of the reactant. This expression is assumed also to be constant for a given oxygen pressure. We can thus define:

$$K_L = 2\Omega \Delta c D_L \quad (5-16)$$

and

$$K_B = 2\Omega \Delta c D_B \quad (5-17)$$

Substituting in the expression for  $K_L$  and  $K_B$  in equation (5-15) we obtain:

$$K_p(t) = K_L + K_B f(t) \quad (5-18)$$

Clearly in the absence of short circuit diffusion,  $f(t) = 0$  and the above relation is reduced to:

$$K_p(t) = K_L$$

$$\text{or } \frac{dx^2}{dt} = K_L \quad \text{and } x^2 = K_L t + C \quad (5-19)$$

which is the familiar parabolic growth rate equation for a reaction product layer governed by lattice diffusion of the reactant.

### 5.3.3 Testing different models of f

Let  $f = f_0 e^{-\alpha t}$  where  $f_0$  is the initial fraction of nickel sites and  $\alpha$  is an adjustable phenomenological coefficient. Using this form of  $f$  we can write:

$$\left( \frac{dx^2}{dt} \right) = K_L + K_B f_0 e^{-\alpha t} \quad (5-20)$$

or

$$\left( \frac{dx^2}{dt} - K_L \right) = K_B f_0 e^{-\alpha t} \quad (5-21)$$

The values of  $K_L$  can be calculated from the self diffusion coefficient of nickel in the oxide. The calculations with the appropriate assumptions are given in section 2.3.2(c) of this thesis. The values on the left of the above expression can be thus experimentally determined. Taking

the logarithm of both sides:

$$\ln \left( \frac{dx^2}{dt} - K_L \right) = \ln K_B f_0 - \alpha t \quad (5-22)$$

Clearly a plot of  $\ln \left( \frac{dx^2}{dt} - K_L \right)$  vs  $t$  should yield a straight line with a slope of  $-\alpha$  and an intercept of  $K_B f_0$ . A plot of this type for the three metal faces of nickel is shown in figure 5.3.2(a). It can be seen from these graphs that the curves are not linear but slightly curvilinear. The (100) face shows the most consistent behaviour characterized by a continuously decreasing rate with exposure time for all temperatures. This type of behaviour is exhibited by the (111) face except for the test at 600 °C. Most of the runs of the (110) face exhibit variable rates with time, a behaviour not expected from the proposed model of  $f$ . The lack of a fit to a linear curve indicated that the first order rate expression of  $f$  should be abandoned.

Let  $f$  be now  $f(t) = \frac{2d}{D_t}$ , where  $D_t$  is the diameter of the grain at time  $t$ . If the grains grow during oxidation as we have seen they do, the following general expression for grain growth derived by Beck<sup>(110)</sup> may be applicable,

$$D_t^2 - D_0^2 = k_3 t \quad \text{or} \quad D_t = (k_3 t + D_0^2)^{\frac{1}{2}} \quad (5-23)$$

where  $D_0$  is the initial grain size and  $k_3$  is the growth constant. The expression for  $f(t)$  is then:

$$f(t) = \frac{2d}{(k_3 t + D_0^2)^{\frac{1}{2}}} \quad (5-24)$$

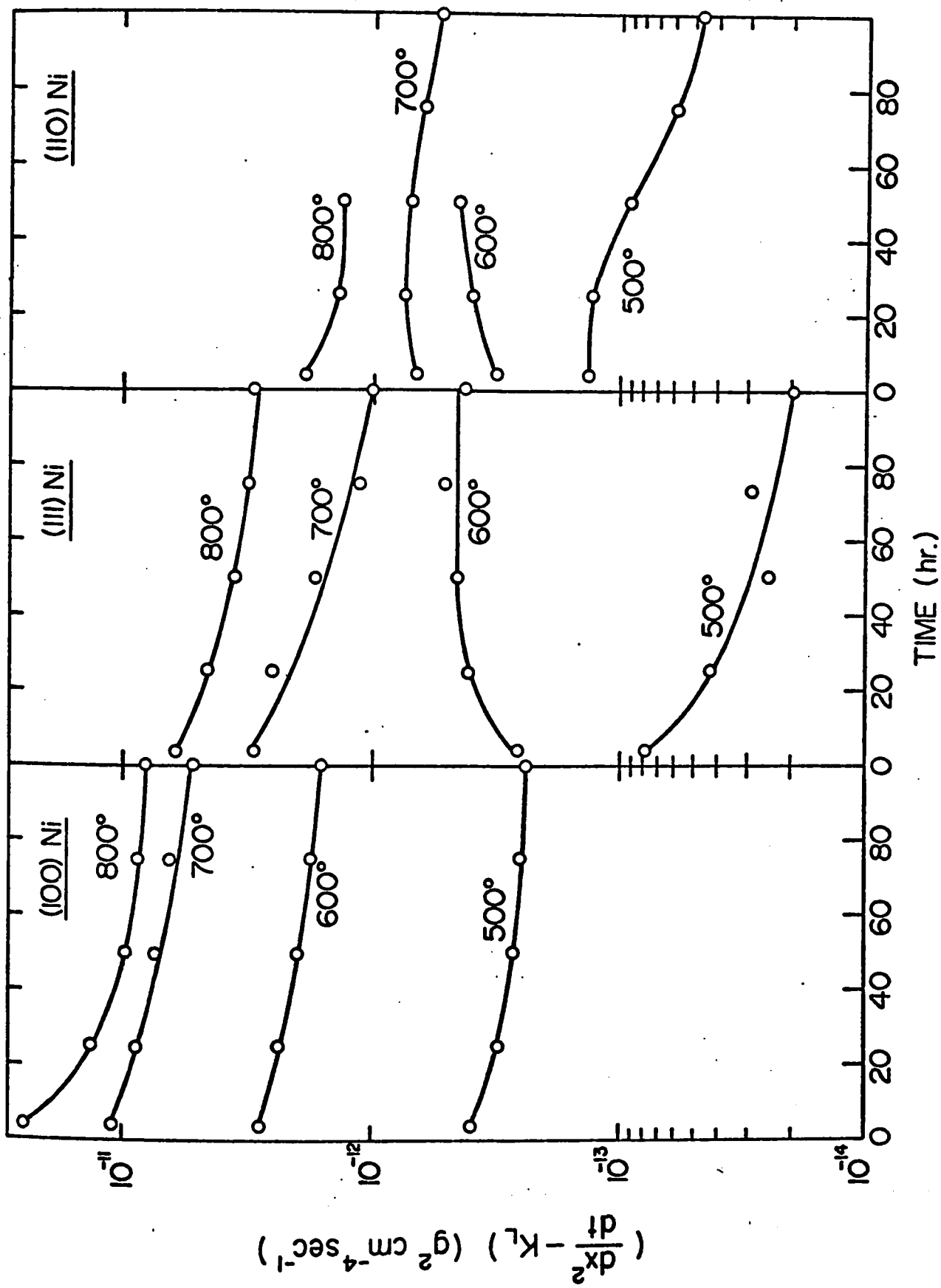


Figure 5.3.2 (a) Plot of  $\ln\left(\frac{dx^2}{dt} - K_L\right)$  versus time for the three metal faces

and the expression (5-21) can be written as:

$$\left( \frac{dx^2}{dt} - K_L \right) = K_B \frac{2d}{(k_3 t + D_0^2)^{1/2}} \quad (5-25)$$

Squaring both sides and taking the inverse, we obtain:

$$\frac{1}{\left( \frac{dx^2}{dt} - K_L \right)^2} = \frac{k_3}{4K_B^2 d^2} t + \frac{D_0^2}{4K_B^2 d^2} \quad (5-26)$$

A plot of  $\frac{1}{\left( \frac{dx^2}{dt} - K_L \right)^2}$  versus  $t$  should yield a straight line with a slope  $S = \frac{k_3}{4K_B^2 d^2}$  and an intercept  $I = \frac{D_0^2}{4K_B^2 d^2}$ .

The results from this type of plot are shown in figures 5.3.2(b) and (c). Linear relationships satisfy all of the results for the (100) and the (111) faces except for one run at 600 °C of the latter face. As illustrated by the plots in Fig. 5.3.2(a), the results for the (110) nickel face are not of a continuous decreasing value as required by the functional relationship of equation 5-12.

#### 5.3.4 Curves fitting of the experimental data

The good fit of the oxidation curves for the (100) metal face and for three of the four oxidation curves for the (111) face to the second model of 'f' will now be tested and justified by deriving an expression relating the thickness (weight gain) to the exposure time from the parameters obtained



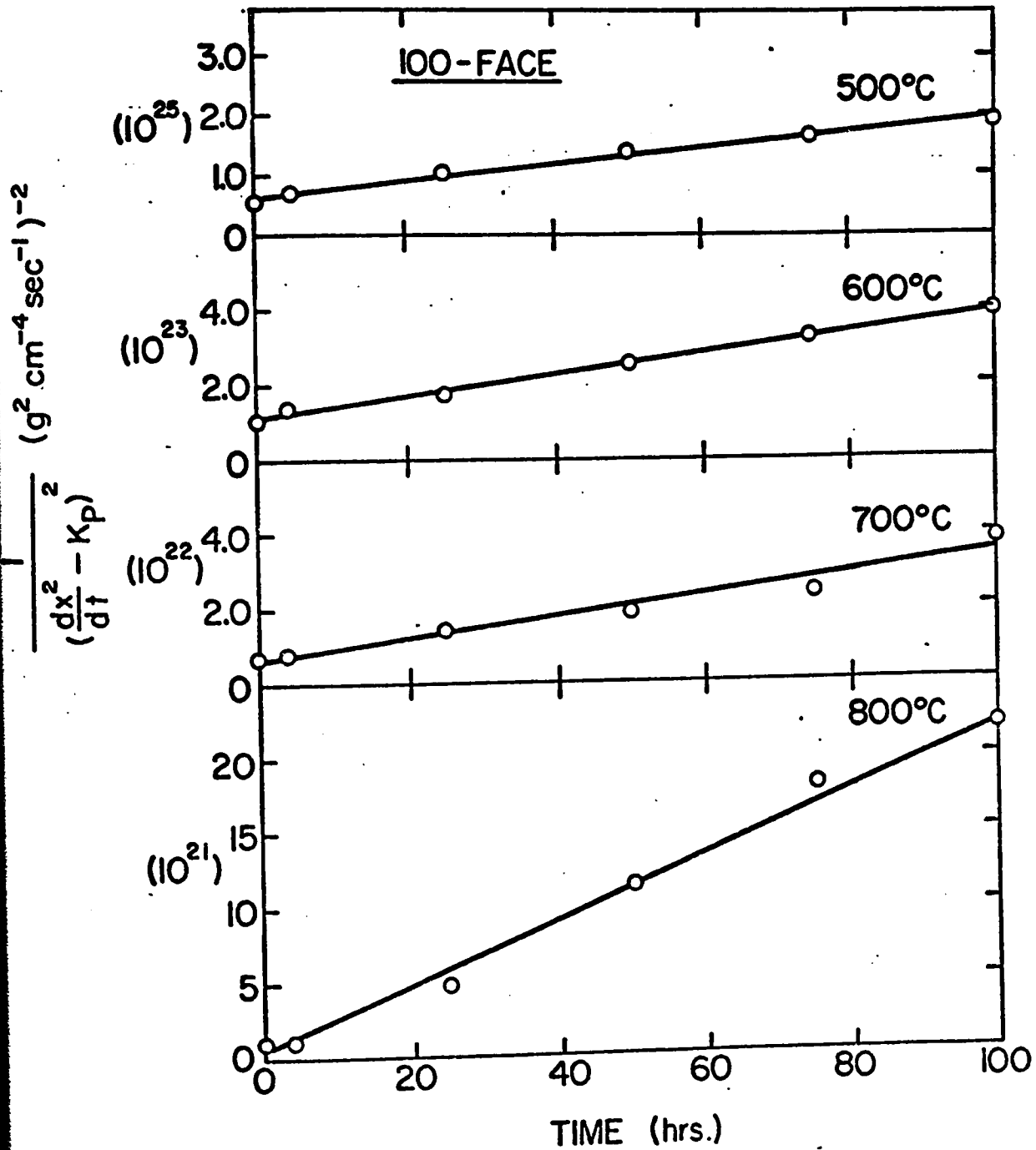


Figure 5.3.2 (b) Plot of  $\frac{1}{\left(\frac{dx^2}{dt} - K_L\right)^2}$  versus time for the (100) nickel face

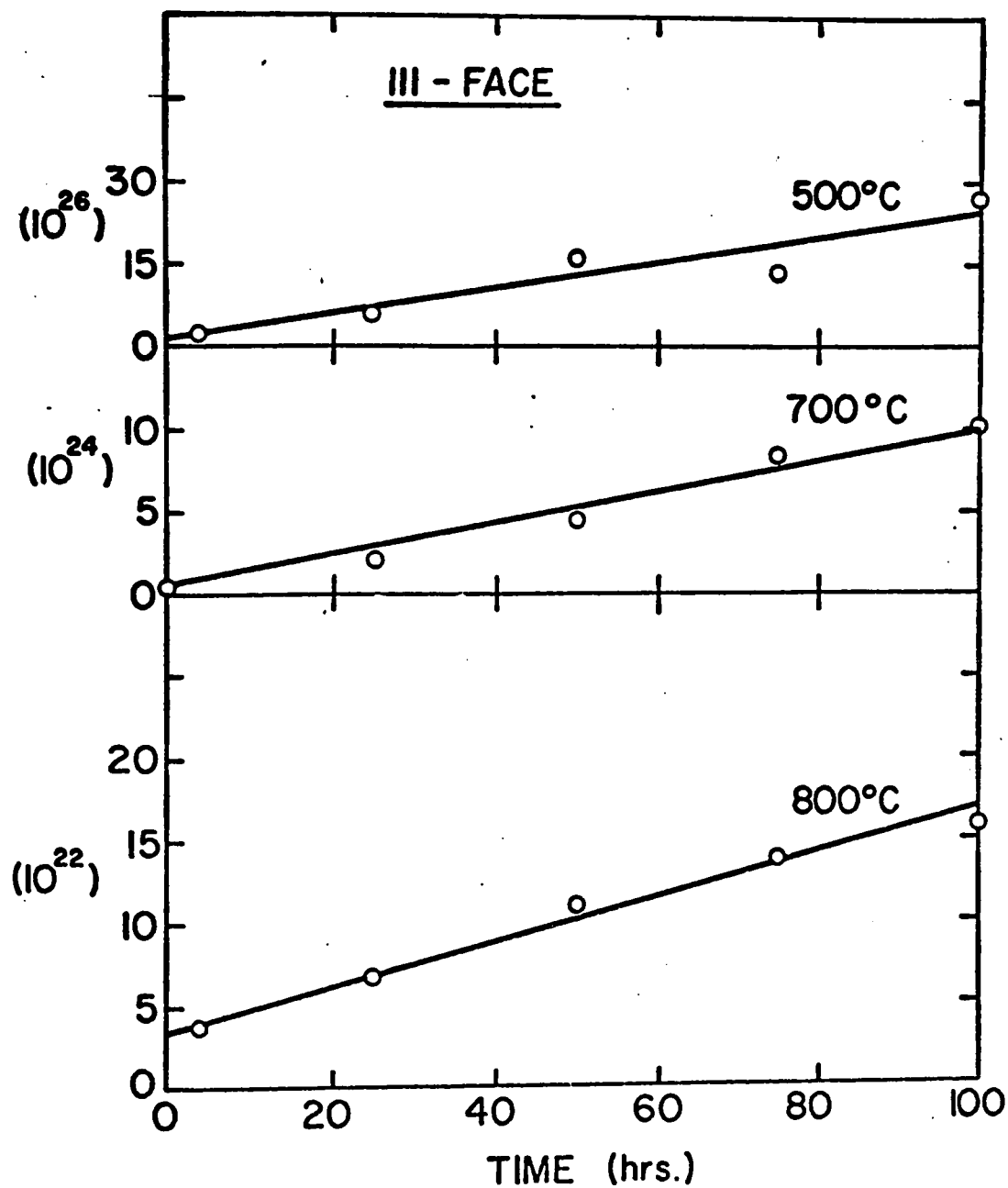


Figure 5.3.2 (c) Plot of  $\frac{1}{\left(\frac{dx^2}{dt} - K_L\right)^2}$  versus time for the (111) nickel face

in the mathematical analysis, namely the slope  $S$  and the intercept  $I$ .

$$\text{If we substitute the expression of } f(t) = \frac{2d}{(D_0^2 + K_3 t)^{1/2}}$$

into the expression:

$$x^2 = K_L t + K_B \int f(t) dt \quad (5-27)$$

and perform the integration, we obtain:

$$x^2 = K_L t + \frac{4K_B d}{k_3} \sqrt{D_0^2 + k_3 t} - \frac{4K_B d D_0}{k_3} \quad (5-28)$$

Noting that the intercept  $I = \frac{D_0^2}{4K_B^2 d^2}$  and the slope  $S = \frac{k_3}{4K_B^2 d^2}$ ,

the above equation can be simply written as:

$$x^2 = K_L t + \frac{2}{S} (\sqrt{I + St} - \sqrt{I}) \quad (5-29)$$

We have thus derived an expression for  $x^2$  in terms of a constant  $K_L$  and two experimentally determined values  $S$  and  $I$ . A test of the model thus consists of calculating  $x^2$  from the values of  $K_L$ ,  $S$  and  $I$  and comparing these values with the experimentally observed values. The results from the calculations are graphically represented in figures 5.3.4(a), (b). The solid line represents the calculated values and the experimental points by the circles. Examination of the graphs shows that good agreement is observed over a wide range of temperatures and exposure time. This good agreement lends support to the proposed model and allows the ratio of the boundary diffusion

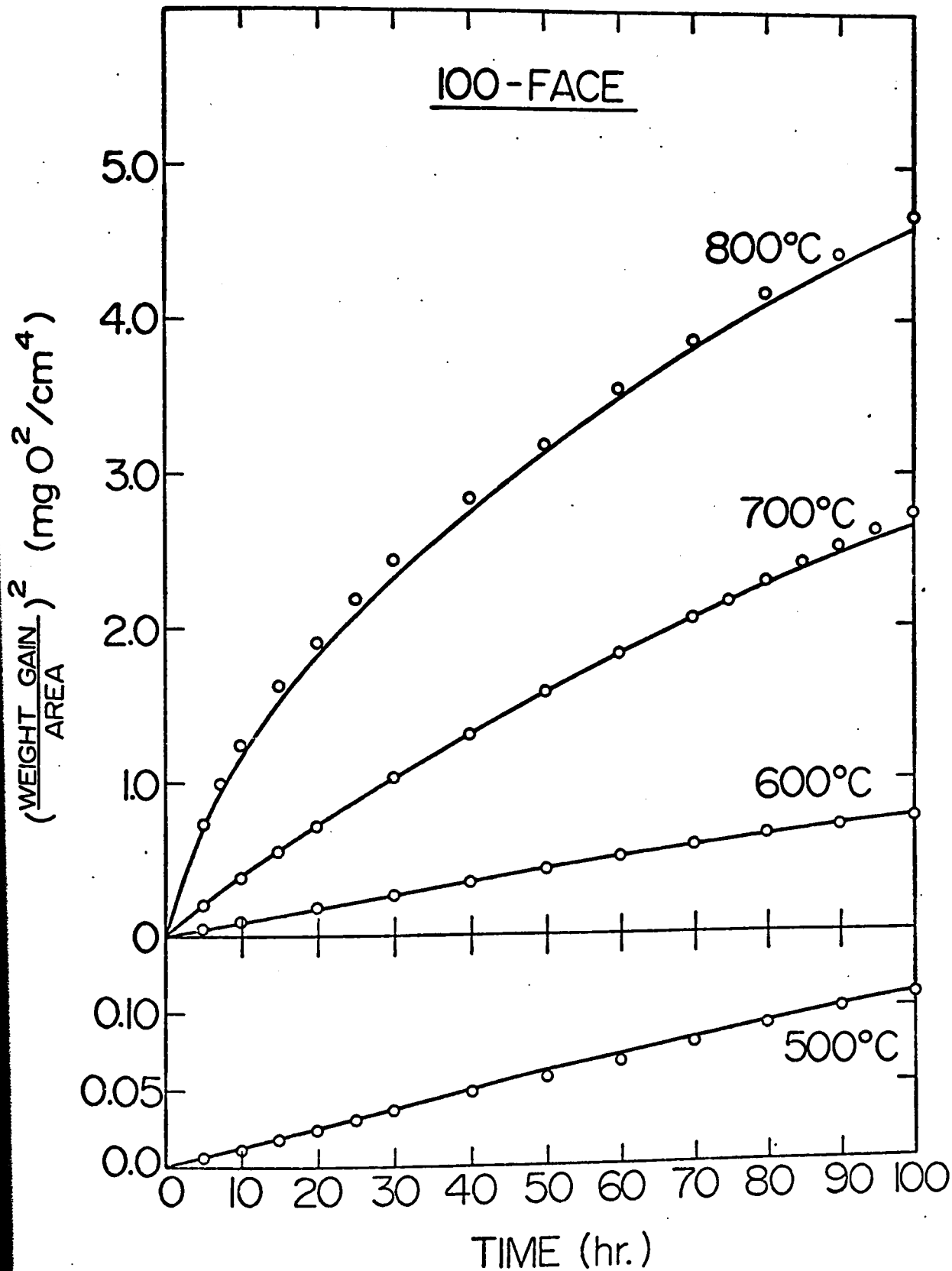


Figure 5.3.4 (a) The experimental results and the curve calculated by eqn. (5-29) for the growth of nickel oxide layers on the (100) nickel crystal face in parabolic form.

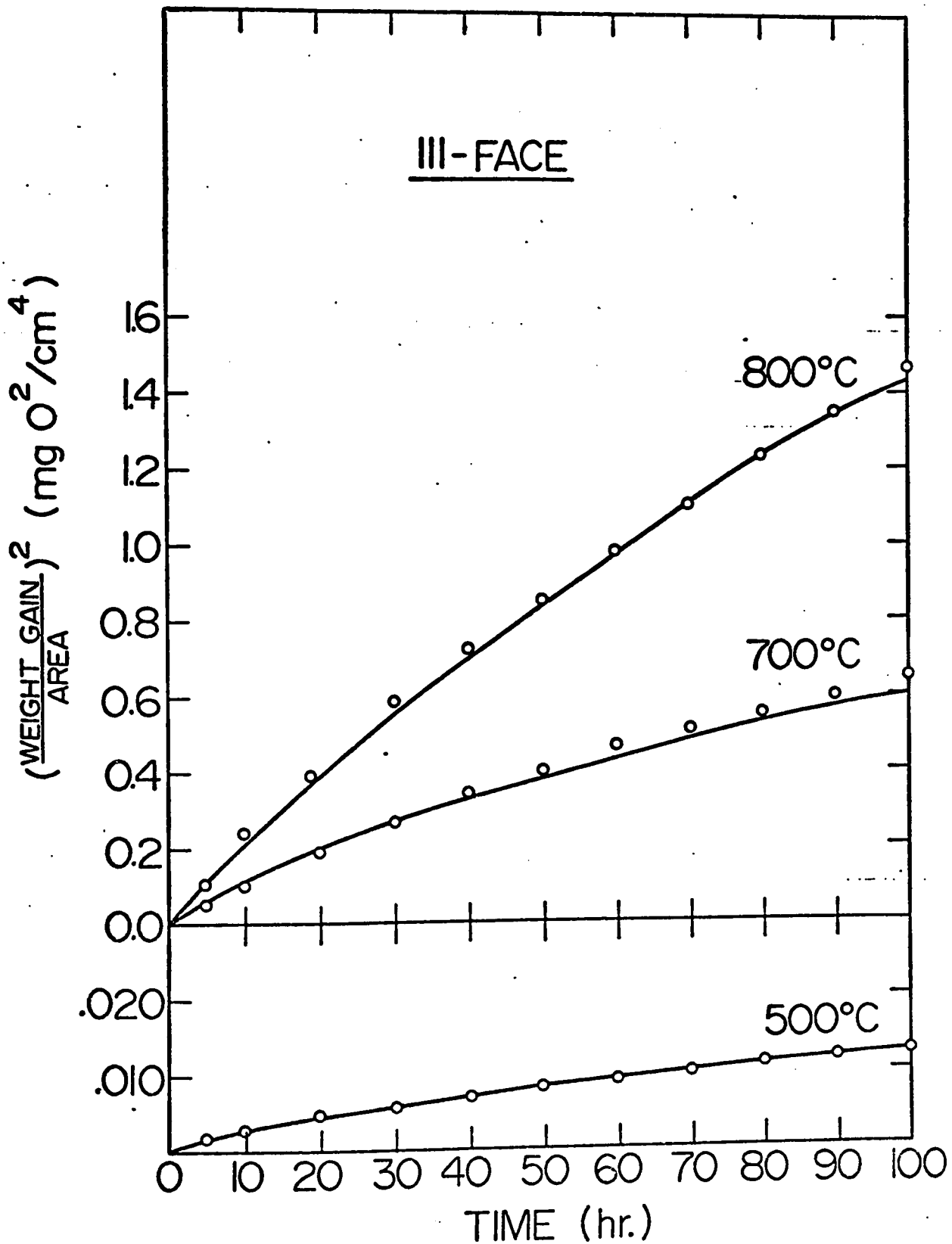


Figure 5.3.4 (b) The experimental results and the curve calculated by eqn. (5-29) for the growth of nickel oxide layers on the (111) nickel crystal face in parabolic form

coefficient for the oxide on two of the nickel crystal faces to be evaluated from the analysis.

5.3.5 Evaluation of the grain boundary oxidation diffusion constant for oxide grown on (100) and (111) nickel faces

From the expression:

$$K_p(t) = K_L + K_B f(t) \quad \text{or} \quad K_B = \frac{K_p(t) - K_L}{f(t)} \quad (5-30)$$

the values for  $K_B$  can be calculated if  $K_p(t)$  and  $f(t)$  are known. The values of  $K_p(t)$  as we have mentioned earlier, are calculated from the tangents to the oxidation curves plotted in parabolic form and the values for  $f(t) = \frac{2d}{D_t}$  from the results of transmission and scanning electron microscopy. The values for  $f(t)$  are chosen at the specific exposure time where the oxide grain sizes are known. The results of these calculations are summarized in table 5.3.5(a).

Temperature (°C)	Time (hr)	$K_p(t) - K_L$ ( $g^2 cm^{-4} sec^{-1}$ )	$f(t)$	$K_B$ ( $g^2 cm^{-4} sec^{-1}$ )	$K_B/K_L = D_B/D_L$
500 ( $.25T_m$ )	4	$3.80 \times 10^{-13}$	$2.86 \times 10^{-2}$	$1.33 \times 10^{-11}$	$8.0 \times 10^7$
	100	$2.40 \times 10^{-13}$	$8.60 \times 10^{-3}$	$3.00 \times 10^{-11}$	
600 ( $.30T_m$ )	50	$1.51 \times 10^{-12}$	$3.18 \times 10^{-3}$	$4.75 \times 10^{-10}$	$2.5 \times 10^7$
	100	$1.59 \times 10^{-12}$	$2.00 \times 10^{-3}$	$8.00 \times 10^{-10}$	
700 ( $.35T_m$ )	50	$5.25 \times 10^{-12}$	$2.16 \times 10^{-3}$	$2.4 \times 10^{-9}$	$2.3 \times 10^6$
	100	$5.20 \times 10^{-12}$	$2.56 \times 10^{-3}$	$2.0 \times 10^{-9}$	
800 ( $.4T_m$ )	50	$1.10 \times 10^{-11}$	$1.13 \times 10^{-3}$	$9.3 \times 10^{-9}$	$4.7 \times 10^5$
	100	$8.13 \times 10^{-12}$	$1.07 \times 10^{-3}$	$7.5 \times 10^{-9}$	

Table 5.3.5 (a)

Boundary Diffusion Oxidation Constants for the Oxide on the (100)  
Nickel Face (evaluated from  $K_p(t)$ )

Another possibility of determining the values for the boundary diffusion oxidation constants is given by the slope S which is equal to  $\frac{k_3}{4K_B^2 d^2}$  where  $k_3$  is the crystallite growth rate

constant. The values for  $k_3$  are calculated from SEM and TEM data. The results are summarized in table 5.3.5(b).

Table 5.3.5(b)

Boundary Diffusion Oxidation Constants for the Oxide on the (100) Nickel Face (evaluated from the slope S)

Temperature (°C)	Crystallites growth constant ( $k_3$ ) ( $\text{Å}^2/\text{sec}$ )	Slope S	$K_B$ ( $\text{g}^2\text{cm}^{-4}\text{sec}^{-1}$ )
500	$1.53 \times 10^1$	$3.3 \times 10^{19}$	$3.4 \times 10^{-11}$
600	$2.36 \times 10^2$	$7.8 \times 10^{17}$	$8.8 \times 10^{-10}$
700	$2.78 \times 10^2$	$7.7 \times 10^{16}$	$2.8 \times 10^{-9}$
800	$1.11 \times 10^3$	$6.1 \times 10^{16}$	$6.7 \times 10^{-9}$

We can see that the  $K_B$  obtained from the slope S differ by 10-20% from the values calculated from the  $K_p(t)$  method. The agreement is rather good considering the fact that the data on grain growth are limited. The same type of calculations were carried out for the (111) face. The results are tabulated in tables 5.3.5(c) and (d). Note again there is a good agreement between the values of  $K_B$  obtained from the two different methods. Since this constant contains the boundary diffusion coefficient,



Table 5.3.5(c)

Boundary Diffusion Oxidation Constants for the Oxide  
on the (111) Nickel Face (evaluated from  $K_p(t)$ )

Temperature (°C)	Time (hr)	$K_p(t) - K_L$ ( $g^2 cm^{-4} sec^{-1}$ )	$f(t)$	$K_B$ ( $g^2 cm^{-4} sec^{-1}$ )	$K_B/K_L = D_B/D_L$
500 ( $.25T_m$ )	4	$6.06 \times 10^{-14}$	$2.50 \times 10^{-2}$	$2.43 \times 10^{-12}$	$(1.1 \times 10^7)$
	100	$1.51 \times 10^{-14}$	$4.25 \times 10^{-3}$	$3.57 \times 10^{-12}$	
700 ( $.35T_m$ )	50	$1.61 \times 10^{-12}$	$1.63 \times 10^{-3}$	$9.89 \times 10^{-10}$	$(9.1 \times 10^5)$
	70	$1.12 \times 10^{-12}$	$1.52 \times 10^{-3}$	$7.35 \times 10^{-10}$	
800 ( $.4T_m$ )	48	$3.01 \times 10^{-12}$	$1.30 \times 10^{-3}$	$2.30 \times 10^{-9}$	$(1.1 \times 10^5)$
	115	$2.81 \times 10^{-12}$	$1.17 \times 10^{-3}$	$1.65 \times 10^{-9}$	

Table 5.3.5(d)

Boundary Diffusion Oxidation Constants for the Oxide  
on the (111) Nickel Face (evaluated from the slope S)

Temperature (°C)	Crystallites growth constant ( $k_3$ ) ( $A^2/sec$ )	Slope S	$K_B$ ( $g^2 cm^{-4} sec^{-1}$ )
500	$5.0 \times 10^1$	$6.15 \times 10^{21}$	$4.5 \times 10^{-12}$
700	$3.9 \times 10^2$	$2.78 \times 10^{18}$	$5.9 \times 10^{-10}$
800	$5.5 \times 10^2$	$3.70 \times 10^{17}$	$1.9 \times 10^{-9}$

its temperature coefficient will yield the activation energy for this diffusivity. All the values of  $K_B$  were then plotted in Arrhenius form. The graphical representation is shown in figure 5.3.5(a). A least square fit of each set of experimental data yield an activation energy of 31.1 and 34.6 Kcal/g-atom for the (100) and (111) faces. These values were found to correspond to about half of the activation energy for true lattice diffusion (61.0 Kcal/g-atom).

It is also reasonable to assume an exponential temperature dependence of the crystallite growth constant which would be of the form:

$$k_3 = k_3^0 e^{-\frac{E_3}{RT}} \quad (5-31)$$

The values for the activation energy of crystallite growth can then be determined. Results from least square fits give 21.8 and 13.6 Kcal/g-atom for the values of the (100) and (111) faces respectively. Thus, the activation energy for crystallite growth is largest for the oxide layer which exhibited the most highly textured structure. The average of these two values corresponds closely to the value of 19 Kcal/g-atom expected for grain growth of the oxide formed on polycrystalline nickel<sup>(72)</sup>.

The two values for the activation energies for boundary diffusion and for crystallite growth will further bear out the validity of the proposed model if we accept the following

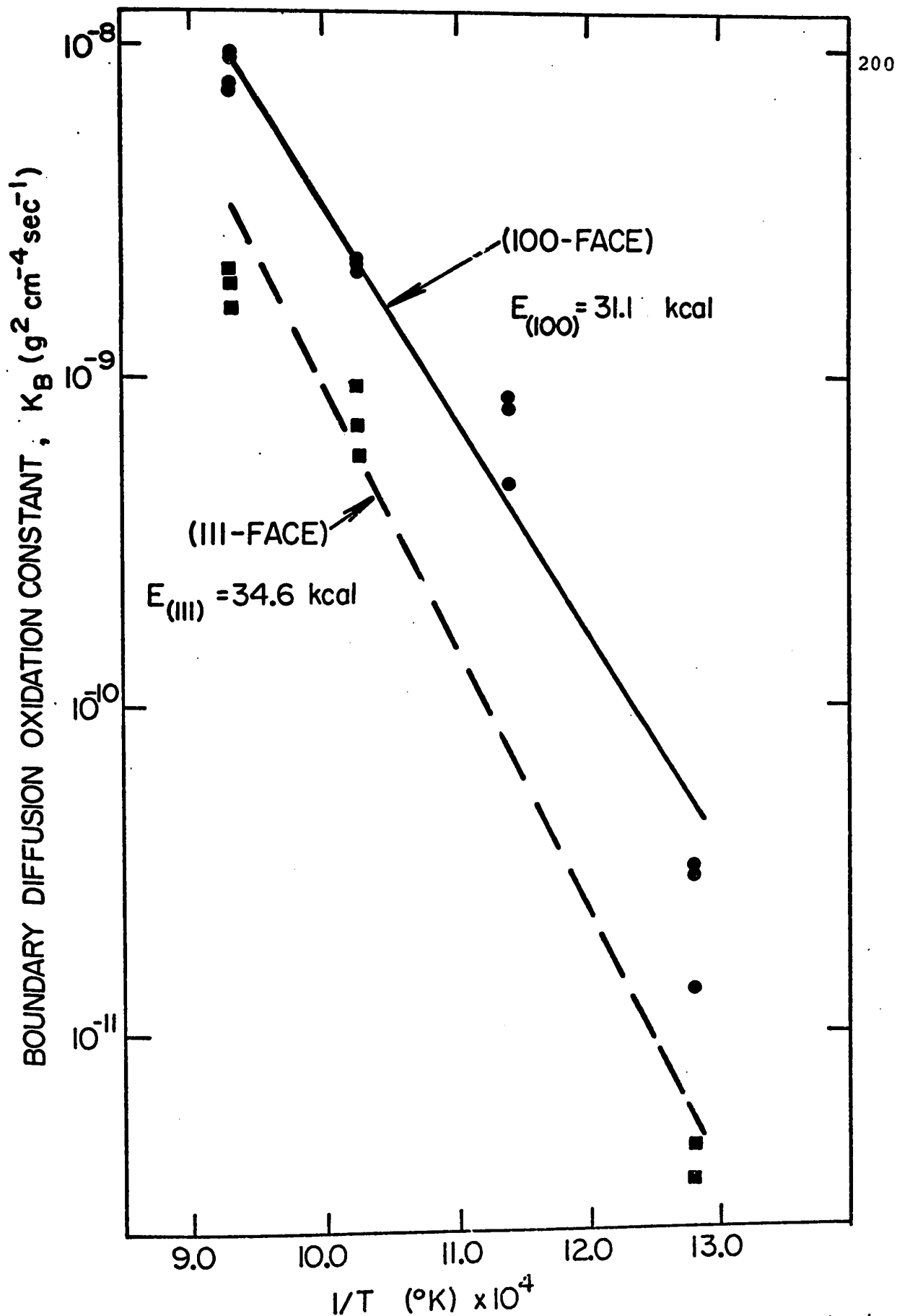


Figure 5.3.5 (a) Plot of boundary diffusion oxidation constant,  $K_B$ , versus reciprocal of temperature.

argument. The expression (5-18) is:

$$K_p(t) - K_L = K_B f(t)$$

If we assume also an exponential temperature dependence for the right part of the relation:

$$K_p(t) - K_L = A_0 e^{-\frac{E}{RT}} \quad (5-32)$$

an activation energy which is dependent upon energies for boundary diffusion and crystallite growth can be determined for the (100) and (111) faces. This type of plot for an exposure time of 50 hr is shown in figure 5.3.5(b). The values for the activation energy were found to be 20.0 and 28.0 Kcal/g-atom for the oxide on the (100) and (111) faces. The expression  $K_B f(t)$  can be written in the form

$$K_B f(t) = K_B^O e^{-\frac{E_B}{RT}} \left[ \frac{2d}{(D_O^2 + k_3 t)^{\frac{1}{2}}} \right] \quad (5-33)$$

The results from transmission and scanning electron microscopy allow the following approximations to be made:

$$D_t^2 \gg D_O^2 \quad \text{at time } t = 50 \text{ hrs.}$$

Thus  $D_t \approx (k_3 t)^{\frac{1}{2}}$  or  $D_t \approx (k_3^O t e^{-\frac{E_3}{RT}})^{\frac{1}{2}}$ . We can now write:

$$A_0 e^{-\frac{E}{RT}} = K_B^O e^{-\frac{E_B}{RT}} \left( \frac{2d}{(k_3^O t)^{\frac{1}{2}} e^{-\frac{E_3}{2RT}}} \right) \quad (5-34)$$

or

$$A_0 e^{-\frac{E}{RT}} = B_0 e^{-\frac{1}{RT} (E_B - \frac{E_3}{2})} \quad (5-35)$$

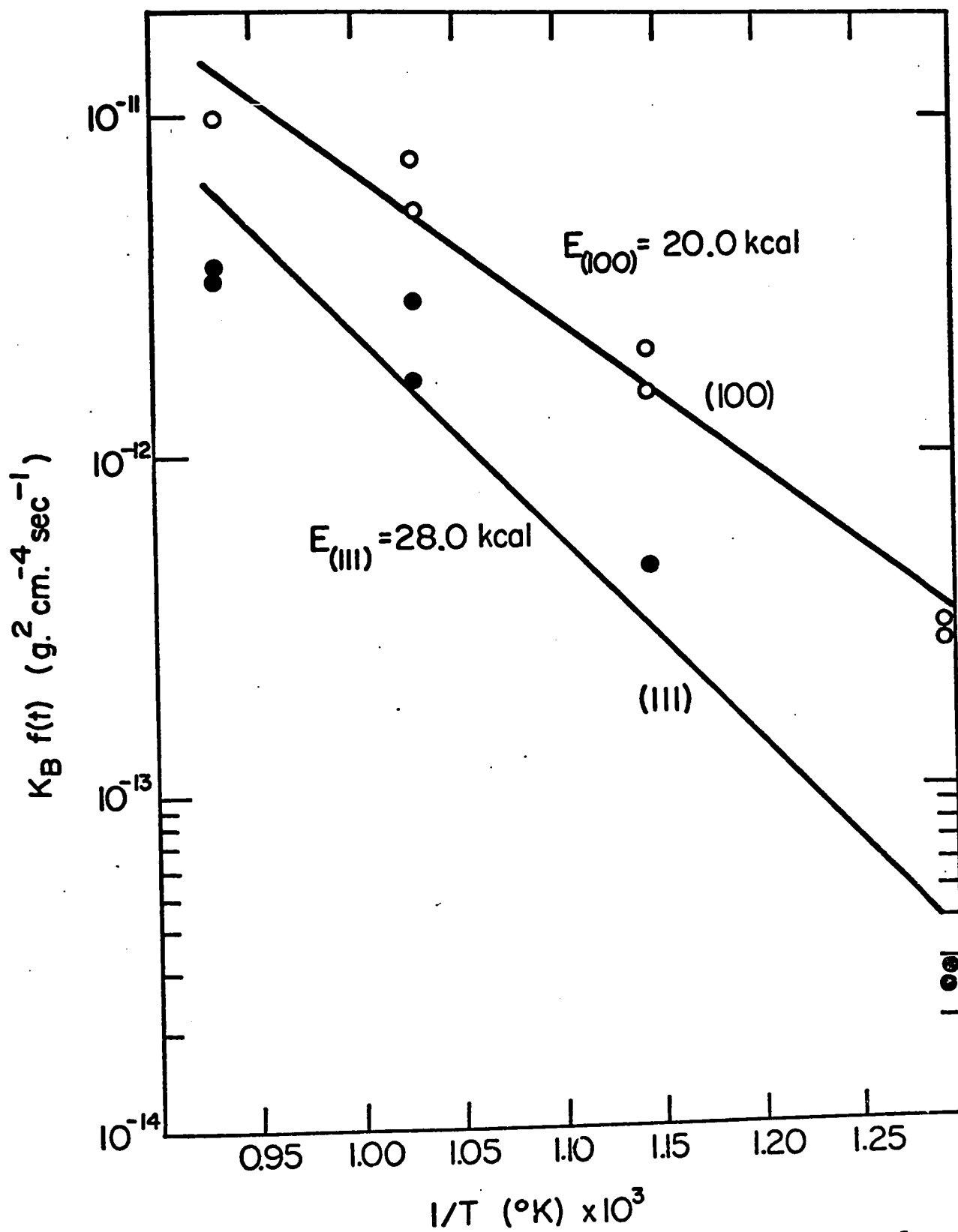


Figure 5.3.5 (b) Plot of  $K_B f(t)$  versus reciprocal of temperature

where  $B_0 = \frac{2dk_B^0}{(k_3^0 t)^{1/2}}$ . Thus  $E = E_B - \frac{E_3}{2}$  (5-36)

The following tabulated values demonstrate that the predicted and observed value of the activation energy E are indeed in very good agreement.

<u>Nickel face</u>	<u>E</u>	<u>E<sub>B</sub></u>	<u>E<sub>3</sub></u>	<u>(E<sub>B</sub> - ½E<sub>3</sub>)</u>
(100)	20.0	31.1	21.8	20.2
(111)	28.0	34.6	13.6	27.8

### 5.3.6 Conclusions from studies of the oxidation kinetics

The reasonable values obtained for the ratios of boundary to lattice diffusion coefficients, for the activation energies and the good agreement between different parameters derived from the analysis are all consistent with the assumption that the oxidation of the single crystal faces of nickel in the temperature range investigated proceeds by the diffusion of nickel via cation vacancies in the lattice and short-circuit boundary paths set up by the growth process in the oxide scales. A modified parabolic equation based on an effective diffusion coefficient which decreases with exposure time has been found to account satisfactorily for the oxidation kinetics of the (100) and (111) faces. The validity of this simple model is however limited. It cannot explain the oxidation behaviour of the (110) face. This face shows large

difference in structure and relative larger grain growth which is probably due to the additional phenomena of extensive recrystallization of the oxide occurring during the oxidation process. Accordingly the simple model assumed in this analysis must be expanded to account for the behaviour of this particular face. The observations to the present, however, do not give sufficient information on the recrystallization processes for advancement of a more detailed model involving the influence of oxide crystallography on the nature of the oxide crystallite boundaries acting as short circuit paths for nickel.

#### 5.4 Correlations between the structure and kinetics

Perhaps the most important conclusion derived from this study is that a definite relationship between the kinetics and the structure of the oxide has been established. The differences in reaction rates and oxidation behaviour of the three metal faces have been shown to be related to the differences in the structures of the oxide films and scales. These differences are characterized by the number and type of orientations, the grain size, the degree of preferred orientation and scale morphology.

The (100) nickel face which exhibits continuous oxidation curves for exposures extending to 100 hr., good reproducibility and consistent oxidation behaviour also possesses the most uniform structure. The (111) face which shows some irregularities in the kinetics, probably due to cracks forming in

the scales, also shows a relatively less uniform structure. The (110) face exhibits frequent breaks in the oxidation curves and poor reproducibility, and the scales have been shown to have large differences in structure.

It was possible to correlate several features of the oxidation kinetics and oxide structures for the (100) and (111) nickel faces by a model involving nickel diffusion through the superficial oxide layers via lattice point defects and short-circuit paths at crystallite boundaries. The (100) face oxidized more rapidly than the (111) face. This effect was most marked at the lowest temperature examined, 500°C, and the oxidation rates differed approximately by an order of magnitude. The analysis demonstrated that this effect was dependent upon the relative size of the crystallites in the oxide layers and upon the boundary diffusion coefficients which was an order of magnitude larger for the oxide formed on the (100) face. This oxide exhibited a textured structure involving both (100) and (111) orientation; the oxide on the (111) face was less textured but it exhibited predominately the (111) orientation parallel to the metal surface. These findings were consistent with the conclusion that a smaller degree of crystallographic orientation in the oxide led to larger incoherency in boundaries and hence more rapid boundary diffusion of nickel.



## CHAPTER 6

### RECOMMENDATIONS FOR FUTURE WORK

The anisotropy in reaction rates associated with the structural differences in the oxide films and scales leads to the following possibilities for further work:

1) The annealing of the oxide should be investigated. A sample is oxidized for a given time and then annealed at the same temperature for different times. Any change in the structure can be monitored by the electron reflection diffraction technique. The sample is then reoxidized and any change in reaction rate can be related to the change in structure. Meijering<sup>(120)</sup> has reported changes in the reaction rate but correlations with the structure have not been investigated.

2) The effect of crystallite size can be studied by oxidizing the sample at very high temperature for a very short time to produce large crystallites. The temperature is then lowered and any change in reaction rate can be then related directly to the grain size. It is feasible, moreover, that a single crystal of nickel oxide containing only dislocations for short circuit diffusion of nickel could be formed by this technique.

3) A sample can be oxidized completely, the grain size and the texture coefficient then determined.  $\text{Ni}^{63}$  is then

deposited and the sample is given a diffusion anneal at a specific oxygen pressure. From the concentration profile determined by the distribution of the radioactive isotope, the grain boundary diffusion coefficient can be evaluated for an oxide with a given texture coefficient.

4) It has been shown that the (111) face of nickel oxidizes most slowly and that it possesses a reasonably adherent scale. A polycrystalline nickel sample can be deformed and annealed to give an (111) texture. Oxidation rate as function of the degree of preferred orientation can be then investigated. This type of study could possibly lead to results having application of industrial importance.

CHAPTER 7  
CONCLUSIONS

1. Under the specified oxidation conditions and sample preparation, exposure of three single crystal faces of nickel to oxygen results in the formation of an oxide composed of small crystallites having different orientations. The number and the type of orientations were found to be different on the different metal crystal faces. These orientations are summarized in table 5.2.1.
2. The majority of these orientations contain at least a cpd which has been shown to be parallel to the cpd in the metal. The preference for a particular oxide orientation in thin films seems to be dictated by the number of cpd in the metal. Thus, in the cases where there are more than one cpd on the metal surface as in the (100) and (111) faces, the parallel oxide orientation is preferred. This type of arrangement maximizes the coincidence of the cpd between the metals and oxide and probably minimizes the interfacial energy between the oxide and metal.
3. The structures of the oxide undergo changes with oxidation time and both the substrate and growth mechanism appear to influence the final orientation of the oxide.
4. The microstructures of the scales on the (100) and the

(111) metal faces show the presence of two oxide layers consisting of equi-axed and columnar grains respectively. The columnar layers showed strong preferred orientations. The oxide on the (110) face exhibits a small degree of preferred orientation and it shows no evidence of a two-layer scale. Both the (100) and (111) oxide planes were found to be the preferred planes in the Ni-NiO system.

5. The oxide films are composed of crystallites ranging in size from a minimum of 300-500 Å in the early stage of oxidation at 500 °C, to a maximum of 2-3µ at 800 °C after 120 hr of exposure. The growth rates of the crystallites were found to be different on the different metal crystal faces.

6. The oxidation kinetics of the three faces show anisotropy in reaction rate and oxidation behaviour. A diffusion model based on the simultaneous diffusion of nickel via lattice cation vacancies and short circuit paths at the crystallite boundaries has been found to account for the oxidation kinetics of the (100) and (111) faces. These faces show consistent oxidation behaviour and relatively uniform structures.

7. The differences in reaction rates, according to the proposed model, can be accounted for by the difference in the values of the boundary diffusion coefficients for oxide boundaries of different orientations. The values for the activation energy for diffusion in the boundaries were found to correspond to approximately one-half the value for lattice diffusion. The analysis also shows that short circuit diffusion is

predominant in the oxidation of nickel at intermediate temperatures less than one half the melting point of nickel oxide.

8. Finally, a simple and direct correlation has been established in several cases between the structure and kinetics.

APPENDIX ATHE CONSTRUCTION OF THE RECIPROCAL LATTICE PLANES

Due to its wave properties, when an electron beam hits a crystal having a periodic structure, constructive interference will give rise to a diffracted beam. The direction of the diffracted beam with respect to the incident beam is related to the wavelength of the electrons and the interplanar spacing of the crystal by the Bragg's relation:

$$n\lambda = 2d \sin\theta.$$

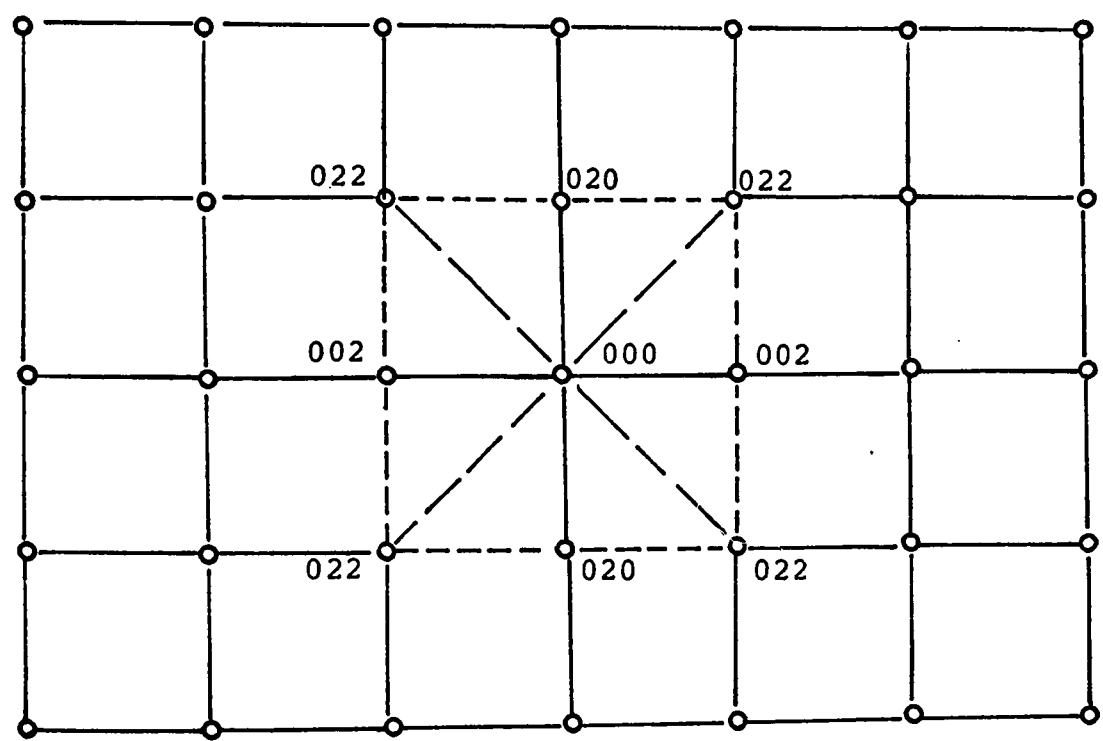
where  $n$  is an integer,  $\lambda$  is the wavelength,  $d$  is the lattice spacing and  $\theta$  is the angle of reflection.

For an electron microscope operating at 100 KV, the wavelength of the electron is  $0.037 \text{ \AA}$  and the radius of the Ewald sphere is about  $27 \text{ \AA}^{-1}$  which is large compared to the lattice spacing and it can be approximated to a plane. Thus the most convenient way to interpret the electron diffraction patterns is by means of the construction of the reciprocal lattice planes whose detailed instruction is given in reference (92).

The drawing of the three reciprocal lattice planes of nickel viz. the (100), (110), (111) are given along with the commonly found orientations of the oxide. They are drawn to

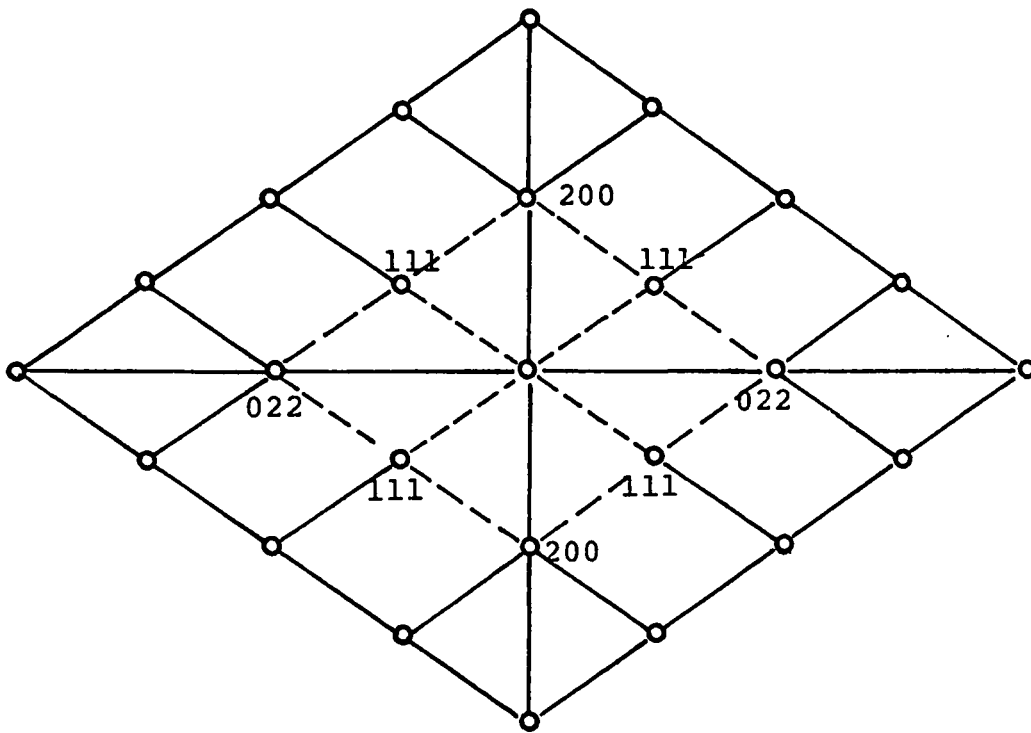
scale so that the interplanar spacing between the metal and oxide can be visually estimated.

(100) RELP OF NICKEL

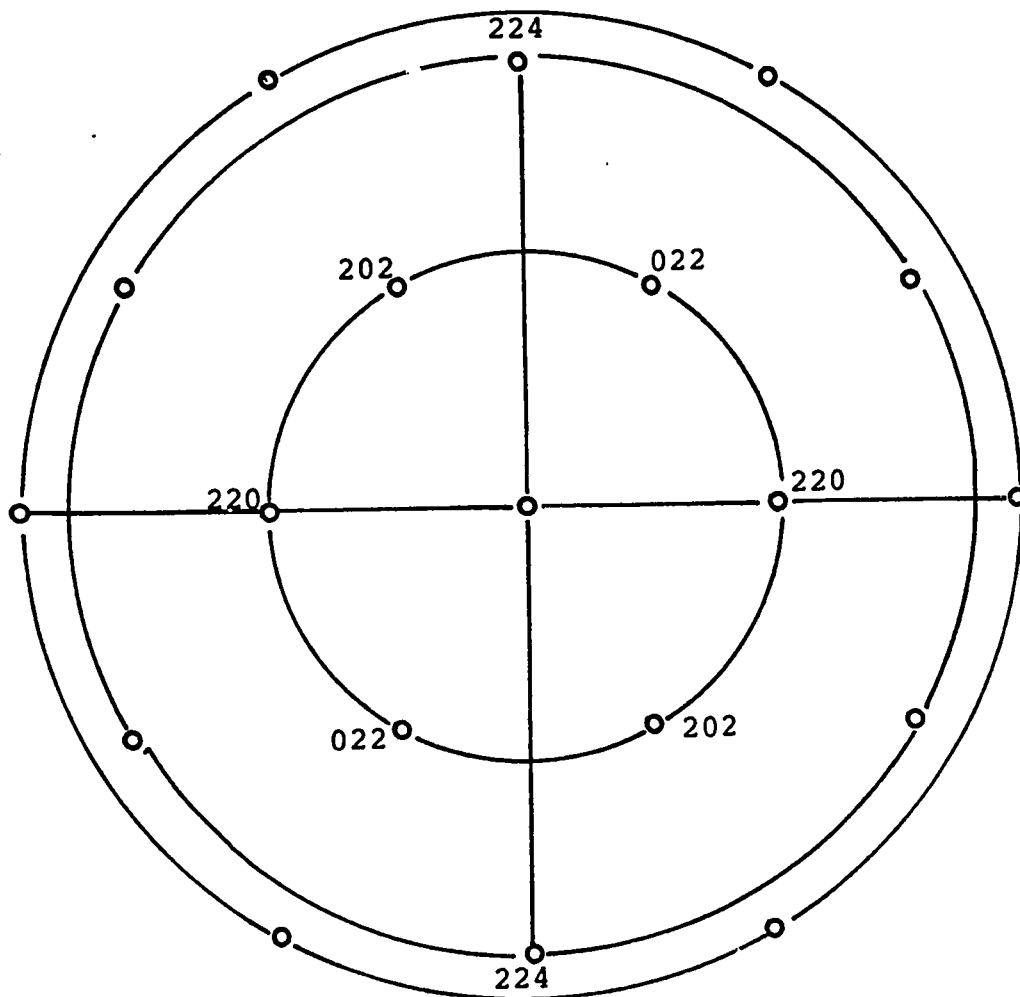




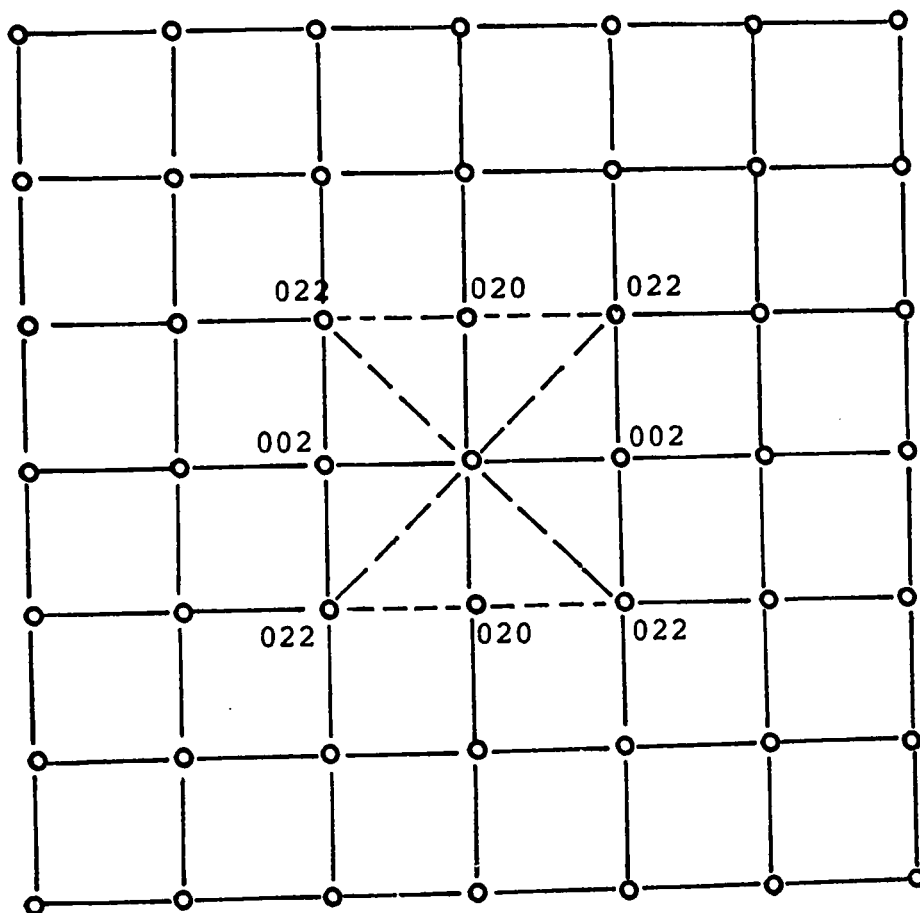
(011) RELP OF NICKEL



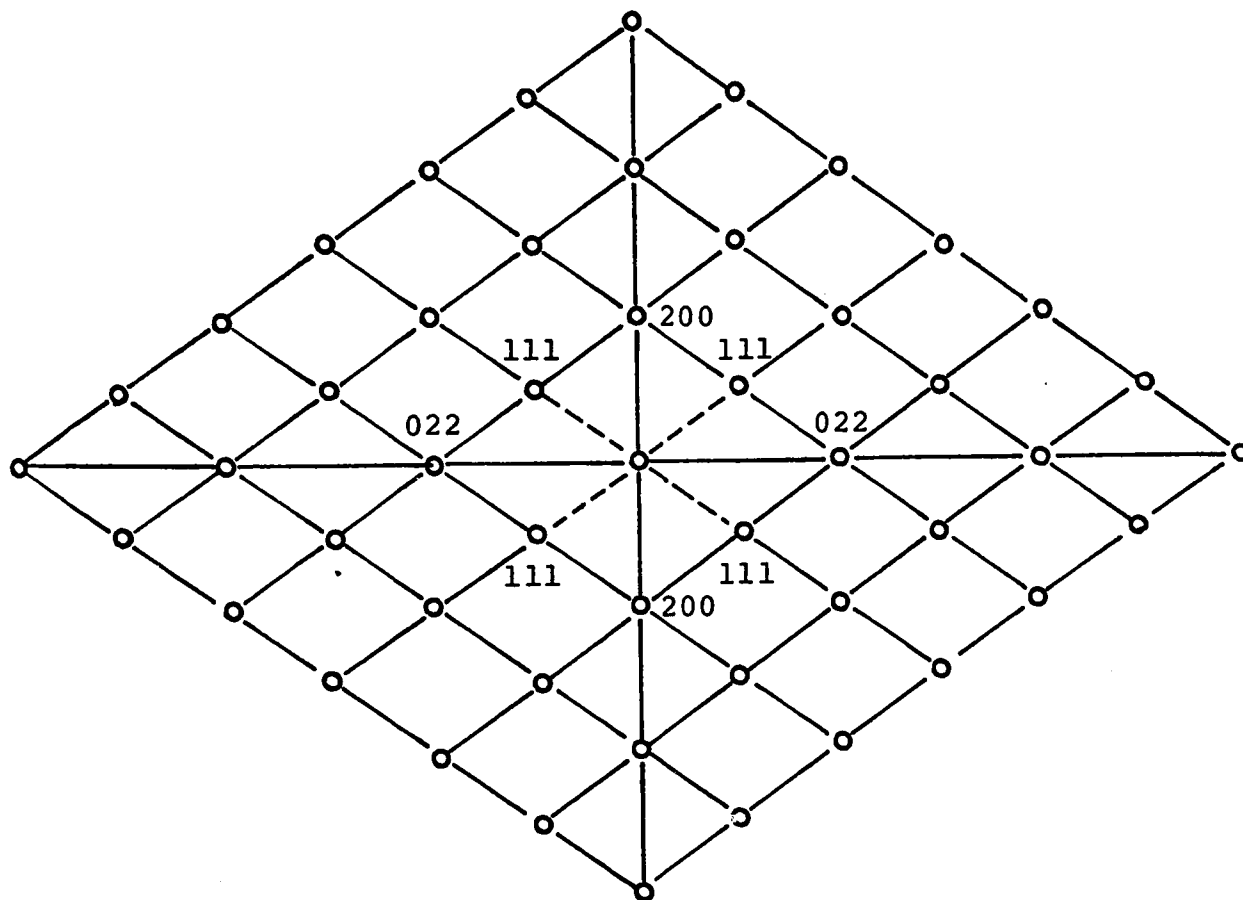
## (111) RELP OF NICKEL



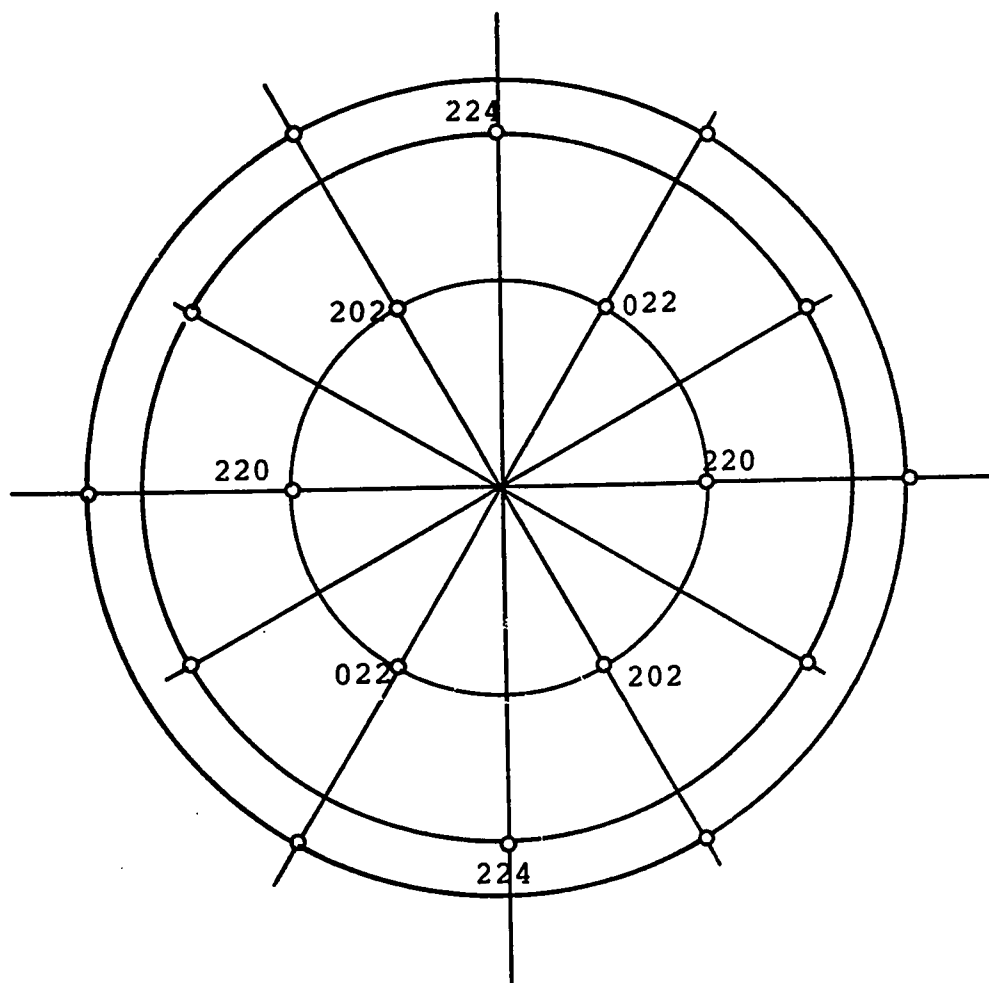
## (100) RELP OF NiO



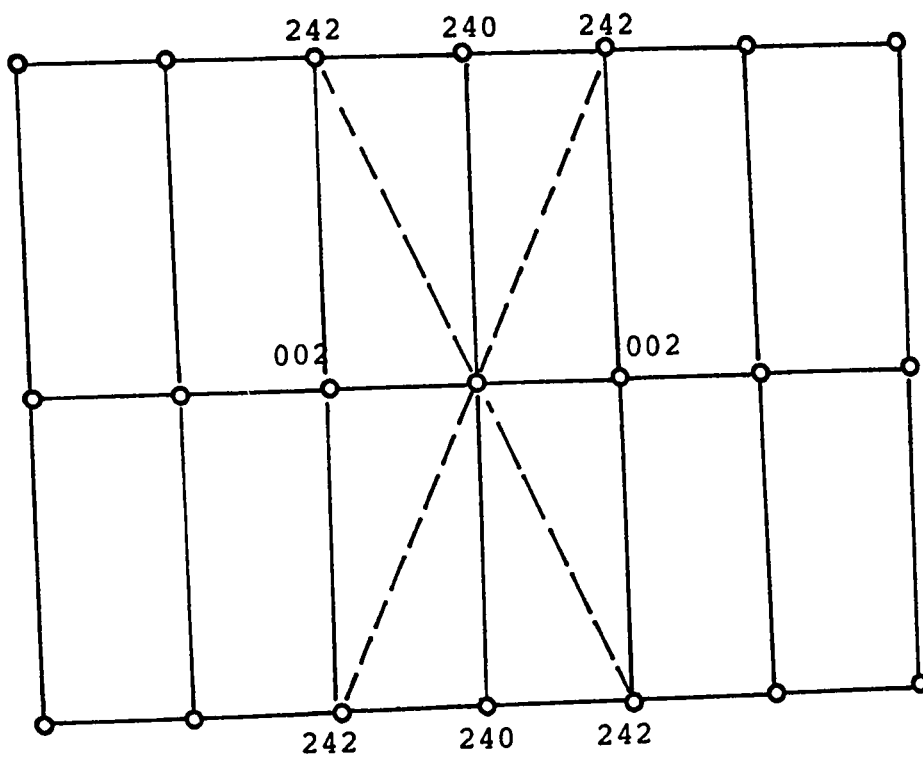
(011) RELP OF NiO



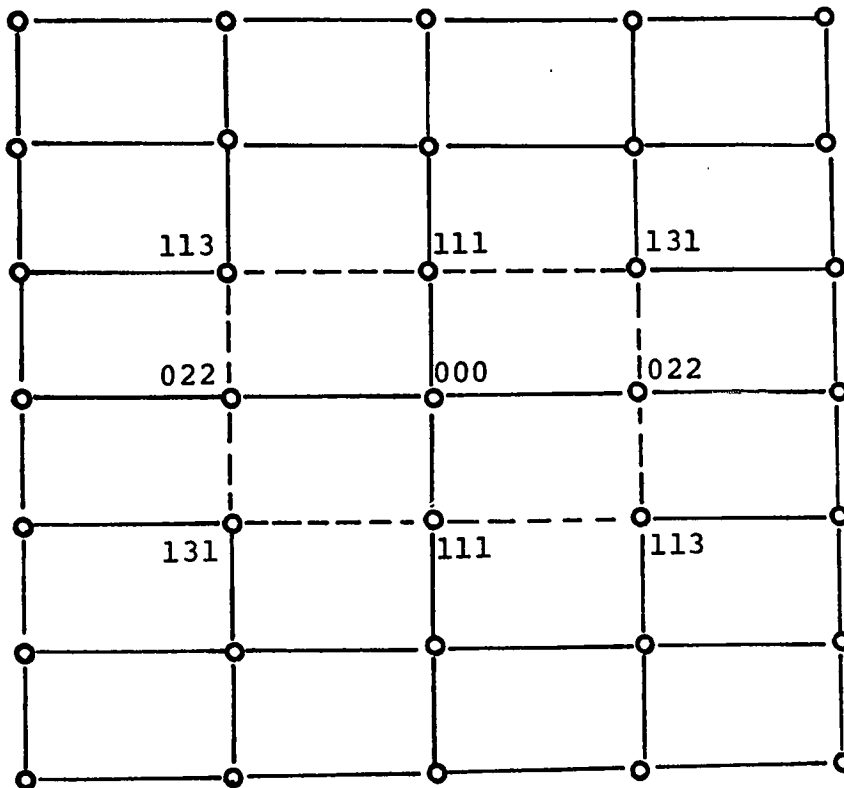
## (III) RELP OF NiO



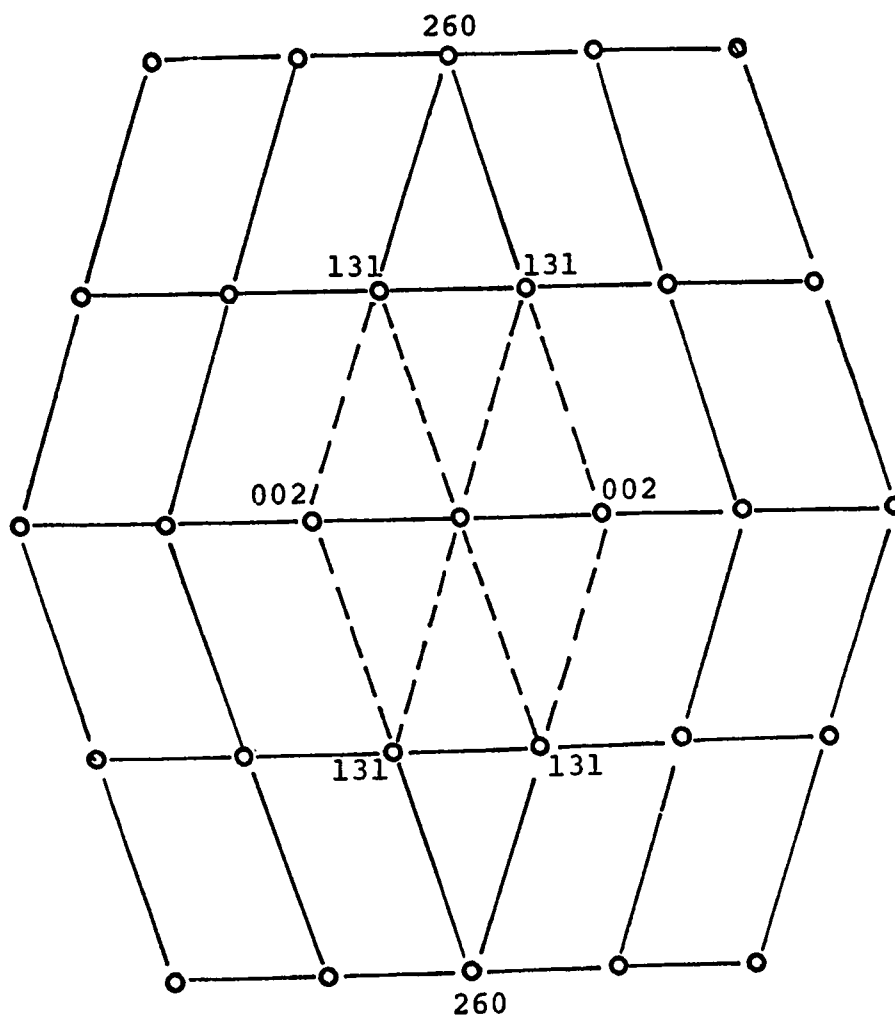
(210) RELP OF NiO



## (211) RELP OF NiO

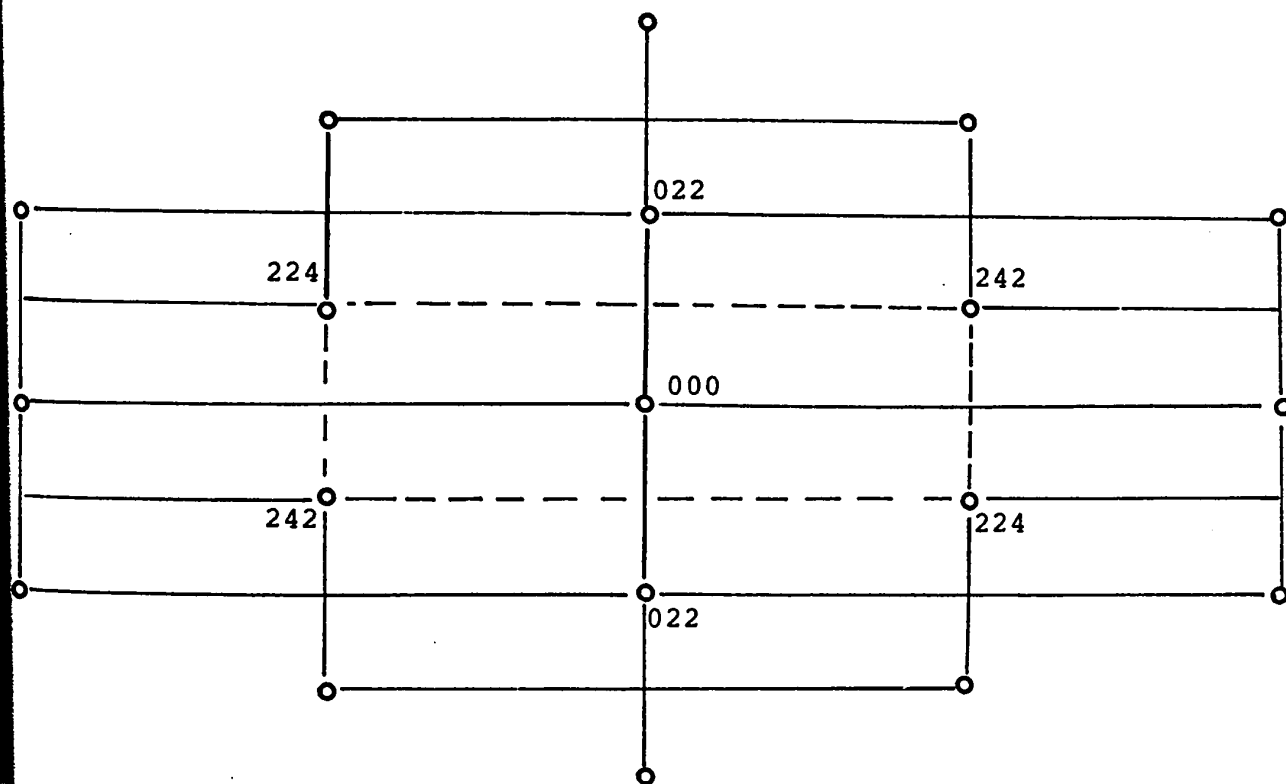


(310) RELP OF NiO

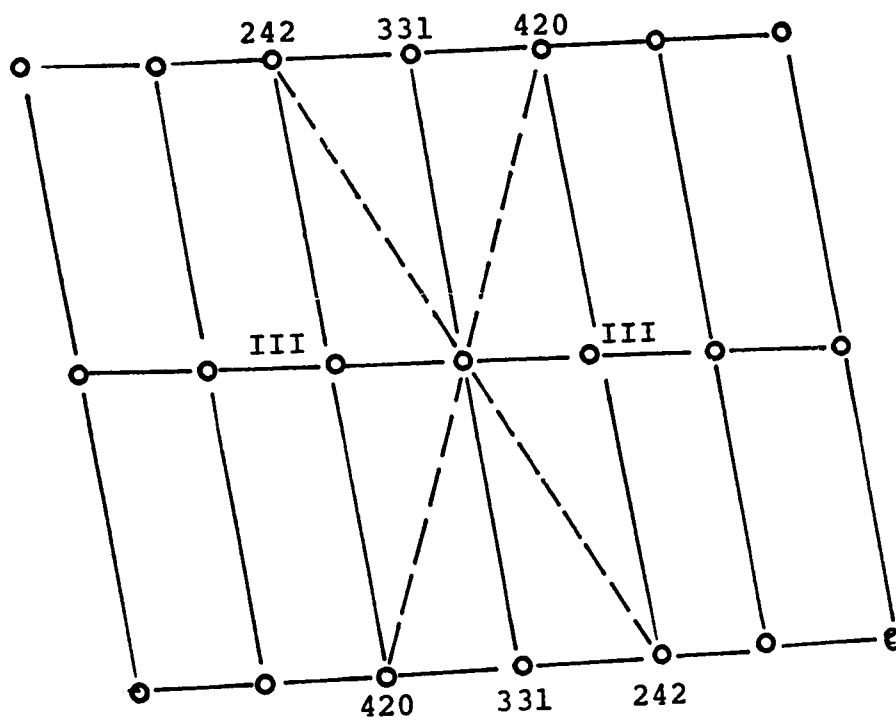




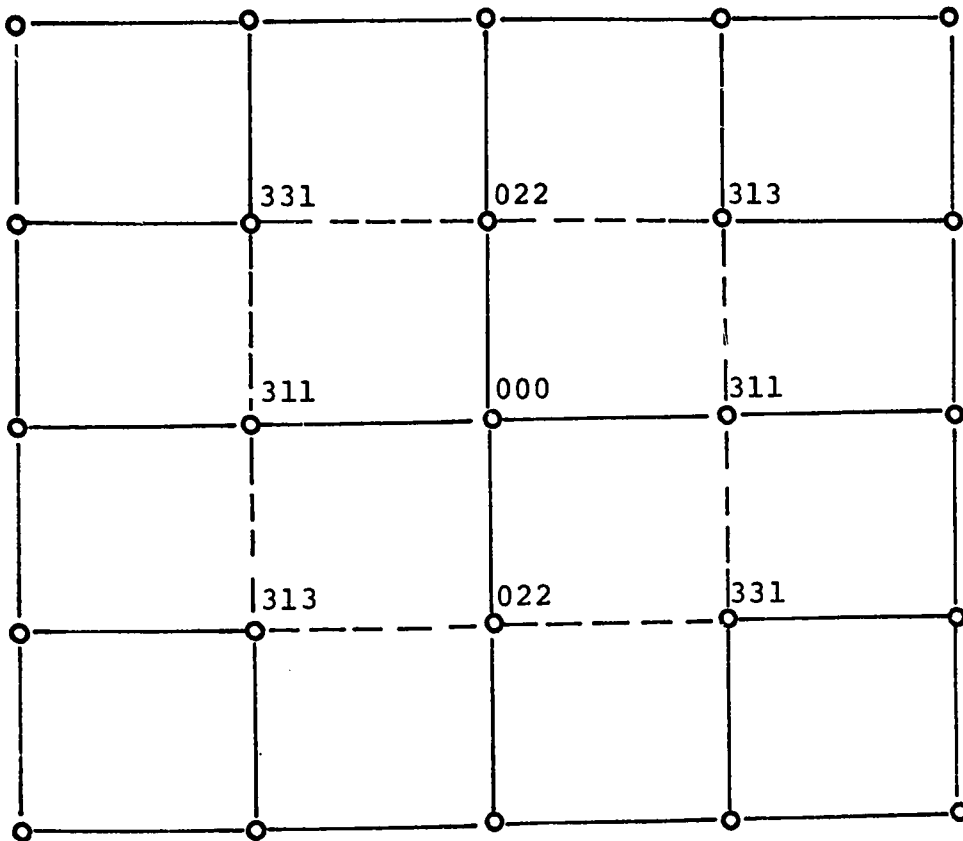
## (311) RELP OF NiO



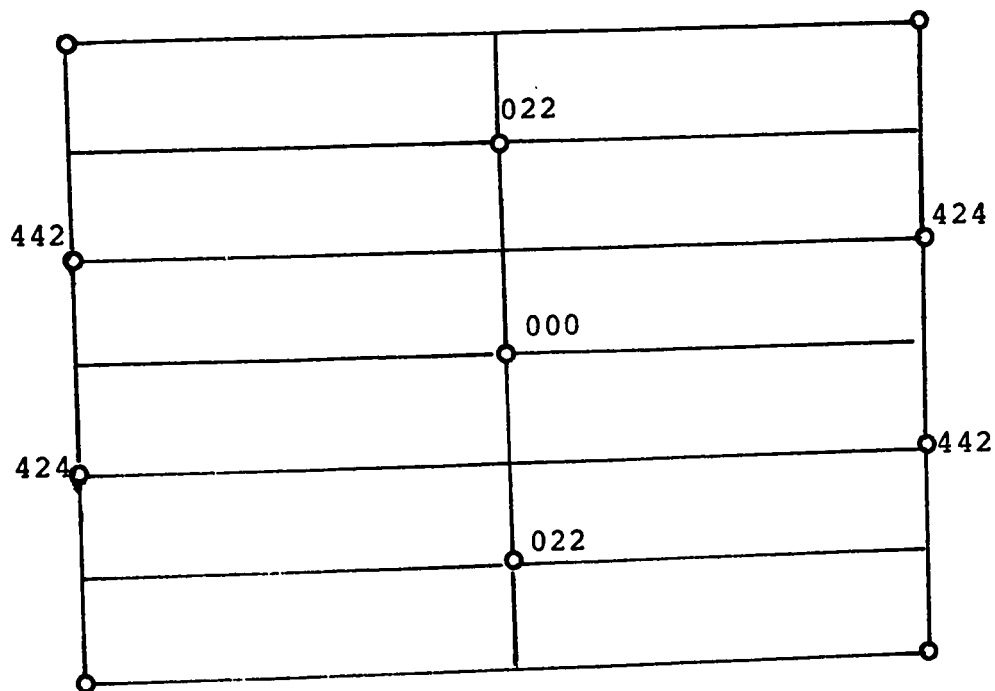
## (123) RELP OF NiO



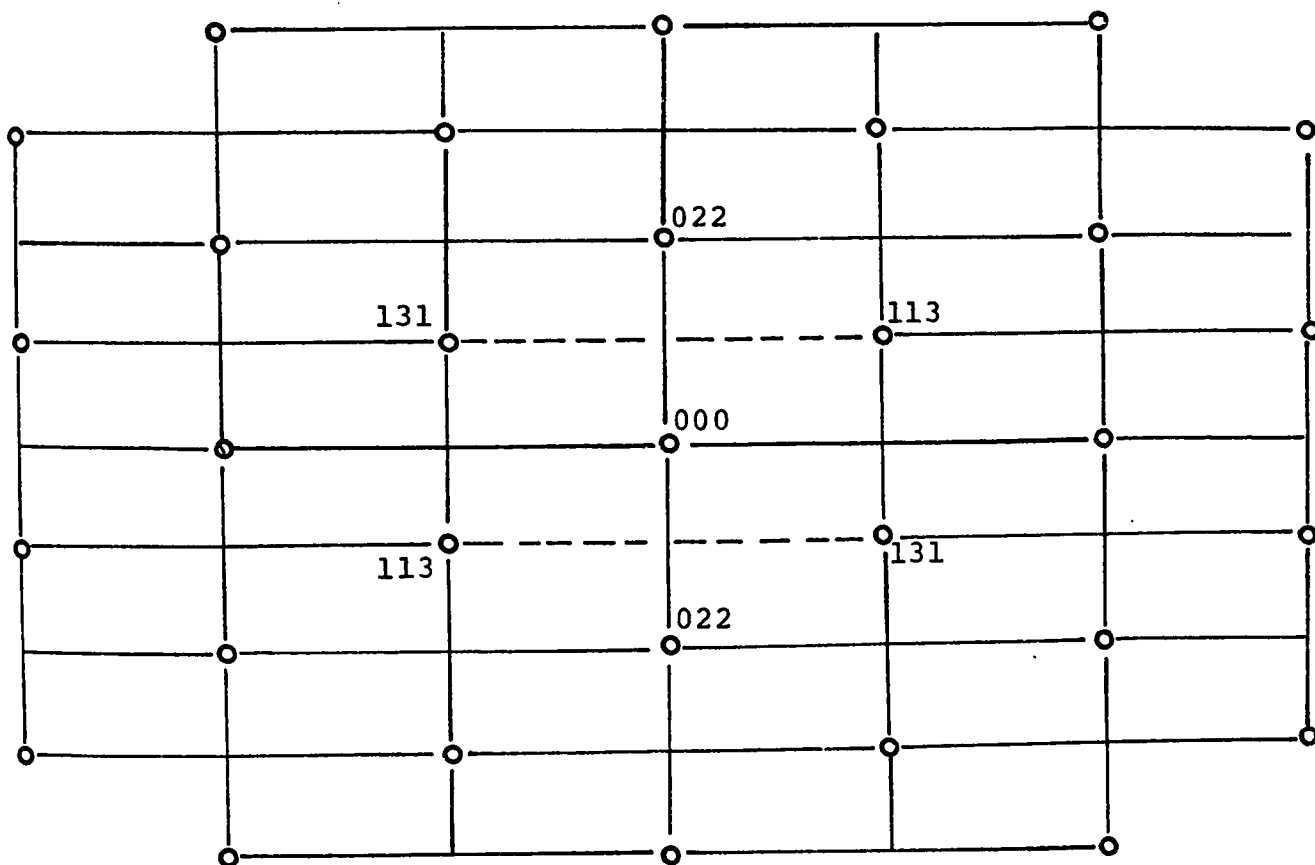
## (233) RELP OF NiO



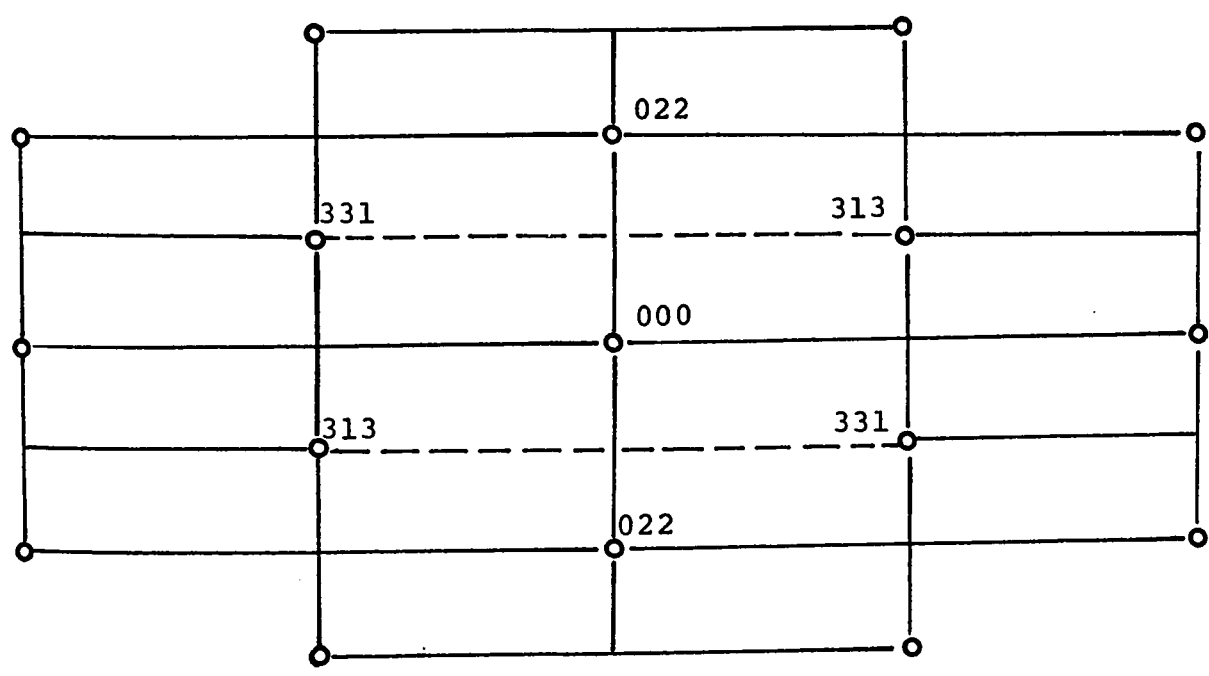
## (322) RELP OF NiO



## (411) RELP OF NiO



(433) RELP OF NiO



APPENDIX BINDEXING OF THE ELECTRON DIFFRACTION PATTERNS1. General considerations

The following interplanar spacings of NiO are given in the ASTM index card no. 4-0835

<u>d-spacing</u> (A)	<u>Relative intensity</u> (%)	<u>Miller indices</u> (hkl)	<u>Ratio of</u> ( $d_{111}/d_{hkl}$ )	<u>Sum of</u> ( $h^2+k^2+l^2$ )
2.410	90	111	1	3
2.088	100	200	1.16	4
1.476	57	220	1.63	8
1.289	16	311	1.92	11
1.206	13	222	2.00	12
1.044	8	400	2.30	16
.958	7	331	2.51	19
.933	21	420	2.58	20
.852	17	422	2.82	24
.804	7	511(333)	3.00	27

In an electron diffraction camera, these interplanar d-spacings will be at a distance R from a central spot of a photographic plate given by the relation:

$$R = \frac{\lambda L}{d}$$

where  $\lambda$  is the wavelength of the electrons,  $L$  is the distance from the specimen to the screen and  $d$  is the lattice spacing. The product  $\lambda L$  is called the camera constant and usually calculated from a known standard such as gold.

For a cubic system as in the case of NiO, the  $d$ -spacings can be expressed by the Miller indices:

$$d_{hkl} = \frac{a}{(h^2+k^2+l^2)^{\frac{1}{2}}}$$

where  $a$  is the cube edge. For each  $hkl$  plane, the distance  $R_{hkl}$  from the central spot can be written as:

$$R_{hkl} = \frac{\lambda L}{a} (h^2+k^2+l^2)^{\frac{1}{2}}$$

By substituting the calculated values of  $\lambda L$  and  $a$  of NiO, different values of  $R_{hkl}$  can be calculated and compared with those experimentally observed. Note that the  $d$ -spacings are proportional to  $(h^2+k^2+l^2)^{\frac{1}{2}}$  and thus the ratio of different  $R_{hkl}$  provide an independent check for the analysis.

## 2. Twinning in the oxide

Often twins are observed and the indexing of the twin patterns can be complicated further by the presence of other orientations. The indexing of the twins is treated in reference (92). A brief analysis is presented here.

When an  $(hkl)$  reciprocal matrix lattice plane is twinned on the  $(pqr)$ , the resulting  $(h^1k^1l^1)$  twin plane can be obtained from the following relations:



$$[hkl] + [h^1k^1l^1] = n[pqr]$$

For a cubic system there exists a parallelism between the (hkl) crystal plane and the (hkl) reciprocal lattice plane. The twin indices can be calculated from the following expressions:

$$n = \frac{2(ph+qk+kl)}{p^2+q^2+r^2}$$

$$h' = \frac{p(ph+2qk+2rl)}{p^2+q+r^2}$$

$$k' = \frac{q(2ph+qk+2rl)}{p^2+q^2+r^2}$$

$$l' = \frac{r(2ph+2qk+rl)}{p^2+q^2+r^2}$$

(a) For a simple case where the twin plane is parallel to the electron beam i.e. the twin axis is perpendicular to the beam, the resulting (h'k'l') can be obtained by a simple rotation of the (hkl) reciprocal lattice plane 180 degrees around the twin axis [pqr]. (see for example figure 4.3.1(g)).

(b) For the general case, (h'k'l') can be calculated from the above given relations. If (h'k'l') is a rational Relp it can be directly superimposed on (hkl) with a proper orientation. (see example given on page 144 of reference (92)).

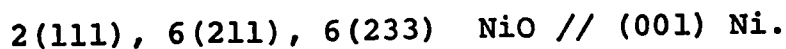
### 3. Indexing of pattern 4.2.1 (g)

The pattern is given in page 57 of this thesis. The first ring closest to the center of the pattern can be indexed

as the 111. It contains 12 equally spaced diffracted spots. Examination of all the reciprocal lattice planes of NiO in the appendix (A) indicates that only the (011), (211) and the (123) contain the {111} reflections. A brief inspection will quickly eliminate the (011) Relp, since the 200 spots are absent. Consider now the 311 and 222 rings which are respectively the 4th and the 5th. These rings can be quickly identified by their being closely spaced. (The sum of the squares of their Miller indices are exactly 11 and 12). There are also 12 equally spaced diffracted spots which can be accounted for by the rotation of the (211) Relp six times around the center. The (211) Relp is shown in the appendix (A). Consider now the 331 (7th) and the 420 (8th) rings. These rings are also close to each other; the sum of their Miller indices are respectively 19 and 20. There are 12 sets of 2 closely spaced diffracted spots. Inspection shows that the following reciprocal lattice planes: the (123), (233) and (433) contain the 331 reflections. Symmetry consideration will eliminate the (123) Relp, and a 6-fold rotation of both the (233) and the (433) Relps yield similar configuration on the 331 rings, but closed inspection of the higher order reflections will rule out the (433) Relp. The schematic drawing of the (233) reciprocal lattice plane is shown in the appendix A of this thesis. The presence of the 12 equally spaced diffracted spots on the 220 (3rd) ring can be rationalized by the 6 (233) Relps, but it can also be explained by

the commonly found orientation i.e. the (111) NiO // (001) Ni with one of the close packed direction of the oxide parallel to the two close packed directions of the metal. This configuration will give rise to the 12 diffracted spots on the 3rd ring. Indeed, inspection of the higher reflections such as the 422 (9th) ring justified this interpretation.

In conclusion the pattern can be indexed as:



The two (111) orientations are justified by the symmetry of the (001) metal substrate but the 6(211) are not. Both the (211) and (233) contain the [011] close packed direction. This direction can be parallel to the two in the metal substrate. This arrangement will only explain the presence of 4 diffracted spots on the 111 and 220 rings.

It is also possible that the (111) crystallites are slightly tilted with respect to the electron beam. Indeed an inclination of 19 degrees will bring in the (211) plane but the question may arise why only 19 degrees tilt? The (221) and (321) planes can be obtained by tilting the (111) fifteen and twenty two degrees exactly yet these two planes are not observed.

Twinning in oxide should also be considered. Twinning in any of the {111} planes of the (111) and (211) reciprocal lattice planes will give the {511} and {255} or {271} twinned reciprocal planes. These planes have not been found in the diffraction pattern.

Another possibility is that the (111) oriented oxide

crystallites are formed first and the (211) and (233) are subsequently formed on top of these (111) crystallites; this interpretation will justify the 6 closed packed directions for the (211) and (233) orientations. It is difficult to justify the presence of the 6(211) orientations in terms of the symmetry of the metal substrate but a small trace of impurity such as graphite can alter the influence of the substrate. In this case, these types of orientations are possible. Finally, it should be mentioned that the same pattern has been reported in the literature (64).

#### 4. Indexing of pattern 4.3.1(b)

The pattern can be seen in page 82 of this thesis. It contains only 2 {111} reflections. The reciprocal lattice planes of the oxide containing these reflections are the (011), (123) and (211). The (011) is easily eliminated by the presence of only 2 reflections on the 111 ring and the absence of the (200) diffracted spots. Symmetry consideration of the higher reflections such as the 311 confirms the (211) Relp. The evidence of the (123) Relp is also justified by considering the reflections on the 331 and 420 rings after matching the common 111 spots with the (211) Relp. The pattern is not complete, however, unless one considers its twinned reflections obtained by a  $180^\circ$  rotation about the (111) twin axis. The (123) Relp is shown in page 223 of the Appendix (A).

The 6 equally spaced spots on the 220 (3rd) ring combined with the higher reflections such as the 422 and 440

indicated that the (111) orientation is also present.

The superposition of the 3 above mentioned orientations still leaves 4 unaccounted reflections on the 311 (4th) ring. The angular relationship between these reflections are  $50^\circ$  and  $130^\circ$ . By picking out 2 random reflections such as the (131) and (113) and taking the dot product, the angle between these reflections was found to be  $50^\circ$ . A cross product yields the (411) zone axis. Thus, by plotting the (411) Relp and comparing with the pattern, it was found that all the reflections of the (411) Relp are accounted for by the pattern.

If one repeats the same procedure to other diffracted spots on the 331 and 422 rings, the (433) and (311) Relps are obtained. The observed angular relationship coupled with the symmetry of the patterns justify the presence of these planes.

Note that all the (111), (211), (311), (411) and (433) Relps contain a common close packed direction namely the [011] direction. This is evidenced by the fact that all these patterns can be superimposed by matching their common {022} reflections. Their existence are in agreement with the symmetry of the (011) nickel substrate which also has a close packed direction.

The (321) reciprocal lattice plane does not have a closed packed direction but it shares a common [111] direction with the (211) Relp. Its presence can be rationalized as being one of the six most densely populated Relps of the FCC

system or by an inclination of only 10 degrees from the (211) plane or a 22 degrees tilt from the (111) plane.

The twinned reflections of the (123) Relp can be justified by their angular relationships. The angle between the (420) and (331) spots and their twins are exactly 30 and 17 degrees which agree very well with observed values. Furthermore, there are no possible combinations of any 420 reflections to give an angle of 30 degrees. The {411} Relp can be obtained from (011) Relp by twinning on the (111). Since the (011) is not observed in the main pattern, this possibility will not be considered.

#### 5. Indexing the pattern 4.3.2(b)

The pattern is on page 86 of this thesis. There are four reflections on the 111 ring and two 200 diffracted spots which can be identified as belonging to the (011) Relp. On the 311 ring (5th) there are four reflections not related to the (011) plane. The angle between these reflections are 35 and 145 degrees exactly. A dot product between two random reflections such as the 131 and 131 yield an angle of 35 degrees and a cross product gives the (310) zone axis. By considering the higher reflections on the 331 ring, the presence of the (310) Relp is confirmed.

The two orientations above however do not explain the complete pattern. There are still two rows of strongly diffracted spots parallel to the  $[100]$  direction. The Miller indices of these reflections are respectively 420, 422 and 442. Inspection of all the Relps in the appendix A indicated

that the (210) contains all the above reflections. Indeed, a composite pattern made up of the above orientations after having matched their common 200 reflections account satisfactorily for all the diffracted spots. The pattern can be thus indexed as:

$$(011), (021), (031) \text{ NiO} // (011) \text{ Ni.}$$
$$[100] \text{ NiO} // [110] \text{ Ni}$$

6. Comment concerning the pattern 4.3.2(e)

The indexing of this pattern has been explained in detail in the section B(4). The two extra reflections on the (200) ring have been assigned to the (210) Relp since all the higher reflections are found to coincide with the reflections of other planes already present in the pattern. The (310) Relp also contains the (200) reflections, however the lack of correspondence of higher reflections rule out this possibility.

## Appendix C

The experimental errors involved in the quantitative measurement of some of the physical parameters in this thesis will now be discussed along with the limitations of the instruments and techniques used.

### 1. Lattice spacings measurement

For positive identification of the oxide film formed, the lattice spacings of the oxide were calculated from the SAD patterns using a calibrated camera constant ( $\lambda L$ ) determined from a gold standard. The values for the d-spacings determined from those measurements all agreed with the values reported in the ASTM index card to less than 1%. Since nickel oxide was the only oxide formed and reported, the use of certain special techniques such as an internal standard was not necessary. Perhaps the major source of error in the change of the d-spacings was the presence of the elastic strain frequently observed in the oxide film of this thickness range. Cathcart et al<sup>(121)</sup>, however, have shown that the elastic strain is usually removed after the film has been stripped from the metal substrate.

### 2. Oxidation kinetic curves

The oxidation kinetics curves which are expressed as weight gain vs. time were obtained on a continuously recording Cahn microbalance. The weight gain of the samples as recorded on the chart was cross-checked by weighing the samples before and after oxidation on a Mettler microbalance. The two values



for the weight gain were found to agree to  $\pm 20\mu\text{g}$  which represents an error of 3% for a typical weight gain of .7mg for a sample oxidized at 700°C for 50 hr. This error is insignificant when compared with the actual reproducibility of the kinetics curves which is in the order of 20-30%.

### 3. Evaluation of the parabolic rate constant, $K_p(t)$

From the oxidation kinetics curves plotted in parabolic form, the values for the effective parabolic rate constant,  $K_p(t)$ , at a given time can be calculated by taking the tangent to these curves. The evaluation of the tangents has been carried out by a finite difference method<sup>(122)</sup> using a computer. The technique consists of evaluating the coefficients for the best fitted polynomial to the seven chosen points of the experimental curve. The derivative of the function was then evaluated at the middle point. The confidence limit claimed by this technique is 3%. Again the error involved in the evaluation of the slope is much less than the actual reproducibility of the experimental which is in the order of 10-20%. (Typical values for the  $K_p(t)$  for the (100) nickel face evaluated at 25 hr at 700°C are respectively:  $8.87 \times 10^{-12}$  and  $7.01 \times 10^{-12}$  ( $\text{g}^2 \text{cm}^{-4} \text{sec}^{-1}$ )).

### 4. Evaluation of the activation energy for grain boundary diffusion and for the growth of the crystallites

The values for the boundary diffusion constant ( $K_B$ ) and for the crystallites growth constant  $K_3$ , which are determined from the physical measurements, both contain an activation energy term. The experimental results can thus be

fitted to an Arrhenius expression of the form  $A = A_0 \exp(-\frac{E}{RT})$ . A computer program based on a least square analysis has been written for this type of data. The program yields the values for  $A_0$ ,  $E$  and a correlation factor  $R$ . A standard deviation can be calculated from the values obtained and the uncertainty in the values of  $A_0$  and  $E$  can be deduced from the standard deviation. The following results have been obtained:

(a) Boundary diffusion constant,  $K_B = K_B^0 \exp(-\frac{E_B}{RT})$

(100) Face	(111) Face
$K_B^0 = 2.3 \pm 1.2 \times 10^{-2}$	$K_B^0 = 3.0 \pm 1.0 \times 10^{-2}$
$E_B = 31.1 \pm 3.5$ Kcal/g-atom	$E_B = 34.6 \pm 2.3$ Kcal/g-atom
$R = .975$	$R = .989$

(b) Crystallites growth constant,  $K_3 = K_3^0 \exp(-\frac{E_3}{RT})$

(100) Face	(111) Face
$K_3^0 = 3.2 \pm 1.4 \times 10^4$	$K_3^0 = 3.7 \pm 1.2 \times 10^5$
$E_3 = 21.8 \pm 2.0$ Kcal/g-atom	$E_3 = 13.6 \pm 1.5$ Kcal/g-atom
$R = .955$	$R = .992$

##### 5. Determination of the crystallite size

The size of the crystallites was determined from the DF micrographs by the linear intercept method<sup>(123)</sup>. The magnification of the microscope was calibrated for different lens settings using a replica of a diffraction grating of known spacings.

The DF pictures are taken with the objective aperture displaced to receive a diffracted beam and the image thus formed can be affected by the spherical aberration of the

objective lens. This spherical aberration has the effect of elongating the image point along the direction joining the central spot of the diffraction pattern<sup>(92)</sup>. The magnitude of the elongation  $R$  is given by the expression:

$$R = \frac{3C_s \lambda^2 \Delta\alpha}{d^2}$$

where  $C_s$  is the spherical aberration,  $\lambda$  is the wavelength of the electrons,  $\alpha$  is the angle the beam makes with the objective axis and  $d$  is the lattice spacing. Taking the typical values for  $3C_s = 10^8 \text{ \AA}$ ,  $\lambda = .04 \text{ \AA}$  and  $\Delta\alpha = 10^{-3}$  radian, an elongation of  $40 \text{ \AA}$  was found with  $d = 2 \text{ \AA}$ . This represents an error of 10% for an average crystallite of  $400 \text{ \AA}$ . This error, however, can be reduced in the Phillip EM300 which is provided with a tilting device to align the chosen diffracted beam along the objective axis.

The size of the crystallites was measured to an accuracy of .5mm on enlarged micrographs having an average magnification of 50,000. This represents an uncertainty of 20% for a crystallite having an average size of  $500 \text{ \AA}$ . Taking into account these different factors, an average error of at least 30% should be assigned to the determination of the crystallites size.

## REFERENCES

1. G. Tammam, Z. Anorg. Chem. 111, 78 (1920)
2. C. Wagner in Atom Movements, ASM, Ohio, 153 (1959)
3. N. Cabrera and N.F. Mott, Rept. Prog. Phys. 12, 163 (1948-49)
4. O. Kubaschewski and B. E. Hopkins, Oxidation of Metals and Alloys, Butterworths, London (1962)
5. W. W. Harris, F. L. Ball and A. T. Gwathmey, Acta Met. 5, 574 (1957).
6. J. M. Perrow, W. W. Smeltzer and J. D. Embury, Acta Met. 15 577 (1967)
7. J. M. Perrow, W. W. Smeltzer and J. D. Embury, Acta Met. 16 1209 (1968)
8. J. V. Cathcart, G. E. Petersen and C. J. Sparks, Jr., J. Electrochem. Soc. 116, 664 (1969)
9. J. Benard, Oxydation des Metaux, Gauthier-Villars, Paris, (1962)
10. K. Hauffe, Oxidation of Metals, Plenum Press, New York, (1965)
11. Kofstad, High Temperature Oxidation of Metals, John Wiley, New York, (1966)
12. Royer, Bull. Soc. for Miner. Cristallogra. 51, 7 (1928)
13. R. J. Gerdes and R. A. Young, Technical Report No. 6, project A644, Office of Naval Research, Metallurgy Branch, July (1967)

14. D. W. Pashley, *Adv. Phys.* 14, 327 (1965)
15. A. Neuhaus, *Fortschr. Miner.* 29/30 130 (1950/51)
16. A. Neuhaus, *Angew. Chem.* 64, 158 (1952)
17. H. Seifert, in Structure and Properties of Solid Surfaces  
University Press, Chicago (1953)
18. D. W. Pashley, *Adv. Phys.* 5, 173 (1956)
19. D. W. Pashley, M. J. Stowell and T. J. Law, *Phys. Stat.*  
*Sol.* 10, 153 (1965)
20. J. R. Drabble, Ph.D. thesis, Univ. of London (1949)
21. O. G. Engel, *J. Chem. Phys.* 20, 1174 (1952)
22. O. G. Engel, *J. Res. Natn. Bur. Stand.* 50, 249 (1953)
23. E. Bauer, *Z. Kristallogr.* 107, 72 (1956)
24. E. Bauer, *Z. Kristallogr.* 110, 372 (1958)
25. E. Bauer, A. K. Green, K. M. Munz and H. Poppa, Basic  
Problems in Thin Film Physics, (edited by R. Niedermayer  
and H. Mayer, Göttingen), (1966).
26. J. H. van der Merve, *Discuss. Farad. Soc.* 5, 201 (1949)
27. F. C. Frank and J. H. van der Merve, *Proc. R. Soc.* A198  
205, 216, 200, 125 (1949)
28. A. Masson, J. J. Metois et R. Kern, *Surface Sci.* 27, 463 (1971)
29. D. Walton, *Phil. Mag.* 7, 1671 (1962)
30. J. P. Hirth and G. M. Pound, *Progr. Meter. Sci.* 11, 45  
(1963)
31. J. L. Robins and T. N. Rhodin, *Surface Sci.* 2, 346 (1964)
32. J. Feder, K. C. Russell, J. Lothe and G. M. Pound, *Adv.*  
*Phys.* 15, 111 (1966)

33. J. L. Kenty and J. P. Hirth, *Surface Sci.* 15 403 (1969)
34. ASTM, card file of X-ray diffraction data
35. A.S.M. Metals Handbook, Cleveland: ASM (1948)
36. V. Martius, *Can. J. Phys.*, 35, 466 (1955)
37. E. A. Gulbransen and J. W. Hickman, Tech. Pub. 2068,  
Am. Soc. Mining and Met. Engrs. (1946)
38. J. P. Baur, R. W. Bartlett, J. N. Ong, Jr. and W. M.  
Fassel, Jr., *J. Electrochem. Soc.* 110, 185 (1963)
39. D. L. Douglas, *Corros. Sci.*, 8, 665 (1968)
40. A. Goswami, *Nature (London)* 191, 160 (1961)
41. J. D. Sartell and C.H. Li, *J. Inst. Metals*, 90, 92 (1961)
42. B. Ilschner and H. Pfeiffer, *Nature*, 40, 603 (1953)
43. L. Berry and J. Paidassi, *C. R. Acad. Sci. Paris*, 258,  
2810 (1964)
44. F. N. Rhines and J. S. Wolf, *Met. Trans.* 1, 1701 (1970)
45. M. O'Keefe and W. J. Moore, *J. Phys. Chem.* 65, 1438 (1961)
46. N. Birks and H. Rickert, *J. Inst. Metals*, 91, 308 (1962)
47. H. E. Farnsworth and R. E. Schlier, *Adv. Cor.* 9, 434 (1957)
48. H. E. Farnsworth and J. Tuul, *J. Phys. Chem. Solids* 9,  
48 (1959)
49. L. H. Germer and C. D. Hartman, *J. Appl. Phys.* 32, 1933  
(1961)
50. L. H. Germer and A. U. MacRae, *J. Appl. Phys.* 33, 2923 (1962)
51. H. E. Farnsworth, *Trans. 9th Natl. Vacuum Symp.* 68, (1962)
52. H. E. Farnsworth and R. L. Park, *J. Appl. Phys.* 35, 2220  
(1964)

53. L. G. Germer, E. J. Scheibner, and D. C. Hartman, *Phil. Mag.* 5, 222 (1960)
54. A. U. MacRae, *Surface Sci.* 1, 319 (1964)
55. K. R. Lawless, I. W. Young and A. T. Gwathmey, *J. Chim. Phys.* 53, 667 (1956)
56. M. Otter, *Z. Naturforschung* 14a, 355 (1959)
57. M. Shrank, Dissertation, Dormstadt (1958)
58. J. J. Trillat, L. Tertian and N. Terao, *Cahiers phys.*, 12, 161 (1958)
59. S. Shirai, *Proc. Phys.-Math. Soc. Japan*, 25, 637 (1943)
60. H. Pu, C. Chien-ti, and K. Ke-hsin, *Scientia Sinica* 14, 632 (1965)
61. E. I. Allesandrini, *J. Appl. Phys.* 35, 1606 (1964)
62. E. I. Allesandrini and J. F. Freedman, *Acta Cryst.* 16, 54 (1963)
63. L. E. Collins and O. S. Heavens, *Proc. Phys. Soc.* B70, 265 (1957)
64. L. B. Garmon, Ph.D. Thesis, University of Virginia, U.S.A. (1966)
65. J. H. van der Merwe, "Interfacial Misfit and Bonding between Oriented Films and Their Substrates" in Single Crystal Films, M. H. Francombe and H. Sato, eds. MacMillan, New York, (1963)
66. J. H. van der Merwe, *J. Appl. Phys.* 34, 117 (1963)
67. J. H. van der Merwe, *Phil. Mag.* 1, 1433 (1962)
68. N. Cabrera, *Surface Sci.*, 2, 320 (1964)

69. G. A. Basset, J. W. Menter and D. W. Pashley, Proc. Roy. Soc. A246, 345 (1958)
70. B. S. Borie and C. J. Sparks, Jr., Acta Cryst. 14, 569 (1961)
71. B. S. Borie, C. J. Sparks, Jr., and J. V. Cathcart, Acta Met. 10, 691 (1962)
72. A. Dalvi, Ph.D. thesis, McMaster University (1971)
73. J. M. Perrow, Ph.D. thesis, McMaster University (1967)
74. D. C. Wood, I. G. Wright and J. M. Ferguson, Corros. Sci., 5, 645 (1965)
75. M. Verway, M. Haaijman, H. Romeijnan and M. von Oosterhout, Phillips Research Repts., 5, 173 (1950)
76. S. P. Mitoff, J. Chem. Phys., 35, 882 (1961)
77. H. Uhlig, J. Pickett and J. MacNairn, Acta Met. 7, 111 (1959)
78. H. J. Engel, K. Hauffe and B. Ilschner, Z. Elektro chem. 58, 478 (1954)
79. K. Hauffe, L. Pethe and R. Schmidtt, J. Electrochem. Soc. 115, 456 (1968)
80. E. A. Gulbransen and K. F. Andrew, J. Electrochem. Soc. 104, 451 (1957)
81. W. J. Moore and J. K. Lee, J. Chem. Phys. 19, 255 (1951)
82. V. V. Ipat'ev and M. A. Ivanova, Ser. Khim. Nauk, No. 14, 80 (1954)
83. G. E. Zima, Trans. Amer. Soc. Metals 49, 924 (1957)
84. F. S. Pettit and F. J. Felten, J. Electrochem. Soc. 111 135 (1964)



85. K. Fueki and J. B. Wagner, *J. Electrochem. Soc.* 112, 384  
(1965)
86. J. Paidassi and L. Berry, *C. R. Acad. Sci. Paris* 262,  
1553 (1966)
87. Y. D. Tretyakov and R. A. Rapp, *Trans. Met. Soc. AIME*,  
245 (1235 (1969))
88. P. J. Harrop, *J. Materials Sci.* 3, 206 (1968)
89. L. M. Volpe and J. Reddy, *J. Chem. Phys.* 53, 1117 (1970)
90. A. T. Gwathmey and A. F. Benton, *J. Phys. Chem.* 46, 969  
(1942)
91. T. Homma, N. N.Khoi, W. W. Smeltzer and J. D. Embury,  
*Oxidation of Metals* 3, 463 (1971)
92. P. B. Hirsch, A. Howie, R. B. Nicholson, D. W. Pashley  
and M. J. Whelan, *Electron Microscopy of Thin Crystals*,  
London, Butterworths (1965)
93. G. B. Harris, *Phil. Mag.* 43, 113 (1952)
94. E. A. Gulbransen and K. F. Andrew, *J. Electrochem. Soc.*  
101, 128 (1954)
95. J. W. May and L. H. Germer, *Surface Sci.* 11, 443 (1968)
96. B. D. Cullity, *Elements of X-rays diffraction*, Addison-  
Wesley, Reading, Mass., 118 (1959)
97. K. R. Lawless and A. T. Gwathmey, *Acta Met.* 4, 153 (1956)
98. N. P. Pilling and R. E. Bedworth, *J. Inst. Met.* 29, 529  
(1923)
99. B. Borie and C. J. Sparks, Jr., *Thin film*, ASM, Ohio, 45 (1963)

100. H. P. Klug and C. E. Alexander, X-ray Diffraction Procedures" Wiley, New York, (1954)
101. B. D. Cullity, Elements of X-ray diffraction, Addison-Wesley, Reading, Mass. 262 (1959)
102. L. G. Schulz, J. Appl. Phys. 20, 1030 (1949)
103. C. S. Barret and T. B. Massalki, Structure of Metals, McGraw-Hill, New York, 203 (1966)
104. L. E. Murr, Electron Optical Application in Materials Science, McGraw-Hill 187 (1970)
105. R. Herchl, N. N. Khoi, T. Homma and W. W. Smeltzer, Oxidation of Metals 4, 35 (1972)
106. A. Nagasawa and S. Ogama, J. Phys. Soc., Japan 15, 1421 (1960)
107. D. W. Pashley and M. J. Stowell, Phil. Mag. 8, 1005 (1963)
108. D. W. Pashley, Phil. Mag. 4, 316 (1959)
109. C. S. Barret and T. B. Massalki, Structure of Metals, McGraw Hill, New York, 568 (1966)
110. R. E. Reed Hill, Physical Metallurgy Principles, D. Van Nostrand, New York, 214 (1966)
111. J. E. Burk and D. Turnbull, Prog. Met. Phys. 3, 220 (1961)
112. A. T. Gwathmey and A. F. Benton, J. Phys. Chem. 46, 969 (1942)
113. L. Lothe and G. M. Pound, J. Chem. Phys. 36, 2080 (1962)
114. G. M. Pound in: Energetics in Metallurgical Phenomena, Ed. W. Mueller (Gordon and Breach), New York, 85 (1958)

115. J. W. Matthews and E. Grünbaum, Appl. Phys. Letters 5,  
106 (1964)
116. J. W. Matthews and E. Grünbaum, Phil. Mag. 11, 1223 (1965)
117. E. W. Hart, Acta Met. 5, 597 (1957)
118. W. W. Smeltzer, R. R. Hearing and J. S. Kirkaldy, Acta  
Met. 9, 880 (1961)
119. P. A. Beck, J. Appl. Phys. 19, 507 (1948)
120. J. J. van der Broeck and J. L. Meijering, Acta Met., 16,  
375 (1968)
121. J. V. Cathcart, G. F. Petersen and C. J. Sparks in  
Surfaces and Interfaces, I. Chemical and Physical  
Characteristics, ed. Burke, Reed and Weiss, Syracuse  
University Press, Syracuse, N.Y. (1967)
122. H. C. Herschey, J. L. Zakin and R. Sinha, Ind. Eng.  
Chem. 6, 413 (1967)
123. H. E. Exner, Int. Met. Reviews, 17, 25 (1972)